UNIVERSITÉ DE STRASBOURG

ÉCOLE DOCTORALE des Sciences Chimiques

UMR 7006 – Institut de Science et d'Ingénierie Supramoléculaires (ISIS)

THÈSE présentée par :

Amélie GODEAU

soutenue le : **27 Séptembre 2016**

co-tutelle

pour obtenir le grade de : **Docteur de l'université de Strasbourg**

Discipline/ Spécialité : Physique Cellulaire

Cyclic contractions contribute to 3D cell motility

THÈSE dirigée par :

RIVELINE Daniel	Directeur de recherche, Université de Strasbourg. Strasbourg
OTT Albrecht	Professeur, Universität des Saarlandes, Saarbrücken

RAPPORTEURS :

LAUTENSCHLÄGER Franziska	Professeur, Universität des Saarlandes, Saarbrücken
PIEL Matthieu	Directeur de recherche, Institut Curie, Paris

AUTRES MEMBRES DU JURY :

CUKIERMAN Edna	Professeur, Fox Chase Cancer Center, Philadelphia
DELANOË-AYARI Hélène	Maître de conférence, Institut Lumière, Lyon
TOMASETTO Catherine-Laure	Directeur de recherche, IGBMC, Strasbourg
WASNIK Vaibhav Hermant	Docteur, Universität des Saarlandes, Saarbrücken

Acknowledgments

Foremost, I wish to thank my PhD supervisor Daniel Riveline for accepting me as a PhD student, the supervision especially the preparation for talks and the animated exchanges. I am grateful for all the things I could learn, the skills I could acquire and your support to keep the project advancing.

I also wish to thank my co-supervisor Albrecht Ott for the co-supervision of the PhD, the inspiring discussions and for being referee for my thesis.

I thank Franziska Lautenschläger and Matthieu Piel for being referee of the thesis and in the jury. I am also grateful to Edna Cukierman, Hélène Delanoë-Ayari, Catherine-Laure Tomasetto and Vaibhav Wasnik for being part of my jury.

Un grand merci à Hélène Delanoë-Ayari pour cette collaboration. Merci pour ton soutien, tes explications, les discussions animées et pour ton hospitalité. Cela a été un plaisir de travailler avec toi!

Merci à Sébastien Harlepp pour le travail sur les pinces optiques. Merci pour cette collaboration agréable et enrichissante.

I thank Mounir Maaloum for the AFM measurement and the pleasant exchange.

I wish to thank Julia Flesch for the help with the magnetic tweezers measurement and the quick answers on the setup.

I wish to thank Jacques Prost, Pierre Sens, Marco Leoni and Raphaël Voituriez for inspiring discussions and for bringing me one step nearer to understand the system.

I wish to thank the French-German University (UFA-DFH) for the support of the cotutelle.

I thank the Programme Doctoral International (PDI) for their support.

I thank H.P. Erickson for kindly sending the plasmids for generating fluorescent fibronectin, Bernardo Reina San Martin for providing murine lymphocytes, Anne-Sophie Thomas-Claudepierre for the extraction of these lymphocytes. I thank Amélie Freimuth and Marion Humbert of the cell culture facility (IGBMC) for the preparation of mouse embryonic fibroblasts and for giving me the protocol.

I want to thank the staff or IGBMC and ISIS for their technical support. I am grateful to the members of the imaging facility Marcel Boeglin, Elvire Guiot, Basile Gurchenkov, Yves Lutz, Nadia Messaddeq, Jean-Luc Weickert, Pascal Kessler, Marc Koch for their support. I am grateful to Christian Rick for the technical support in microfabrication and mask design. I am also grateful to the cell sorting platform.

I thank Jacky Goetz (Inserm) for the transmission of the CDM protocol and fruitful discussion.

I thank Ana Grabaraz and Evi Soutoglou (IGBMC) for providing BANF-1 cells and the collaboration.

I thank Naël Osmani for teaching me plasmid amplification and his advice on cell culture.

I thank Daniel Riveline, Jordi Comelles, Markus Rollinger, Johanna Blass, Jonas Dörr, Viktoria Wollrab, Émilie Le Maout and Iwona Mochol for commenting, proofreading the manuscript and for help on Latex.

I want to thank my amazing colleagues for the good times in the lab and the support. I want to thank Iliana Nedeva for teaching me immunostaining. Gracias David, por enseñarme el cultivo cellular, tu apoyo y tu buen humor en el lab. Ein Danke an Viktoria Wollrab für die vielen Diskussionen physikalischer und feministischer Natur und deinen Optimismus. Gracias Jordi, por todo lo q me has enseñado, tu paciencia (por mostrarme las basicas de matlab por ejemplo ;)), tu ayuda, tu apoyo y para aguantarme. Thank you Raghavan Thiagarajan for the discussions and your wise advice. I wish to thank my student Basile Jacquel for his experiments on microchannels. Merci à Émilie Le Maout pour les bons moments passés au labo et ton soutien moral. I want to thank Alka Bhat for the good mood and your positive nature. Un Merci à David Rodriguez pour la préparation de gelatine. Un merci à Claire Menouna pour l'aide administrative et son "oreille ouverte". Tristan Rupp pour nos discussions CDM autour d'une bière. Ebenfalls ein Dank an Jennifer Hepper für die administrative Unterstüzung und an Mathias Sander für sein schnelles Feedback.

Merci à tous mes amis, ma "famille" à Strasbourg. Merci pour votre soutien, les bons moments passés ensemble et les fous rires qu'on a pu partager.

Ein Dank an meine Familie, meine Eltern, Großeltern und meine Schwester für die Unterstützung. Merci de m'avoir permis et donné envie d'aller jusqu'ici.

Summary

Abstract: Cell motility is an important process in Biology. It is mainly studied on 2D planar surfaces, whereas cells experience a 3D environment *in vivo*. A key factor for motility is the force cells apply to their surrounding allowing them to move. The knowledge of the spatio-temporal distribution of these forces in combination with focal adhesions connecting the cell to its surrounding, acto-myosin cytoskeleton able to generate force, and fibronectin, the extracellular protein to which cells bind, permit to understand cell motility. We let cells move in a Cell Derived Matrix (CDM) and strikingly cells managed to deform the matrix with a specific pattern: contractions occur cyclically with two contraction centers at the front and at the back of the cell with a period of 13-14 min and a phase shift between contraction-relaxation of 3.5 min. The cycles enable the cell to optimally migrate through the CDM, as perturbation of cycles led to reduced motility. Cell confinement was found to be essential for contraction-relaxation cycles in contrast to the chemical environment of the CDM. We identified the cortex as a good candidate for contraction-relaxation cycles, as it contracts when mechanically challenged by laser ablation. The concept of two alternating contractions front and back of the cell was confirmed as we were able to trigger cell motility externally. Altogether, this study reveals a new mechanism of dynamic cellular behaviour linked to cell motility.

Cell migration is a fundamental process occurring during embryonic development [1] [2]. Many alterations in this process are usually considered as lethal. Cell migration also plays a role in cancer metastasis: during this process, cells invade other tissues and cross spaces where they are highly confined [3]. Although these phenomena take place in a 3D environment, cellular migration has been mainly investigated so far on 2D planar surfaces.
Actually, cell behaviour in 3D environment is quite different from the one observed on 2D flat surfaces. For example, the focal adhesions change from being restricted to the basal side of the cell to being distributed over the whole surface of the cell. The morphology of cells becomes more stellate and does not show a predetermined apico-basal polarity [4]. Also new modes of migration have been reported. In particular, cells change partially from a lamellipodia-based migration in 2D to a lobopodia-based migration in determined 3D environments. In this migration mode, cells have a voluminous cylindrical protrusion and show increased blebbing. It also requires a higher contractility of cells [5] and is based on a pressure driven mechanism [6]. Moreover, a prominent role for nucleus has been reported in 3D migration compared to 2D. The nucleus a "bulky" organelle in the cell could be a limiting factor in migration depending on the organization of the 3D environment as reported in [7]. For collagen matrices, migration is stalled for small pore sizes.
Another important factor for cell migration is the force applied to the surrounding. The distribution of forces together with the elastic modulus of the material and the visualization of cellular structures give access to the constraints to which the cell is submitted and allows to better understand cell motility. The vector character of the force and its amplitude permit to determine how a cell manages to pass through a dense entangled network where it is confined.

The starting point to investigate cellular migration in 3D is to generate a 3D environment. We chose to use Cell Derived Matrix (CDM) produced by cells for its physiological characteristics. As focal adhesions bind to fibronectin (FN), we decided to visualize this extracellular matrix protein and genetically modified cells which then secrete fluorescent FN. Together with the focal adhesions, the anchoring points of the cell and acto-myosin, the force generating proteins, we visualize all components to characterize and understand the deformation applied by cells. The CDM mechanics is characterized by optical tweezers measurement. We observe cell migration and quantify the displacement of FN fibers. Cell migration is perturbed by application of drugs and by mechanical probing of cells by laser ablation. This work has been conducted with various collaborations, Sébastien Harlepp (IPCMS, Strasbourg) for the optical tweezers measurements and Hélène Delanoë-Ayari (Université Claude-Bernhard, Lyon) for calculating the displacement of the FN network. Further collaborations on other projects include the ratcheting of cells on structured surface [8] and the wetting effect for the fusion of two cortical layers [9].

Characteristics of CDM
CDMs were synthesized by cells and we visualized the fibronectin meshwork by fluorescence. To study applied forces, it is important to have the mechanical characteristics of the material, therefore we measured the Young's Modulus of the CDM by optical tweezers. A bead incorporated in the CDM was trapped in a laser beam and the stage moved leading to two opposing forces: the restoring force of the network and the force of the laser

beam. The comparison of the movement of the bead inside the trap with the movement of a reference bead, which only follows the movement of the stage, gives access to the elastic modulus. The distribution of Young's Modulus revealed a mean value of about 50 Pa. This represents a soft material for a cell which it should be able to deform. The viscoelastic properties of the CDM were evaluated by comparing the network before and after passage of cells. The network stayed unchanged, the CDM is assumed to be fully elastic, thus we discarded plastic deformation. This was further confirmed by the quick relaxation in the order of seconds of the network by optical tweezers measurements.

Cells deformation is required to pass through dense entangled network
Cells were integrated in the matrix and cell migration studied. To migrate through the CDM, cells either deform themselves or apply deformation to the network. The nucleus deformed during migration: it had to squeeze to pass through small pores of the mesh. A deformation factor was calculated as the ratio of the area of the nucleus and the convex area. The deformation factor is lowest for highest deformation. It also allowed to align deformation of various sequences and to center them on the highest deformation, thus allowing to investigate the dynamic behaviour of the squeezing. Interestingly the speed was maximal for the unsqueezing process. A peak was obtained right after the highest nucleus deformation is observed when tension upon the nucleus is released. This suggests that the nucleus is being pushed by the back of the cell. It also indicates that cells are highly confined in this 3D environment. This is confirmed by the respective measure of the nucleus size of 11 μm and the typical pore size of the CDM of 2 μm.

Deformations occur front and back of cell in a cyclic manner
The most striking phenomenon observing cells migrate is that they deform the FN network. To investigate the characteristics of the deformation, displacement was calculated with the KLT method. This method is based on identifying bright features and calculating their displacement between two pictures. This revealed a deformation pattern: Contractions occur at the front and the back of the cell in cycles. The mesh was pulled to centers at the front or at the back of cells and is released again. The arrows of KLT analysis converged to these spots. Autocorrelation analysis was used to extract periods for the front and the back of the cell 13.8 ± 1.7 min and 13.0 ± 1.4 min respectively. Arises the question of the relation between front and back contraction. Do they occur simultaneously or is there a time lag between both? To clarify this question, we performed cross correlation analysis and obtained a mean value of 3.5 ± 1.2 min. This means that contraction-relaxations do not occur simultaneously but have a phase shift.

Contraction at the back precedes cell translocation
The next question was how these cycles are connected to movement of the cells? What is the role of each contraction? Therefore, we compared displacement of the mesh with displacement of the cell with the nucleus as a reference. Cross correlation analysis was performed on both and peak positions extracted. Peak positions indicate a possible time shift between two events. The time shift between back contraction and cell movement was determined to be -3.4 ± 1.8 min and front displacement and nucleus movement 1.9 ± 1.3 min. This means contraction at back precedes cell movement and displacement at the

front occurs after cell movement. It suggests that back contraction is the actor of cell displacement. Another oscillatory phenomenon has been observed. Instantaneous speed is not constant, but exhibits pulsatile behaviour. Autocorrelation has been performed and a period of 17.9 ± 1.6 min obtained. Plotting the persistent speed against the period of speed oscillation reveals that the higher the frequency the faster the cell is able to migrate. The curve follows an exponential decay. We suspect a link between contraction-relaxation cycles and pulsatile behaviour visible in cell speed. Altogether, cell movement would be generated as follows: Contraction at the back precedes cell movement which is followed by a relaxation at the front.

Cyclic behaviour is connected to 3D confining environment
As it can not be excluded that a compound of the CDM synthesized by cells triggers contraction-relaxation cycles, we used another 3D setup to see if cyclic behaviour occurs. Microchannels with appropriate dimensions represent as CDM a confining environment with a higher elastic modulus. Cell migration was observed in microchannels of 4-8 μm width and 5 μm in height. Morphology and cytoskeletal structures are similar to cells in CDM. Cells exhibited acto-myosin cortex, stress fibers, the actin gel and the focal adhesions. When studying cell movement in confining microchannels, we observed that movement is not continuous but pulsatile. We extracted the period of these oscillations and obtained 24 ± 1.4 min which is higher compared to CDM ($17,9 \pm 1.6$ min). We deduce that the chemical environment is not essential for the generation of contraction-relaxation cycles. These seem to rather rely on 3D confining environment.

Key molecular actors of contraction-relaxation cycles
To investigate the molecular origin of the contraction-relaxation cycles in deformation patterns, actin, myosin and microtubules were inhibited. We compared persistent speed, trajectories, differential force and speed fluctuations.
First, the Rho pathway was tested by using Y27632, a ROCK inhibitor (10 μM). ROCK phosphorylates Myosin Light Chain Kinase (MLCK) in particular. Morphology of the cells changed, they showed more branched protrusions. Persistent speed was nearly unchanged and trajectories were similar to control case. Differential force dropped by 44 ± 10 %. Cyclic behaviour of speed with a mean period of 20.7 ± 1.3 min could still be observed. Except for morphological changes and differential force drop, no difference was detected for inhibition of ROCK compared to control.
Myosin was inhibited by Blebbistatin (25 μM) and ML-7 (10 μM), inhibiting the MLCK. In both cases migration was reduced, persistent speed diminished compared to control and derivative force dropped by around 73 ± 5 % and 81 ± 1 % respectively. Cells treated with ML-7 still showed oscillations in speed with a larger period of 24 ± 3 min compared to control. For blebbistatin treated cells, no oscillation could be detected. To study if contractions can be externally triggered, we performed laser ablation experiment in the presence of the drug. No contraction could be induced, therefore we deduce that myosin activity is required for contraction-relaxation cycles and that it is the main actor of force generation. Increasing myosin activity by adding Calyculin A 1 nM, led cells to round up and to bleb. No migration could be observed. Surprisingly increased contractility did not lead to higher motility in our CDM.

Latrunculin A was applied to cells in CDM to harvest actin monomers leading to depolymerization of the actin cytoskeleton. A low dose of the drug (1 μM) stopped migration, cells became spherical with some remaining thin protrusions and the differential force was reduced by 96 ± 1 %. Then, we acted on actin dynamics with C8, a synthetic polyamine promoting lamellipodia growth [10] and CK666, an Arp2/3 inhibitor (100 μM and 50 μM respectively) which both lowered migration. Persistent speed was lower and trajectories shorter. For both cases, cyclic behaviour in speed could be detected thus period had higher values of 27 ± 4 min and 27 ± 3 min than for control case. Altering the actin cytoskeleton stalled migration and changing actin dynamics lowered motility of cells and shifted dynamics of contraction-relaxation cycles.
Inhibition of microtubules by Nocodazole (10 μM) ended persistent migration. Cells were still motile and oscillated around a center of mass. Contraction-relaxation cycles were still present after altering the function of microtubules. The period of oscillation was higher at 22 ± 1 min than for control case. Microtubules might not be needed for contraction-relaxation cycles but for maintaining polarity in cells which is crucial for persistent migration. Moreover, cyclic behaviour could be detected for cells lacking nucleus, the cytoplasts. They performed a forward backward movement with a period of 36 ± 2 min of in the CDM. Therefore, we deduce that cycles do not require a nucleus, pointing towards an intrinsic property of the acto-myosin cytoskeleton.
Altogether, the probing of molecular structures revealed that acto-myosin is the driving actor of contraction-relaxation cycles, as these disappeared for actin cytoskeleton depolymerization and inhibition of myosin by blebbistatin. In the other cases, dynamics of cyclic behaviour was affected and cell motility reduced. Contraction-relaxation cycles still occur upon Nocodazole incubation, pointing again to an essential role of acto-myosin.

Mechanically induced contractions
To further probe the cellular structures involved in the deformation pattern, regions of the cell were laser ablated. We differentiate between polarized and non-polarized cells. A polarized cell has a broken symmetry where a front with a protrusion and a back with a trailing or round rear can be identified. A non-polarized cell does not have a predetermined polarity. We concentrated on cutting holes in stress fibers, in the gel around the nucleus and in the cortex at the front and the back of the cell. Ablation in the stress fibers led to a relaxation of the cell. Stress fibers were moving away from the cut location and no further contraction occurred. Ablation in cortex yielded an interesting reaction of the cell. First, a relaxation of CDM and cell could be observed, an actin rim appeared around the nucleus, then the actin intensity at the ablated spot increased and a contraction occurred. In polarized cells, ablation in the cortex at the front of the cell produced a rather symmetric contraction. Cutting in the cortex at the back of the cell also triggered a contraction and moreover a movement of the cell. The contraction led to the detachment of the cell back and a net forward movement. Ablation in the gel at the back of the nucleus produced only a small relaxation followed by the actin rim and an intensity increase at the ablation spot. Globally, no contractions were observed in these experiments, except for two cells. We deduce from these experiments that contractions are produced by the cortex and not by the gel.
To further confirm our hypothesis that it is the synchronized front and back contractions

which allow cells to move forward in CDM, we triggered contractions front and back of cell. A first contraction at back was induced and led to detachment of cell rear. Then, a second cut was placed at the cortex in front of the nucleus. Also here ablation was followed by the continuation of the forward movement. The third cut was placed at the back of the cell again and motility was maintained. Interval between cuts was 10 min. This was performed for various cells with 2-3 cuts. These experiments show that cyclic contraction front back lead to cell motion in 3D CDM, thus confirm our hypothesis.

We observed deformation patterns on CDM while cells migrate. We also revealed deformation cycles of contraction-relaxation, both at the front and the back of the cells, pointing to the presence of two force dipoles. The connection with the movement of cells was investigated and revealed that contraction at the back preceded cell movement which was then followed by relaxation at front. By using microfabricated channels of the same dimension as CDM, cyclic behaviour in speed was recapitulated, establishing a link with the 3D environment of the cell and excluding a chemical component as the key triggering factor. By targeting the cytoskeletal components, the role of actin and myosin in generating the contraction-relaxation cycles was revealed. The supramolecular structures such as cortex and gel were mechanically probed by laser ablation. Cutting in cortex triggered contraction of cells and with a proper location of ablation spot, led to cell motility. Actin gel did not show the same response and was therefore discarded from the list of potential generators of contraction-relaxation cycles. Multiple ablations in the cortex triggered and sustained cell motility. This suggests that cycles of contraction-relaxation effectively lead to cell motility in 3D CDM. The faster the oscillation, the larger the speed, which suggests a functional role for this built-in property of acto-myosin gels. Potentially, these oscillations may contribute to open pores thereby allowing the passage of the nucleus. Future work includes the development of a physical model allowing to explain the origin of contraction-relaxation cycles.

Résumé

Résumé court: La motilité des cellules est un phénomène fondamental en biologie, notamment lors de l'embryogénèse, le cancer ou la cicatrisation. Ce phénomène est principalement étudié dans des conditions peu physiologiques comme des surfaces planes. Pour mieux comprendre le pénomène *in vivo*, nous avons utilisé une matrice synthétisée par des cellules (CDM) pour étudier la migration tridimensionnelle. Nous portons notre intérêt sur les déformations de la matrice appliquées par les cellules qui permettent avec la connaissance de la distribution de la fibronectine, des points d'ancrage de la cellule, les contacts focaux et l'acto-myosine capable de générer une force, de mieux comprendre comment la cellule interagit avec son environnement. L'analyse du champ de déformation révèle que, contrairement aux surfaces 2D, les cellules ont un comportement cyclique d'applications de déformations. Il y a deux centres de contractions à l'avant et à l'arrière de la cellule. Par le biais de l'autocorrélation des déformations, nous révélons une période de contraction et un décalage entre contraction-relaxation à l'arrière et à l'avant. La motilité est étroitement liée à cette déformation. Après la contraction à l'arrière, la cellule bouge et le mouvement est suivi d'un relâchement à l'avant. Les oscillations de vitesse observées sont également liées à une force oscillante. Pour exclure une cause chimique du CDM comme étant responsable des contractions, nous avons fabriqué des micro-canaux chimiquement neutres. Dans ces canaux, les cellules migrent de manière pulsatile. Cela nous permet d'exclure un effet chimique du CDM et de confirmer que ces cycles sont connectés au confinement des cellules. Grâce à l'utilisation de drogues spécifiques, nous avons identifié l'acto-myosine comme étant l'acteur principal de ce phénomène de contraction-relaxation. Par la suite, nous distinguons les différentes structures cellulaires impliquées. Les résultats indiquent que le cortex est l'acteur responsable des contractions-relaxations, comme il est le seul à provoquer un mouvement après ablation laser. Nous appliquons également plusieurs ablations sur une cellule pour reproduire des contractions avant-arrière et sommes capables de provoquer une motilité cellulaire. L'ensemble de cette étude met en évidence un nouveau mécanisme fondamental de dynamique cellulaire, impliqué dans le mouvement des cellules.

La motilité tridimensionnelle des cellules est un processus clé de la biologie par exemple dans l'embryogenèse [1] [2] et la dissémination du cancer [3]. Historiquement, avec le développement de la boîte de Petri, la motilité des cellules a principalement été observée sur des surfaces planes. Cela ne correspond pas à l'environnement physiologique que les cellules peuvent trouver dans un organisme et peut ainsi entraîner des résultats artéfactuels. D'où la nécessité d 'étudier le déplacement des cellules dans un environnement tridimensionnel. Par ailleurs, en augmentant la dimensionnalité, les cellules changent de morphologie et deviennent plus longilignes, leurs adhésions sont distribuées différemment, notamment sur toute la surface du corps cellulaire et en termes de mécanotransduction, l'axe normale à la surface peut jouer un rôle plus important [4]. Par ailleurs, on peut s'attendre à un empêchement stérique du déplacement, car en 3D la cellule est entourée de fibres de protéines extracellulaires. Cela a été rapporté pour des cellules migrant dans des matrices de collagène. La rapidité du déplacement dépend de la taille des pores de collagène et de la déformabilité du noyau. Avec des "petits" pores, la migration est stoppée [7]. De plus, d'autres modes migratoires peuvent émerger en 3D. Il a été découvert que, dans des matrices dérivées de cellules, les cellules migraient principalement avec des lobopodes au lieu de lamellipodes, la structure classique de la migration sur surface plane. Les lobopodes sont des structures volumineux à l'avant de la cellule formant la protrusion. Ce mode migratoire est associé à une augmentation du nombre de 'blebs' et il dépend de la contractilité cellulaire [5]. Un mécanisme basé sur la différence de préssion a été proposé pour ce mode migratoire [6].
Un autre facteur important pour comprendre la migration cellulaire est la force appliquée par la cellule. Cette force visible par la déformation du réseau permet à la cellule de se déplacer. Le champ de déformation donne accès aux contraintes auxquelles est soumise la cellule. Dans l'ensemble, la direction et l'amplitude des déformations combinées avec les caractéristiques de la motilité permettent d 'établir de quelle manière la cellule arrive à traverser un environnement dense tridimensionnel.
Pour étudier la motilité tridimensionnelle, nous avons choisi une matrice synthétisée par des cellules pour ses caractéristiques physiologiques, et nous avons observé la migration de cellules à l'intérieur de cette matrice. Nous avons identifié les entités nécessaires pour caractériser la migration en 3 dimensions et les avons marquées avec des molécules fluorescentes. Il s'agit des contacts focaux, établissant un lien entre les cellules et leur environnement, points de transmission de force. Nous visualisons également l'actine, acteur du cytosquelette capable d'exercer une force et la matrice synthétisée par des cellules. La déformation est caractérisée par des mesures de pince optique, puis analysée et mise en relation avec la migration cellulaire. Différentes entités moléculaires et supramoléculaires ont été perturbées pour évaluer leur rôle dans les phénomènes observés. Plusieurs collaborations notamment avec Sébastien Harlepp (IPCMS, Strasbourg) pour les pinces optiques, Hélène Delaonë-Ayari (Université Claude Bernhard Lyon) pour l'extraction du champ de déformation ont permis à ce travail d'avancer. J'ai également collaboré sur des projets portant sur la question de la possibilité de diriger des cellules grâce à la topographie de l'environnement [8] et sur l'effet de mouillage entre deux couches de cortex à l'endroit de fusion [9].

Les caractéristiques mécaniques de la matrice
La matrice dérivée de cellules (CDM) est produite par des cellules cultivées 8-9 jours sur une lamelle de verre pré-traitée avec de la gélatine. Durant cette période, les cellules produisent et sécrètent des protéines notamment de la matrice extracellulaire. Au terme de la culture, les cellules sont extraites de la matrice et les matrices sont disponibles pour des expériences. La fibronectine est la protéine à laquelle se lient les intégrines des contacts focaux établissant ainsi un contact entre l'environnement et l'intérieur de la cellule. En conséquence, nous modifions génétiquement les cellules qui produisent le CDM afin d'obtenir le réseau de fibronectine fluorescent. Résultat frappant, les cellules déforment ces matrices. Pour pouvoir interpréter ces déformations appliquées par la cellule, il faut connaitre les caractéristiques visco-élastiques voire plastiques de la matrice. Pour cela, des billes sont introduites lors de la culture du CDM et manipulées avec des pinces optiques. La mesure de pince optique consiste à capturer une bille dans le faisceau de laser et de déplacer le support. Ainsi vont s'opposer la force élastique de la matrice à laquelle est liée la bille et la force du piège optique. En comparant le déplacement des billes dans le piège avec une bille de référence dans le CDM, nous avons accès au module élastique du réseau. La moyenne du module de Young est de 50 Pa, ce qui correspond à un matériau "mou", amplement déformable par l'amplitude de force qu'est capable d'appliquer une cellule. Pour évaluer s'il s'agît d'un comportement complètement élastique, nous avons comparé les tracés de billes à l'entrée et à la sortie du piège optique. Ces tracés sont symétriques indiquant un comportement élastique. De plus des CDMs ont été visualisés avant, pendant et après migration cellulaire. Le réseau reste inchangé après déformation. Nous excluons tout écoulement du réseau et le traitons par la suite comme un matériau élastique.

Déformation de la cellule pour intégrer et passer à travers de la matrice
Les cellules sont déposées sur le CDM et leur migration étudiée. Elles entrent toutes dans le réseau. Pour entrer dans la matrice, les cellules déforment d'une part leur corps cellulaire et d'autre part le réseau. Cela est aussi valable pour la migration à l'intérieur de la matrice. Celle-ci est formée par un réseau enchevêtré de fibronectine où, vu les dimensions de la matrice, la cellule est à l'étroit; elle est confinée. Nous avons constaté pour certaines cellules une déformation du noyau, point de référence étant le plus rigide et le plus volumineux de la cellule. La déformation peut se quantifier par le facteur de déformation que nous définissons comme le quotient de la superficie projetée et de la superficie projetée convexe du noyau. Ce facteur évolue au fil de la déformation. Cela permet de comparer les vitesses instantanées des noyaux lors de la déformation. La dynamique de déformation du noyau est intéressante: la vitesse du noyau augmente après le relâchement des contraintes. Cela veut dire que la vitesse la plus élevée est observée au moment où le noyau sort du pore qui lui imposait la déformation. Cela nous suggère qu'il y a un mécanisme à l'arrière qui pousse le noyau.

Le déplacement des cellules est lié aux motifs de déplacement de fibres
Lors de la migration, les cellules appliquent une force à leur environnement. Notre montage nous permet de visualiser ce déplacement de fibres. La carte des déplacements montre qu'il y deux centres de contraction, un à l'avant et l'autre à l'arrière de la cellule. Les

flèches représentant le déplacement de fibres convergent vers ces centres. Ces contractions ne sont pas continues, elles sont suivies de relaxation du réseau. La cellule contracte et relâche périodiquement le réseau à l'avant et à l'arrière. Pour caractériser ces cycles de contraction-relaxation, nous appliquons une analyse de corrélation pour le déplacement des fibres avant et arrière de la cellule. Cette analyse montre que la période des contractions arrières et avant est respectivement de 13.0 ± 1.4 min et 13.8 ± 1.7. Pour savoir si les contractions ont lieu en même temps, nous calculons la corrélation croisée des déplacements. Cette analyse révèle un décalage d'une moyenne de 3.5 ± 1.2 min entre contraction à l'arrière et relaxation à l'avant. Les contractions et relaxations sont quasiment en opposition de phase. Quel rôle jouent ces oscillations pour la motilité tridimensionnelle et pour la migration? Pour élucider cette question, nous comparons le déplacement du réseau et de l'arrière du noyau. Quel mouvement précède l'autre? La distribution du temps de décalage démontre que le mouvement du réseau à l'arrière de la cellule est de -3.4 ± 1.8 min ce qui veut dire qu'il précède le mouvement du noyau. Le décalage avec le mouvement avant de la cellule est 1.9 ± 1.3 min, indiquant que le mouvement à l'avant suit le mouvement à l'arrière. En analysant les valeurs du coefficient de corrélation, nous voyons qu'elles sont positives pour l'arrière et négatives pour l'avant. Cela signifie qu'il y a contraction à l'arrière et un relâchement à l'avant. La suite du mouvement serait donc une contraction à l'arrière provoquant le mouvement de la cellule suivi d'un relâchement à 'avant de la cellule. En plus des contractions périodiques, nous observons également que la vitesse de la cellule n'est pas constante. En appliquant une analyse d'auto-corrélation de la vitesse, nous voyons que la période est de 17.9 ± 1.6 min. La vitesse de persistance décroit de manière exponentielle en fonction de la periode d'oscillation. Une cellule ayant une fréquence d'oscillation plus élevée se déplacera plus rapidement. Nous supposons que ces phénomènes d'oscillation sont liés et qu'une force appliquée en cycles génère une vitesse oscillante. Une periode plus courte permetterait à la cellule de migrer plus vite.

Le confinement comme élément nécessaire aux cycles de contraction-relaxation
Pour être sûrs que ce phénomène d'oscillation n'est pas dû à une composante de la matrice synthétisée par des cellules, nous avons étudié la migration dans des micro-canaux aux dimensions similaires du CDM de 5 μm d'épaisseur et 4 μm à 8 μm de large. Nous restons dans un milieu confinant mais avec un module de Young plus élevé que le CDM, et que les cellules ne peuvent plus déformer. D'abord, nous avons constaté que la morphologie et la structure des composantes supramoléculaires de la cellule dans les micro-canaux étaient les mêmes que dans le CDM. En observant la migration des cellules dans les canaux, nous avons de plus constaté que la migration avait une forme pulsatile, le mouvement paraissait plus saccadé. Pour cela, les périodes de ce mouvement avant arrière ont été extraites. Une période plus élevée dans les canaux a été mesuré (de 24 ± 1.4 min), comparée à la période dans le CDM ($17,9 \pm 1.6$ min). Par la suite, nous excluons qu'un acteur chimique du CDM puisse être responsable des cycles de contraction-relaxation et affirmons que ces effets de contraction-relaxation ont pour condition un environnement confinant tridimensionnel.

L'acto-myosine est l'acteur principal des cycles de contraction-relaxation
Quel est le mécanisme de ces cycles de contraction-relaxation et quels sont les acteurs moléculaires impliqués? Pour répondre à cette question, nous avons inhibé ou dépolymérisé

plusieurs acteurs moléculaires notamment la myosine et ses voies de régulation, l'actine et les microtubules. Nous comparons les trajectoires parcourues, les vitesses observées et la force appliquée. Pour commencer nous avons inhibé Rho kinase avec de l'Y27632 (10 μM). La vitesse de migration des cellules est inchangée ainsi que la longueur des trajectoires. Le charactère oscillatoire est toujours présent avec une période de 20.7 ± 1.3 min. Cependant la force exercée diminue de 44 ± 10 %.
Ensuite, nous avons inhibé la myosine par la blebbistatine (25 μM) et le ML-7 (10 μM). Dans le cas de la blebbistatine, les tracés sont nettement inférieurs au contrôle et la vitesse de persistance est divisée par deux. Pour le ML-7 les trajectoires sont plus courtes et la vitesse de persistance plus basse, de 0.43 ± 0.03 μm/min. Dans les deux cas, la force diminue de 73 ± 5 % et 81 ± 1 % respectivement. Le charactère oscillatoire est toujours présent avec une periode de 24 ± 3 min pour l'inhibition avec le ML-7. Nous constatons l'absence de cycles de contraction-relaxation sous influence de la blebbistatine. Quand nous augmentons le degré d'activité de la myosine par le biais de la calyculine (1 nM), nous observons que les cellules s'arrondissent et forment des "blebs". Apparemment elles ne sont plus en mesure de maintenir de contacts focaux. Aucune migration n'a pu être observée.
La seconde structure moléculaire à être testée est l'actine, protéine du cytosquelette présente dans le cortex, le gel d'actine formant les lamellipodes et les fibres de stress. D'abord, nous avons dépolymérisé l'actine avec la latrunculine A (1 μM). Dans ce cas, aucune migration n'a pu être observée et la force diminue de 96 ± 1 %. Ensuite nous avons inhibé le complexe Arp2/3 (50 μM) responsable du branchement d'actine dans le gel agissant en tant que nucléateur. La vitesse est diminuée à 0.40 ± 0.03 μm/min ainsi que les trajectoires. Nous avons aussi testé la drogue C8 [10] (100 μM) qui est un polyamine synthétique et il a été démontré qu'elle pouvait agir comme nucléateur. Dans ce cas également la motilité des cellules est diminuée, les trajectoires plus courtes et une vitesse de persistance plus lente à 0.39 ± 0.06 μm/min. Nous observons toujours des vitesses oscillantes pour ces conditions expérimentale avec une période de 27 ± 4 min pour le C8 and 27 ± 3 min pour le CK666. De ce fait, désassembler le cytosquelette d'actine a une conséquence décisive sur la migration. Augmenter ou diminuer l'activité de gels d'actine (lamellipode ou cortex) donnent le même résultat, la motilité étant diminuée.
Un autre acteur du cytosquelette ayant une caractéristique dynamique est le microtubule. Nous dépolymérisons les microtubules par addition de nocodazole (10 μM). Les cellules changent de morphologie, deviennent plus compactes. Les cellules ne migrent plus, étonnamment, elles oscillent sur place. Une période d'oscillation a pu être extraite en appliquant l'analyse d'autocorrélation sur la déformation avant/arrière de la cellule. Les points de retour ont été extraits avec origine "peak finder" et la période calculée. Les résultats des deux analyses sont cohérents. Des oscillations ont même pu être détectées sur des cytoplastes - fragments de cytoplasme qui se sont détachés du corps de la cellule et ne comportant plus de noyau. Cela indique que les cycles de contraction-relaxation sont indépendants de microtubules, et indépendants du noyau de la cellule. Ces cycles sont des phénomènes basés sur l'activité de l'acto-myosine.

Le déclenchement local de centres de contractions induit la motilité contrôlée des cellules
Ces expériences ne donnent pas encore accès à l'acteur supramoléculaire qui est respons-

able de la génération de cycles de contraction-relaxation. L'acto-myosine peut s'organiser en fibres de stress contractiles, en cortex de la cellule ou bien en gel d'actine qui a pu être observé autour du noyau. Pour approfondir cette question, nous coupons les structures en question avec un laser et étudions la réponse de la cellule. Nous faisons la différence entre une cellule polarisée, exhibant une brisure de symétrie avant-arrière, et une cellule non polarisée qui a priori est symétrique. Une coupure dans une fibre de stress a pour résultat un relâchement de la tension exercée par la cellule et visible dans le calcul de déplacement du réseau. On voit également que les deux extrémités de la fibre coupée s'éloignent l'une de l'autre. La seconde structure ciblée est le cortex. En coupant, nous observons un relâchement du réseau. Cet évènement est suivi de la formation d'un anneau d'actine autour du noyau, puis d'un flux d'actine à l'endroit de la coupure et enfin d'une contraction de la cellule. Quand nous coupons dans le cortex à l'arrière d'une cellule déjà polarisée, nous observons la même réaction décrite précédemment et un mouvement de la cellule dû à la contraction stimulée par la coupure du laser. Une ablation dans le gel d'actine visible autour du noyau (coupure à l'arrière) ne génère pas le même effet qu'une coupure dans le cortex. Très peu de relaxation est visible et quasiment pas de contraction. L'anneau d'actine autour du noyau et l'augmentation du signal d'actine à l'endroit de la coupure sont toujours présents. A une ou deux reprises, une contraction a pu être observée dans des cellules polarisées. Par contre, l'origine de la contraction n'était pas située à l'endroit de l'ablation, mais à l'arrière de la cellule dans le cortex. Nous supposons que l'effet de l'ablation peut se transmettre au cortex de la cellule et provoquer une contraction. Ces résultats indiquent que le cortex est le moteur principal des cycles de contraction-relaxation que nous avons reproduits artificiellement. Cela nous mène à la question suivante : peut-on provoquer la migration dirigée des cellules en ablatant de façon localisée? Pour confirmer notre hypothèse de travail que deux sites de contraction-relaxation sont nécessaires pour permettre à la cellule d'avancer, nous appliquons plusieurs coupures à intervalles dans le cortex d'une cellule. Nous avons d'abord ablaté à l'arrière induisant une contraction et générant un début de mouvement. La deuxième ablation a lieu à l'avant du noyau et est suivi de la continuation du mouvement de la cellule. Ensuite la troisième coupure est appliquée à nouveau à l'arrière de la cellule et nous pouvons toujours observer le maintien du mouvement. Ce phénomène a été reproduit sur plusieurs cellules à deux ou trois coupures. Nous en déduisons que deux contractions avant-arrière dans une cellule génèrent la motilité cellulaire.

Pour conclure, nous avons mis en évidence que des cycles de contraction-relaxation avec différents centres de contraction avant-arrière et un délai entre contraction-relaxation induisaient la migration de cellule dans des matrices synthétisées par des cellules. L'origine du phénomène observé n'est pas dû aux composantes chimiques du CDM mais au confinement des cellules. L'acto-myosine est l'acteur principal de ces cycles et nous sommes en mesure de reproduire contractions et cycles de contraction permettant d'induire une motilité cellulaire. La relation entre période d'oscillation et vitesse de persistance suggère un rôle fonctionel pour cette propriété intrinsèque du gel d'acto-myosine. Les oscillations pourraient permettre à la cellule d'élargir les pores du CDM pour faciliter le passage. Pour mener le projet au-delà, nous proposons de développer un modèle physique dont la perspective est d'expliquer l'origine des cycles de contraction-relaxation.

Zusammenfassung

Kurzzusammenfassung: Zellmigration ist ein fundamentaler Bestandteil der Biologie, involviert u.a. in die Ebryonalentwicklung oder die Metastasenbildung. Dieser Prozess wurde bisher hauptsächlich auf flachen zweidimensionalen Flächen untersucht. Eine entscheidende Rolle für die Fortbewegung der Zelle spielt die Kraft, die diese auf ihre Umgebung ausübt. Die Deformation in Kombination mit den Verbindungspunkten der Zelle mit der Matrix, den fokalen Adhäsionen, den Kaft erzeugenden Strukturen und dem Matrixprotein Fibronektin an das die Zellen binden, erlaubt es die Zelllokomotion besser zu verstehen. Wir beobachten Zellmigration in einer dreidimensionalen Matrix und identifizieren zwei kontraktile Zentren im vorderen und hinteren Teil der Zelle, welche mit einer Phasenverschiebung zyklisch kontrahieren und relaxieren. Die einengende Umgebung spielt eine entscheidende Rolle für die beobachteten Phänomene im Gegensatz zu den chemischen Komponenten der Matrix. Kontraktionen sind Aktomyosin abhängig, was durch Inhibition von Aktin, Myosin und Mikrotubuli festgestellt wurde. Des Weiteren schränken wir die Zytoskelettstruktur auf den Zellkortex als möglichen Verursacher der Zyklen ein. Durch Laserablation erzeugen wir lokale Kontraktionen, alternieren wir diese vorne und hinten sind wir in der Lage Zelllokomotion zu reproduzieren. Wir schlagen vor, dass in dreidimensionaler Umgebung zyklische Kontraktionen im vorderen und hinteren Teil der Zelle die Migration ermöglichen.

Zellmigration spielt eine wichtige Rolle in diversen biologischen Prozessen [1] [2] [3], allerdings wurde diese bisher hauptsächlich auf Flächen wie z.B. in einer Petrischale beobachtet. Dies entspricht nicht einer physiologischen Umgebung, der Zellen *in vivo* ausgesetzt sind, und kann zu Artefakten führen. Aus diesem Grund ist es wichtig Zellmigration in dreidimensionaler Umgebung zu erforschen.
Es wurde beobachtet, dass bei dem Übergang zu einer dreidimensionalen Umgebung Änderungen verschiedener Zellstrukturen auftreten. U. a. ändert sich die Verteilung der fokalen Adhäsionen. Befindet sich die Zelle auf einer flachen Oberfläche sind die Adhäsionen zwischen der Oberfläche ausschließlich an der apikalen Seite der Zelle. Ist die Zelle in einer dreidimensionalen Umgebung, sind die fokalen Adhäsionen über die komplette Oberfläche der Zelle verteilt. Auf einer zweidimensionalen Oberfläche haben Zellen eine von außen vorgegebene, apiko-basale Polarität, welche in einer dreidimensionalen Umgebung nicht gegeben ist. In 2D treffen Zellen nicht auf Hindernisse, wohingegen in einer dreidimenisonalen Umgebung, die aus einer fibrillären Matrix besteht, die Zelle sterische Hinderungen erfahren kann. Dies kann vor allem eine Rolle für den Nukleus spielen, der das größte und härteste Zellorganell darstellt [7].
Bei Änderung der Dimensionalität wurde ebenfalls eine Anpassung des Migrationsmodus beobachtet. Statts der in 2D vorkommenden Lamellipodien an der Spitze der Zellen bilden Zellen in 3D Lobopodien aus. Ein Lobopodium wird als voluminöse, zylindrische Membranausstülpung an der Spitze der Zelle beschrieben [5]. In diesem Fall basiert der Mechanismus der Migration auf einen Druckunterschied innerhalb der Zelle zwischen dem Volumen vor und hinter dem Nukleus und auf eine erhöhte Kontraktilität der Zelle, was auch an Bläschen beobachtet werden kann [6].

Ein wichtiger Faktor für die Zellmigration ist die Kraft, die die Zelle auf ihre Umgebung ausübt. Die Verteilung der auf das Netzwerk ausgeübten Kräfte kann Aufschluss über die intrazelluläre Zellkraftverteilung geben, welche wiederum Einblick gewährt, wie eine Zellbewegung zu Stande kommt. Wir untersuchen die Deformation der Umgebung der Zelle und korrelieren diese mit der Zellmigration. Dazu sind ein verformbares Substrat mit bekannten Materialeigenschaften, die Kenntnis der Adhäsionspunkte der Zelle mit dem Substrat und die Verteilung bestimmter Komponenten des Zytoskeletts nötig. Die Deformation wurde in Kollaboration mit Hélène Delanoë-Ayari (Université Claude-Bernhard, Lyon) untersucht. Um Aufschluss über die Materialeigenschaften zu bekommen, wurde die optische Pinzette in Kollaboration mit Sébastien Harlepp (IPCMS, Strasbourg) verwendet.
Der erste Schritt zum Studieren von Zellmigration in einer 3D Umgebung ist die Erzeugung einer solchen Umgebung. In unserem Fall haben wir uns für eine von Zellen produzierte Matrix entschieden (engl. Cell Derived Matrix CDM) [11]. Zellen wurden 8-9 Tage auf einem auf Gelatine basierenden Substrat gezüchtet. In dieser Zeit produzierten und sekretierten sie Proteine der Extrazellulären Matrix. Eines dieser Proteine ist Fibronektin (FN), an das fokale Adhäsionen mit Integrinen binden. Im Anschluss wurden diese Zellen aus der Matrix entfernt. Um die Verteilung von FN zu bestimmen, wurden Zellen genetisch modifiziert, so dass sie fluoreszierendes FN sekretierten.

Um Kräfte bestimmen zu können, ist die Kenntnis der viskoelastischen Eigenschaften der

Matrix notwendig. Dazu wurde das Elastizitätsmodul via optischer Pinzette bestimmt. Eine Polystyrol Kugel, die während der Produktion des CDMs integriert wurde, wird in einem Laserstrahl gefangen. Wird der Mikroskoptisch bewegt auf dem sich das Substrat befindet wirkt die Rückstellkraft der Matrix der Kraft des Lasers gegenüber. Aus der Bewegung innerhalb der optischen Falle in Relation zu einer Referenzbewegung einer Kugel außerhalb des Laserstrahls, kann das Elastizitätsmodul ermittelt werden. Wir erhielten eine durchschnittlichen Wert von rund 50 Pa. Wir überprüften ebenfalls die Plastizität des Polymernetzwerkes. Dazu wurde das CDM vor und nach Zellmigration aufgenommen und die Verformung festgestellt. Durch Vergleich des Zustands der Matrix vor und nach Zellmigration, konnten wir feststellen, dass keine plastische Verformung stattgefunden hatte. Somit kann das CDM als elastisch angesehen werden.

Das CDM stellt eine einengende Umgebung für die Zelle dar. Um das dichte Netzwerk der Matrix zu überwinden, mußen Zellen entweder (i) ihren Zellkörper oder (ii) ihre Umgebung verformen. Ersteres konnte man vor allem am Nukleus beobachten, der bei kleinen Poren durch Deformation die Form einer Sanduhr annahm. Die Verformung des Nukleus wurde durch einen Deformationsfaktor charakterisiert und die Geschwindigkeit während der Verformung untersucht. Interessanterweise war die Geschwindigkeit des Nukleus maximal für den Moment nach der höchsten Deformation, wenn die Spannung auf den Nukleus nachließ. Dieser Prozess weist auf ein Drücken bzw. eine Kontraktion des hinteren Teils der Zelle hin.

Die zweite Möglichkeit der Zelle im Netzwerk voranzukommen ist durch die Deformation der Matrix gegeben. Die Deformation wurde nach einer auf dem Kanadé-Lucas-Tomasi (KLT) Algorithmus basierenden Methode berechnet und wir konstatierten, dass diese nach einem bestimmten Muster erfolgt. Kontraktion war im vorderen Teil der Zelle sichtbar, anschließend im hinteren Teil der Zelle bevor die Zelle wieder vorne kontrahierte. Wir registrierten Zyklen von Kontraktion-Relaxation im vorderen und hinteren Teil der Zelle. Um Aufschluss über die Perioden dieser Kontraktionen zu erlangen, wendeten wir eine Autokorrelationsanalyse der Deformationen im vorderen und hinteren Bereich der Zelle an. Für den vorderen Teil erhielten wir einen durchschnittlichen Wert von 13.8 ± 1.7 min und hinten 13.0 ± 1.4 min. Um zu bestimmen ob diese Kontraktionen und Relaxationen zeitgleich erfolgen oder ob ein gewisser Phasenunterschied auftritt, berechneten wir die Kreuzkorrelation zwischen beiden Deformationen. Wir erhielten eine durchschnittliche, zeitliche Verschiebung von 3.5 ± 1.2 min der Kontraktion und der Relaxation. Dies bedeutet, dass Kontraktionen nicht zeitgleich im vorderen und hinteren Teil der Zelle stattfinden.

Welcher Zusammenhang besteht zwischen diesen Kontraktionszyklen und den unterschiedlichen Kontraktionszentren mit der Zelllokomotion? Um diese Frage zu beantworten, untersuchten wir zu welchem Moment sich die Deformation des Netzwerkes im Verhältnis zur Nukleusbewegung ereignet. Durch das Berechnen der Kreuzkorrelation zwischen der Netzwerkdeformation und der Bewegung des Nukleus, erhielten wir für den hinteren Teil der Zelle einen durchschnittlichen Wert von -3.4 ± 1.8 min und für den vorderen Teil 1.9 ± 1.3 min. Dies bedeutet, dass zuerst eine Kontraktion im hinteren

Teil der Zelle erfolgt, was darauf hindeutet, dass diese die Bewegung der Zelle hervorruft. Anschließend findet eine Deformation am vorderen Teil der Zelle statt. Interessanterweise stellten wir fest, dass auch die Geschwindigkeit der Zelle nicht konstant war. Diese schwankte mit einer mittleren Periode von 17.9 ± 1.6 min. Wir konnten feststellen, dass die Geschwindigkeit der Zelle mit ansteigender Periode abnimmt. Eine höhere Periode ermöglicht ein schnelleres Vorankommen in der Matrix. Wir vermuten einen Zusammenhang zwischen der periodischen Variation der Geschwindigkeit und den Kontraktions-Relaxations-Zyklen.

Da eine Rolle der chemischen Komponenten des CDM in der Generierung der Kontraktions-Relaxations-Zyklen nicht ausgeschlossen werden kann, untersuchten wir ob Zyklen ebenfalls in einer weiteren, dreidimensional einengenden Umgebung beobachtet werden können. Dazu analysierten wir Zellmigration in einer definierten, chemisch neutralen Umgebung, den Mikrokanälen. Die Kanäle wurden aus Polydimethylsiloxane (PDMS) hergestellt und entsprechen den Dimensionen des CDMs. Wir prüften, ob Zellen die gleiche Morphologie haben und die gleichen Zytoskelettstrukturen aufweisen wie im CDM. Wir stellten fest, dass auch hier die Zellen in einer oszillatorischen Weise migrieren. Die Geschwindigkeit ist nicht konstant sondern durchläuft periodische Schwankungen. Wir folgern, dass die dreidimensionale, einschränkende Umgebung des CDMs für die zyklische Bewegung ausschlaggebend ist und nicht die chemische Umgebung.

Um die beteiligten molekularen Akteure zu identifizieren, inhibierten oder depolymerisierten wir unterschiedliche Komponenten des Zytoskeletts: Myosin Aktin und Microtubuli. Myosin wurde mit Blebbistatin (25 μM) und ML-7 (10 μM) inhibiert. Bei Inhibition mit Blebbistatin wurde eine verringerte gerichtete Geschwindigkeit und ein kürzerer zurückgelegter Weg bei Zelllokomotion festgestellt. Keine Kontraktions-Relaxations-Zyklen wurden beobachtet. Der Effekt von ML-7 war weniger ausgeprägt: Zurückgelegte Wege waren kürzer und die gerichtete Geschwindigkeit niedriger als im Kontrollfall. Periodische Geschwindigkeitsänderungen erfolgten mit einer höheren Periode von 24 ± 3 min. Für beide Substanzen, wurde eine Verringerung der relativen Kraft um 73 ± 5 % und 81 ± 1 % festgestellt. Bei Erhöhen der Kontraktilität durch Calyculin A (1 nM) erfolgte keine Migration mehr. Die Zellen wurden rund und bildeten Bläschen. Es wirkte als könnten sie keine fokalen Adhäsionen mehr bilden.
Wurde Aktin durch Latrunculin A depolymerisiert (1 μM) wurden Zellen rund und keine Migration wurde mehr beobachtet. Auch Deformation war kaum noch vorhanden und nahm um 96 ± 1 % ab. Wie erwartet wurde durch Latrunculin A die Integrität des Zytoskeletts zerstört, was weitreichende Folgen für die Zellmigration nach sich zog und die Kontraktions-Relaxations-Zyklen unterbindete. Wurde die Aktindynamik mit C8 (100 μM) oder CK666 (50 μM) beeinflusst, konnte eine verringerte Motilität festgestellt werden. Geschwindigkeitsvariationen wurden mit einer Periode von 27 ± 4 (C8) min and 27 ± 3 min (CK666) beobachtet.
Microtubuli sind ein weiterer, dynamischer Bestandteil des Zytoskeletts. Wir depolymerisierten sie durch Zugabe von Nocodazole (10 μM). Als Reaktion konnten wir beobachten, dass Zellen auf der selben Stelle blieben und sich um einen Schwerpunkt hin- und herbewegten. Dies konnte durch die Bestimmung der Autokorrelation der Deformation

und durch Autokorrelation der Geschwindigkeit des Nukleus bestätigt werden. Daraus schließen wir, dass die beobachteten Zyklen auf Aktomyosinaktivität basieren.
Zytoplasten, Zellen ohne Nukleus, die sich spontan formen, wiesen auch ein oszillatorisches Verhalten auf, was deutlich macht, dass für Kontraktion-Relaxations-Zyklen der Nukleus nicht benötigt wird und es sich um eine intrinsische Eigenschaft des Aktomyosins handeln könnte.

Welche Zellstruktur genau für die Zyklen verantwortlich ist, stellten wir durch Laserablation fest. Als Strukturen stehen der Zellkortex oder ein Aktingel um den Nukleus zur Auswahl. Beide Strukturen wurden durch einen Laserstrahl mechanisch getestet. Beim Schneiden in den Zellkortex konnte zunächst die Relaxation der Zelle und der Matrix beobachtet werden. Darauf folgte die Bildung eines Aktinrings um den Nukleus und Erhöhung des Aktinsignals an der ablatierten Stelle. Zuletzt konnte eine Kontraktion beobachtet werden. Ablation des Aktingeles rief eine geringere Reaktionen der Zelle hervor. Eine leichte Relaxation, ein Aktinring um den Nukleus und die Erhöhung des Aktinsignals konnten auch hier beobachtet werden. Allerdings trat keine Kontraktion auf. Wurde an einer polarisierten Zelle, einer Zelle, die eine definierte Spitze mit Membranausstülpungen aufweist, der Kortex am hinteren Teil der Zelle ablatiert, löste die Kontraktion eine Vorwärtsbewegung aus. Durch die unterschiedlichen Reaktion auf Laserablation folgern wir, dass der Kortex mit hoher Wahrscheinlichkeit die Zytoskelettstruktur ist, die Kontraktion-Relaxation-Zyklen hervorruft.
Wir nutzten diese Methode daraufhin, um zu untersuchen, ob wir ebenfalls durch alternieren der Kontraktion, Migration erzeugen und weiterführen können und somit unsere Hypothese testen können, wonach zwei zyklisch kontrahierende Zentren in der Zelle Lokomotion ermöglichen. Wir ablatierten zunächst im Kortex am hinteren Teil der Zelle, bevor wir vorne in der Zelle Kortex ablatierten. Der dritte Schnitt wurde wiederum am hinteren Teil der Zelle im Kortex angesetzt. Der erste Schnitt erzeugte das Loslösen des hinteren Teils der Zelle, beim zweiten Schnitt führte die Zelle die Bewegung fort, was ebenfalls für den dritten Schnitt der Fall war. Wir sind in der Lage die nativen Kontraktions-Relaxations-Zyklen zu reproduzieren. Dies bestätigt, dass zwei Kontraktionszentren die zyklisch kontrahieren und relaxieren Lokomotion erzeugen können.

Wir haben gezeigt, dass Zellen in elastischer dreidimensionaler Umgebung Zyklen aus Kontraktion und Relaxation durchführen welche zwei Zentren im vorderen und hinteren Teil der Zelle haben. Diese Kontraktionen haben spezifische Perioden, die zueinander phasenverschoben sind. Die Zellbewegung folgt auf die Kontraktion des hinteren Teils der Zelle, bevor vorne die Deformation erfolgt. Die Zyklen basieren auf Aktomyosinaktivität und die chemischen Umgebung des CDMs spielt nur eine untergeordnete Rolle. Der Kortex ist die Zellstruktur, die solche Kontraktionen erzeugen kann und durch künstlich hervorgerufene Kontraktion im vorderen und hinteren Teil der Zelle kann Zellmigration erzeugt werden. Je höher die Periode der Oszillation der Geschwindigkeit, desto schneller ist die Vorwärtsbewegung der Zelle. Dies deutet auf eine funktionale Rolle der auf intrinsischen Eigenschaften des Aktomyosingels beruhenden Kontraktions-Relaxations-Zyklen hin. Wir schlagen vor, dass diese Oszillationen dazu beitragen es den Zellen zu erlauben Poren im CDM zu vergrößern und somit ein Vorankommen in der Matrix zu ermöglichen.

Contents

Movies

Movie 01: Bead in CDM trapped by a laser beam. Stage moves in x-direction. Jump-out and jump-in of the bead can be observed. Scale bar 5 μm and movie in real time.

Movie 02: REF52 migrating in CDM. Scale bar 25 μm and time in hh:mm.

Movie 03: Mouse embryonic fibroblast WT migrating in CDM. Scale bar 25 μm and time in hh:mm.

Movie 04: Lymphocyte migrating in CDM. Scale bar 25 μm and time in hh:mm.

Movie 05 : HeLa cell migrating in CDM. Scale bar 25 μm and time in hh:mm.

Movie 06 : SW480 cell migrating in CDM. Scale bar 25 μm and time in hh:mm.

Movie 07: Cell migrating in CDM and performing nucleus squeezing. Scale bar 10 μm and time in hh:mm.

Movie 08: Cell expressing mCherry Lifeact migrating through CDM. Fibronectin visible in yellow. Scale bar 10 μm and time in hh:mm.

Movie 09: Overlay of phase contrast images of migrating cell with result of KLT analysis. Green arrows describe mesh displacement. Scale bar 25 μm and time in hh:mm.

Movie 10: Cell expressing mCherry Lifeact in CDM (YFP) contracting periodically at the back. Scale bar 20 μm and time in hh:mm:ss.

Movie 11: Cell expressing mCherry Lifeact in CDM (shown in previous movie) contracting periodically at the back. Scale bar 20 μm and time in hh:mm:ss.

Movie 12: Phase contrast movie of cell migrating in CDM. Scale bar 25 μm and time in hh:mm.

Movie 13: Cell migrating in CDM in the presence of 25 μM blebbistatin. Cell has branched protrusions and cell body mainly consists of nucleus. Scale bar 25 μm and time in hh:mm.

Movie 14: Cell in CDM in the presence of 1 μM Latrunculin A. Cell rounds up and does not deform its environment anymore. Scale bar 25 μm and time in hh:mm.

Movie 15: Cell in CDM in the presence of 10 μM Nocodazole. Cell oscillates on the spot, but does not migrate anymore. Scale bar 25 μm and time in hh:mm.

Movie 16: Cell expressing RFP zyxin and GFP-NMHC2A migrating in microchannel. Top, middle and bottom planes of channel are acquired. Movement is non-continuous, pulsatile. Scale bar 10 μm and time in hh:mm.

Movie 17: Cell expressing mCherry Lifeact gets laser ablated at 7 s. Scale bar 20 μm and time in mm:ss.

Movie 18: Cell gets laser ablated at 7 s. Scale bar 20 μm and time in mm:ss.

Movie 19: Cell is being ablated 3 times in time interval of 10 min. Ablation spots are situated at the back, front and back. Time in mm:ss and scale bar 20 μm.

1 Introduction

Cell migration belongs to one of the fundamental processes in cell biology. Cancer metastasis may start with a cell escaping the primary tumor [12]. In embryogenesis cell migration contributes to have the proper tissue distribution [2]. Wound healing relies on the motile properties of the cell closing the wound [13]. The immune system has lymphocytes, leukocytes and dendritic cells fighting off intruders [14] [15]. Hence, cell migration which takes place within the context of a 3D environment inside a body has for historical or practical reasons mainly been studied on flat 2D surfaces.
We aim at understanding cell migration under a physics perspective. In high Reynolds number[1] environment, one needs to apply force to move an entity. This is intuitive, as for example climbing up a tree. Force needs to be applied with the arms to lift the body up. The same applies to cells, even though they live at low Reynolds number without inertia. This implies that their movement stops when the force disappears. Cells need to perform a time irreversible movement to obtain a net forward movement. Otherwise they only move around a center of mass. Cells have to apply forces to the surrounding in a specific manner to move forward. Biophysics allows to describe the dynamics of the traction force and its role in cell migration [16].
In this chapter I present cell migration and introduce the different steps needed to obtain a net movement. As we follow the path of the cell, I establish the basics to understand our work and convey the motivation. I will start to describe cell migration in 2D where cells need a **cytoskeleton** which forms **supramolecular structures**. These are controlled by the **Rho pathway**. Via **focal adhesions** cells are connected to the cytoskeleton and the **extracellular matrix**. These allow them to apply **forces** to their surrounding enabling them to move forward. Then, we integrate all the elements and revisit the state of the art for 3D cell migration.

1.1 Cell migration

1.1.1 Cell migration on flat 2D surfaces

Here, we treat the 2D mesenchymal migration mode which is the most prevalent one. Other modes as the ameboid migration or migration with blebbing can also appear on surfaces. The physical description of how force is applied to obtain motion is introduced in the section 1.6 Forces. Cell migration is described in five canonical steps (1.1) [17]: establishment of front-rear polarization, cell protrusion at the front, attachment of the leading edge, cell contraction and detachment of the rear. Upon repetition of this cycle a net translocation is achieved. Without external cue, cells exhibit a persistent random

[1] *Definition in Appendix*

walk [18] which can be modified with external chemical or mechanical cues.

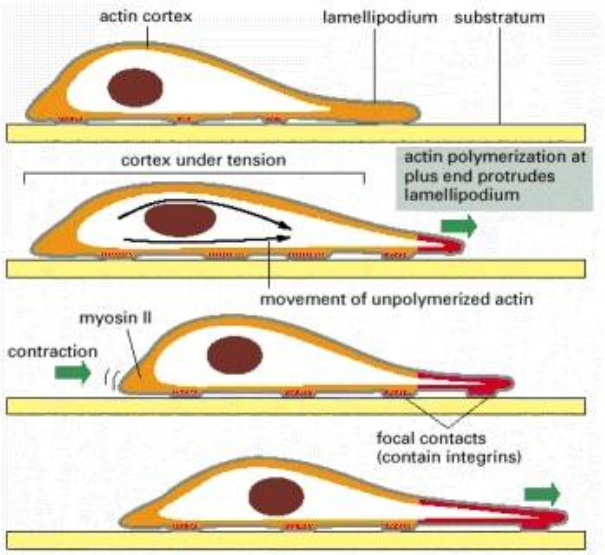

FIGURE 1.1: Steps of migration: Cell extends at the front via actin polymerization in the lamellipodium followed by the nucleation of a new adhesion. Upon myosin II contraction at the back of the cell, trail retrieves and nucleus is pushed forward, a net translocation is obtained (Figure from [19]).

Cell migration is tightly regulated by the Rho A pathway and integrates spatial and temporal information [19]:

> From an isotropic state the first event of cell migration is the polarization of the cell [20]. A symmetry breaking must occur determining a front and a back of the cell with different adhesion properties, actin distributions and a gradient of myosin contractility. The cell needs to maintain this polarization throughout the subsequent steps of migration.
>
> Once the cell structure organized, actin polymerization takes place at the leading edge, pushing the membrane forward and hence extending the cell forward. To convert the force applied by the protruding edge into movement, the cell must be anchored to the substrate. Focal contacts which mature to focal adhesions are formed and the membrane is attached at the leading edge [21].
>
> It is not sufficient to grow at the front, the cell body also needs to translocate. This is obtained by a myosin II dependent contraction. Myosin II activity is dependent on its degree of phosphorylation controlled by the Rho pathway [22]. Force is transmitted to the substrate via focal contacts but to move forward the cell needs to detach from the substrate. Force transmission and focal contact density depend on the availability of ligands. As a consequence cell migration speed has a biphasic behaviour and the relation of ligand density and cell speed has a dumbbell shape [23]. At an optimal ligand density cells have enough focal adhesions to apply the traction

force but not too many to not prevent detachment from the surface. Migration relies on this cooperation of signals and any variation can have huge impact such as virtually "gluing" the cell to the substrate [24].

For the retraction of the rear focal adhesions need to disassemble. This can be mediated by different mechanisms. The actin assembly at the front of the lamellipodium leads to a disassembly of the focal contact at the lamellum level. The stress fibers tension might also lead to a disassembly of the adhesion. For instance trails of extracellular domains of adhesions receptors have been reported [25]. Also protease activity can cleave talin and integrin β_3 [26]. Another way for the cell are kinases which phosphorylate proteins loosening the focal contacts. The later ones tend to disassemble under the actin retrograde flow [27] .

The migration cycles are also controlled by RhoGTPases which integrate different signals and coordinate the migration steps. Furthermore, environmental conditions can also influence or even dictate cell migration. In chemotaxis, the cell follows a soluble gradient of chemical biomolecules [28], in durotaxis a gradient of elasticity [29] in haptotaxis a gradient of adhesion molecules [30]. Cells can sense surface pattern and be directed [31] [8] to migrate persistently in one direction.
This description corresponds to cell migration on flat 2D surfaces such as Petri dishes. What impact has cell migration *in vivo*? A short overview is given in the next section.

1.1.2 Cell migration *in vivo*

Cell migration is implicated in various processes *in vivo*. It is relevant for immune response, wound healing, cancer dissemination and embryogenesis, where various processes are linked to oscillatory phenomena (reviewed in [32]). Single and collective cell migration can be observed.
During development, cell migration allows the formation of structures with stereotyped pattern. These form the basis of later proper functioning tissue connected to different parts of the organism. For instance Benazeraf *et al* [1] have reported the importance of single cell migration for elongation of amniote embryo. The connection between motility gradient of fibroblasts and axis elongation in the presomitic mesoderm (PSM) has been established. In *C. elegans* neuroblasts, QL (left) and QR (right), migrate along the anteroposterior body axis to produce three neurons. This migration is specified by Wnt signaling leading to two patterns of cell migration [33]. During *Zebrafish* gastrulation, cells migrate extensively to form ectoderm, mesoderm and endoderm germ layers. Whereas ectodermal progenitors form and migrate as a pseudo-epithelial layer, mesodermal and endodermal progenitor cells show characteristics of mesenchymal phenotype with lamellipodia and bleb-like protrusion [2]. In *Drosophila*, tracheal cells migrate to form the tracheal branches spanning throughout the embryo [34]. A certain amount of cells coming from tracheal pits, generate the characteristic network called tracheal tree.
Dendritic cells, involved in the immune response, can sense haptotactic chemokine gradient within the perilymphatic interstitium and migrate accordingly [15]. These cells seem to combine cell motility and antigen processing [35]. Leukocytes and lymphocytes are as

well motile cells of the immune system. Defects in migration of these cells lead to impairment of the immune response [36]. Leukocytes traffick into lymphoids and peripheral tissues for immune cell development, effector function and immunosurveillance. During this process, cells show a large variety of migration strategies (reviewed by Friedl and Weigelin [14]).
Cell migration *in vivo* has been observed for cancer cells [37] [38] [39]. In cancer, one possibility for spreading of a primary tumor is when cells escape from a primary tumor. They can be found in body fluids as circulating tumor cells [40] and form a secondary tumor elsewhere in an organism. From a primary tumor, cells undergo an epithelial to mesenchymal transition (EMT) [41] loosing their epithelial polarity, allowing them to be more motile. Cells form podosome and invadopodia, by deterioration of the basement membrane, they have access to blood stream [42]. This is not the only mechanism of cell migration in cancer. Collective migration as mesenchymal cells following each other or an epithelial tissue maintaining its characteristic cell-cell contacts can also be observed. Expansive growth or tissue folding can as well be seen as cell migration (reviewed in [3]). Cancer dissemination is a complex process and shows specificity for each cancer type. Cancer cell migration represents an abnormal cell migration. But it still has various characteristics of "normal" cell migration. Therefore, it is important to have all the keys for standard 3D cell migration to gain new insight into cancer cell migration.
With this short overview of cell migration *in vivo* one can see that cell migration is involved in many processes where cells need to change location to perform a specific task (e.g. immune response) or the migration itself is the aim for example for putting into place tissues. The cytoskeleton gives cells structure and allows them to perform cell migration. It is presented in the following section.

1.2 The Cytoskeleton

The cytoskeleton is an important component of the cell. It gives mechanical stability and through its dynamic reorganization, it allows the cell to move and to apply forces. In the following section I will present the relevant components and characteristics of the cytoskeleton and give an overview of the formed supramolecular structures. I will introduce the *active gel*[2] theory which allows to model the interactions of appearing supramolecular structures and to describe the physical interactions.

1.2.1 Actin

Actin is a 45kDa monomeric protein which forms a filamentous structure [43]. It has a binding site for a nucleotide (ATP, ADP). It assembles head to tail and forms polar filaments [19]. These filaments consist of two parallel protofilaments twisted around each other creating a right-handed helix. One makes a distinction between the '+' or *barbed* end and the '-' or *pointed* end (Figure 1.2). The monomers are added up to the filament until the critical concentration is reached and the binding and un-binding are at steady state. After assembly into the polymer the tightly bound ATP hydolyzes to ADP. This

[2] *Definition in Appendix*

reduces the binding affinity to the neighboring subunits and makes dissociation from the polymer more likely. As a consequence, the two ends of the filament have different rate constants and by this 'see' different critical concentrations, the one on the minus end being higher than the one on the plus end. With the same monomer concentration, the plus end will continue to undergo a net assembly whereas the minus end will grow more slowly or disassemble. This creates a flux of subunits through the polymer called *treadmilling*. It allows the cell to keep the same filament length while the monomers of the filaments and the cytosol exchange. This comes at an energy cost as the cell needs to hydrolyze a certain amount of nucleotides. The benefit of this system lies in a higher spatial and temporal flexibility. Monomers can diffuse fast through the cell [43].

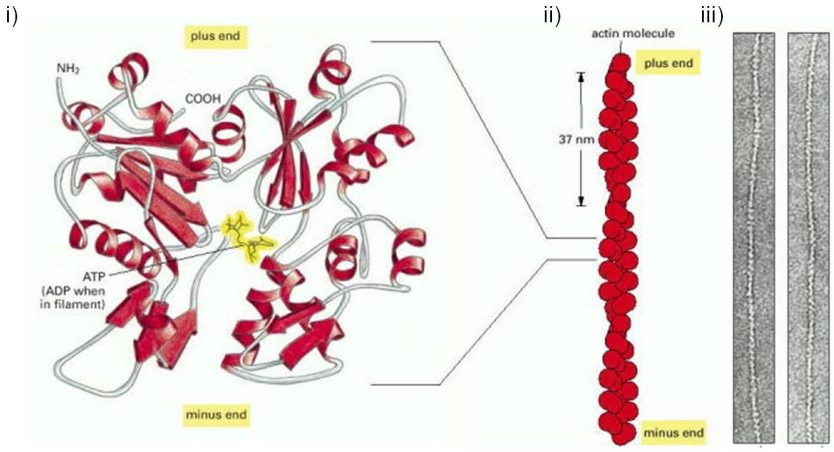

FIGURE 1.2: i) Actin is a polar monomer with a binding site for ADP and ATP. ii) Actin forms polar helical filaments. The polarity is denoted as the "+" or *barbed* end and the "-" or *pointed* end. iii) Electron microscope picture of actin fibers (Figure from [19]).

Nucleators Formins nuclate actin growth at the barbed end [44]. They attach to the + end, while the filament still grows on that side. Therefore, they are called leaky cap nucleators. By their presence, they also prevent other capping proteins to bind to actin [45]. Formins and also profilins accelerate actin polymerization [46]. The Arp 2/3 (actin-related-protein) complex nucleates actin growth [19]. While it binds to the minus end, rapid elongation occurs on the plus end. It has also the capacity to attach to a second actin filament and by this allows the actin filaments to grow into a 'treelike' web structure [47].

Crosslinkers Actin filaments are forming two types of structures: bundles and gel-like structures among others. Therefore, a connection between different filaments is required. This is established by crosslinker proteins such as α-actinin, fimbrin, spectrin and filamin. Fimbrin, which generates a tight packaging and α-actinin [48], which creates a loose packaging are bundling proteins. These proteins have straight 'stiff' connections between their actin-filament-binding domain in contrary to actin crosslinking proteins forming a web-like structure which have flexible connections [19].

An important protein that can bind to actin and move filaments is myosin, presented in the next section.

1.2.2 Myosin

Myosin is a motor protein which is able to exert a force. It is composed of two heavy chains and two copies of each of two light chains (Figure 1.3). The heavy chains have a head domain on the N-terminus with a force generating machinery and a long amino acid sequence which allows heavy chain dimerization. The two light chains bind the N-terminal head domain.

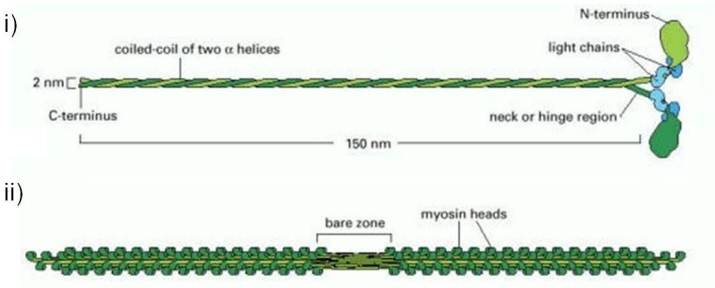

FIGURE 1.3: i) Myosin is composed of four light and two heavy chains. The heavy chains coil, whereas the light chains form the neck of myosin. ii) Myosin can organize into filaments as for example in muscles (Figure from [19]).

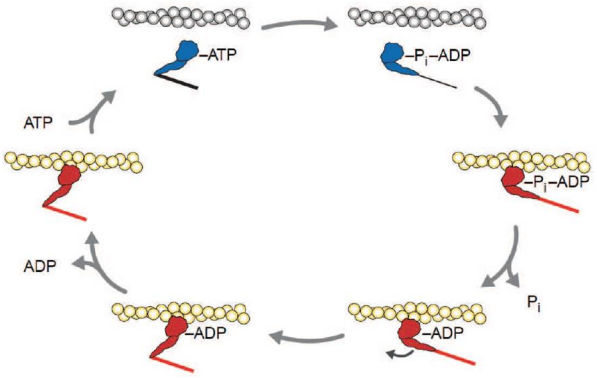

FIGURE 1.4: Schematic representation of the powerstroke: Myosin head is tightly bound to filament when ATP binds, thus lowering binding affinity and allowing head to detach. Conformational change leads to reaching of next binding site along the fiber. After hydrolysis of ATP inorganic phosphate is released and power stroke occurs provoking a sliding of the fibers of 11 nm. ADP is released and initial state reached. (Figure from [49]).

The coiled-coil tail bundles with the tail of other myosins. The tail-tail interactions can lead to the formation of thick bipolar filaments (Figure 1.3). The myosin head is able to bind and hydrolyze ATP and walks in direction of the plus end of the actin filament.

The force is generated by coupling the hydrolysis of ATP to a conformational change [19]. The different steps are as follows (Figure 1.4) [19] [50]:

The myosin head is tightly bound to the actin filament without nucleotide in the rigor state.

Upon binding of ATP a conformational change which lowers the affinity of the binding to actin occurs. Now the head is able to move along the actin filament.

A large shape change leads to a displacement of 5 nm of the myosin head. Hydrolysis of ATP occurs but both components stay tightly bound to the head.

The release of the inorganic phosphate leads to a tight binding of the head to actin and triggers the *power stroke*, the force generating change in which the myosin head regains its initial conformation.

The ADP is released and the myosin has moved to a new position along the actin fiber.

This conformational change generating the power stroke has been studied intensively with structural biology methods. Another approach is to describe it by brownian motion and the ratchet model [43].
Myosin activity is regulated by phosophorylation which affects motor activity or the assembly of thick filaments. For instance the calcium-dependent myosin light-chain kinase (MLCK) phosphorylates the myosin light chain and by this causes a conformational change to the extended state. In this state, the myosin spontaneously assembles into bipolar filaments and contracts [19] [43].
Actin and myosin are organized in different supramolecular structures involved in different cellular processes. Before I want to introduce you another component of the cytoskeleton the microtubules, which also have some dynamical properties.

1.2.3 Microtubules

Another important cytoskeletal component is microtubules (MT). They consist of α and β subunits which form heterodimers the tubulin. Both have nucleotide binding sites for GTP, but whereas the GTP of the β subunit can be hydrolyzed, the one bound to the α subunit never hydrolyzes. The tubulins assemble head to tail into protofilaments which then form a cylindrical structure out of 13 parallel protofilaments [19].
The GTP hydrolyzes to GDP and phosphate shortly after incorporation in the filament structure. The critical concentration for GDP tubulin is greater than for GTP tubulin. For a certain concentration, a GDP end MT would shrink, but a GTP end MT would grow. As GTP tubulin is added to the polymer, it forms a GTP cap and prevents depolymerization of microtubule. For an intermediate concentration of tubulins between the critical concentration of GTP and GDP tubulin, an end with a GTP-bound tubulin will grow whereas an end with a GDP tubulin will shrink. When a GTP end turns into a GDP end thus hydrolysis, it also shrinks. After some time, it may regain a GTP end and start growing again. This rapid interconversion between growing and shrinking is called

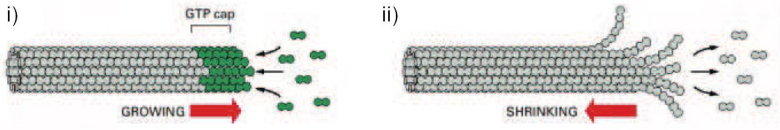

FIGURE 1.5: i) Globular $\alpha\beta$ heterodimers are added to microtubule. GTP is hydrolyzed to GDP after incorporation to microtubule with a certain rate. When polymerization is fast enough, GTP does not hydrolyze and a cap is generated. ii) When polymerization is slow GTP is hydrolyzed and depolymerization of the microtubule is faster than polymerization and the polymer shrinks (Figure from [19]).

dynamic instability (Figure 1.5 [19]).
There are two types of microtubule motor proteins: kinesin which is moving towards the plus end of microtubules and dynein which is moving towards the minus end. Both molecular motors use the energy of hydrolysis for a conformational change and thus movement [19].
The molecular entities can assemble to supramolecular structures. These have different characteristics depending on their organization. Here we concentrate on acto-myosin supramolecular structures.

1.2.4 Supramolecular acto-myosin structures

Actin and myosin can assemble into various supramolecular structures such as lamellipodia, filopodia or cortex. These structures and their characteristics are introduced in the following section.

1.2.4.1 Lamellipodia

The lamellipodia is an important cellular structure involved in 2D cell migration. It was first described in the 1970s by Abercrombie *et al* [51] [52] [53]. They saw a flat 0.2 μm high structure in electron microscope pictures at the front of the cell traversed with a dense actin meshwork (Figure 1.6). They identified dark areas to be contact points with the surrounding. The lamellipodium is best studied in fish keratocytes, even after disruption of the lamellipodium from the cell body forming a cytoplast, it continues migrating and preserves its polarity [54].
The actin network in the lamellipodium stays stationary in an external reference framework: via RhoA pathway nuclear-promoting factors (NPFs) are activated and stimulate Arp 2/3 to promote growth of actin fibers. Actin filaments are assembled with the barbed end in a 70° angle [56] to existing fibers, thus creating a web-like structure [55]. Globular actin is incorporated in the structure. Accelerated by profilin, this structure undergoes treadmilling: the front assembles whereas the back disassembles. The movement is produced by the pushing of growing actin filaments on the membrane, which unfolds at the front of the lamellipodium. The advancement of the membrane and the incorporation of actin monomers has been proposed to be based on the elastic brownian ratchet model [57]. In this model, the actin fiber is in contact with the membrane and due to thermic fluctuations a space between the membrane and the fiber is temporarily free, as the fiber bends.

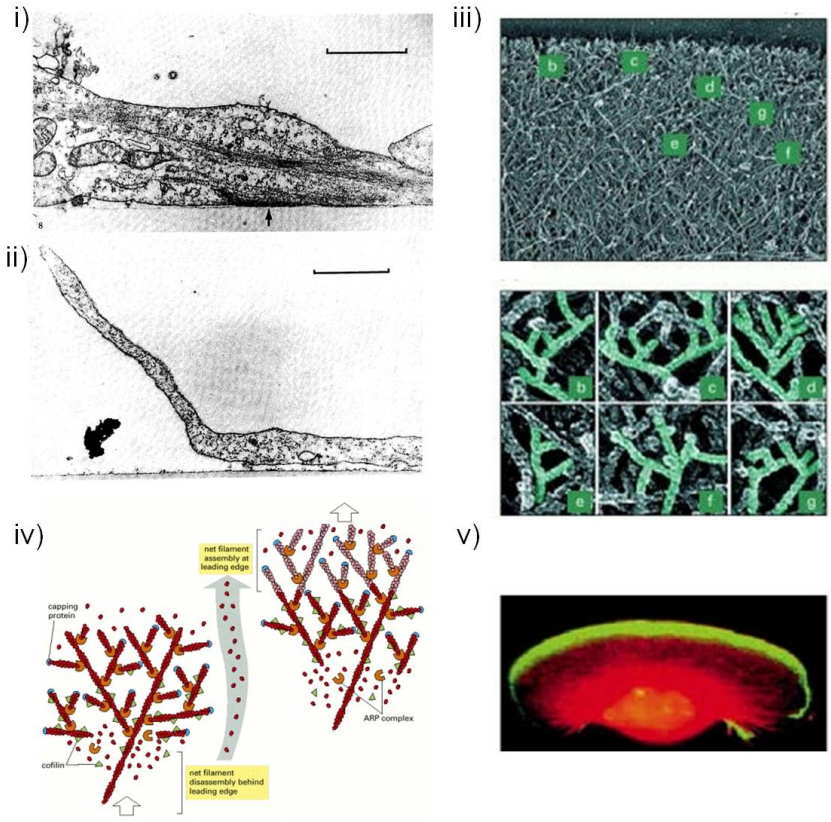

FIGURE 1.6: i) Electron microscopy image of lamellipodia cross section. ii) The lamellipodium can bend dorsally and form a ruffle when it is not attached at the front (Figure from [53]). iii) Electron microscopy image of the leading edge of migrating keratocyte showing a branched actin structure. Branching is highlighted in green [55]. iv) Model of actin polymerization at the leading edge of the lamellipodia: Arp2/3 binds to actin filaments and generates branching resulting in a network structure. Cofilin (green triangles) destabilizes the back of the structure (Figure from [53]). v) Migrating fish keratocyte on a planar structure. Actin labeled in red and Arp2/3 in green [55].

This leaves space for a new actin monomer to attach to the end of the barbed end. When the fiber moves back to its initial position a recovery load force is pushing the membrane as the fiber is behaving like a spring. Capping proteins terminate growth of actin filaments. By this means the pool of actin monomers is kept high so that more integration in other filaments takes place. This mechanism is known as funnelling treadmilling. From the edge of the cell inwards actin retrograde flow can be observed. This flow is a consequence of filament growth at the membrane [58] and myosin contractility [59]. Lamellipodium can be modeled by *active gel* theory [60]. Its activity and growth is controlled by the Rac signaling pathway [22].

1.2.4.2 Filopodia

Filopodia, finger-like membrane protrusions are composed of actin filaments, have a diameter of 0.6-1.2 μm and a length up to tens of μm. They are a dynamic, contractile structure able to exert forces thus sensing and exploring their environment [61]. For this they are able to extend and retract rapidly and sense directional cues [62]. The extension is based on actin polymerization at the barbed end and retraction on retrograde flow [63]. Filopodia are formed by parallel actin fibers (15-30) aligned with the barbed ends to the

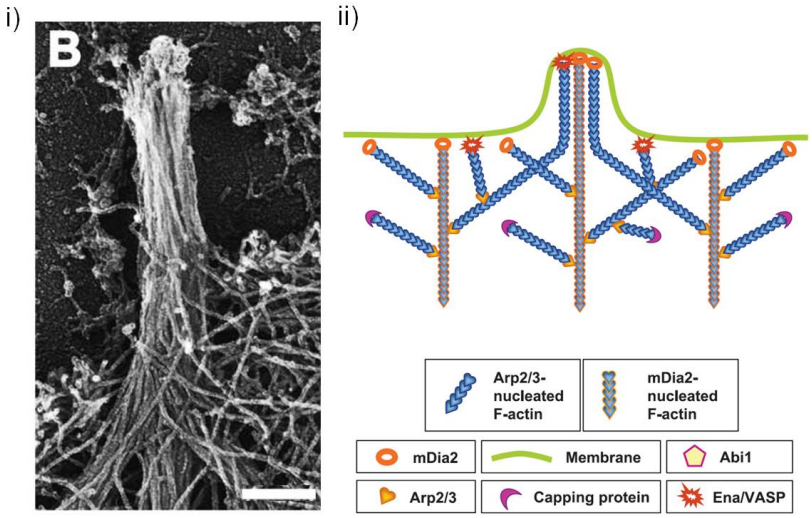

FIGURE 1.7: i) Electron microscopy image of filopodia. ii) Growing filopodia on Arp2/3 nucleated actin and mediated by mDia [64].

distal tip, where new actin monomers are added up [65]. The filaments are crosslinked by bundling proteins such as α-actinin, fascin, fimbrin, etc. (Figure 1.7). This ensures their mechanical stability and prevents them from buckling [66]. The ERM complex (ezrin, radixin, moesin) stabilize the filaments at the shaft [67]. Growth of filopodia is mainly regulated by Cdc42, which via WASP activation is able to trigger Arp2/3 dependent actin filament polymerization. At the tip of the filaments, numerous proteins are located such as VASP, Ena and Mena. The clustering of receptors confers it the sensory ability, giving them an important role in neuritogenesis [68], pathogen phagocytosis [69] and embryonic gap closure [70]. Interestingly lamellipodia and filopodia are spatially coordinated forming locally nearby each other and share the main components but differ in their structure. Given that they are formed by the same building blocks, they are expected to be present in the cell. However, it is not totally clear how filopodia form, two models coexist, the extension model [71] and *de novo* formin-driven growth [72].

1.2.4.3 Stress fibers

Stress fibers are contractile acto-myosin bundles crosslinked with α-actinin and with myosin. One distinguishes between dorsal and ventral stress fibers connected to focal adhesions at their ends and transverse arcs which are curved and not typically connected

to focal adhesions but to the dorsal stress fibers [73]. Transverse arcs are positioned centripetal throughout the lamella until they disappear in front of the nucleus [74]. Via myosin contraction, the filaments shorten and stress is applied via focal adhesions to the surrounding of the cell. This tension of stress fibers can be probed by laser ablation [75] leading to cell retraction and remodeling [76]. Stress fiber contractility is controlled by the RhoA signaling pathway.

1.2.4.4 Cortex

The cortex is a thin acto-myosin structure lying under the cell plasma membrane with a thickness of 50-100 nm [77]. Electron microscopy images show that the actin fibers are mainly running parallel to the membrane and the mesh is forming with a mesh size of 20-250 nm [77]. Whereas the cortex is well visible in cells rounded up as in suspension [78] or for cytokinesis [79], it is harder to spot on spread cells [80]. Additionally to acto-myosin there is also the crosslinker α-actinin, formins which nucleate actin [81] and proteins of the ERM- family (Ezrin-Radixin-Moesin) present in the cortex [77] [82].

Viscoelastic properties The central mechanical properties of the cortex are its viscoelasticity and the cortex tension. The viscoelasticity allows the cortex to resist external mechanical stresses [84] and to oppose to intracellular osmotic pressure [85]. A viscoelastic medium has an elastic response on short timescales and a viscous response for longer timescales. The elastic properties appear for timescales shorter than its turnover (Figure 1.8). An elastic modulus, which relates to applied stress, can be derived upon perturbation. Experimentally the cortex elasticity can be evaluated by laser ablation [86], stretching cell by optical forces [87] or AFM indentation [88]. Another option of evaluating the elasticity of cells is to probe them by microplate manipulation [89] [90]. The viscous properties emerge upon remodeling of the network due to actin turnover and dissociation of crosslinkers thus dissipating stresses. This corresponds to a flow. The actin turnover within the cortical actin is approximately of 1 minute and has been measured by FRAP experiments on different systems [83]. The turnover rate can be modulated by crosslinkers and actin-binding proteins. There are hints that timescale of relaxation is largely dependent on the turnover of crosslinkers and not that much on actin turnover [91] [43]. The simplest way to model the viscoelastic properties of the cortex is with springs and dashpots [92].

Cortex tension The cortex tension is defined as the force per unit length exerted locally by the surrounding network on a cortex cross-section. The tension is generated by the contractile forces of the myosin motors. Whereas the contraction produced by myosins in an ordered structure such as muscle sarcomeres is well understood, the mechanism in isotropic medium is not yet elucidated. It is not clear why contractile effects dominate over expansion. The sliding of actin filaments relative to each other by myosin motors will induce contraction as long as the fibers come closer. When the filaments completely overlap, myosin pulls them apart again which then results in an expansion [43]. Elastic

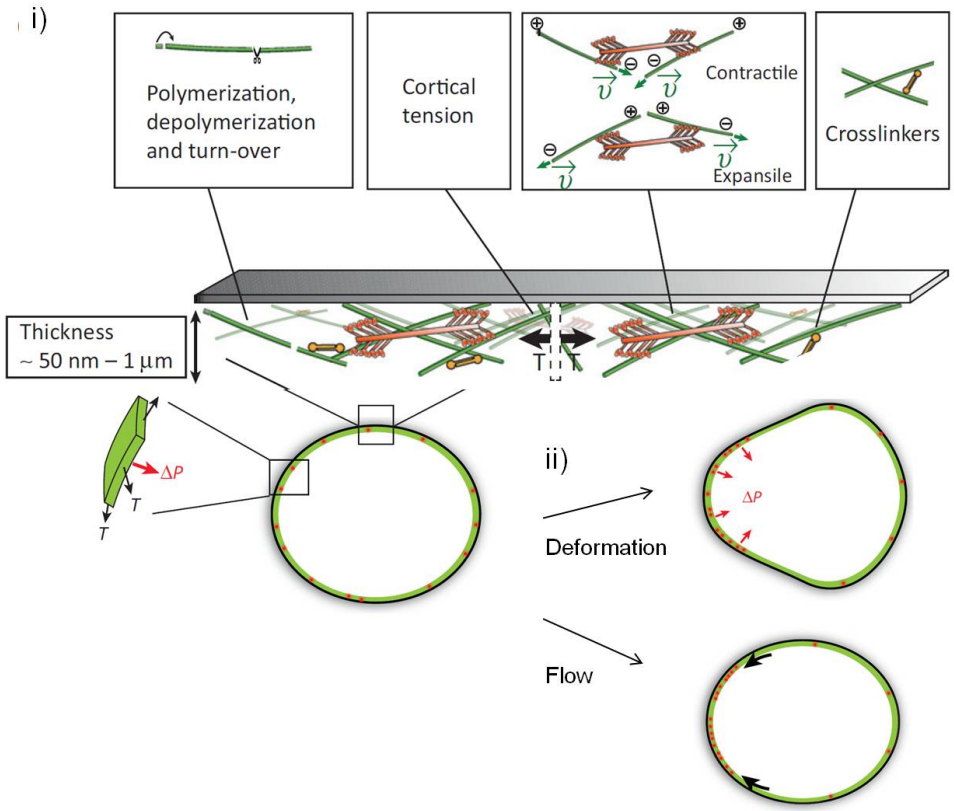

FIGURE 1.8: i) Cortex is situated underneath the plasma membrane. Actin filaments form a thin network, with crosslinkers and undergo continuous turnover. Forces are generated by myosin motors generating cortical tension T. Myosin assembles into mini-filaments which slide actin filaments relative to each other resulting in contractile or expansile stresses. ii) The curvature of cell allows the cortical tension to generate a hydrostatic pressure. Tangential flows can be driven by gradients of motor-generated contractility. Deformations of the cell with net displacement of the cytoplasm can be driven by normal forces (Figure adapted from [83]).

stretching or viscous flows can also contribute to the increase of surface tension when cortex experiences deformation [93]. An inhomogeneous cortex tension leads to contractility gradients within the cell which will drive cell shape changes [94] (Figure 1.8). To estimate the tension, micropipette experiments are used [95]. It can also be evaluated from laser ablation experiments.

Bleb formation Blebbing is a phenomenon of cells forming spherical membrane protrusions commonly observed during cytokinesis, virus uptake and cell spreading [97]. It was largely considered as a sign of apoptosis [98]. Blebs occur when the hydrostatic pressure exerted by the contractile cortex leads to a local breakage of the cortex [96] or when the membrane detaches locally from the cortex [99]. The bleb life cycle can be divided in 3 steps (Figure 1.9): initiation, growth and retraction. Once the breakage has occurred

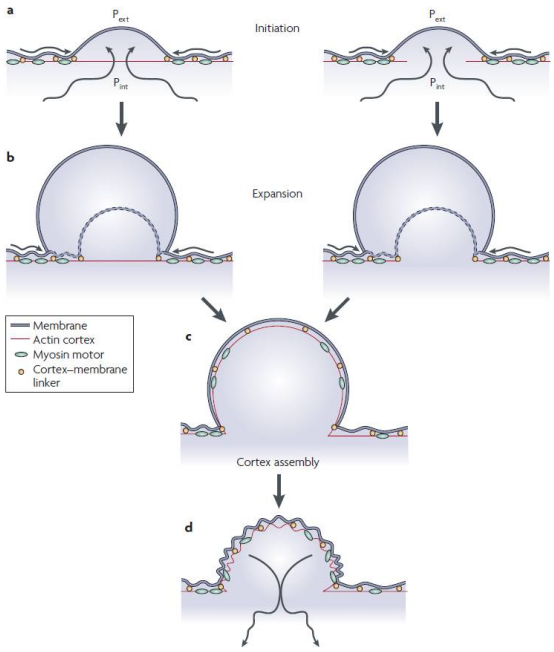

FIGURE 1.9: Bleb is initiated upon detachment of membrane from cortex (left) or cortex rupture (right) and expands due to hydrostatic pressure. Cortex is reassembled underneath the membrane and bleb retracts (Figure from [96]).

intracellular pressure drives bleb expansion for 5-30 s [100]. During this time, the surface of the membrane needs to increase. Once the final size of the bleb is reached, the actomyosin cortex repolymerizes and retracts the bleb. Retraction is slower than expansion and a new bleb often forms shortly after retraction at the same spot [101]. Bleb formation is strongly dependent on the cortical tension, lowering the tension under a critical limit abolishes bleb formation [86].
How can all these supramolecular structures be described physically? Commonly they are described by the *active gel* theory introduced in the following section.

1.2.5 Active gel theory

As introduced before, the cytoskeleton is involved in many cellular processes such as cytokinesis, cell migration or force transmission. These processes are quite different from each other but rely on the same built-in structures: biopolymers crosslinked by passive crosslinkers to networks and 'active crosslinkers'. These components form an active gel whose interaction leads to different shapes and dynamics [102].
As the cytoskeleton is mainly composed of crosslinked filaments it can be described as a gel. One can distinguish physical and chemical gels, the first one based on physical bonds such as dipole or van-der-Waals interactions the later one being connected by covalent bonds [103]. Upon stress application physical bonds can be remodeled. The gel has active components converting chemical energy in mechanical work. By dissipating energy, a shape transformation is obtained. Length of actin filaments changes dynamically upon addition of actin monomers as described previously. The myosin motors slide the filaments

relative to each other, leading to stress generation. The system hydrolyses nucleotides, mainly ATP as an energy source. This makes it an out-of-equilibrium system constantly consuming energy. Other characteristics are the existence of internal stress, spontaneous appearance of flows and macroscopic polar order. The same accounts for microtubules and their molecular motors [43].
There are two major complementary ways to describe *active gels* (reviewed by [102]): The hydrodynamic and the microscopic approach. (i) In the hydrodynamic approach the system is viewed as a gel of viscoelastic fluid comparable to newtonian fluids and the molecular details are neglected. The description is similar to hydrodynamics of fluids, the extracted characteristics analogous and it allows to capture behaviour on long time and length scales. This approach as it is lacking molecular description and based on the symmetry of the system thus more universal [104] is applicable to a large variety of systems. The characteristics of the gel depend on the lifetime of bonds: short timescales lead to elastic behaviour and long timescales to plastic behaviour. Active gels are thus viscoelastic, their characteristic Maxwell time describing the transition is $\tau = \frac{\eta}{E}$ with η the viscosity coefficient and E the elastic modulus [43]. A hydrodynamic theory for active polar gels has been proposed by Kruse *et al* [105]. They write three constitutive equations relating rate of ATP hydrolysis, changes in polarization and momentum flux with the orientational field h, velocity gradients and the activity $\zeta\Delta\mu$. Upon simplification and for linear hydrodynamic theory one obtains [106]:

$$\sigma = 2\eta u - \zeta\Delta\mu \tag{1.1}$$

where σ denotes the stress η the viscosity coefficient, u velocity gradient and $\zeta\Delta\mu$ describes the energy component linked to free energy by ATP hydrolysis. In this equation $\zeta\Delta\mu$ corresponds to the active stress and $2\eta u$ to the viscous stress. ζ is the activity coefficient a material property and $\Delta\mu$ the free energy. The velocity gradient is a tensor, which is neglected for 1D approaches. To account for polarity the orientational field h needs to be coupled to the stress.
(ii) The microscopic approach includes the characterization of molecular structures and the interaction rules between the structural components. The system is based on a mean-field description [107]. With this method, descriptions on shorter time- and lengthscales can be obtained and molecular mechanisms identified. As dynamics of single elements are included, material parameters which are linked to molecular interactions can be obtained from the model [108] [109].
Another option is to use numerical simulation to investigate active gels [110]. Therefore, all information of the molecular structure of the components and their interaction has to be incorporated in the simulation. Knowledge about a large range of parameters is required and to be fed to the simulation. These parameters might not be available or not measured under physiological conditions potentially shifting results. The robustness reliability of the simulation relies on the number of free parameters as a large number of free parameters may introduce errors.

In this section, the cytoskeleton structures involved in cell migration, their dynamics and their theoretical description have been introduced. These dynamics are controlled by

the Rho A pathway which I will present in the following section.

1.3 The Rho pathway

Processing of external stimuli in cells involves signal transduction cascades [22]. A wide variety of signal transduction pathways in eukaryotic cells are controlled by Rho GTPases such as force application or cell migration. Rho GTPases belong to the Ras superfamily and are best known for regulating the actin cytoskeleton. They are also associated to other signaling pathways, such as the regulation of cell polarity, gene transcription, microtubule dynamics, vesicular transport and some enzymatic activities [22] [111].
They are molecular switches that exist in a GTP-bound the "active" state and the GDP-bound state the "inactive" state (Figure 1.10). Guanine nucleotide exchange effectors (GEFs) catalyze nucleotide exchange and thus mediate activation. In the "active" state GTPase recognizes target proteins. GTPase-activating proteins (GAPs) stimulate GTP hydrolysis and mediate inactivation and the RhoGTPase returns to the off-state.
Due to the complexity of the family and the pathways, not all target proteins or all

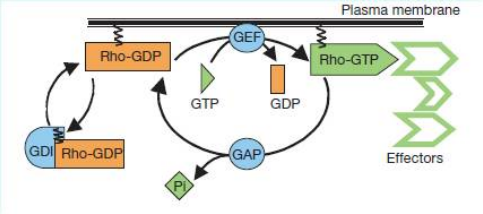

FIGURE 1.10: Schematic representation of Rho GTPase cycle. GEFs mediate activation and GAPs stimulate GTP hydrolysis thus inactivation (Figure from [22]).

connections within the pathway have been discovered yet. In general for regulation of the actin skeleton one can say that Rho A regulates actin cytoskeleton and stress fibers. Rac controls actin-rich surface protrusions (Lamellipodia) and Cdc42 filopodia [112] [22] (Figure 1.11).

RhoA RhoA plays an important role in regulating cell contractility. It acts on the activation state of myosin via Rho-associated kinase (ROCK) which activates LIM kinase activating cofilin which stabilizes F-actin [113]. ROCK also inhibits Myosin Light Chain Phosphatase and by this increases myosin activity. It also promotes actin polymerization via mDia [114].

Rac1 Rac1 regulates actin polymerization during protrusive activity by different means: It activates formins such as mDia1, an actin nucleating proteins (WAVE-Arp2/3 complex) increases availability of actin monomers by interacting with cofilin and removes capping proteins by this freeing actin barbed end [115]. A gradient of active Rac1 is formed towards the leading edge [116].

Cdc42 Cdc42 is responsible for setting cell planar polarity, by its activity it defines a front and a back of a cell. This effect is reached by positioning the microtubule organizing center (MTOC) along the front rear axis, linking Rac1 to the leading front membrane [117] and by stabilizing microtubules [118]. It regulates filopodia formation by activating WASP which can trigger Arp2/3 dependent actin filament polarization [47].

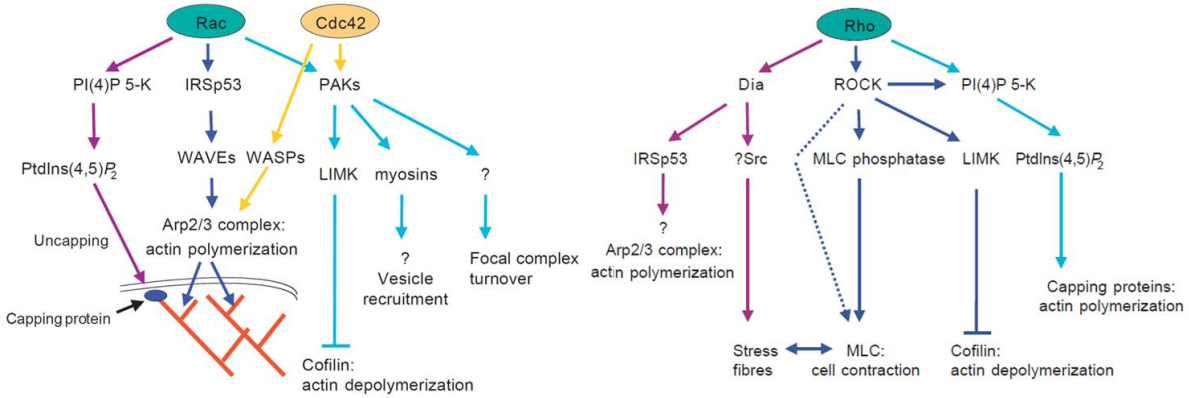

FIGURE 1.11: Rac1 and Cdc42 have multiple independent or combined effectors affecting actin structure at the leading edge. Rac1 induces actin polymerization via Arp2/3, mDia and the actin turnover via cofilin. Cdc42 acts also on actin polymerization and turnover but mainly in filopodia. RhoA targets myosin II activity via ROCK thus acting on contractility (of stress fibers) and via mDia on actin polymerization (Figure from [119]).

Rho A pathway controls cell cytoskeleton dynamics thus cell migration. The cell does not evolve in free space, it adheres on a 2D surface or in the physiological case is embedded in a 3D environment, the extracellular matrix. It is important to understand how the environment of the cell influences its behaviour. Therefore, we take a closer look on the following pages on the extracellular matrix and its characteristics.

1.4 The extracellular matrix

The biochemichal and biophysical properties of the extracellular matrix (ECM) greatly influence cell behaviour in different tissues. The structure of the ECM varies with its composition and leads to a unique topography and tissue specific functions. This confers the ECM an important role in cell development and homeostasis. The matrix consists of macromolecules produced and assembled by cells, among other fibroblasts to a three-dimensional meshwork [120]. Its tasks is to provide cells a physical support, to act as a diffusion barrier between different tissues, to establish complex adhesion surfaces, to offer binding domains for growth factors and chemokines and to provide physical and chemical cues [121].

The ECM is formed by two main classes of polypeptide chains: fibrous proteins such as elastin or collagen and glycoproteins such as fibronectin laminin and polyglycanes (PGs).

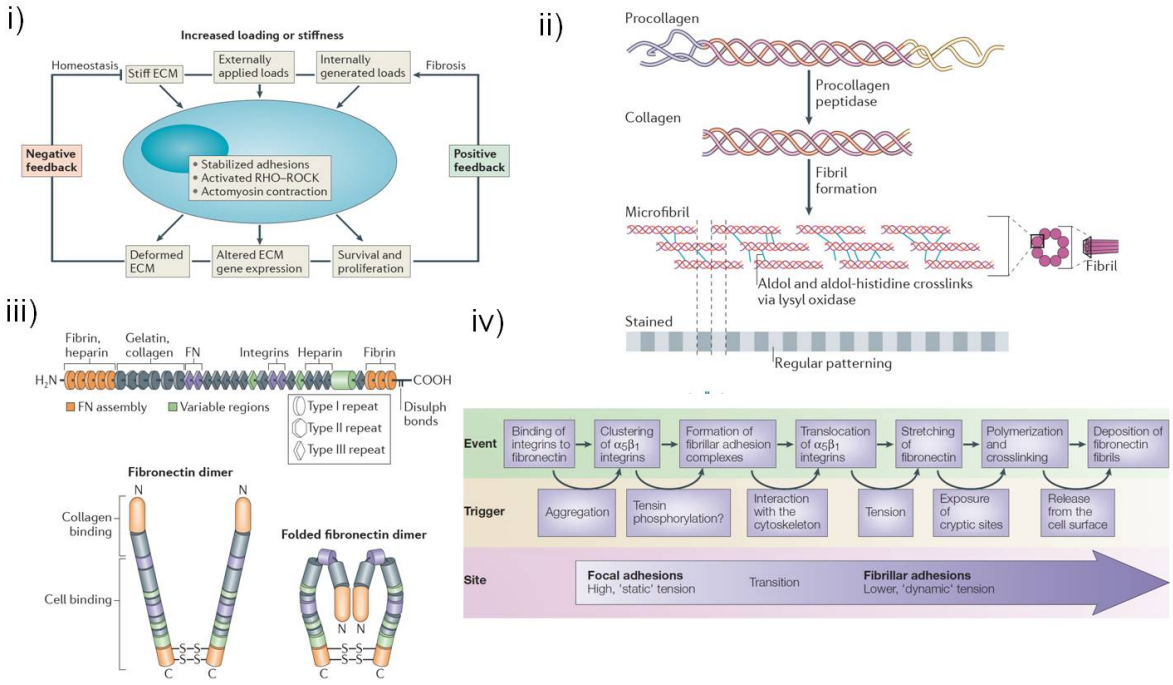

FIGURE 1.12: i) Flow chart describing feedback loops that regulate extracellular matrix structure and function. Increased mechanical load leads either to homeostatic regulation (negative feedback loop, left) or to fibrosis (positive feedback loop right) (Figure from [120]). ii) Protocollagen is secreted, processed to collagen and assembled into cross-striated microfibrils. Long fibrils form by merging of shorter ones. iii) Fibronectin forms dimers via disulphide bonds at C-terminus. Folding occurs due to ionic interactions of FN-III domain. Mechanical force can reveal cryptic sites for integrin binding (Figure from [121]). iv) Description of fibrillogenesis. Events trigger intermolecular interactions, tension and conformational changes at different locations (Figure adapted from [122]).

Collagen is the most abundant polypeptide in the ECM and it exists in 28 different types. It is composed of homotrimers and heterotrimers formed by three polypeptide chains. These form a right handed α-helix. The rod domain of the collagen binds to cell surface receptors, nucleic acids and glycosaminoglycans (GAGs). The assembly of fibrillar collagen is a highly complex procedure including multipe intra- and extracellular post-translational modifications rendering a fibrillar structure with a highly mechanical resistance able to withstand high forces (Figure 1.12 ii)) [121].
Elastic fibers formed by elastin surrounded by a sheet of microfibrils are the most chemically, thermally and biologically stable components of the ECM. Fibers can extend up to 150% and recoil when unloading. Their organization in humans takes place before adulthood and have a lifetime of 50 -70 years in human arteries. By this, they represent a sort of "mechanical memory" of the tissue [123]. Any mechanical damage cannot be repaired in adulthood and leads to proteolytic degradation or stiffening [124].
Proteoglycans form the basis of a higher order ECM around cells. The GAG component binds water and thus provides hydratation and compressive resistance to the ECM. Major GAGs are heparin-sulphate and chondroitin-sulphate proteoglycans. The heparin-

sulphate proteoglycans for instance form the basal membrane. It has a high negative charge and binds easily to other ECM structural proteins or also to fibronectin growth factos (FGFs). Chendroitin suphate proteogylcane (CSPGs) is found in cartilage and neural ECM.
Fibronectin (FN) a large ECM glycoprotein assembles via a cell mediated process and forms fibrillar structures around cells. It has three different subdomains: FN-I, FN-II and FN-III (Figure 1.12 iii), iv)). Their binding motifs can interact with collagen, gelatin and also integrins. It has antiparallel disulphide bonds at the C-terminus leading to a dimeric structure of the FN. The fibronectin mesh assembly is mediated primarily by the $\alpha 5\beta 1$ integrin. Once bound to the cell, the globular fibronectin is stretched and cryptic binding sites exposed [125]. This is a crucial step for fibrillogenesis. The binding sites might also be exposed upon conformational change when binding to integrins [126]. These unfolding mostly situated in the FN-III domain is reversible [127] and it has been proposed that unfolding of FN is the triggering factor for fibronectin polymerization [128]. The reversibility of this process would also account for the elasticity of FN which is tightly stretched in cell culture [127]. A seven-fold increase of soluble FN binding is observed when stretching of FN on a rubber substrate [125]. This confirms the idea that tension is necessary for matrix assembly. 3.5-5 pN are required to unfold various FN-III domains to its fivefold length of 860 nm [129]. Whereas disruption of bonds are only obtained at 10-30 pN [128]. Förster resonance energy transfer (FRET) analysis has confirmed that fibronectin unfolds within fibrils when force is applied [130]. FN might provide the scaffold for further collagen deposition as it is required for collagen I matrix assembly [131] and by this, it might be one of the ground building block of ECM.
As the ECM production highly relies on its tension and the tension applied by cells, the mechanical homeostasis is quite important. Apart from putting the ECM under tension and remodel it, cells can also secrete proteases to degrade the ECM. In the case of the ECM it is the metallo-proteinase family able to degrade various components [132]. The rates of protease activity correlate negatively with mechanical load of the ECM. Inversely, synthesis correlates positively with mechanical load [133]. This corresponds to a process controlled by a negative feedback loop (Figure 1.12 i)). The ECM integrity is protected by stress [134]. For instance metallo-proteinase genes can be induced by acto-myosin inhibitors or by ECM unloading [135]. Another challenge arising from mechanical homeostasis is to incorporate freshly synthesized components without changing the stress state of the ECM. Computational studies suggest that the incorporation or replacement of fibers can only occur with components having the same properties [136].
Anomalous structure of ECM can promote development of cancer cell migration. After overloading, a homeostatic response of the cell or a fibrotic response leading to a change in ECM can follow [120]. Hypoxia in tissue can induce fiber alignement in ECM and promote tumor cell migration along these fibers [137]. Over-expression of cancer associated factors, such as fibronectin associated protein [138] or caveolin1 [139], generates an abnormal structure of ECM *in vitro* and thus mediates tumor invasion [138]. Pathologic remodeling is also mediated by metalloproteinases such as MMP-11 and MMP-14, which seem to have a functional relation [140]. The relation of cancer and biochemical and biophysical matrix remodeling has been reviewed in [141].
The complexity of the ECM will greatly influence the migratory behaviour of cells. Its

wide range of characteristics in terms of elasticity either soft or rigid, its ligand density and its topology leading to a continuous or interdiction space require a high mechanical adaptability of cells. Confinement of the cell also plays a role, as it may prevent lateral expansion of protrusions and allows non-integrin based friction [142].
In my PhD project we studied the deformation of the cell environment and its relation to cell motility. Therefore, the connections of the cell with its environment play a key role in mediating the deformations of the matrix. Connections are established via focal adhesions which also transmit forces. These cellular structures will be presented in the next part.

1.5 Focal adhesions

Focal adhesions are complexes of proteins connecting the cell inside with the cell outside, in the physiological case the extracellular matrix, with the cytoskeleton. On the outside part the connection is established via α- and β- integrins which are transmembranous proteins [122]. The cytosolic parts have intracellular binding partners such as vinculin, zyxin, paxilin, talin, focal adhesion kinase (FAK), and α-actinin [143] which bind to actin stress fibers (Figure 1.13 i)). The proteins forming those complexes are termed 'adhesome' and undergo a maturation process depending on mechanical force [144] [145].

Building up focal adhesions The first adhesion established with the ECM or any other environment is the nascent adhesion. It forms at the edge of the cell at the front of the lamellipodium region and either it progresses to the state of a focal complex or it disappears again. If the integrin finds a corresponding binding partner (fibronectin, collagen, etc.) it is activated and the cytoplasmic part can bind to actin via other binding partners such as vinculin. Compared to their size, these small adhesions can exert significant traction force and contribute to the forward propulsion of the leading edge [146] [147]. The focal complex is the precursor of the focal contact a transitional state in which vinculin is recruited to the adhesion [148] and the resulting structure bound to F-actin. The focal complex can either turnover rapidly or mature into a focal adhesion [142]. It is supposed that its formation at the leading edge of the cell depends on Rac through actin polymerization and Arp2/3 complex [149]. Upon maturation the nascent focal adhesion converts to a focal complex into a focal adhesion (FA) which has a slower turnover, is more stable and locates rather to the center of the cell. These FA are responsible for anchoring the cell and they are typically linked to stress fibers and sustain forces up to tens of nN. Their typical area is of about 2 μm^2 [145] and can reach up to 10 μm^2 [150].

Fibrillar adhesions Another adhesion type is the fibrillar adhesion, which is larger and more elongated observed on fibronectin-coated surfaces [151]. These adhesions are involved in the fibrillogenesis [152]. It has been proposed that these fibrillar adhesions can convert tension into directed movement along the fiber as the $\alpha5\beta1$ integrin moves from focal adhesion along fibrillar adhesion to small actin-microfilament bundles [152] [122].

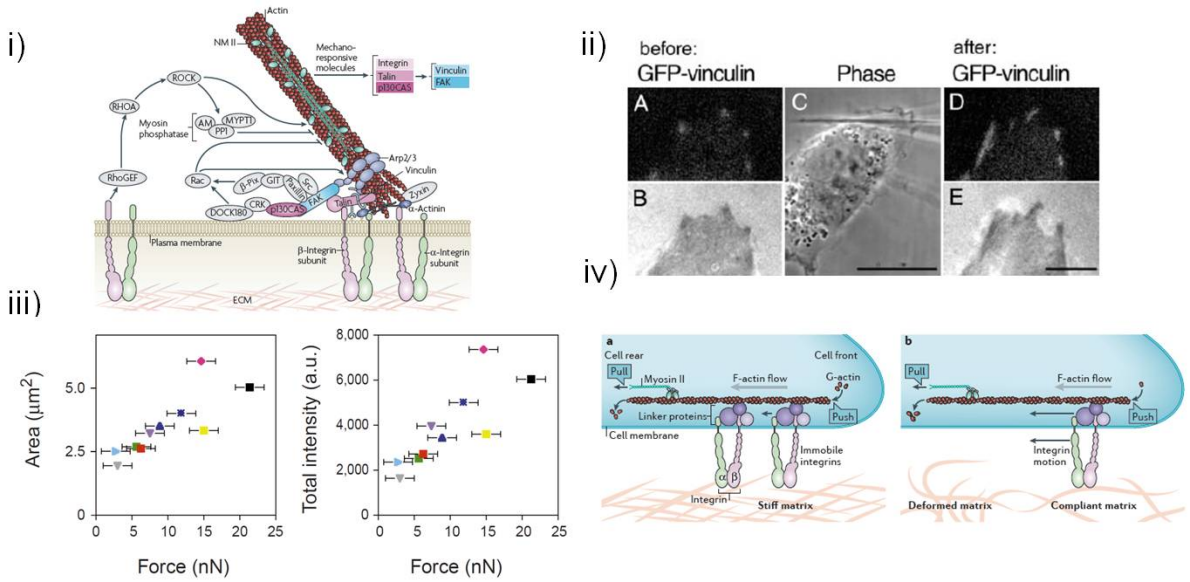

FIGURE 1.13: i) Representation of a focal adhesion and its components: $\alpha\beta$ extracellular domains of integrins bind to extracellular matrix. On the cytosolic side binding partners are talin, vinculin, zyxin among others, which are then establishing the connection to stress fibers which can upon contraction apply a force. This activates recruitment of new proteins and regulatory feedback via RhoGTPase signaling pathways (Figure from [94]). ii) Growth of focal contacts can be imposed by external force (Figure adapted from [145]). iii) Force applied by focal contact is proportional to its size (Figure adapted from [144]). iv) Stiffness sensing by focal contacts: Linker proteins (vinculin, talin, etc) move under retrograde flow or acto-myosin contraction putting load on integrins. A stiff matrix resists to the force, whereas a compliant matrix will deform and integrins move backward lowering the load on the whole machinery. This is followed by an altered cellular response (Figure adapted from [120]).

Focal adhesion composition may vary from one type of focal adhesion to another but also when changing the dimensionality of the cell environment to the third dimension, a change in composition and function of focal adhesion is observed. Especially the $\alpha5\beta1$ integrin percentage in the 3D case is higher and an enhanced cell biological activity can be observed [153].

Reaction to and application of force The growth of focal adhesions is force dependent as shown in [145]. The focal adhesion grows in direction of the applied force (Figure 1.13 ii), iii)). The process is Rho-dependent. External force bypasses the need for ROCK-mediated myosin II contractility. It has also been shown that the force applied by the focal contact scales with the area of the focal contact leading to 5 nN per μm^2 [144]. A similar mechanism is encountered for cell-cell junctions [154] [155]. The force-size relation does not necessarily account for nascent focal adhesions, where even small focal adhesions can exert a considerable force [146]. The exact relationship between force and focal adhesion size is not fully understood, especially not for mature adhesion as it depends on

the localization of the focal adhesion within the cell. For nascent adhesions, myosin II activity is dispensable, whereas it is required for maturation to focal adhesion. Myosin does not have a direct binding site to integrins but is coupled to the focal complex via actin and actin-binding proteins [94]. Focal adhesions permit the cell to integrate mechanical information from their surrounding and to trigger an intracellular response (mechanical or biochemical).
Cells sense the stiffness of their surrounding via focal contacts. Upon retrograde flow or acto-myosin contraction, linker proteins (vinculin, talin, etc) move, putting load on integrins, which is transmitted to the surrounding (Figure 1.13 iv)). A stiff substrate resists to the force and as a feedback response the focal adhesion grows whereas a soft substrate deforms and lowers the load on the whole machinery followed by an altered cellular response [120].
It has also been shown that individual focal adhesions can apply a constant or a dynamical, a tugging, traction [156]. Tugging traction is supposed to be crucial for durotaxis. This dynamical sensing process is modulated by a FAK/Paxillin/Vinculin signaling which also defines the operational range of the sensing process [156]. Experimental evidence shows that mature adhesions can sustain a sixfold increase in traction force without changing area. Also the adaptation of the cell response upon increasing traction force occurs instantaneously similar to muscle adaptation to load excluding a mechanochemical signal transduction way but a mechanical answer [157].
The cytoskeleton may also act as mechano-sensitive units [158]. Due to the stiffness sensing of the focal contact, cells cultured on glass or plastic substrate will exhibit much larger focal contacts than on soft substrates where the focal adhesions will be smaller and more dynamic [159].
Altogether, focal adhesions anchor the cell and allow it to sense its surrounding. They also permit the cell to apply forces to its environment. How can these forces be described, what are their characteristics and how do they allow a cell to move? These are questions I will try to answer in the following section.

1.6 Forces

Cells apply forces, to their surroundings especially when they migrate. The biomechanics field was inspired by D'Arcy Thompson and his observation of forms and shapes [160]. Since then, a wide range of discoveries going from the cell scale to the molecular structure of mechanosensitve proteins has been done: The sliding filament model for muscle contraction has been proposed in the 1950s [161]. Force exerted by cells has first been observed in the 1980s while putting cells on a rubber band [162]. Traction force microscopy was performed on migrating cells [163] in the 1990s, discovering different force profiles at the front and the back of the cell [164]. In the 2000s the force dependent growth of focal contacts was demonstrated [144] [145] and a microneedle assay relying on bending generated by the cell was developed [146]. To fully understand cell motility, the relationship between mechanical force and migration must be uncovered. Until now, it remains elusive. In the following, I will introduce the physical description of cells as dipoles, the forces exhibited in cell migration and methods to measure the force. The role of focal

adhesion in traction force has been previously described.

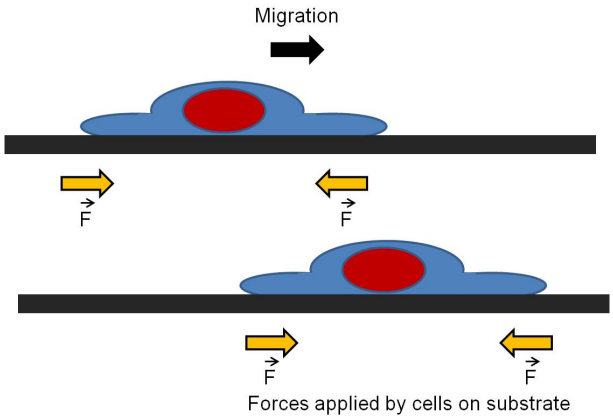

FIGURE 1.14: Schematic description of migrating cell on 2D surface and corresponding applied forces. Figure adapted from [165], [166] and [16].

A difference can be made between static deformation, generated by a non moving cell probing its environment and dynamic deformation when the cell is actually migrating. Also the scale of the system has to be taken into account. One can either observe a deformation generated by the whole cell on a large scale or on a smaller scale the force exerted by one focal contact. In both cases, knowledge about the elastic properties of the substrate is required. The experimental setup needs to match these requirements. For small deformations micropillar setup can be used. Cells are placed on an array of micropillars fabricated using lithography. The mechanical characteristics of the pillars can be tuned by their height and diameter. Upon traction force the cantilevers beam bends. From the deflection of the pillar and its elastic modulus the applied force can be calculated [167]. This method has the restriction that it can only be applied to the flat 2D case and that it does not offer a continuous surface. In a gel based assay, to calculate the force, the deformation of the substrate needs to be evaluated. To obtain the absolute force the mesh needs to be acquired at its strain free state to have a load free reference. Extraction of force can be basically described in two steps: Track substrate surface displacement via optical phase or wide-field microscopy and from there calculation of force. Particles or references in the image are identified and the spatial correlation between two images determined. Either single particle tracker or digital image correlation algorithm are used for calculation of displacement, such as particle image velocimetry (PIV), where micrographs are subdivided into smaller elements and cross correlation is performed [168] or Kanade-Lucas-Tomasi algorithm (KLT). KLT identifies bright features in images in subsequent images and correlates their displacement [169].
The relation of force to deformation can be related by Fredholm integral of first kind [170]. The relation is not straightforward as it is an ill-posed inverse integral problem [170]. Due to its complexity, it is sensitive to noise and there is no unique, continuous solution. Forward modeling the substrate as infinite half space, introduced by Dembo *et al* [163], is used to obtain the force from a displacement field. Also inverse computational models, determining continuous displacement field and then directly evaluating the strain, are

used for extraction of force [171]. Fourier Transform Traction Cytometry (FTTC) and Green's function approach (displacement field caused by a point force) or the boundary element method are some strategies to overcome this problem. The solution of the Green's function is known as the classical Boussinesq solution and can be obtained analytically from linear elastic theory [172]. The displacement equilibrium solution inside a semi-finite half-space with applied force at its free boundary is described by the Boussinesq theory [173]. For an isotropic medium only the elastic modulus and the Poisson ratio of the substrate are required for force calculations. 3D force traction microscopy was introduced in 2007 by Ravichandran *et al* [174]. In principle, 3D traction force relies on the same method as 2D traction force except for being more complex. In terms of experiments balancing spatial, temporal resolution and keeping the phototoxicity low might be challenging. Furthermore, the Green function does not have an analytical solution but must be approximated with numerical tools. The anisotropic characteristics of most of the gels must also be overcome [171].

A polarized cell (or contractile subunits) can be modeled by a source of force. This source is composed of two forces F which need to be equal, opposite and separated by a nanoscale distance d [166]. They are named force dipoles in analogy with electrostatics. The local elastic dipole is defined by $P_{ij} = d_i F_j$ the dyadic product[3] of the force F_j and the distance d_i. The elastic dipole is a tensor. For large scales the coarse-grained force density is evaluated and upon different steps, one can show that the interaction energy of the dipoles with the external strain can be described as [166]

$$F_e = \int dr p_{ij}(r) u^e_{ij}(r), \tag{1.2}$$

u^e_{ij} denotes the external strain and $p_{ij}(r)$ the local force dipole tensor per unit volume. This description can account for dipoles in infinite medium. The case of a cell in an elastic matrix with a rigidity differing from cell rigidity is more complex. The elastic interaction of an active cell with soft material can be modeled as anisotropic force contraction dipoles. In analogy to condensed matter systems, cell can be described as point defects in an elastic medium if the distance between cells is much larger than their spatial extent. The force is limited to a small space and the force distribution can be described by its force multipoles [175] [176]

$$P_{i_1 \ldots i_n i} = \int s_{i_1} .... s_{in} f_i(\vec{s}) d^3 s \tag{1.3}$$

f_i is the force density and $d^3 s$ denotes a volume integral. P_i is the first order term the vector of the overall force and the second order term is the force dipole P_{ij}. For point defects it can be assumed that overall force vanishes due to Newton's third law. The force exerted on the environment, thus the elastic medium and on the defect have to balance each other. Cells are in contact with an elastic medium and an aqueous medium at the same time, rendering the description more complex. Unbalanced forces, balanced by viscous forces in the aqueous medium, might appear. According to their symmetry properties dipoles are classified: isotropic and anisoptropic dipoles, with or

[3] *see Appendix*

without moment. The isotropic dipoles are centers of contraction also called pullers in reference to hydrodynamic swimmers [177]. Hence, expansive dipoles are called pushers. Anisotropic dipoles without moment are used to describe probing force patterns of cells. The driving force for dipol orientation is energy minimization. Mechanical properties of the environment such as elastic rigidity and prestrain, but also sample geometry and boundary conditions influence the buildup of these dipoles [176].
In Figure 1.14 a cell migrating on a 2D surface applying equal force at the front and the back is depicted. For the dynamic equation of the cell center one needs to consider [16] $\sum_i m^i \frac{dv^i}{dt} - (\sum_i, f^i_{int} + \sum_i f^i_{fluid} + \sum_i f^i_{sub}) = 0$ denoting $m^i \frac{dv^i}{dt}$ the inertial force, f^i_{int} the internal forces of the cell, f^i_{fluid} the fluid forces and f^i_{sub} the force on the substrate. The sum of internal forces of the cell is zero due to Newton's third law. The force of the fluid is negligible and the inertial force due to the low Reynolds number environment as well. This leaves us with the force on the substrate being zero $\sum_i f^i_{sub} = 0$. Therefore, instead of looking at the sum of forces the dynamic of forces is informative for the cell migration. The zero order of multipole analysis is zero, so the first relevant term is the first order term, the dipole. The second order term is a quadrupole. These moments are tensors, having a magnitude and a direction [16]. The spatial properties of the moments allow us to make assumptions about the directionality or outcome of a cellular process.

Dembo *et al* investigated the traction force of cells while migrating with traction force microscopy (Figure 1.15 i)). Cells apply forces while locomotions and contraction centers could be identified [163]. Since then, various groups have been investigating traction force [180] [181] [182]. For instance, a multipole analysis has revealed a force-motion relation for *Dictyostelium* cells [16]. The first two terms (dipole and quadrupole), reflecting rotational and front-rear asymmetries were calculated. Cells migrated along the force axis of the dipole, whereas the direction was set by the force quadrupole (Figure 1.15 iv)- vii)). Traction force analysis has been performed for neuronal migration [178]. Neurons typically migrate during embryogenesis and exhibit low traction force [183]. Three contraction centers (CCs), dipoles have been observed in these cells, two at the front and one at the back of the cell. The contraction correlates with soma translocation (Figure 1.15 ii)). For traction force of cancerous cells in 3D non-linear biopolymer networks constant force and a gliding motion have been reported [184].
Bergert *et al* [179] studied integrin-independent migration in microchannels for Walker cells (Figure 1.15 iii)). On 2D surface integrin dependent migration showed a contractile dipole pattern, whereas integrin-independent migration was based on an extensile dipole. The force applied by the cells in channels was computed and it was shown that non-specific friction can account for cell motility in channels and it is based on an extensile dipole.
Altogether recent discoveries suggest that traction force the description of the cell as one dipole might not be sufficient.
Force is applied by acto-myosin structures within the cell. Connections are established via focal adhesions. Both, dynamics of acto-myosin structures and focal adhesions assembly are controlled by the Rho pathway. So how are these factors influencing cell migration in a three dimensional environment?

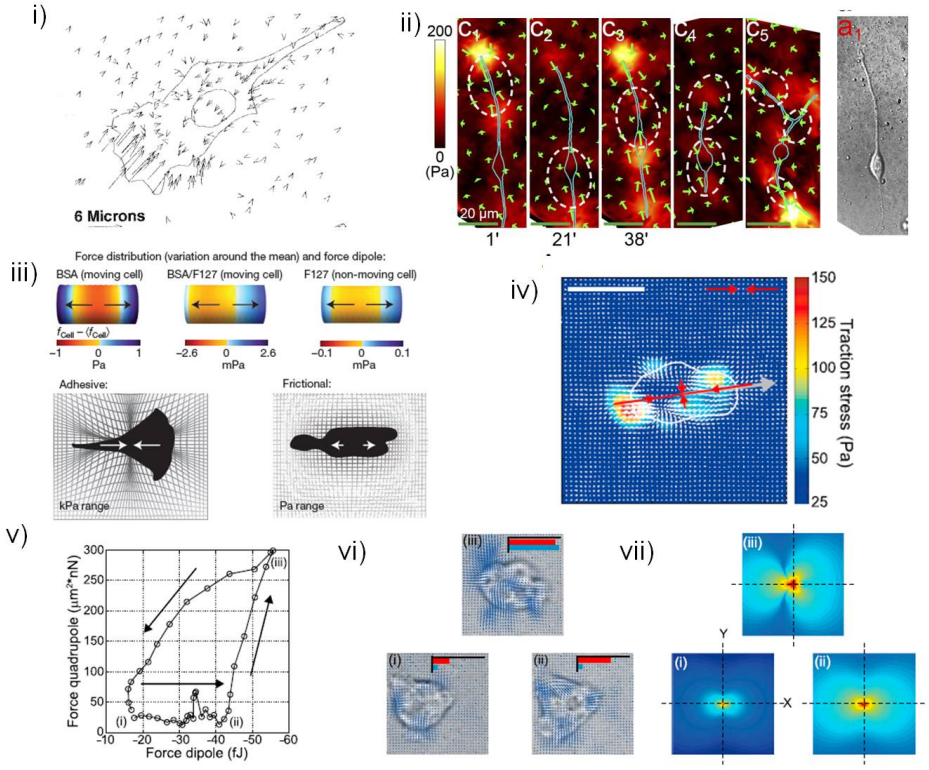

FIGURE 1.15: i) Traction force applied by cell on a 2D surface (Figure from [163]). ii) Migrating neuron having contraction centers along the cell body. Area of highest gradient of force in white (Figure from [178]). iii) Calculated force applied by Walker cells in non-adhesive microchannel compared to 2D force pattern shows an extensile force [179]. iv) Traction stress field snapshot applied by *Dictyostelium* migrating on a surface with corresponding force dipole. Values of the eigenvector are represented in red and cellular velocity vector in gray, scale bar 10 μm and -30 fJ for dipole amplitude. v) Dipole quadrupole relation and evolution from one state to the other. vi) Force maps for stages (i)-(iii) shown in v) Red bar indicates amplitude of force dipole and blue of quadrupole. vii) Deformation field induced by multipoles (Figures from [16]).

1.7 Cell migration in 3D

2D migration takes place on a 2D planar surface which makes the definition of a 2D space straightforward. There are two degrees of freedom on a 2D surface. On the other side 3D, migration might include three degrees of freedom x, y and z or refer to a 3D environment. We concentrate thereafter on migration in a three dimensional environment. Furthermore, cells need to be in contact with the environment to be able to sense it, which often leads to a confining environment (Figure 1.16). These environments are either a gel formed by extracellular matrix proteins as collagen, for example, or microchannels. In the following, I will introduce observed migration types in different 3D environments.

Cell migration in 3D has been studied in gels [5] [7] [185] microchannels [186] [187] [188] or cells sandwiched between two plates [188]. Various efficient migration types apart from mesenchymal migration have been reported such as ameboid migration [189] and bleb

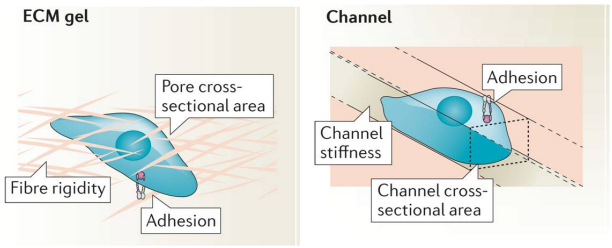

FIGURE 1.16: Main physical variables for gel and microchannel environment: Fiber rigidity or channel wall stiffness, pore cross-sectional area and adhesion (Figure from [142]).

based migration [5]. Different physical models have also been developed to account for these migration types [190] [188]. Questions arise concerning the role of the nucleus: On a 2D surface cells do not encounter external physical resistance to move the nucleus which might not be the case in an entangled meshwork [7] [191] or a small channel [192]. Another open debate is if 3D migration is more similar to 1D (cells on a line) than to 2D migration and if 1D migration can be used as a simplified model for 3D migration [193] [194] [195]. To which extent results on 1D stripes or fibers can be transposed to 3D migration will strongly depend on the system and the studied relation.

For instance, comparing 1D, 2D and 3D migration both 1D and 3D migration show higher migration speed independent of ligand density and dependent on myosin II activity [193]. Pointing in the same direction HT-1080 fibrosarcoma cells depleted in zyxin, a protein of the focal contact, have an oscillatory migration behaviour in 3D collagen matrix and on 1D stripes but not on 2D surfaces [194]. Cells can also migrate on suspended fibers [196]. Cells on these fibers generate lateral actin based waves which propagate to the protrusion of the cell. These waves are cyclical, have a fin-like shape and can travel up to several hundred micrometers extending the leading edge [195]. Actin-based waves have also been proposed for *Dictyostelium* [197].

To a certain extend 1D might mimic 3D migration. However, in this configuration the confinement is not taken into account. Hence, Tozluoglu *et al* [198] have developed a computational model to predict the optimal migration strategy for cancerous cells dependent on the surrounding of the cell. They compare a continuous confined such as microchannels, a non-continuous confined environment such as a gel and a 2D surface. In the computational model, contractility and adhesion are tuned, different geometries lead to different optimal migration configurations. Whereas a high contractility is impeding the cell movement on a surface, as it is not able to adhere and tends to detach from the surface, in 3D environment a high contractility was favoring cell migration. Also cells in 2D could not migrate without attachment to the surface in 3D highest migration speed was obtained for adhesion free migration. The higher the confinement was, the better the migration with these parameters.

Adhesion-free migration can be studied with leukocytes. It has been reported that their migration is integrin-independent (Figure 1.17 iv)). Cell migration in this case is driven by actin protrusive flow at the front and myosin II dependent contractions when passing through small pores [185].

The influence of pore size, matrix rigidity and contractility has also been evaluated [7]. It shows that migration linearly depends on pore size and arrest of migration is reached for

deformations of 10% of nuclear cross-section (Figure 1.17 v)). Acto-myosin- and integrin-dependent mediated force generation are required for efficient propelling of the nucleus. Stiffness of nucleus probed by lamin A levels, was also reported to influence nucleus passage [191].
As mentioned above, there are various 3D environments. Apart from the matrix structure, 3D cell migration is as well studied in microchannels: in microchannels myosin II driven contractility is required and integrin mediated signaling promotes migration [199]. Nevertheless, cells are able to migrate in microchannels without focal adhesions. A model of coupling actin polymerization at the cell membrane to geometric confinement shows that nonspecific friction is sufficient to account for forward movement. Myosin II activity is not needed to generate motion but is shown to increase the velocity [190]. Confinement might also influence distribution of biomolecular aggregates or even organelles in the cell [200]. Bergert *et al* investigated the force transmission during adhesion-independent migration using blebbing Walker cells in microchannels. In these cells, actin cortex flows drive cell movement [179].
Cells can adapt their migration mechanism in channels: thus experimental evidence combined with a theoretical approach has shown that MB-231 breast cancer cells and S180 sarcoma cells are able to migrate in confining channels when actin polymerization and myosin II activity are inhibited. These cells establish a polarization of Na^+/Ca^{2+} pumps and aquaporins and the driving force for migration is water permeation leading to the osmotic engine model [201]. Also involving pressure, in another study neutrophils showed the ability to sense hydraulic pressure gradients in microchannels and "choose" direction of migration in consequence for example avoiding dead ends in microchannel mazes [187]. Cells adapt to the confinement for example by changing morphology like in this study: cells confined between two plates in a microfluidic device show a high plasticity in their migration characteristcs depending on the degree of adhesion, contractility and confinement [188]. Under low adhesion, high contractility and confinement even non-motile cells such as epithelial cells form uropods and have a high speed. The observed phenotype could be related to a strong retrograde actin flow induced by myosin II contractility and asymmetric actin turnover (Figure 1.17 iii)).

A similar mechanism has been investigated in early *Zebrafish* progenitor cells termed stable-bleb migration [202]. Here a switch to stable-bleb migration can be induced upon cortical contractility fluctuations and maintained due to a positive feedback between cortical flows and gradients in contractility. These cells seem to be able to migrate with and without integrin-binding to ligands (Figure 1.17 ii)). In both migration types the physical model underlying motility is based on spontaneous contractility-mediated cortical flow. This mechanism is widely independent of actin treadmilling. Deriving non linear dynamical equations for a round cell and inserting a perturbation to determine the linear stability and reducing the approach to a 1D problem leads to a threshold beyond which the instability appears [203]:

$$Pe = \frac{-\zeta\mu_0}{\tilde{D}\xi} > Pe_c. \tag{1.4}$$

with $\tilde{D} = \frac{(D_c k_1^{off} + D_\mu k_1^{on})}{k_1^{on}}$ where D_c denotes the diffusion coefficient of myosin, D_μ the diffusion coefficient of actin cortex, ξ the friction, k^{on} and k^{off} binding rate to cortex.

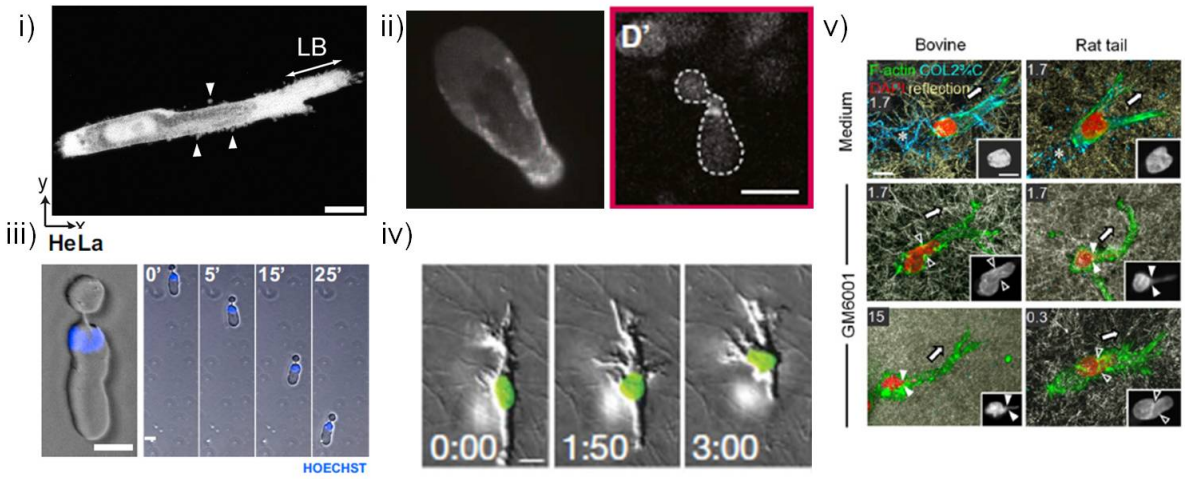

FIGURE 1.17: i) Lobopodia structure indicated with white arrow of a HFF cell in 3D CDM and side blebbing (Figure from [5]). ii) Polarized blebbing of a *Zebrafish* progenitor cell between plates (left) and *in vivo* [202]. iii) Hela cell migrating in a highly confined environment with no adhesions. Cell forms uropod [188]. iv) Leukocyte migrating in 3D collagen [185]. v) GM6001 cancerous cells migrate in 2 different types of 3D collagen and deform their nucleus. Nucleus shape ranges from an ellipsoid, an hourglass over a round to a prolapse deformation depending on the pore size (Figure from [7]).

Following calculation shows that homogeneous state is unstable and that above a critical value of the Péclet number Pe_c, describing the relative importance of diffusive and advective transport, the system reaches a non-homogeneous steady-state marked by a nonvanishing steady-state cortical flow [203]. This model shows that cortical flows are sufficient to induce cell migration in a three dimensional environment.
In 3D matrices, myosin II seems to have an additional role: it has been reported that myosin II minimizes cell-surface curvature in collagen matrices for invasive endothelial cells. Low curvature stabilizes myosin II cortical association and cycles of localized cortical myosin II assembly have been observed. This might guide 3D cell migration as it controls branching morphogenesis [204].
Also, in matrix environments, new migration modes have been discovered: Petrie *et al* [5] established a relationship between a new mode of migration, termed lobopodia (Figure 1.17 i)) and the environment characteristics in a Cell Derived Matrix (CDM). This type of protrusion is cylindrical, blunt and voluminous in contrast to the flat lamellipodia in 2D. It does not show polarized Rac and Cdc42 at the front of the cell and is contractility dependent thus lobopodia disappear upon treatment with MyosinII/Rho inhibitors. The appearance of lobopodia is connected to the linear elasticity of the CDM and to blebbing, suggesting a pressure driven mechanism for migration. This was investigated by measuring the intracellular pressure at the front and back of the nucleus [6]. The cell is compartmentalized in a high and low pressure compartment where the nucleus divides the cell and acts as a piston. Pressure is higher at the front of the nucleus. The mechanism is contractility dependent and relies on nucleoskeleton-intermediate filament linker protein nesprin-3 member of the SUN-complex.
So far we have seen the variety of migration modes in 3D environemnts. Also the migra-

tion description needs to be adapted in 3D. In terms of migration characteristics, cells in 3D are not well described by the persistent random walk[4] model as shown in a study with fibrosarcoma cells in 3D collagen matrices [205]. Inserting cell heterogeneity and local anisotropy to the PRW model yielded in a description of 3D characteristics. A superposition of several different stochastic processes termed superstatistical analysis has also been proposed for modeling heterogeneous random walks and uncover migration strategies [206].

In conclusion, studies on 3D cell migration have been focusing on the role of confinement probing focal adhesions, contractility, environment elasticity and behaviour of protrusion. New migration mechanisms have been reported for 3D cell migration such as pressure driven migration and lobopodia. Still there remains some aspects of 3D cell migration which have not yet been understood. For instance the force distribution and the connection to movement has not yet been completely revealed. How does a cell manage to pass through a dense entangled network? This is the question which motivates this work. One approach to answer this question is to look at the spatio-temporal distribution of forces the cell applies to its surrounding while migrating.

[4] *see Appendix*

2 Material and Methods

In this chapter I will introduce the experimental techniques used. First I will start with the procedures for creating the 3D environments, then describe cell culture and related techniques. I will also describe the setups used for image acquisition and matrix characterization. Finally, I will explain how deformation applied to the *Cell Derived Matrix* (CDM) is quantified. Tables of used products and catalog numbers can be found in the Appendix.

2.1 Cell Derived Matrix (CDM)

In this section, I will present the technique to produce a CDM my main setup for investigation of cell migration in 3D. First the protocol [11] is presented and then the different modifications of the CDM introduced.

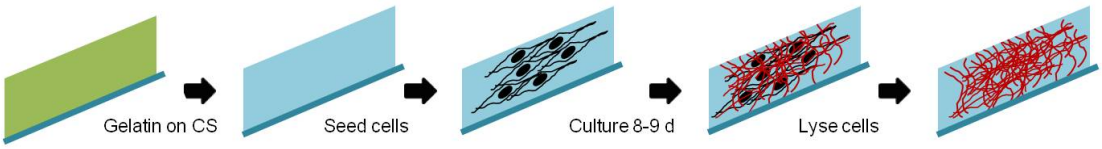

FIGURE 2.1: Schematic description of CDM production steps: The glass coverslip (CS) is covered with gelatin and further treatment with glutaraldehyde and gelatin is performed before cells are seeded. Culture is maintained 8-9 days before lysis of cells leaving only the secreted proteins forming the CDM.

Cell Derived Matrix protocol. The Cell Derived Matrix is a matrix produced by cells. The protocol is schematically depicted in Figure 2.1. All the components of CDM production are bought sterile, autoclaved or for the 1 % glutaraldehyde solution filtered before usage. A glass coverslip (#1, Marienfeld Laboratory Glassware) is covered with 1% gelatin (gelatin from cold water fish skin, Sigma) and put at 37°C in the incubator for 1 h. The pre-coating of the CS will allow later to retain the proteins when removing cells. After the CS has been washed twice with 1 % PBS the gelatin is incubated for 20 min at room temperature with 1 % glutaraldehyde (Sigma). This compound crosslinks the gelatin and gives a certain stability to the later protein scaffold. The CS is rinsed again

twice with PBS before incubation for 20-30 min with 1 M glycine (Sigma). This allows to saturate the aldehyde groups in the gelatin. Subsequently the CS is washed twice with PBS and NIH3T3 fibroblasts are plated on the CS. Cells need to be plated at high density in order to produce CDM. For NIH3T3 this corresponds to 1 million cell per 10 mm Petri dish. Alternatively at this step the gelatin can be stored at 4°C in the fridge. The culture medium is supplemented with 50 μg/ml L-ascorbic acid and changed every second day. L-ascorbic acid should promote collagen secretion of cells. The culture is maintained for 8-9 days. Cells are removed by a lysis medium consisting of 20 mM NH_4OH and 0.5 % Triton (both Sigma) in 1x PBS after washing twice with PBS. NH_4OH stabilizes the CDM in presence of Triton. The pre-warmed lysis medium is carefully pipetted on the CS and incubated for up to 10 min at 37°C in the incubator. PBS is added and the CDM stored at 4°C in the fridge, this gives the CDM more stability. The next day, PBS is carefully changed 3 times to remove all residues of Triton which might affect cells during experiments. The matrices are covered with PBS and stored for up to 1 month in the fridge [11]. It is recommended to use the CDM in the following two weeks as probability of detachment increases with time.

Inserting beads in the CDM We use magnetic and optical tweezers measurements for characterization of CDM. Therefore, beads of 2 μm diameter (Sigma) and magnetic beads of 1 μm diameter (Invitrogen) need to be inserted in the CDM. Before insertion, beads are diluted in a 1:1000 ratio from the initial solution and rinsed three times with PBS to remove any toxic components for cells. Therefore, latex beads are centrifuged at 10000 rpm. They form a pellet, the PBS is carefully removed before they are again resuspended in PBS. Magnetic beads are harvested via a magnet and retained at the bottom of the Eppendorf tube. After washing, beads are added and plated with cells on gelatin. They remain in the CDM after lysis of cells.
A reference framework for drift analysis is created via fluorescent 200 nm beads (Invitrogen). CS are plasma-activated to become hydrophilic and to ensure a homogeneous covering of the surface. Beads are diluted in a 1:5 000 ratio. A 100 μl drop is deposited on the CS and spin-coated at 1000 rpm for 15 s. The CS is put in the oven at 65°C overnight to increase the adherence of beads. CS are sterilized under the cell culture hood UV light for 3 min and used as described above for CDM production. The sterilization time is kept minimal to prevent bleaching the beads.

Fibronectin We concentrated on the extracellular matrix protein fibronectin (FN) of the CDM. Therefore, we elaborated two methods to visualize FN for live imaging. In the first one rhodamine labeled fibronectin is added twice (1 μg) (Cytoskeleton Inc.) for a 96-well plate while changing culture medium. The second method consists in using genetically modified cells which are producing fluorescently labeled fibronectin. Transfection and establishing a stable cell line is described further in this chapter. The used construct is Ypet-FN from Erickson laboratory [129].

2.2 Microfabrication

The following section introduces microfabrication techniques to produce microchannels. First I will explain the different photolithography and then the soft lithography steps.

2.2.1 Photolithography

Photolithography is a commonly used technique for microfabrication [207] which is normally performed in a particle/dust-free environment, a clean room. This guarantees a high resolution for fabricated structures. The procedure is schematically depicted in Figure 2.2. A Silicon wafer is heated at 200°C on a hot plate for at least 10 min or plasma-activated with an oxygen plasma. Both methods serve to remove any humidity which would affect adhesion of the resist to the wafer. Then, after cooling down it is spin-coated with a photoresist (SU-8) for 30 s at a given speed resulting in a certain thickness (see table in Appendix). The wafer and photoresist are pre-baked at 65°C and 95°C corresponding to the resist thickness. The wafer is inserted in the mask aligner where it is put in contact with the mask and exposed to UV-light. Due to the mask, the resist is only illuminated in certain areas. Resines are either positive or negative resists. For a positive photoresist, the illuminated structure disappears. For the negative photoresist on the other hand the illuminated structure remains and the inverse structure of the mask is obtained. SU-8 is a negative photoresist. Afterwards, a post-bake at 65°C and 95°C is performed and the wafer is incubated under slight shaking in SU-8 developer for 2 min. The developing process can be reiterated if the structure has not been fully developed. The wafer is rinsed with isopropanol and dried with a nitrogen pistol. When the structures are not developed enough, white traces can be seen on the SU-8 after rinsing with isopropanol.

If structures of different heights are required a second lithography step is performed. In

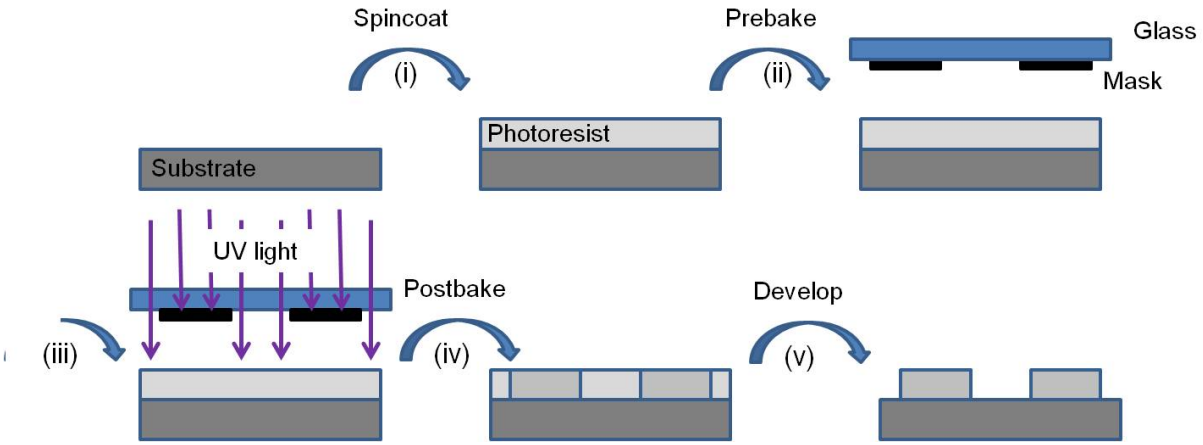

FIGURE 2.2: Photolithography steps (i) The photoresist is spin-coated on the substrate (ii) then pre-baked. (iii) The structure of the mask is transferred to the resine by exposing to UV-light. (iv) The crosslinking occurs via the post-bake (v) and the not-crosslinked resist is removed with the developer. For a negative resine such as SU-8 only the exposed parts remain.

this case, after developing the first layer, a second layer of SU-8 is spin-coated, a pre-bake

performed and the wafer put in the mask aligner. To insert a second layer on top of the first motif a second mask is used and aligned via alignment crosses which have been inserted in the design of both motifs while creating the masks. The same steps as described above are then performed to develop the motifs. Depending on the structure, the first developing step can be skipped.

2.2.2 Soft lithography

PDMS To transfer the structure from the silicon mask to the negative of the structure the replica molding technique is used [208]. For this, the pre-polymer and the curing agent are mixed in a 10:1 mass ratio. The "solution" is mixed with a pipette during approximately 3 min and then centrifuged at 4000 rpm for 5 min to remove air bubbles. The PDMS-solution is poured on the photoresist microstructures of the silicon wafer and put into a desiccator until air bubbles have disappeared. This process can be fastened by releasing every 5 min the vacuum in the desiccator. Then, the PDMS is put at 65°C in an oven for at least 4h. In the case of a smaller volume of PDMS 2h of curing are sufficient. To extract the structure, each motif is carefully cut with a scalpel. The steps are schematically depicted in Figure 2.3 (i)-(ii).

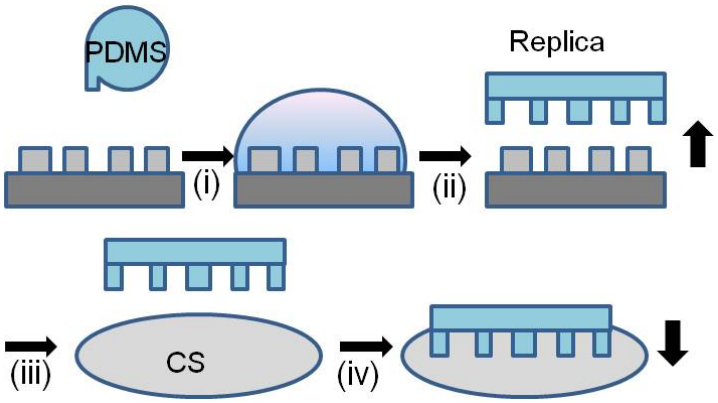

FIGURE 2.3: (i) PDMS is poured on the SU-8 structure and cured at 65°C. (ii) Then the PDMS is removed from the mold, a replica has been obtained. (iii) After plasma-activation of a CS and the PDMS (iv) both surfaces can be permanently bonded.

Bonding CS for bonding are washed with water and soap, rinsed with water and acetone before being carefully dried by a nitrogen pistol. The removal of small particles (dust) is critically important for a good bonding and a neat structure. Holes are punched with a biopsy needle into the chambers of the PDMS microchannel structure. The direction of punching is from the structured side towards the non structured side. To remove PDMS residues due to punching and dust, microchannels are sonicated in ethanol and dried by a nitrogen pistol. Glass CS and PDMS channels are plasma-activated in an oxygen plasma before the CS is put with the activated side centrally on the PDMS microchannels. To ensure good bonding, the PDMS is carefully pressed to the glass (Figure 2.3 (iii)-(iv)). The microdevices are used subsequently as filling of the chambers is easier when PDMS is still hydrophilic.

2.3 Experimental procedures

This section introduces the experimental procedures and setups including cell culture, DNA handling and drug use during experiment. We give an overview of all used constructs and drugs in the Appendix.

2.3.1 Cell culture of stable cell lines

Cells are cultured at 37°C under 5% CO_2 in Petri dishes, multiwells or flasks in an incubator. The culture medium is high glucose D-MEM with 1% penstrep (Penicillin Streptomycin, antibiotics to avoid contamination with bacteria) supplemented with 10% Bovine Calf Serum (BCS). REF52 cells are cultured in high glucose D-MEM with 1% penstrep supplemented with 10% Fetal Calf Serum (FCS). SW480 cells are cultured in D-MEM with 1% penstrep supplemented with 10% Fetal Calf Serum (FCS).
Cells are replated when having reached 90 % confluency. For this, cells are rinsed once with medium to remove all dead cells and floating cell fragments. Optionally one can also rinse with 1x PBS having the advantage that also medium gets removed, which would inactivate trypsin. 1-2 ml trypsin is added to a 5 ml dish and the Petri dish incubated for 3.5 min in the incubator. Under the microscope it is checked if cells have detached, if not the Petri dish is gently shaken until all cells have detached. The cells in trypsin are added to medium and centrifuged at 1000 rpm for 5 min. The medium is carefully removed until just the cell pellet is remaining. Cells are resuspended in the initial volume and diluted.

2.3.2 Preparation of primary cells

2.3.2.1 Lymphocytes

In the following we describe the LPS/IL4 (Lipopolysaccharide/ Interleukin-4) stimulation and CFSE labeling of lymphocytes [1]. Composition of RPMI medium and other cell reagents is indicated in Appendix. Image acquisition was performed under temperature and CO_2 control.

Red Blood Cell (RBC) lysis Spleen is recovered in 10 ml of ice cold PBS 1% FCS and centrifuged for 5 min at 1200 rpm. The pellet is resuspended in 3 ml of ACK (lysis buffer) and incubated for 5 min at RT and 7 ml of PBS 1% FCS added. The cell solution is spun down for 5 min at 1200 rpm and the obtained pellet resuspended in 900 μl of PBS 1% FCS.

Resting B cell purification CD43 beads are added in a volume of 100 μl and incubated at 4°C for 30 min. After adding of 10 ml of PBS 1% FCS the solution is centrifuged at 1200 rpm for 5 min. The pellet is subsequently resuspended in 900 μl of PBS 1% FCS. Then the MS column (cell sorting column) is prepared with 500 μl of PBS 1% FCS and

[1] Cells obtained from Bernardo Reina San Martin's lab (IGBMC) prepared by Anne-Sophie Thomas-Claudepierre

the cell suspension added. It is washed 3 x with 500 μll of PBS 1% FCS. CD43 cells are recovered by flow, counted, washed with complete RPMI and concentration adjusted to 1.2x 10^6 c/ml. Stimulation is started. LPS is used at 25 μg/ml and IL-4 at 50 ug/ml.

2.3.2.2 Mouse embryonic fibroblasts

Extracting of MEF from embryo Mouse embryonic fibroblasts [2] are extracted from mice embryos, amplified and frozen down:

- Dissect mouse embryos (12.5 to 13.5 days postcoitum) into 10 to 20 ml sterile DPBS in a 100-mm tissue culture dish. Embryonic internal organs are removed from the abdominal cavity using dissecting forceps.
- Transfer the carcass to a clean dish with fresh DPBS.
- Dissociate embryos with small pointed scissors, put in Erlenmeyer with agitator and glass beads and add trypsin.
- Agitate for 5 min and aspire supernatant. Repeat 3 times.
- Filter and transfer to 50 ml falcon, add some medium to inactivate trypsin.
- Centrifuge at 1200 rpm for 5 min, aspire supernatant and resuspend pellet in 50 ml medium.
- Put 10M cells in P14 and with 20 ml medium and incubate at 37°C at 5% CO_2 and change medium every day until confluency is reached.
- Freeze in 90 %FCS Es tested+10% DMSO with 1 P14 per cryotube (1ml).

Cell reagents and culture medium composition are listed in the Appendix.

Unfreezing of MEF MEF medium consists of DMEM (4,5 g/l glc) w/GLUTAMAX-I +10% FCS ES tested+gentamycine. Vial is unfrozen in waterbath before it is centrifuged in 15 ml of medium at 1400 rpm for 5 min. Supernatant is removed and cell pellet resuspended in 6 ml. Cells are counted to be used in the wished concentration for experiment.

2.3.3 DNA transfection

The list of used plasmids can be found in table A.10 (Appendix). DNA was amplified, purified and used for transfection. The protocols are described in the Appendix.
Transfection is performed by liposome transfection with Lipofectamin 2000 Reagent (Invitrogen).

- Cells are replated up to 3 h before transfection so that they are 50% confluent for transfection.

[2] MEF were obtained, unfrozen and seeded in CDM by Marion Humbert and Amélie Freismuth of the cell culture platform directed by Betty Heller (IGBMC).

- For transfection in 2 ml dish, 2.5 μg DNA is diluted in 125 μl Opti-MEM. If a double transfection is performed 1.25 μg of each DNA is taken and the solution is vortexed to guarantee a homogeneous distribution of the DNA.

- Lipofectamine is diluted in 150 μl Opti-MEM.

- The DNA and the Lipofectamine solution are mixed and left for 5 min.

- The culture medium is changed to serum-free medium.

- the DNA Lipofectamine mix is added to the cells.

- After 4-6 h medium is changed to standard medium again.

2.3.4 Sample preparation

Cells were trypsinized, deposited on the CDM and allowed to settle down at least 2 hours preceding the experiment. The CDM with cells was mounted on a customized holder and the medium changed to Leiboviz medium (L-15) supplemented with 1% BCS.
For microchannel experiments, cells are deposited in the chambers with a syringe or pipette. As cells tend to settle underneath the punched hole, the device is carefully knocked on the table (inside Petri dish) to deposit the cells to the entrance of the channels. As cells are deposited on two opposite sites of the channels only one side can be brought nearer to the channels.
Time-lapses were performed at 37°C with acquisition rate from 10 s to 5 min. Transfected cells were left for 24 h before image acquisition, trypsinisation and deposition could take place during this period.

2.3.5 Inhibitor treatments

Different drugs were used for probing different hypothesis (Table 2.1). Before adding drugs a control acquisition of at least one hour was performed. To avoid flows, defocusing and damaging the CDM with pipettes, medium with drugs was added to the running experiment without removing the medium already present. The dissolved drugs in pre-warmed L-15 medium of the double wished concentration was prepared for this purpose. Image acquisition was performed in presence of the drug except for Calyculin A 1 nM experiment where cells are solely incubated for 60 min and then the drug is washed out [188].

Table 2.1: Cytoskeleton drugs, their effect and concentration

Compound	Effect	Stock solution concentration	Concentrations in experiment
Blebbistatin	Myosin inhibition	10 mM in DMSO	25 μM
ML-7	Myosin regulatory light chain kinase inhibition	10 μM in DMSO	10 μM
Y27632	Inhibits ROCK	10 mM in DMSO	10 μM
Latrunculin A	Sequesters monomeric actin	1 mM in DMSO	1 μM, 5 μM, 10 μM
Nocodazole	Depolymerizes microtubules	10 mM in DMSO	10 μM
C8	Nucleates actin	10 mM in DMSO	100 μM
Calyculin A	Phosphorylates MLCK	2mM/200 μM	10,1 nM
CK666	Inhibits Arp2/3 complex	10mM in DMSO	50 μM
TGN	Blocks aquaporin 4	20 mM in DMSO	100 μM
EDTA	Calcium chelator	prepared fresh before usage	4mM
Gd^{3+}	Blocks calcium channels	10 mM in ddH_2O	100 μM

2.3.6 Immunostaining

Immunostaining was used to visualize different proteins when live imaging was not required. It allows to increase the statistics. The advantage is that one can go back to the slide and re-image the stained structure after some time. In the following the used standard protocol is explained.

- Cells adherent on CS or inside CDM (on CS) are incubated with pre-warmed 3% PFA for 17 min. The CS are washed with PBS. The protocol can be interrupted here and the CS be stored at 4°C for some time.
- CS are incubated for 3 min in a 0.5% Triton solution to permeabilize the membrane
- To prevent unspecific binding, a BSA blocking step is performed with 5% BSA
- CS are washed 3x with 1% PBS for 5 min
- Fixed cells are incubated with primary antibody for 45 min in PBS 5% BSA
- CS is washed 3x with 1% PBS for 5 min
- Fixed cells are incubated with secondary antibody for 60 min in PBS 5% BSA
- CS is washed 3x with 1% PBS. The protocol can be stopped here and fixed cell guarded in 1% PBS at 4°C or imaged at this stage.
- A 10 μl drop of 1:1 Glycerol:PBS (v:v) is deposited on a glass slide
- The CS is carefully mounted upside down on the glass slide. It is important that the CS is completely covered with the solution. Also it is recommended not to move the CS once upside down as this might damage cells or CDM.
- To prevent drying, the CS is sealed with nail polish. First four drops are deposited and let dry to prevent moving of the CS. Then the rest of the space is filled.

Nucleus labeling with DAPI To visualize the nucleus (DNA) in live cell imaging a DAPI (4',6-Diamidino-2-phenylindole) staining protocol has been used. DAPI was diluted in medium to a final concentration of 1:250 from the stock solution. Cells were incubated 4-6 h in the solution. After rinsing once, cells were trypsinized and deposited in CDM or microchannels. Experiments were performed 4 h after seeding.

2.4 Setups

This section introduces the microscopes used for image acquisition and other imaging techniques. It also explains the different characterization methods used for investigating the structure and accessing material properties of the CDM.

2.4.1 Optical setup

Different microscopy imaging systems were used for different experiments. If not stated differently, epifluorescence imaging with a Nikon Ti Eclipse was used for time-lapse in microchannels and CDM drug experiments. For a high time resolution z-stack acquisition we used Leica SP5 and Spinning disk. Images were processed with Fiji or Image J.

2.4.1.1 Conventional setups

A Nikon Ti Eclipse inverted microscope equipped with a Lambda DG-4 (Shutter Instruments Company), a charge coupled device (CCD) camera coolSNAP HQ2 (Photometrics), a temperature control system (Life Imaging Services) and occasionally CO_2 control was used. The objectives were a PhLL 20x (air, 0.95 NA, phase contrast, Nikon), a Plan Apo 60x objective (oil, 1.40 NA, DIC, Nikon) and a x40 (air, 0.95 NA, Olympus) objective with a home-made adapter to fit the Nikon microscope. Images were acquired with the NIS Elements software (v3.10, SP3, Nikon) and then exported for further processing. A CKX41 inverted phase-contrast microscope (Olympus) was additionally used. For acquisition a cooled CCD camera (Hamamatsu) and the ImageJ plugin Micro-Manager were used. The system is equipped with a temperature control (Cube box system) and 4x, 10x, 20x and 40x phase contrast air objectives.

2.4.1.2 Confocal setups

Leica TCS SP5-MP inverted equipped with a Leica Application Suite Advanced Fluorescence LAS AF 2.6.3.8173/LAS AF 3.1.2.8785 acquisition system with hybrid detectors (HyD), photomultiplier tube (PMT) and a heating system (Cube box system) was used with a HCX PL APO 63X oil objective (1.4 NA, Leica).
Additionally a Leica DMI6000 inverted microscope was used as a spinning disk, equipped with a Andor iQ 1.9.1 acquisition system, Yokogawa CSU22 spinning disk unit and a heating system (Tokai Hit Stage Top Incubator, INU incubation system for microscopes). A HCX PL APO 40x oil objective (1.25 NA, Leica) was used.

2.4.2 Laser ablation

For laser ablation, a Leica TCS SP8-MP based on a Leica DM6000 CFS upright microscope was used, equipped with a Leica Application Suite Advanced Fluorescence LAS AF 2.6.3.8173/LAS AF 3.1.2.8785 acquisition system with photomultiplier tube (PMT) and hybrid detectors (HyD) and an environmental chamber for temperature control (Cube box system). A 25X HCX IRAPO L water objective (0.95 NA, Leica) was used and ablation performed with infrared pulsed laser (Coherent Vision II with precompensation).
FRAP module was used with point ablation with a wavelength set at 800 nm and exposition time of 100-200 ms. During experiment, parameters such as laser power and gain were set to minimum to have the smallest cut possible and to minimize heating and boiling inside cells or CDM.

2.4.3 Electron microscopy

Native CDMs or CDMs with integrated cells were imaged by electron microscopy [3].
To have the z-information of CDM, they were grown on Polystyrene sheets. The CDMs were fixed by immersion in 2.5% glutaraldehyde and 2.5% paraformaldehyde in cacodylate buffer (0.1 M, pH 7.4), and post-fixed in 1% osmium tetroxide in 0.1M cacodylate buffer for 1 hour at 4°C. The samples were dehydrated through graded alcohol (50, 70, 90, 100%), and critical point dried with hexamethyldisilazane. After mounting on stubs with conductive carbon adhesive tabs, the CDMs were coated with gold-palladium in sputter coater (BAL-TEC SCD 005). In case of z-imaging CDMs were cut and mounted upright with conductive carbon tape. Then CDMs were examined by XL SIRION 200 FEG SEM (FEI company, Eindhoven, The Netherlands).

2.4.4 Atomic force microscopy

An atomic force microscope [4] (AFM) [209] relies on the interaction between the tip of a cantilever and the studied surface. These interactions make the cantilever deflect, which is detected by a photodetector. A feedback mechanism allows the distance of the lever to be constant to the substrate. By scanning the probe, a topographical image of the probe can be obtained. Different modes can be conducted on the AFM: the contact or the tapping mode. In contact mode the tip is in contact with the substrate and in tapping mode the tip is at a defined distance from the substrate oscillating with its resonant frequency. Depending on the interaction with the probe this resonant frequency is shifted. For mapping the force surface relation the peak-force tapping mode is used similar to the tapping mode. A force curve is captured for every point of the sample.
CDM was cultured on 1cm x 1cm glass CS to fit AFM chamber. Atomic force microscopy (AFM) images were obtained by scanning the samples using a Nanoscope 8 (Bruker) operated in Peak-Force tapping mode. Ultra-sharp silicon cantilevers with a nominal tip radius < 5 nm and spring constant of 0.7 N/m were used. AFM images were operated in buffer solution (PBS 1x) at room temperature. The force was reduced in order to avoid dragging of molecules by the tip. Integral gain was adjusted to give sharp images. Images were taken without on line filtering and were subsequently processed only by flattening to remove the background slope. Image analysis and processing were performed on integrated software.

2.4.5 Optical tweezers

Optical tweezers [5] setup is schematically depicted in Figure 2.4. The laser is sent through a mirror, a dichroic mirror and focused via a x100 high numerical aperture oil objective onto the sample. The sample is imaged via a broadband light source and a CCD camera

[3] CDM were treated for imaging by Nadia Messaddeq and imaging performed by Jean-Luc Weickert.
[4] AFM measurements have been performed by Mounir Maaloum (IPCMS).
[5] Optical tweezers measurements have been performed in collaboration with Sébastien Harlepp (IPCMS).

and further processed. The bead is trapped in the laser focus. To access the material characteristics, the bead is moved via an xyz-stage movement out of the trap.
CDM with fluorescent beads were mounted on a holder and put on a home-built microscope described in [210] [211] or an inverted microscope (Olympus IX71). A Spectra Physics YAG laser (1064 nm) is used and focused through a high numerical oil immersion objective (Zeiss achromat x100 1.25 NA) onto the sample. The laser output power is variable from 0.9 W to 2 W (laser head output). A second objective (Olympus X40 0.6 NA) capturing the light scattered by the bead is used. For image acquisition, LabView 9 (National Instruments) and a CCD camera (DCC3240C, thorlabs) are used. Beads are centered in the optical trap. The position of the CS (bottom of CDM) is registered to obtain the z position of the measured beads in the CDM. Stage is moved in 0.2 μm/s or 0.1 nm/s steps, covering a distance of 2-4 μm in x,-x and y,-y directions. The laser power is calibrated with beads in solution. Subsequent data processing was performed with ImageJ bead Tracker Plugin and further post-processed with IgorPro Wavemetrics.

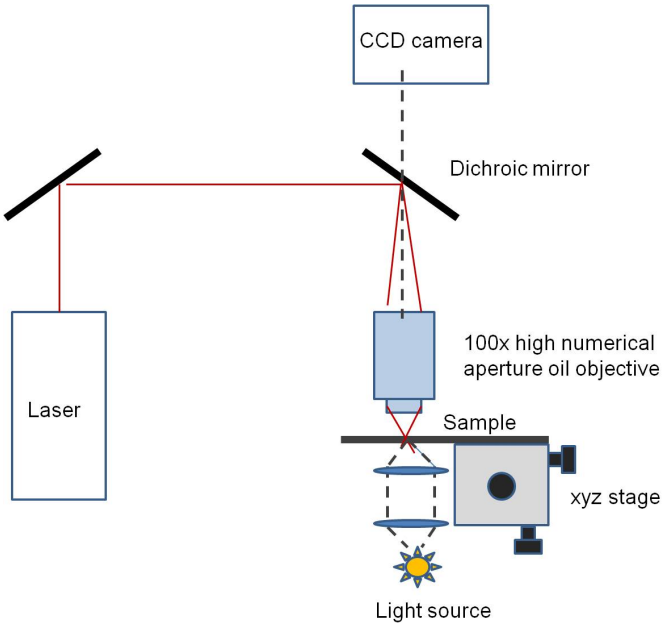

FIGURE 2.4: Optical tweezers setup: Laser focused via a mirror and dichroic mirror through a x100 high numerical aperture (1.25) objective onto the sample. Bead is placed into the laser trap and moved through xyz stage. The sample is imaged with a CCD camera.

2.4.6 Magnetic tweezers

Magnetic tweezers [6] rely on the behaviour of magnetic particles in an electromagnetic field. These particles are submitted to force and behave accordingly. From the movement of the particles one can derive the applied force which enables to calculate material properties as for example for cells [212].

[6]Magnetic tweezers measurement have been performed in collaboration with Julia Flesch (Master student Saarbrücken, Albrecht Ott lab).

CDM with magnetic beads was mounted on a homemade magnetic tweezers setup. Electromagnet consisted of a μ-metal rod with a tip size of approximately 30 μm with a magnetic wire winded with 70 turns on the rod. A μ-stage (Physik Instruments) was mounted on an inverted microscope (Olympus CKX41) with 10x (Zeiss Achrostigmat 10x/0.25) or 20x (Olympus UPlanFl 20x/0.6 Ph1) objective and a red LED (LEDXon) light source. The coil current was produced by a programmable current source (Telemeter Electronic GmbH) reaching amplitudes up to 2 A. It was made sure that CDM was covered with 1x PBS and would not dry. The tip of the magnetic tweezers was approached as near as possible to the CDM without getting into contact. Current application was set in a step manner generating a radial magnetic field around the tip and displacement of the beads while switching on and off was observed and recorded with a camera (Moravian Instruments). Current was controlled by LabView and image acquisition was controlled by SIPS software, image acquisition frequency was 0.5 s. Calibration was performed with magnetic beads in Methylcellulose (0.98 ± 0.01 Pas, Sigma Aldrich). Movement of beads is observed in viscous medium and via Stokes law $F = 6\eta R v \pi$, with F force, η viscosity, R bead radius, v speed of bead the force calculated in dependence to tip distance.

2.5 Quantification of displacement

Image pre-treatment Detection of mesh displacement [7] was performed on fluorescent images of fibronectin mesh or on phase contrast images. Images were pre-treated for detection of displacement. If a z-stack had been acquired a z-projection in ImageJ was performed, with maximal or average intensity depending on the signal quality. When the cell moved in between two images, they had to be stitched. When outliers appeared in frames "remove outliers" was performed (ImageJ). To diminish calculation load, large frames were recut to the relevant part.
For calculation of the drift the displacement of the beads on the CS was detected. In case no beads had been put in the CDM a non deformed area was taken as a reference.

KLT A "pyramidal implementation" of KLT tracker method was used to detect deformation in the mesh. This method is based on Kanade-Lucas-Tomasi algorithm developed by Kanadé and Lucas which follows bright features from one image to another [213] [214]. It extracts local regions of interest from each image and identifies the corresponding feature in every image. Therefore, a textured patch with high intensity variation in x and y is required. A multi-resolution pyramid of the image intensity and its gradients are computed before tracking is performed. This means that the resolution of the images to be analyzed is decreased. Then the KLT algorithm is first applied to lower resolution image, where it detects coarse movement. Then, a higher resolution image is taken, where the fine movement is detected. The interrogation window size is constant but the analyzed image becomes more resolved. After having reached the maximum iteration for all pyramid levels the displacement of the feature is extracted (between two frames) (Figure

[7] In collaboration with Hélène Delanoë-Ayari (Université Claude-Bernhard, Lyon).

2.5 [215]). This method allows for higher accuracy in displacement detection. The implementation of more than one pyramid can generate numerical noise but is necessary for exact calculation.

The Computer Vision Toolbox for Matlab was used with a customary written code with

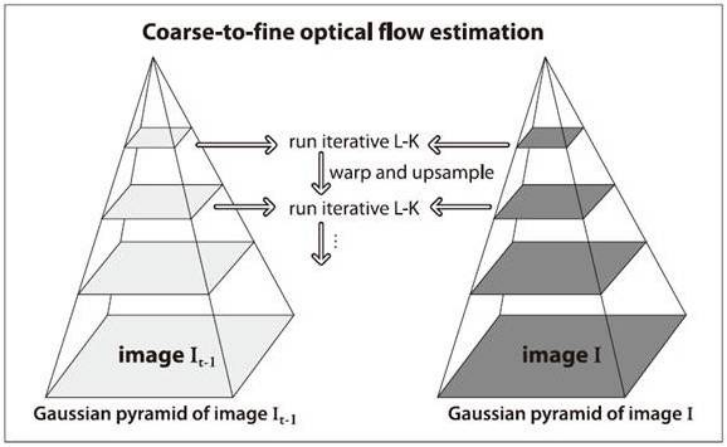

FIGURE 2.5: Schematical description of pyramid construction and KLT tracker function construction [215]. First a multi-resolution pyramid is built from the images, then for all pyramid levels from coarse to fine the features are tracked and their displacements calculated.

number of features varying between 5000-10000 and a minimum distance from 8-14 px depending on image size, making sure that features were sufficiently spaced. Parameter window interrogation size was set to 40 px and maximal iteration to 20 px. The number of pyramids was two for all calculations. For each image an overlay of displacement vectors and phase contrast or fluorescent image of cell is generated. This allows to see if the code runs correctly or if artifacts are generated.

Drift calculation was performed with maximum of 40 px features with a minimum distance of 8 px with a window size of 20 px and one pyramid. The displacement due to drift was subtracted from the cell induced displacement of the mesh.

3 Results

3.1 Characterization of Cell Derived Matrix

An adequate setup or environment is required for the study of cell migration in 3D. Furthermore, as discussed in the introduction chapter, migration is strongly influenced by the mechanical and chemical characteristics of the environment. Hence, in the following section I will present our working setup, the Cell Derived Matrix (CDM) and its characterization. Experiments in this section have been done in collaboration with Sébastien Harlepp for the optical tweezer (IPCMS, Strasbourg), Mounir Maaloum for the AFM (ICS, Strasbourg), Julia Flesch for magnetical tweezer measurements (Master student Albrecht Ott's lab, Saarland University), Nadia Messaddeq for the electron microscopy (Imaging facility, IGBMC) and Jean-Luc Weickert for image acquisition on electron microscope (Imaging facility, IGBMC). We were introduced to CDM protocol by Jacky Goetz (INSERM, Strasbourg) [11].

3.1.1 Synthesis of CDM

As described in Materials and Methods cells are seeded at confluency on the modified gelatin. Already the next day, individual cells are less distinguishable inside the culture and until the end the secretion of macromolecules is visible. A layer of secreted proteins can be observed on top of the cell layer. When the lysis of the cell is performed, cells seem to disappear gradually and the nucleus comes out of the matrix. The different stages of the lysis process are shown in Figure 3.1. Upon addition of lysis buffer (see methods chapter for composition), cells are removed instantaneously. After 5 min no cell remains inside the matrix and the CDM stays unchanged. The former location of cells inside the matrix can still be identified as areas with less coverage and fibers seem to span around those islands. The dark roundish accumulations are supposed to be proteins deposited by cells.

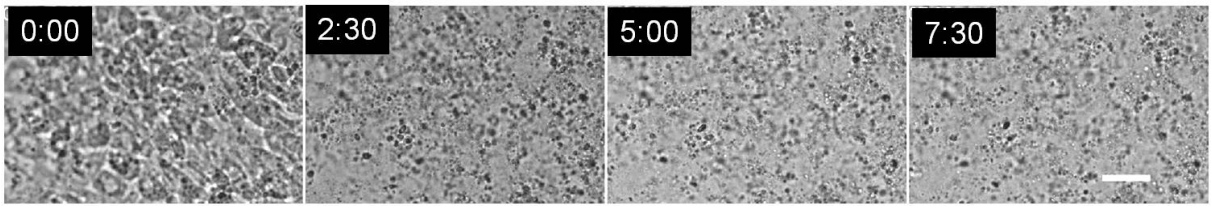

FIGURE 3.1: DIC images of lysis of cells producing CDM. Scale bar 20 μm, time in m:ss.

For cells seeded with local high density, as happens when cells are not well separated during trypsinization and form clumps, the lysis is not complete. The nucleus is not

released from the matrix and stays inside. These CDMs were discarded. DIC or phase contrast images give a hint of fiber structure inside the CDM, but visualization of the fibronectin fibers of the mesh would be more convenient. We choose to visualize fibronectin over collagen because $\alpha_5\beta_1$ integrins [153] bind to fibronectin. It has been used in previous studies in the lab for studying ratchetaxis [31] [8].

3.1.1.1 Integration of fluorescent fibronectin in CDM

Red fluorescent fibronectin was introduced while culturing of CDM when changing medium. The fluorescent fibronectin is incorporated in the CDM as shown in figure 3.2 and forms a network structure. This also indicates that fibronectin (non-fluorescent) or other proteins from the serum contained in the medium are integrated in the CDM mesh.

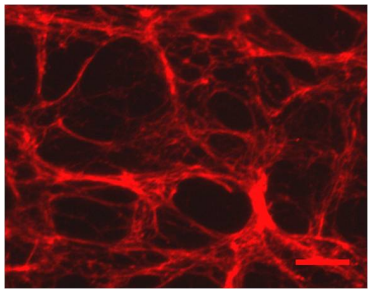

FIGURE 3.2: Typical fibronectin distribution in CDM. Scale bar 25 μm.

However, it raises the question to which extend the incorporated fibronectin matches the native fibronectin secreted by cells. Therefore, we performed immunostaining on the CDM with the integrated fluorescent fibronectin and compared both images (Figure 3.3). The incorporated FN rather marks big fibers, whereas the immunostaining reveals smaller structures as well. Overlaying both shows that incorporated and stained FN are in good agreement (yellow colour). It is noted that fluorescent fibronectin does not allow to visualize the smallest FN fibers, a trade-off between phototoxicity and sufficient mesh information must be reached. But including fluorescent FN is a costly approach and requires a large amount of the compound to be incorporated. To overcome this limitation, we decided to genetically modify cells so that they produce fluorescent fibronectin [129].

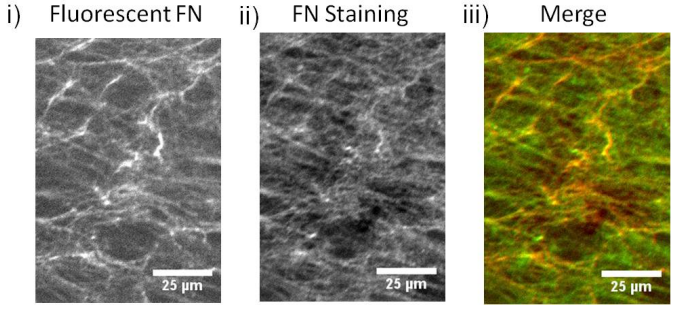

FIGURE 3.3: Pictures of fibronectin i) fluorescent FN added to CDM in culture (red). ii) Immunostaining of FN in CDM (green). iii) Merge of both pictures. Note the scale bar 25 μm.

3.1.1.2 Secretion of fluorescent FN directly into the CDM

The fluorescent FN construct (Ypet-FN) was obtained from Erickson lab [129]. The sequence was amplified and NIH3T3 fibroblast cells were transfected with it. Finally a stable cell line was created as described in Material and Methods. These cells were fluorescent and able to produce and secrete fluorescent FN. We let them in culture to produce

CDM. It resulted that we were able to obtain fluorescently labeled CDM without incorporation of external FN (Figure 3.4). The amount of fluorescent FN is not substantially higher than for fluorescent FN added to CDM culture. The thickness of the CDM was determined via z-stacks acquisition and compared to cell size. As shown in Figure 3.4 the CDM is about 12.8 ± 0.8 μm and the cells are 7.8 ± 0.3 μm. It perfectly offers a 3D environment to cells.

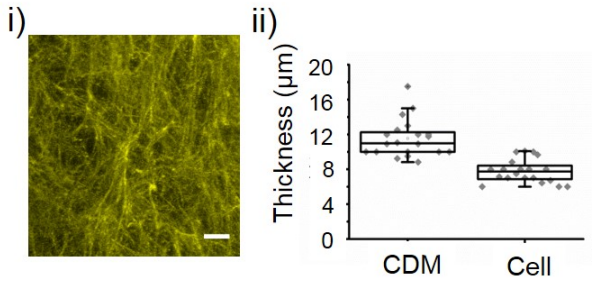

FIGURE 3.4: i) Image of fibronectin tagged with Ypet secreted by cells, Scale bar 25 μm. ii) Thickness of CDM 12.8 ± 0.8 μm (N= 14) and cells inside CDM 7.8 ± 0.3 μm (N>3, n=21).

3.1.2 Structure of CDM

Once the fibrous structure of the CDM was established, we wanted to know if the microscopic architecture corresponded to the fluorescent image of the mesh. Therefore, we performed electron microscopy on the CDMs.

3.1.2.1 Electron microscopy acquisition

CDM was treated as described in Materials and Methods and observed with the electron microscope. In Figure 3.5 the top layer and the inner layer of the CDM as seen with the electron microscope are depicted. Strikingly on the top layer there were more fibers than in fluorescent images. Some larger fibers could be detected but also a significant amount of small fibers, as well as some round accumulations or decorations along the fibers.

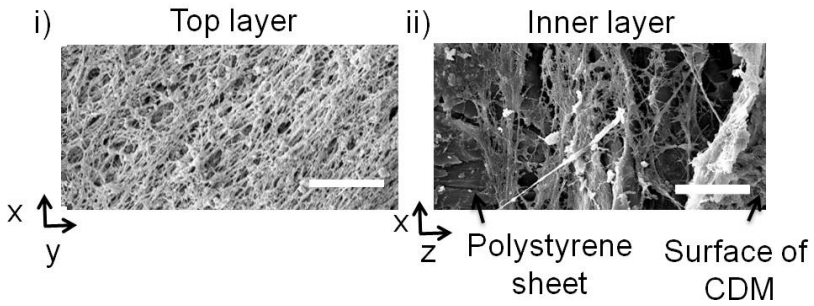

FIGURE 3.5: i) EM image of top layer of CDM. ii) x-z cut of CDM. Polystyrene sheet is visible and surface of CDM (arrows) of i). Scale bar 10 μm.

To also access the fiber structure information in xz, CDMs were cultured on polystyrene (PS) sheets. After treatment they were cut and glued upright on the substrate support, so the cut (xz-plane) could be imaged. The fiber distribution along the z-axis is far less

dense than on the top layer of the CDM in the xy plane. Larger holes can be observed. The thickness of the CDM can be established from the z cuts as being $\sim 15\mu$m. Another

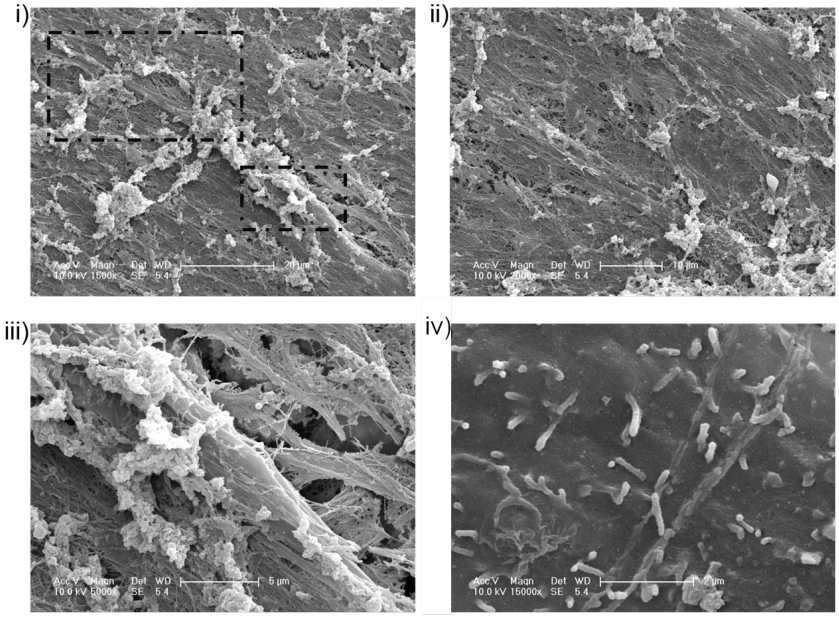

FIGURE 3.6: EM pictures of cell inside CDM i) whole cell, black dashed squares indicate cut magnified areas of ii) and iii) ii) front protrusion of cell iii) center part of cell. iv) Filopodia on top of cell. Scale bar in image.

upcoming question was if cells were leaving tracks in the CDM. As these tracks were not visible neither in phase contrast nor in fluorescent imaging of the FN, we put cells inside the CDM and imaged them under the electron microscope. No tracks in the CDM were visible, leading to difficulties in finding the cells inside the CDM. Fiber distribution was homogeneous throughout the images. As checked earlier by z-stack in fluorescent acquisition cells are embedded in the matrix and completely covered by fibers. The cell seems to have a smoother surface compared to fibers. On the back of cells, finger like structures emerge, filopodia (see Figure 3.6).

3.1.2.2 Pore size of CDM

As it can be seen from the fluorescent images, the FN of the CDM is organized as a network with a certain pore size. As this might be a limiting factor for cell passage it would be interesting to know the dimensions of the mesh and the pores. We should be able to extract this parameter from fluorescent images. The first issue is encountered when thresholding for image treatment. Except for a very homogeneous strong signal thresholding takes into account either large or small holes. It is not possible to have a proper representation of small and large pores at the same time in one binary image. One solution is to binarize twice the image and extract the pore size twice to take into account larger and smaller pores. Hence, some pores are counted double so that the distribution is not completely representative. Another option is to manually measure the pore size by outlining each pore. The same issue while binarizing occurs for electron microscopy

images, leaving the same options as described above. For both types of images a pore distribution can be extracted (Figure 3.7). For xy a minimum of 0.1 μm^2 extracted from electron microscopy pictures and maximum pore area of 550 μm^2 , extracted from fluorescent image can be observed. The peak of the distribution is located at 0.1 μm^2 (d= 0.35 μm) for electron microscope image (Figure 3.7 ii)) and at 50 $\pm 28 \mu m^2$ (d=8 μm) for fluorescent image (Figure 3.7 i)). A mean pore area of 1 μm^2 (d= 1 μm) was extracted from x-z cuts of EM pictures (Figure 3.7 iii)).

As this measure does not capture the whole picture, we thought about microrheoloy of

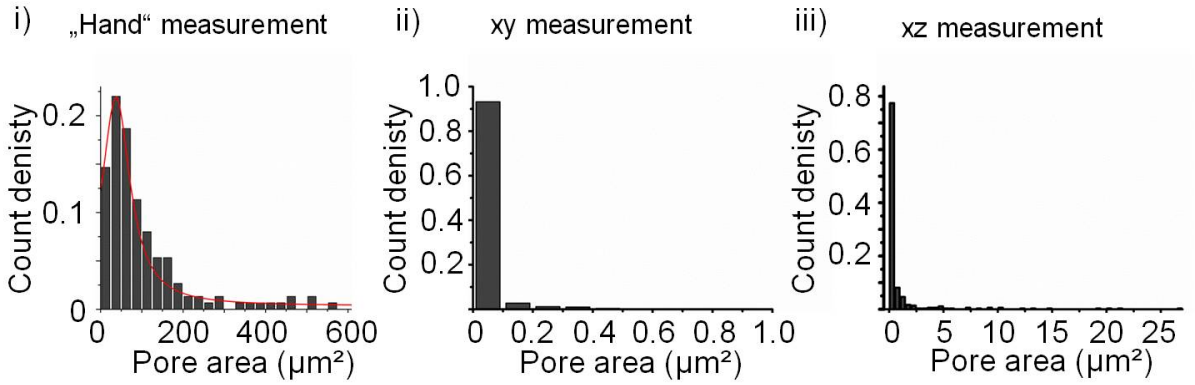

FIGURE 3.7: i) Distribution of hand measured pore size. Lorentz fit was applied and mean pore size of 50 μm^2 detected and highest pore size 550 μm^2 (outlier at 700 μm^2 not shown). ii) Pore size distribution in xy extracted from EM pictures and binarized twice for smaller and larger pores. Highest contribution of 0.1 μm^2. Pore size reaches up to 1μm^2. iii) Pore size distribution in xz extracted from EM pictures and binarized for both pore size types (large and small). Mean pore size at 1 μm^2.

gels [216] . In this field, beads are used to determine the elastic modulus and the pore size. A bead diffuses within a pore and performs random walk. After a specific time depending on the pore size, the bead will have covered the entire volume of the pore. Plotting the MSD against the time interval of random walk reveals a linear increase which reaches a plateau. The plateau corresponds to the pore size as no larger mean distance is obtained for any additional step.

In the next step, we aimed at introducing beads of different sizes from 20 nm- 2 μm inside the CDM. Beads were deposited with PBS on top of the CDM and left to Brownian motion at 37°C. After 24h beads mainly sticked on the top layer of the CDM. Only a few beads entered the CDM and performed random walk. Even those did not reach the center of the CDM, but stayed right under the top layer of the CDM, eventually biasing the measurement. This was the case for all bead sizes. We propose to pre-coat beads to prevent binding with the CDM. To access beads moving inside the CDM some beads from time-lapse experiments could be used and analyzed (Figure 3.8) reaching four data points. These four values fall in the range of the other obtained values and show as well a broad spectrum of pore size. Overall range of values corresponds to what has been reported for other CDMs [217]. From images of ECM *in vivo* it can be evaluated that dimensions are corresponding [218]. Although the statistic is low, we can estimate a pore size between 100 nm and 10 μm diameter. However, the pore size should be limited by the cell size

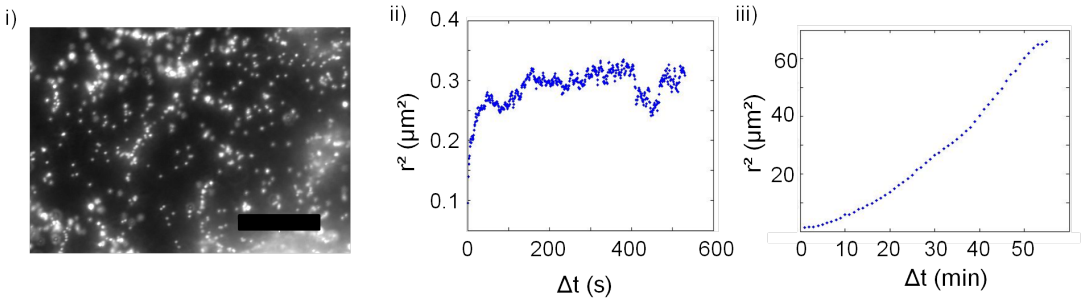

FIGURE 3.8: i) Beads form "carpet" and stick to CDM surface. Scale bar 20 μm. ii) RMS as a function of interval for two beads of 1 μm size located on the upper part iii) and in the center of the CDM. First bead reaches plateau at 0.3 μm^2 and second bead starts reaching plateau for 60 μm^2.

producing the CDM. Cells secrete proteins in such a manner that they are surrounded by fibers. Once the cells are extracted from the matrix they leave a pore at their former location. This means that the cell volume is a fibronectin free space and determining the largest available pore in CDM.
To summarize, the CDM is a porous FN network (among other proteins). The top layer of the CDM is dense, whereas in z the pore sizes range from 100 nm to 10 μm diameter. Comparing these dimensions and the thickness of CDM to cell dimension, it is visible that the mesh size is smaller than cell size. It indicates that cell deformation is potentially required for cell fitting in and moving through the CDM. Cells are most likely confined in CDM.

3.1.2.3 Modification of the CDM

Different methods were considered for modifying the structure of the CDM and at the same time the elastic modulus: (i) Varying the number of culturing days, (ii) modifying its structure and composition chemically (iii) creating defects (holes, cuts) by laser ablation.

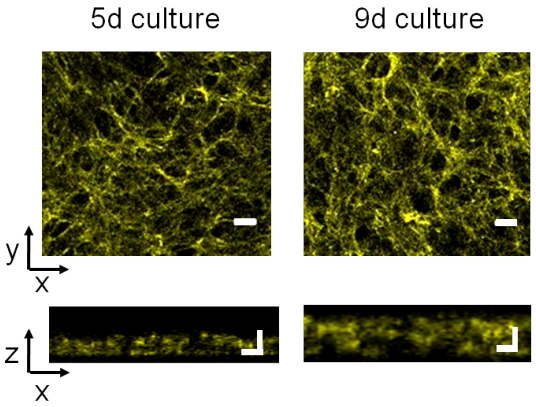

FIGURE 3.9: Image of CDM in xy and xz after 5 days and 9 days of culture. Scale bar in xy 20 μm and in xz 10 μm.

Culture period. As it is not clear what is the temporal sequence of the protein secretion, we followed the hypothesis that the first days the larger fibers are built and that this initial network would become denser with culturing time. Therefore, shortening the culturing days we could generate a different structure of the CDM. We compared two CDMs with different culturing period: 5 days and 9 days. It resulted that the structure of the pores is not affected by the cultur-

ing time, but the overall height of the CDM was indeed changed (Figure 3.9). After 5 days of culture the CDM was less than 10 μm thick, whereas it had a thickness of about 15 μm after 9 days. This gives a clue of how the CDM is formed by cells: It is growing in height during culture at least between 5 days and 9 days. 9 days is the maximum of culturing days as CDMs tends to detach when this number of culturing days is exceeded. This detachment could be caused by the traction force applied by cells to the matrix, which eventually detaches from the glass CS. An option to overcome this problem would be to increase adhesion of gelatin if a thicker CDM is required.

Chemical modification. Trypsin was used as described in [5] to change the elastic modulus. CDM was visualized before and after addition of trypsin. After addition of trypsin no fluorescent fibronectin was left. We deduced that the whole structure was decomposed. A previous treatment to stabilize matrix has to be performed before application of trypsin. This option for modification was discarded.
Another option would be to make the CDM more rigid by rendering chemical bonds permanent such as peptide bonds of proteins. We treated the CDM with PFA in a similar way as for immunostaining and washed extensively with PBS. Cells were seeded on this CDM and rounded up, cell death was observed. It was not possible to remove all the PFA, as with each washing step detachment of the CDM from the surface was more likely to occur. This option of modification was also discarded.

Laser ablation. As the chemical methods were not conclusive for modification of the CDM we chose to try laser microsurgery. Therefore, laser ablation was performed on the CDM. Regions of interest (ROI) were chosen for laser cut. It was possible to cut holes in the CDM (shown in Figure 3.10).
This method for altering CDM structure is functional. Nevertheless it would be time consuming to modify large areas of a CDM. To overcome this limitation, an automatized stage and laser might be an option. A second limitation is to recover it for an experiment with cells afterwards. Since laser ablation with cell inside would also be problematic as shooting a considerable number of holes might heat up the medium and result in an altered cellular response.

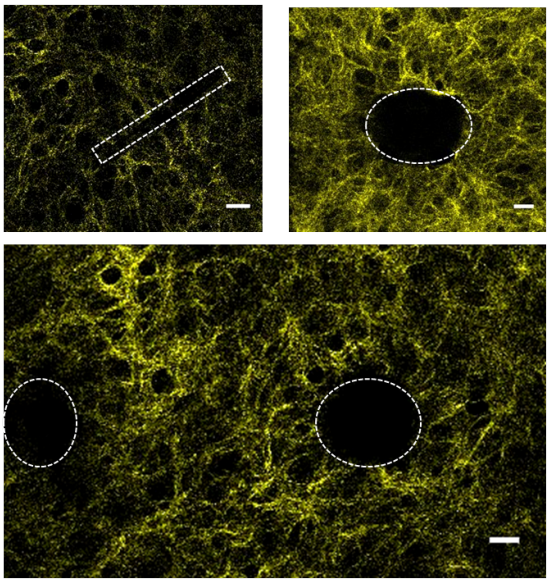

FIGURE 3.10: Different laser ablation geometries are probed: rectangular and circular. The cutting spot is depicted with a white dashed line. Scale bar 25 μm.

Another option, we have not probed, for modification would be using different cell lines for synthesis of CDM. Another cell line would generate different CDMs in terms of protein distributions and depending on the size of the cell, other pore size. This would not permit to tune only one of the parameters of the CDM. Using drugs for changing contractility is another option. Lowering contractility should not yield results as suggested in [134], whereas increasing contractility might result in more aligned fibers as for cancer cells which have been reported to produce aligned FN fibers [219]. Still modifying the contractility level of the cells producing the CDM might also activate other pathways and result in a different protein composition of the CDM.
In conclusion, we tried different methods for changing pore size and by this the elastic modulus. None of the methods was sufficiently convincing to pursue in this direction.

3.1.3 Elastic modulus

Knowledge of the elastic modulus is required for characterization of the cell environment as a material relates to stress σ with $E = \frac{\sigma}{\epsilon}$, E elastic modulus and ϵ the strain and to the force F with $\epsilon = \frac{F}{A_0}$ where A_0 denotes the area [220]. It describes the behaviour of a material under application of a force. Knowing the elastic modulus allows to calculate the force using an inverse problem approach. Elastic modulus is low in soft materials and high in stiff materials. Different methods are available for determining the elastic modulus. We used the AFM, the magnetic and the optical tweezers. After having performed pre-experiments for all methods we determined the optical tweezers to be the proper method to extract the elastic modulus of the interior of the CDM, the one cells can feel.

3.1.3.1 Elastic modulus measured by AFM

As shown in [5], we tried to extract the elastic modulus of CDM by atomic force microscopy measurement. The CDM was placed in a specific chamber flooded with PBS and subsequently the measurements were performed in Peak Force Tapping Mode. The tip of the cantilever can only probe the surface of the CDM, no information about changes in the Young's modulus along the z-axis can be obtained. In Figure 3.11 a typical acquisition result is shown. The AFM probes the top layer of the CDM, the obtained image (Figure 3.11 i)) is similar to the one obtained by EM for the top layer (Figure 3.5 i)). The scale is in log(Pa). A linescan is also represented (Figure 3.11 ii)) and shows a mean value of 4 log(Pa) which corresponds to 10 kPa with some peaks up to 7 log(Pa) which corresponds to 1 MPa. It is possible that 1 MPa values belong to the glass surface which is located under the CDM.

The measurement was performed a second time (2 biological repeats) yielding similar results. Thus, the elastic modulus measured by AFM is about 10 kPa. This value is high if we consider the capacity of the cell to deform their environment. Petrie *et al* obtained values of 500 Pa measuring elasticity with AFM [5]. Tello *et al* obtained values ranging from 2 to 14 kPa for different CDMs [221]. Ahlfors *et al* [222] reported values in the range of 200-300 kPa for tensile strength. For CDM derived from lung fibroblasts values ranged around 100 Pa [217]. Measurement was performed by microsphere indentation. Knowing

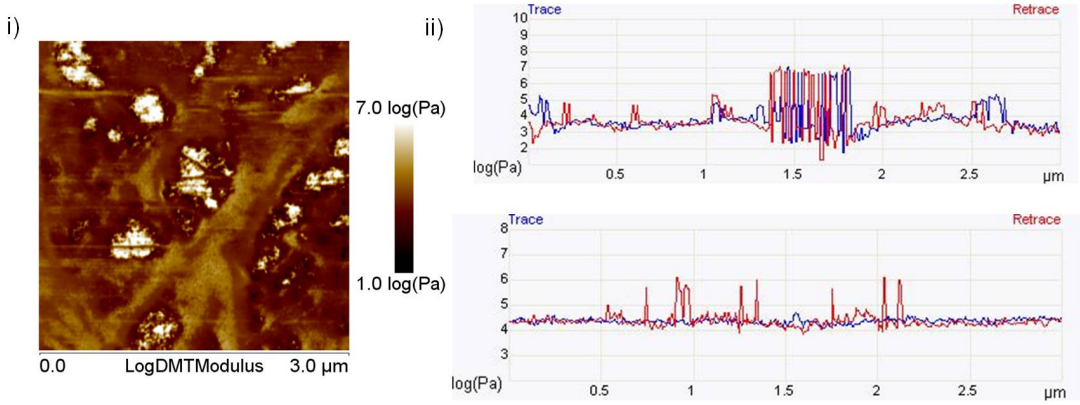

FIGURE 3.11: i) AFM image of CDM, whole picture correspond to 3 μm. ii) Linescan of left at two different points. Elastic Modulus in log(Pa).

that a cell applies a force in the range of 5 nN per μm^2 [144], we would have expected a elastic modulus in the 1 kPa range. As the AFM is probing the surface of the CDM we chose another method to measure what cells see inside the CDM: the magnetic tweezers.

3.1.3.2 Elastic modulus determined by magnetic tweezers

We used the magnetic tweezers in the static mode therefore, as a first step the force as a function of the distance to the tip is established by tracking beads in a viscous medium with known viscosity in our case, methylcellulose. This serves as calibration since the force can be related to the viscosity by the Stokes equation: $F = 6\eta v \pi r$ (Figure 3.12). Where η is the viscosity, v the speed of the bead and r the radius of the bead. The viscosity is 0.98 ± 0.01 Pas and the radius of the bead 0.5 μm. The speed was obtained by manually tracking the bead. As it is a magnetic tweezers, the force generated by the magnetic field diminishes with a $1/r^2$ dependence. Therefore, the calibration curve was obtained by fitting with r^{-2} decay. Once the tip is in the vicinity of the surface of the CDM, current is applied in a step-wise manner. When the force is present, the bead shows displacement until the force of the magnetic field balances the restoring force of the CDM (similar to a spring). The elastic modulus E relates to the force F with $E = \frac{F}{2\pi r_{bead} x}$ where r_{bead} denotes the bead radius and x the bead displacement [223]. This expression was derived from the relationship of bead displacement and restoring force exerted by a linear elastic medium [223]. The force at each bead position was determined via the calibration curve. The distance to the nearest point to the tip was measured and bead displacement tracked via Manual Tracker plugin of Image J.

From all the beads in the CDM, only some moved when switching on the magnetic field. We suspect that the force is not high enough to displace all the beads. The elastic modulus was calculated with four beads and maximum error evaluated with pixel accuracy of 75% and mean force error of 1.93 pN. The mean elastic modulus was established as 12.3 ± 1.4 Pa (Figure 3.12). Materials of this elasticity can easily be deformed by cells. The magnitude of the result seems probable. However, this result is 10^3 smaller than the one obtained by AFM. For the magnetic tweezers measurement, it needs to be considered

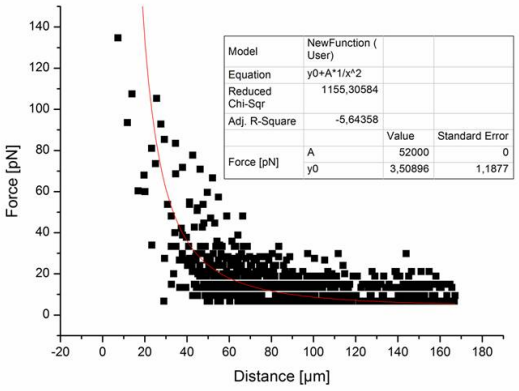

E [Pa]
4.8 ±0.7
4.4 ±0.6
12.4 ±1.7
19.3 ±2.9
10.6 ±1.0
17.2 ±1.8
12.8 ±1.0
16.5 ±1.4

FIGURE 3.12: Calibration curve for magnetic tweezers: Force as a function of distance to tip. Table of obtained values for elastic modulus.

that the maximum force which can be reached is of around 100 pN in the vicinity of the tip. The objective resolution is of 0.2 μm/px. From an estimate it can be deduced that an elastic modulus larger than 30 Pa could not be detected. Additionally, the effect of the applied force to the magnetic beads is too low to be detected by this objective. A higher magnification would be preferable. Hence, only beads in soft environment were analyzed leading to a systematic error.
We observe an order of magnitude difference between elastic modulus obtained by AFM and magnetic tweezers measurement. Additionally, AFM is probing the surface of the CDM and the magnetic tweezers resolution is not resolving our Young's modulus. Therefore, we apply a third method for evaluating the elastic modulus: optical tweezers.

3.1.3.3 Elastic modulus determined by optical tweezers

The principle of the optical tweezers measurement is similar to the magnetic tweezers to some extent. A force is applied on a bead in the CDM and from its force dependent behaviour the elastic modulus can be calculated.
We are following the theory of the restoring force exerted by a linear elastic medium:

$$F_e = -2\pi ERx \tag{3.1}$$

where R denotes the radius of the bead, E the elastic modulus and x the displacement of the bead. Since the elastic modulus depends on the frequency of mechanical probing ω, quasi-static experimental conditions should be reached. The experimental time of about one minute for optical tweezers is higher than the characteristic time defined by $\tau = \frac{\eta}{E}$ with η the viscosity and E the elastic modulus [223]. The characteristic time describes the time a system needs to go back to its initial state and was calculated in our system to be 1.38 ± 0.19 s. Therefore, step size speed was chosen adequately at 0.2 μm/s. First, experimental step consists in calibrating the laser trap and the optical setup. The laser can operate at different power and each power value leads to a different force. For calibration of the camera a grid with known dimensions is used to extract the pixel-μm relation. The same beads, which will be later used in the CDM, are first trapped by the tweezers in aqueous solution for calibration of the laser. As the force of the optical tweezers opposes

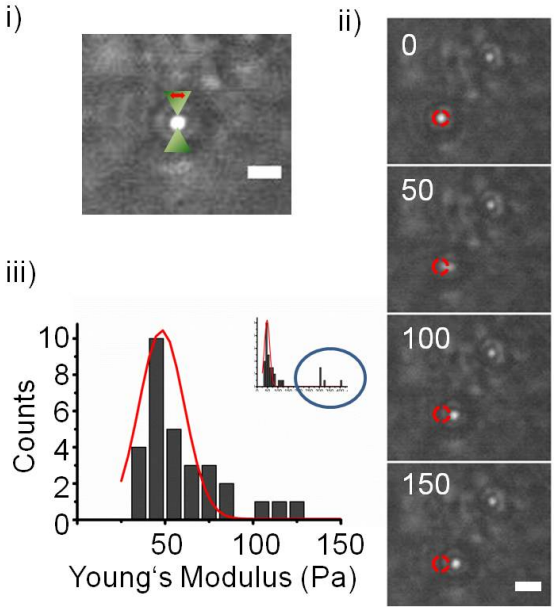

FIGURE 3.13: i) Schematic picture of the laser beam trapping the bead in the focus, red arrows indicate movement of stage. Scale bar 5 μm. ii) Time-lapse of a bead trapped in laser focus and reference bead. The red outline of the bead shows the position of the bead solely due to stage movement. The jump of the bead of the trap is clearly visible. Scale bar 5 μm and time in ms. iii) Count distribution of Young's Modulus fitted with Lorentz. Three outliers shown in inset indicated with blue circle.

the elastic force of the network a "rigidity" of the trap can be calculated which is proportional to the laser power. By applying a Lorentz fit to the power spectrum the it can be obtained. The rigidity of the trap is calculated to be $k_{trap} = 1.34093\ e^{-7} * P_{lasertrap}$ Nm.

The measurement of beads in CDM is performed as described in Materials and Methods. Beads are chosen at different z-positions throughout the volume of the CDM. To test the nonlinear behaviour of elasticity of CDM different laser powers are used ranging from 1070 to 2410 mW (five different powers). At the start, the bead is located at the center of the trap (Figure 3.13 i)) and then the stage is moved. It can be observed when moving the stage that the bead is retained by the laser trap (Figure 3.13 ii) and Movie 01). Whereas the non-trapped beads in the frame follows the movement of the stage, the bead in the trap is retained by the laser. When the bead gets to the limit of the trap and the restoring force of the CDM overrules the force of the laser trap, the bead jumps out of the trap and follows the stage movement as the reference bead. The same behaviour can be observed when the bead is moved back in the vicinity of the optical trap. The bead jumps back into the trap. The trajectories of the bead in the trap and reference bead were extracted via Image J Plugin. From these tracks two values are extracted: the bead displacement in the trap δx related to the equation of a spring $F = k\delta x$ and the difference between displacement of the bead in the trap and of the reference bead Δx. The resulting equation for the elastic modulus is $E = \frac{k_{trap}\delta x}{2\pi r_{bead}\Delta x}$.

A quantity of 23 beads was measured at different heights and different laser power, yielding in elastic modulus values from 30 Pa to 120 Pa with 3 outliers at 300-400 Pa resulting in a mean value for the elastic modulus of 48 ± 25 Pa. Except for the outliers the distribution follows a Gaussian distribution (Figure 3.13). The obtained values for elastic modulus seem to be in the range of what a cell would be able to deform [150]. The next question we were asking was if this value is still true for speeds able to be sustained by

cells. Therefore, we lowered the speed of the motorized stage to 20 nm/s. This speed was roughly estimated from a protrusion retraction of a cell. As in the previous measurement, beads were chosen at different heights in the CDM. As the movement was slow and the steps of 2 μm and 4 μm were maintained the image acquisition of the camera was reduced to 2 per second. Six beads could be analyzed in total and the same order of magnitude was obtained.

In conclusion, we characterized the CDM by three different methods. Considering that AFM is probing the surface of the CDM and that we reach the limit of the setup resolution for the magnetic tweezers, we only consider the values obtained by optical tweezers in the following as they correspond to what the cell sees inside the CDM.

3.1.3.4 Evalutation of degree of elasticity

The relation of the elastic and the plastic component of a viscoelastic material is described by the Maxwell relation. The elastic modulus E relates to stress σ and strain ϵ with $\sigma = E\epsilon$ and the viscous component is modeled as a dashpot with viscosity $\sigma = \eta\frac{d\epsilon}{dt}$ with viscosity η. The Maxwell and the Voigt model are used to describe the visocelastic material [224]. For the CDM the question that arises is: does it have a viscosity a certain plasticity or can we treat it as an elastic material? Since the structure of the CDM does not seem affected by cells, we tried to get a deeper understanding of this relationship.

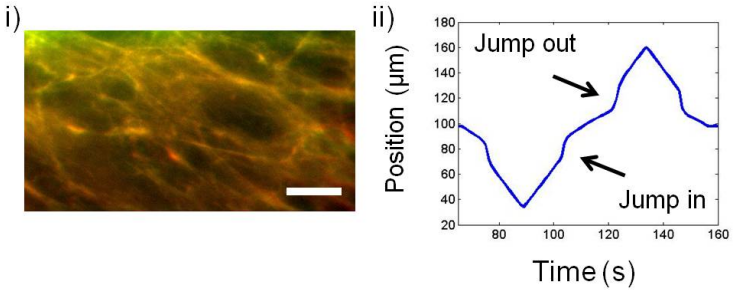

FIGURE 3.14: i) Overlay of FN meshwork before deposition and after removal of cells. Scale bar 10 μm. ii) Trajectory of bead jumping in and out of optical tweezers. Trajectory is point symmetric.

Therefore, we compared the CDM before and after application of traction force by cells. We imaged the mesh, seeded cells under the microscope, let them settle and evolve for 24h. Afterwards we lysed the cells by addition of Triton. The mesh was imaged subsequently. The images were aligned with help of reference beads. It results that the mesh is not changing and no plastic deformations occurs (Figure 3.14). Microsphere indentation measurements yielded similar results for CDMs derived from lung fibroblasts [217].
Another option is to take the results of the optical tweezers measurement and to compare the trajectories of the bead leaving and entering the trap. The fibers to which the bead is attached is stretched by the movement of the stage while held by the optical trap. If it is elastic once out of the trap, it should move to its initial position. If the mesh is viscous the deformation will remain in the mesh. If the mesh is elastic the bead should

enter and leave the laser trap at the same spot. The trajectories should be symmetric. The trajectories should be asymmetric when a force was applied, if a plastic deformation occurred. The deformation applied in this setup is comparable to deformation applied by cells such that the comparison is valid. It results that the trajectory of the bead is symmetric (Figure 3.14ii)).
We conclude that our system can be treated as an elastic material and that the viscous part is negligible.

3.2 Introducing cells in CDM

Viewing the dense entangled network of FN of the CDM, the question arises of how a cell enters and migrates through the CDM. It results that cells deform their bodies and the CDM to this purpose. Once the characteristics of our system established, we went on to put cells in this environment and to study their migration in 3D. Lymphocytes have been extracted and prepared by Anne-Sophie Thomas-Claudepierre from Bernardo Reina San Martin's team (IGBMC, Strasbourg). Mouse embryonic fibroblasts have been extracted and prepared by Amélie Freismuth and Marion Humbert from Betty Heller's team (IGBMC, cell culture platform).

3.2.1 Cell types

To test if the system is suitable for a wide range of cell types, we introduced different cells, both primary and immortalized cell lines. The primary cells that we used were: mouse lymphocytes and mouse embryonic fibroblasts. Among the different cell lines that we

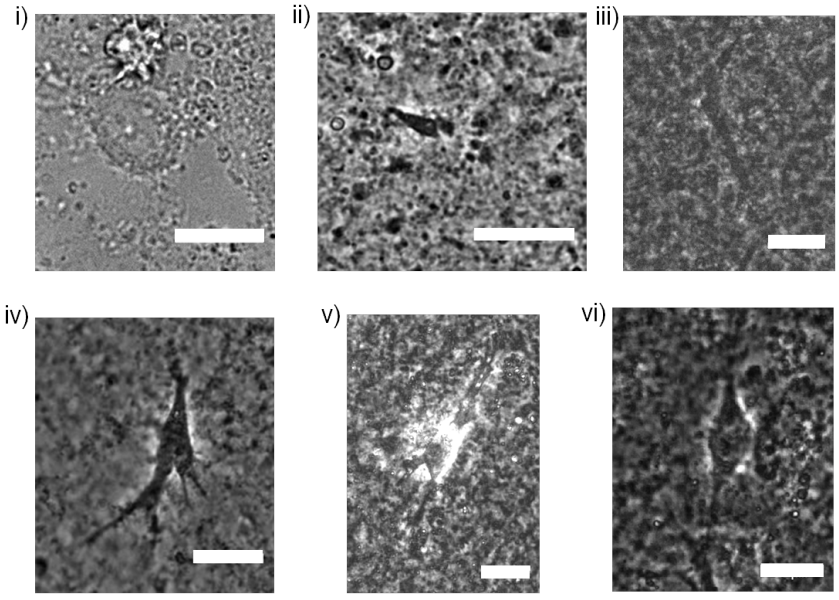

FIGURE 3.15: i) HeLa cell (DIC image) ii) Murine lymphocyte iii) Mouse embryonic fibroblast WT iv) REF52 v) SW480 vi) NIH3T3 fibroblast cell inside CDM, all phase contrast. Scale bar 25 μm.

observed in the CDM we used: NIH3T3 fibroblasts, the same cells producing the matrix, REF52 fibroblast, known to have a large spreading area in 2D, HeLa cells, an epithelial cell line and SW480, a cancerous cell line (Figure 3.15). Cells moving in CDM can be visualized in the movie section: Movie 02, Movie 03, Movie 04, Movie 05 and Movie 06.

All cell types, except SW480 which only partially entered the matrix, penetrated the CDM and experienced a 3D environment. Cells survived in CDM at least 48 h and were able to migrate with different migration characteristics. Strikingly there was nearly no morphological difference between NIH3T3 and REF52 cells. REF52 have a considerably larger spreading area in 2D than NIH3T3. They form a large lamellipodia and one can easily distinguish them. In 3D CDM no size difference between both cell types could be detected by eyes. Even HeLa cells, which are not motile on 2D surfaces compared to other cell types, were migrating. SW480 migrated half on top of the CDM half inside. These cells seemed to migrate in small colonies.
These experiments show the versatility of our CDM as it is a setup suitable for various cell types. In the following, experiments were performed with NIH3T3 fibroblasts as they have a high motility. They also present some technical advantages such as being easily transfectable for visualizing different cellular structures and more robust than primary cell lines. Moreover, by studying the migration of the same cell type producing the CDMs, we are sure that every eventual chemical cue encountered in the CDM belongs to the same cell type.

3.2.2 Entry of cells

The next step after choosing a cell type is to introduce cells in CDM. The first question arising after having seen the mesh structure in the previous chapter is: how do cells manage to enter the matrix (see Figure 3.5 i) and Figure 3.4 right panel)? After trypsinization cells are spherical and they have no protrusions. They are deposited with medium on top of the CDM. First protrusions grow at the bottom of the cell until the main part of the cell is inside the CDM except for the nucleus (Figure 3.16 ii) time point 24 min). In the last step the nucleus passes through the mesh and gets into the CDM (Figure 3.16 iii)). This squeezing in is simultaneous to fiber deformation, a pore is enlarged and the nucleus passes through. The entering process can take from 20 to 90 min depending on how fast cells settle and grow protrusions. Surprisingly, all cells enter the CDM, there is no cell migrating on top of the CDM. Moreover, they stay inside the CDM except when adhesion of the CDM to the glass CS is low. Then the CDM detaches and cells sense the glass surface. Hence, they go down and exhibit a 2D morphology (Figure 3.16 iv)). This behaviour could be associated to durotaxis.

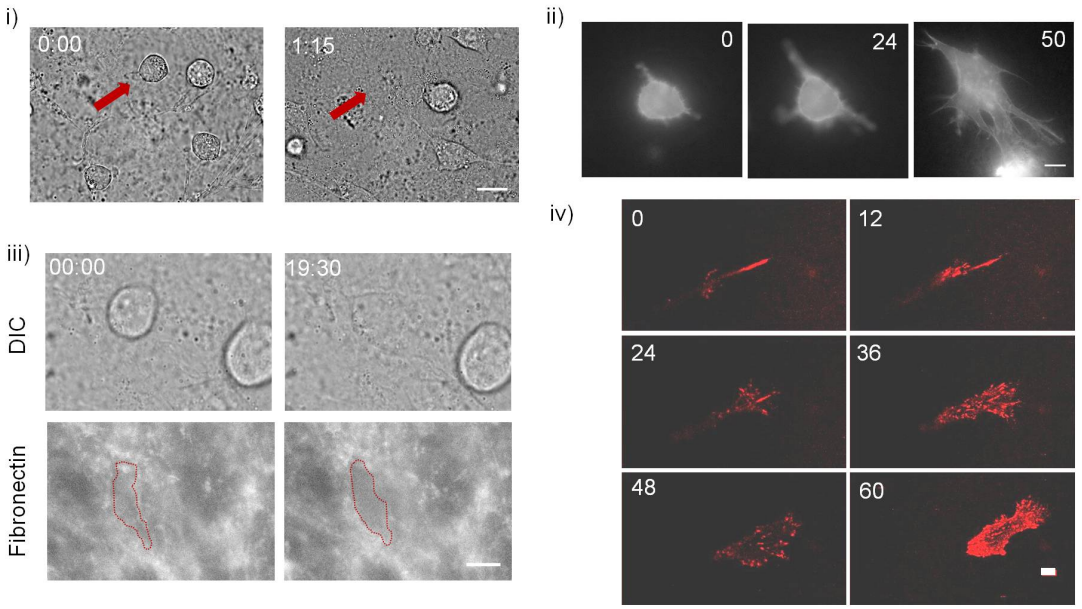

FIGURE 3.16: i) At time zero the cell is round on top of the CDM. 1h15 later cell has entered CDM. Scale bar 25 μm and time in h:mm. ii) mCherry LA expressing cell entering CDM: protrusions grow at basal side of cell and go deeper in CDM before the whole cell is inside. Scale bar 10 μm and time in min. iii) Cell at time zero with corresponding FN mesh underneath. 19min30s later cell has entered CDM and FN pore has been widened (red outline). Time in mm:ss and scale bar 10 μm. iv) RFP-zyxin expressing cell sensing and going down to spread on the glass. The focal adhesion distribution corresponds to a 2D distribution. Scale bar 10μm and time in min.

3.2.3 Cell motility in the CDM

Once inside the CDM cells exhibit a more stellate, elongated morphology compared to cells on 2D surfaces. This has been previously reported in [225]. Migrating cells have a spindle like morphology with a round or trailing rear. Protrusions of the cell are different as well. No flat lamellipodia sheet could be observed for cells inside 3D CDM. Leading edge protrusion is fragmented meaning that more than one protrusion is present at the front of the cell. In Figure 3.17 a montage of a typical migrating cell is shown. The cell

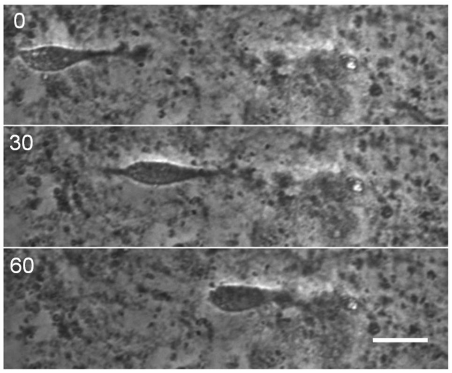

FIGURE 3.17: Phase contrast images of a migrating cell. Cell migrates to the right. Time in min and scale bar 25 μm.

has a short trailing edge at time point zero and a round edge at 30 min. The protrusion at the front is thin and has various lateral protrusions. The cell migrates in a persistent manner without stopping. It deforms its body when passing through the CDM, partially adapting to the fibrous meshwork. However, it also deforms its environment, displacing the CDM meshwork while moving. Therefore, we can link the deformation patterns to cell migration. To do so, we need to visualize the FN network and various cell components such as the focal adhesions of the cell, anchoring points to the surrounding allowing to transmit force. Therefore, we observe RFP zyxin, an intracellular protein of the focal adhesion. We also visualize acto-myosin, the molecular actor that generates the force, by observing F-actin by mCherry Lifeact expression, or myosin with mCherry MHLC2A. With these three factors at hand: network, focal adhesion and molecular actors of force generation, we should be able to understand cell migration in 3D CDM.

3.2.3.1 Migration behaviour

Cells are not necessarily migrating continuously during the whole experiment. Non-polarized cells polarize and migrate. At some moment, cells can stop migrating and depolarize again before they repolarize. This splits the whole migration in different trajectories which have pauses in between where the cell does not perform a net movement forward. We define as persistent movement or trajectories this migrating phases. During the pause cells might still jiggle on the spot. To each persistent trajectory a length, a time and a speed can be attributed. We term these entities persistent time, persistent length and persistent speed [31] [8] (Figure 3.18 i)). Count distribution of persistent length, time and speed are shown in Figure 3.18. Mean persistent length is 41.2 ± 49.9 μm, mean persistent time is 52.5 ± 146.3 min (Lorentz fit) and mean persistent speed is 0.49 ± 0.24 μm/min (Gauss fit). The error values are extracted from the Lorentz and Gauss fit and

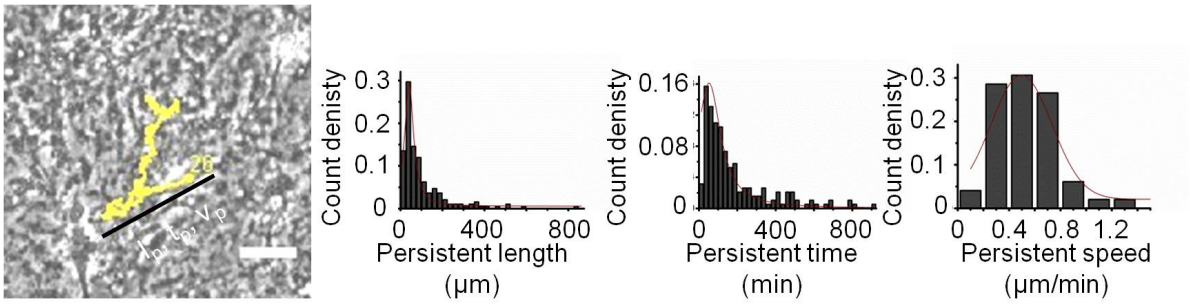

FIGURE 3.18: Typical image of cell path (yellow). Cell has performed turns and changed direction various times. The path can be subdivided in trajectories in between the directional changes. The last trajectory is highlighted by a black line retracing it. The trajectories can be described by a corresponding persistent length l_p, persistent time t_p and persistent speed v_p. Scale bar 50 μm. Count density of persistent length, persistent time and persistent speed. For persistent length and time a Lorenz fit has been performed (shown in red) and for the speed a Gaussian fit (shown in red). Distributions include N=3 and n= 49 cells.

correspond to the full width at the half maximum (FWHM) explaining the large values. The distribution shows certain variability for different trajectories especially for length and time. There is a considerable number of trajectories longer than average. On the contrary, persistent speed distribution is rather peaked. In comparison with persistence values on 2D surfaces cells in 3D CDM are slightly slower (0.7 μm/min) and also persistent length and time are shorter (reference David Caballero unpublished data).

3.2.3.2 Cell deforms while migrating

As mentioned above, cells deform when migrating. This becomes striking when cell passage requires a nucleus deformation. We term this nucleus deformation squeezing. The nucleus is a large bulky organelle in the cell [7], it would be expected that it could prevent cell migration as reported in Wolf *et al.* When a cell migrates the nucleus deforms, even adopting an hour-glass shape for extreme cases of deformation as shown in Figure 3.19 i). The cell migrates and at 20 min the nucleus shows deformation. This deformation is reversible: at 30 min the nucleus has recovered. With a higher time resolution one has access to the dynamics of the squeezing. First the nucleus tip engages and shows a small deformation, followed by a non-symmetric hourglass shape where the front part is smaller than the back part. This ratio is inverted as the cell migrates. Before recovering shape, the nucleus has a small back deformation (see Movie 07). The nucleus deformation is reversible: somehow it needs to conserve its structural integrity [226]. In control case nucleus have a width of 11.0 ± 0.7 μm and in the deformed state 7.6 ± 0.4 μm which corresponds to a change of width of 1.4 in average (Figure 3.19 ii)). Squeezing seems to be a fast process, which can even be observed live under the microscope. We further characterized this process, we quantified the deformation of the nucleus and the speed of the nucleus (tracking at the back of the nucleus). The deformation factor is given by Deformation $= \frac{A}{A_{convex}}$, with A being the area of the nucleus and A_{convex} the convex area associated to A which corresponds to the deformed area. Deformations along the nucleus

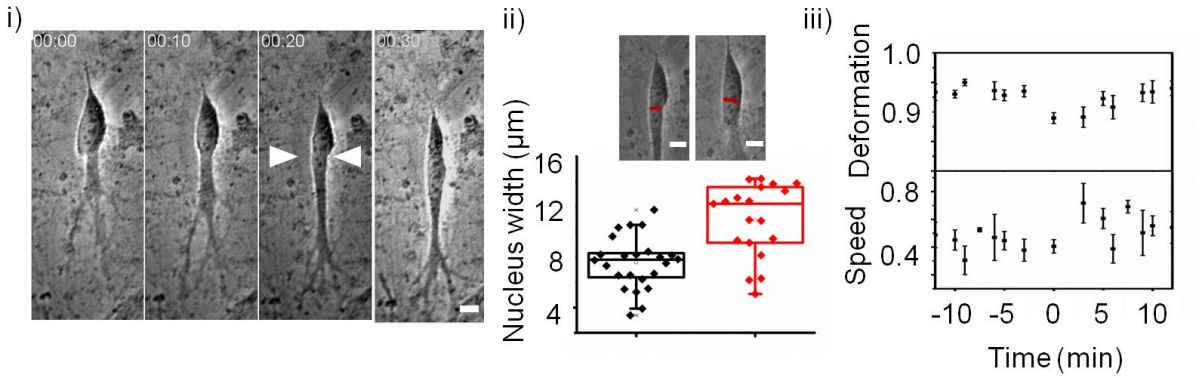

FIGURE 3.19: i) Time series of a migrating cell performing squeezing at 20 min. Time in hh:mm and scale bar 10 μm. ii) Schematic of nucleus width measurement line in red and distribution of nucleus width in control (red) and squeezed state (black). Mean values are 11.0 ± 0.7 μm and 7.6 ± 0.4 μm (N>3 and n=19). iii) Deformation factor and normalized nucleus speed during squeezing centered at zero the highest deformation. (N>3 and n=26 cells).

axis such as stretching or compression are not taken into account in the deformation factor. A stretching of a nucleus which would correspond to a change of axis ratio in ellipse fitting does not vary the deformation factor. For high deformations, the deformation factor reaches a minimum. The speed of the nucleus is normalized by the maximum speed

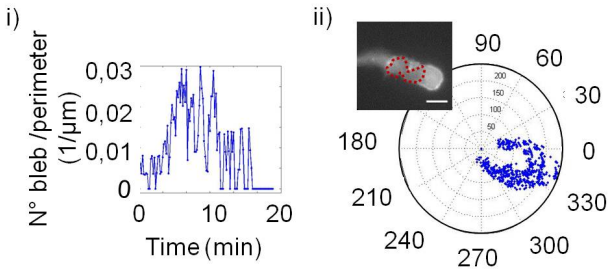

FIGURE 3.20: i) Bleb frequency normalized by cell perimeter during squeezing. ii) Bleb distribution on cell perimeter. Localization of the bleb is mainly the back of the cell. Inset shows analyzed cell expressing mCherry Lifeact. Nucleus is outlined in red to highlight the hourglass shape. Scale bar 10 μm.

of the nucleus on the trajectory for each cell individually. Results are shown in Figure 3.19 iii). The time point of the highest deformation is set as zero. Before squeezing, the deformation factor is stable around 0.95. Then squeezing engages and it goes down to 0.85 before going up again. The speed is not lowered before squeezing and is highest for the first time point after the highest squeeze that corresponds to the speed between the highest deformation and the following point. Then speed goes down again, although not to its initial value. This measurement confirms that squeezing is a fast process.
Another interesting observation is that during the squeezing process blebbing activity is increased. This can only be measured on cells acquired with a high acquisition rate such as 10 s between frames. Blebs were marked with the point picker function of Image J. The time evolution of the bleb was not taken into account. The distribution represents the average number of blebs during a time period. To avoid a bias through comparing

larger and smaller cells, bleb numbers were normalized by the cell perimeter (Figure 3.20 i)-one cell is shown). During the squeezing period the number of blebs increases before they disappear after squeezing. Also the location of blebbing is mainly at the back of the cell. Blebbing itself in CDM is nothing exceptional but the large number of blebs is unusual. Commonly blebbing is perceived as a sign of death, but in our experiments it might be suggestive of tension/contractility increase at the back of the cell, which might be pointing to a pushing mechanism for cell migration in 3D CDM. Nucleus squeezing could also be viewed as the limit of migration in CDM. So what happens when the cell does not manage to make the nucleus squeeze?

Different options can be taken into account. Cells are not able to continue their path,

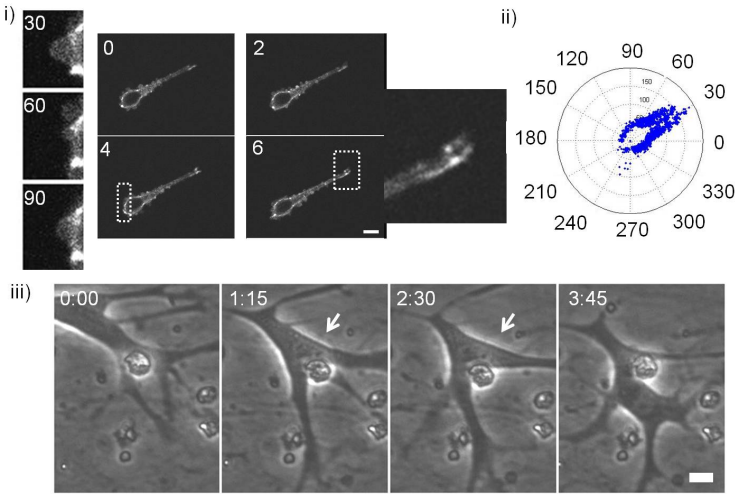

FIGURE 3.21: i) Blocked cell in CDM. Scale bar 10 μm and time in min. Inset at the back shows blebbing dynamics, time in s. Inset at the front of the cell highlights the focal adhesion size. ii) Distribution of blebs around cell perimeter. iii) Migrating cell encounters an obstacle, deforms and reorients its migration path. Deformed state is highlighted with white arrow. Scale bar 10 μm Time in h:mm.

stop migrating, depolarize and eventually repolarize and continue migrating. These are difficult to identify, as depolarization cues are not visible. Other cells stay blocked and do not depolarize. Such a cell is shown in Figure 3.21.i) It has an elongated shape with the round nucleus at the very end of the cell. It shows enhanced blebbing activity and has large focal adhesions at the front in the protrusion. Also looking at the location of the blebs (Figure 3.21 ii) one can see that now they are principally located on the side of the protrusion and not restricted to the back of the cell. As deformation increases,

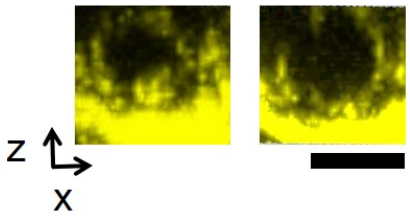

FIGURE 3.22: Pore of CDM shown in x-z plane that opens between two time points while cell is passing through (not shown). Scale bar 10 μm.

focal adhesions grow and blebbing occurs over the whole cell surface which might be a signature of an overall tension increase. In Figure 3.21 iii) a migrating cell encounters an

obstacle. The nucleus is heavily deformed and cell reorients its path. This is an example of how a cell overcomes a blockage. In Figure 3.22 the opening of a pore while cell passes through is depicted. This might be another option to overcome an obstacle.
Different cell types enter and migrate in CDM. Migration behaviour is completely different in 3D CDM compared to 2D. Until now, we presented cells deforming themselves and their nucleus while migrating. But as previously described the matrix has a low Young's Modulus potentially allowing us to see deformation applied by cells. In the following part, we will take a closer look to these deformation of the environment.

3.3 Deformation patterns applied by migrating cells

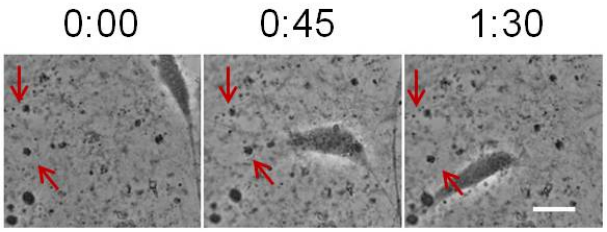

FIGURE 3.23: Time series of a migrating cell deforming the CDM. Deformation is indicated with red arrows. Scale bar 25 μm and time in h:mm.

Cells inside the CDM deform the matrix even when they do not migrate. Cells are pushing and pulling on the fibers forming the CDM. In Figure 3.23 a time series acquired with phase contrast imaging is shown. The cell is migrating to the bottom left. The red arrows indicate the movement of the mesh. At 45 min the two dark points on top of the CDM have moved to the right towards the cell compared to the initial time point. In the next frame one can see that these protein accumulations have moved back to their positions of the first frame. Moreover, cells deform the network while migrating (see Movie 08). Therefore, we could use the deformation of the mesh to visualize the force exerted by the cells while moving in the CDM. In the following, we will further analyze the matrix deformation and correlate them with cell migration. This work has been done in collaboration with Hélène Delanoë-Ayari (Université Claude-Bernhard, Lyon) who is also author of the codes to extract mesh displacement, perform plotting of deformations and heatmaps.

3.3.1 Cyclic contractions with various centers

To further analyze the mesh deformation generated by cells KLT analysis was performed. Z-stacks were projected with maximum or average projection such that only x-y displacement was taken into account.

Figure 3.24 and Movie 09 show the KLT calculation of the mesh displacement (green arrows). A contraction at the front is observed for time point 0 followed by a relaxation. Apparently, the relative contraction is more important than the relative relaxation visible in the size of the arrows. Since the total displacement is not calculated, the prestress of the mesh is not known. These contraction-relaxation points have different locations in

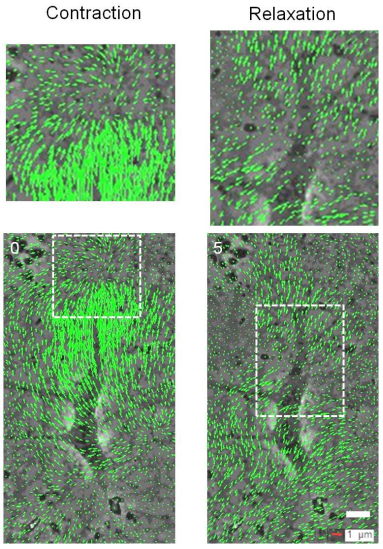

FIGURE 3.24: Two time points of migrating cell. Overlay of phase contrast image and KLT determined displacement of the mesh. Contraction is visible at the front of the cell followed by relaxation. Scale bar 10 μm and time in min.

the cell (Figure 3.25) and appear repetitively.

The insets shown in Figure 3.25 are always from the front and the back side of the cell. In the first time point one can see that the arrows converge at the front of the cell whereas displacement at the back of the cell is parallel to the cell axis. At 5 minutes, the arrows converge at the back of the cell (see inset) whereas, at the front of the cell, mesh displacement takes place parallel to the cell axis. At 30 min, arrows at the front of the cell converge at the top right of the inset. At the inset of the back, mesh displacement is directed outwards. The arrows point to the top and right. At 50 min, the arrows converge to the center of the inset at the front of the cell. At the back of the cell, mesh displacement occurs parallel to the cell axis. Each time, arrows converge at the front or the back of the cell we have a contraction center, a so-called "pinching point". The displacement of the

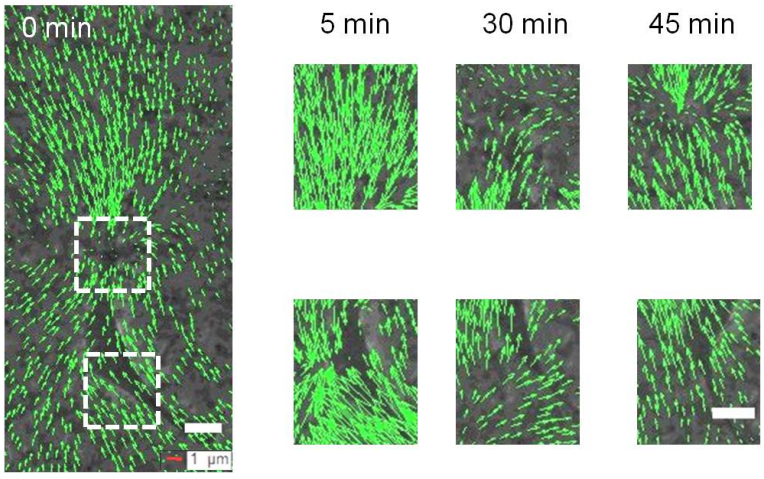

FIGURE 3.25: Overlay of phase contrast images and results of KLT. Cell is migrating to the top. Insets show front and back of cell respectively for different time points. Scale bar 10 μm

mesh does not necessarily show a pinching point. Displacement without converging also occurs. For example, the mesh might move towards the cell at the front of the cell and not move in any specific direction at the back of the cell. In this case, we have a contraction but cannot identify a contraction center. A relaxation of the mesh as shown in previous

Figure 3.24 follows the contraction. Contraction-relaxation patterns have been identified for 15 cells in 12 biological repeats. This was done by visually identifying contraction centers in videos of KLT overlapped with FN mesh or phase contrast images. If we divide by time of observation, we get a mean number of 1.9 ± 0.3 pinching points per hour. Moreover, to analyze the mesh displacement we constructed deformation heatmaps. When possible, the drift was evaluated with incorporated beads on the CS (see Materials and Methods) or on an area where no cells were applying forces. Displacement of the fibronectin mesh was observed. Then the deformation was projected on the cell axis to allow a one-dimensional representation. Only the area around the cell representing 25-40 % of the length of the cell axis was taken into account. We made sure that the cell was completely integrated in this area. For better visualization, the cell was set as a fixed reference: we selected the back of the nucleus. Instead of having a cell moving in the heatmap, we obtain displacement of the mesh using the cell as the reference framework. In this configuration, positive and negative are defined by the direction of the cell movement. Therefore, we decided to invert the sign of mesh displacement at the back of the cell. Thus, red corresponds to a movement towards the cell (a contraction), and blue to a movement away from the cell (a relaxation).

In Figure 3.26 such a heatmap is shown. The cell moves to the left. At the front of the

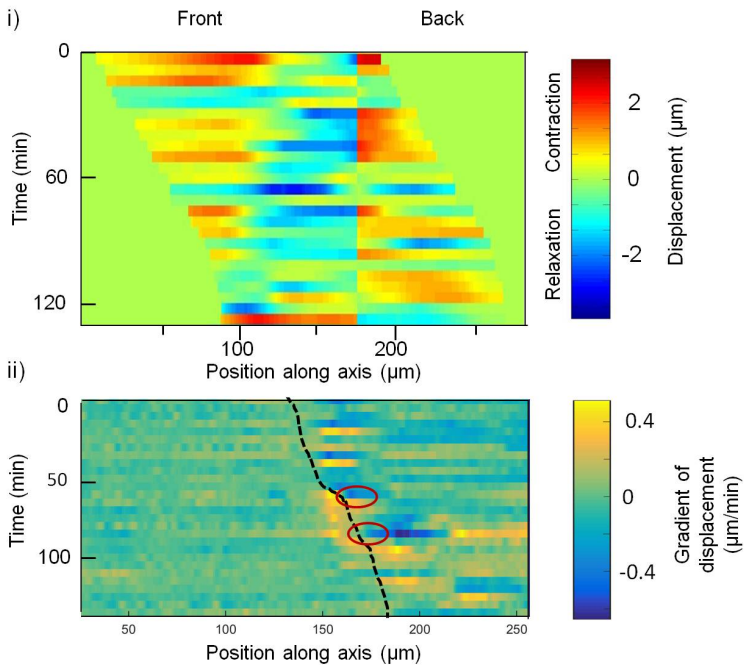

FIGURE 3.26: i) Heatmap of mesh displacement. Rows are centered at back of nucleus. Cell is migrating to the left such that bars become shorter at the left and longer on the right. Signs of displacement are inverted at the back of the nucleus. Red indicates contraction and blue relaxation. Time between rows 5 min. ii) Heatmap of gradient of mesh displacement. Cell moves to the right, cell back is indicated with black doted line. Pinching points where mesh converges is indicated with red circles.

cell, bars get shorter and at the back of the cell bars get longer. It can be seen that at the back and the front red and blue colours alternate. Thus, contractions and relaxations occur in cycles. Pinching points can be identified as a positive displacement lying next to a negative displacement of the mesh such as for 45 min in Figure 3.26 i). For further identification of pinching points, gradient heatmaps have been prepared (Figure 3.26 ii)). These allow to see the speed of displacement of the mesh. In the case that the pinching

point is covered by a global contraction so that all movement is positive, the gradient allows to identify areas where mesh moves closer together. In Figure 3.26 ii) cell migrates to the right. Cell rear position is indicated with black doted line. Pinching points are highlighted with a red circle. At this point the movement of the mesh converges to one center, leading to a positive and negative gradient at this point.

3.3.2 Characterization of contraction-relaxation cycles

After having identified contraction-relaxation cycles and pinching points, we decided to further analyze these oscillations. We wanted to investigate the spatio-temporal relation of the contraction-relaxation cycles and their connection to cell migration.

Therefore, we performed auto- and cross correlation analysis. The displacement of the

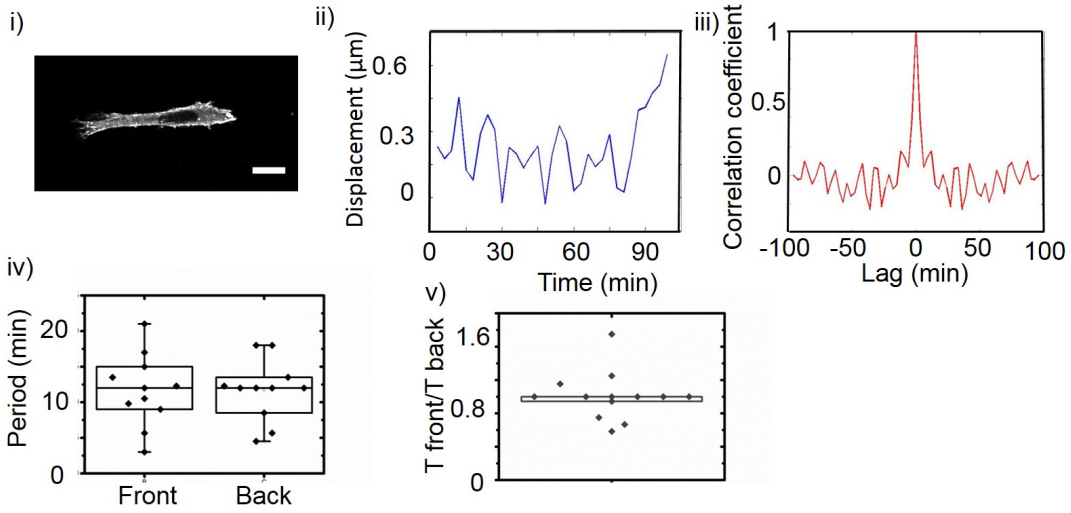

FIGURE 3.27: i) Example cell expressing RFP zyxin. Scale bar 20 μm. ii) Average mesh displacement for area at front of the cell. iii) Autocorrelation of data shown in ii) Peak is obtained for 12 min. iv) Distribution of results of autocorrelation for the front and the back of the cell. Mean value for the front 13.8 ± 1.7 min and for the back is 13.0 ± 1.4. Distribution of relation between period front and back. Mean value 1.0 ± 0.1. n= 12.

matrix centered at the back of the cell nucleus was used. The drift was corrected as described in Material and Methods. Beads allow to evaluate the drift of the external framework. In cases where we did not have beads inserted on the CS, we used the FN mesh displacement at the periphery of our frame far away from our cell. It can not be completely excluded that the calculated drift displacement does not have components due to deformation applied by cells. Therefore, we are currently evaluating the drift of the microscopic system without cells. It will allow us to access the potential thermal fluctuations of the system and its possible periodicity and to completely remove the drift form the displacement data. Periodicity of the drift might be generated by the feedback of the heating system.

We looked at the displacement relative to cell movement such that heatmaps with inverted sign of displacement at the back of the nucleus were taken for this analysis. A point at the

front or at the back of the cell was taken and displacement averaged for 1-8 μm around this point. An autocorrelation was performed on this data with

$$\hat{R}_{xy}(m) = \begin{cases} \sum_{n=0}^{N-m-1} x_{n+m} y^*_{n'} & m \geq 0, \\ \hat{R}^*_{yx}(-m) & m < 0. \end{cases} \tag{3.2}$$

The correlation coefficient $c(m)$ is given as

$$c(m) = \hat{R}_{xy}(m - N), \quad m = 1, 2, ..., 2N - 1. \tag{3.3}$$

Data from different image acquisition frequencies were added to the statistics. In Figure 3.27 an example cell and the averaged displacement at the front of the cell is shown (panel ii)). An oscillation can already be identified. On the bottom left the result of the autocorrelation analysis is depicted (Figure 3.27 iii)), a peak appears at 9 min. As the acquisition interval for this specific cell is of 3 min an error or uncertainty of 1.5 min is introduced for the measurement and the calculation. This analysis was performed for 12 cells and their corresponding deformation pattern. It was not possible to extract a peak from every autocorrelation analysis. Sometimes bumps on the graph might give hints of peaks, but they were not taken into account. We only considered peaks with a correlation coefficient above 0.2 as this is the value 10% white noise reaches (see Appendix). To make the difference between bumps, we only took peaks into account when the preceding minimum had a difference of 0.05 and the following minimum a difference of 0.15 in correlation coefficient. In average preceding minimum had a difference of 0.19 and the following minimum 0.22 to the extracted peak. In case of the cross correlation analysis the highest peak (or deepest minimum) was taken into account. (Further information about error calculation can be found in the Appendix.) At the bottom right of Figure 3.27 (panel iv) the distribution of the extracted peaks is shown for the front and the back. A mean value of 13.8 ± 1.7 min and 13.0 ± 1.4 min for front and back respectively could be obtained. The relation of period front and back was also calculated. The distribution is shown at the bottom left panel v) of Figure 3.27. The mean is at 1.0 ± 0.1. This means that in average back and front perform cycles of contraction-relaxation with the same periodicity. We wanted to know next if contractions at front and back occurred at the same time or if there was a phase shift.

To assess the relation of front and back contraction-relaxation, the averaged displacement of the back of the cell was correlated with the averaged displacement at the front of the cell (see equation 3.2). We subtracted the mean signal of deformation before application of cross correlation. Input of the back always preceded input of the front in the calculation.

In Figure 3.28 the curve obtained by cross correlation is shown for a typical cell. In this curve one minimum is obtained at 9 min. When the minimum was lying within the value obtained for autocorrelation it was taken into account, otherwise it was discarded. Except for one cell, all the minima had a positive time shift or no time shift. We obtain a minimum, which means the correlation analysis shows anticorrelation. Taking into account the directions of displacement, this minimum corresponds to the relation between contraction and relaxation. The distribution ranges from 0 to 10 min with a mean of

3.5 ± 1.2 min. This suggests that there is a phase shift for contraction-relaxation at the front and the back of the cell and that the contraction at the back precedes relaxation at the front.

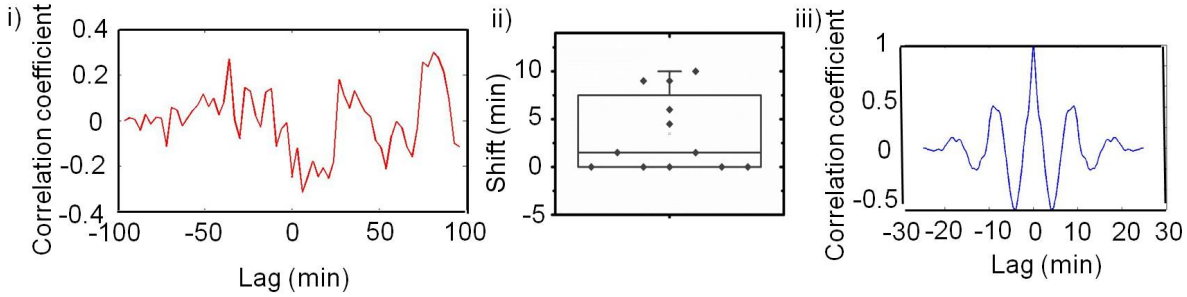

FIGURE 3.28: i) Cross correlation of average mesh displacement at back and at front of cell. Minimum for 9 min. ii) Distribution of phase shift between front and back contraction. Mean value 3.5 ± 1.2 min. n=12. iii) Autocorrelation of displacement at back of cell. Minimum at 4 min with correlation coefficient of -0.6. Intercept at 2.2 min. First peak at 9 min with correlation coefficient 0.4.

Another information might be extracted from the autocorrelation analysis for cells acquired at high frequency: the duration of contraction. As shown in the autocorrelation of Figure 3.28 iii). After the peak in 0 min the curve reaches a minimum at 4 min with a correlation coefficient of -0.6, then it reaches the first peak at 9 min with a correlation coefficient of 0.4. The intercept is at 2.2 min. This might indicate the duration of a contraction. In Movie 10 a cell embedded in the CDM deforming in a cyclic manner the FN network and also contracting periodically is shown. In Movie 11 the same cell is shown without the CDM, the cyclic behaviour is visible in the cell morphology as cell is condensing while contracting.
Contractions at front and back of cell occur in a cyclic manner with a corresponding period of 13.8 ± 1.7 min for the front, 13.0 ± 1.4 for the back and a phase shift between contraction and relaxation of 3.5 ± 1.2 min. Are these contraction-relaxation cycles important for cell movement?

3.3.3 Contraction at rear precedes cell translocation

As we identified cycles of contraction-relaxation in the deformation of the surrounding, we wanted to see if this oscillatory behaviour is somehow reflected in cell migration behaviour.

Observing the movies of migration with higher acquisition rate (at least 3 min) one has the impression that cells behave in a pulsatile manner, that their speed is not constant (Movie 12). When tracking the position of the cell along time the points are not equidistantly distributed, but have denser and more sparse regions indicating speed fluctuations. To access these speed fluctuations the tracks were projected on the cell axis to obtain the one-dimensional displacement and an autocorrelation of speed was performed. The distribution is shown in Figure 3.29 with values ranging from 2 min to the maximum of 35 min. Mean value is 17.9 ± 1.6 min.

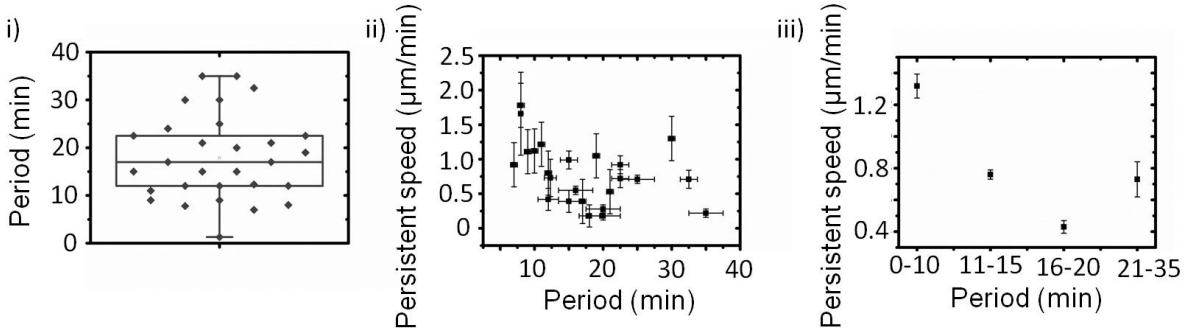

FIGURE 3.29: i) Distribution of oscillation periods yielding a mean value of 17.9 ± 1.6 min. ii) Persistent speed in dependence of oscillation period. Error for the oscillation period was evaluated as half of time between two acquisitions. For the tracking, an error of one pixel was estimated and multiplied by acquisition frequency to obtain a speed. A tendency of decreasing persistent speed for higher periods is shown. iii) Average of ii) over 0-10 min, 11-15 min, 16-20 min and 21-35 min. n= 29 and N>3.

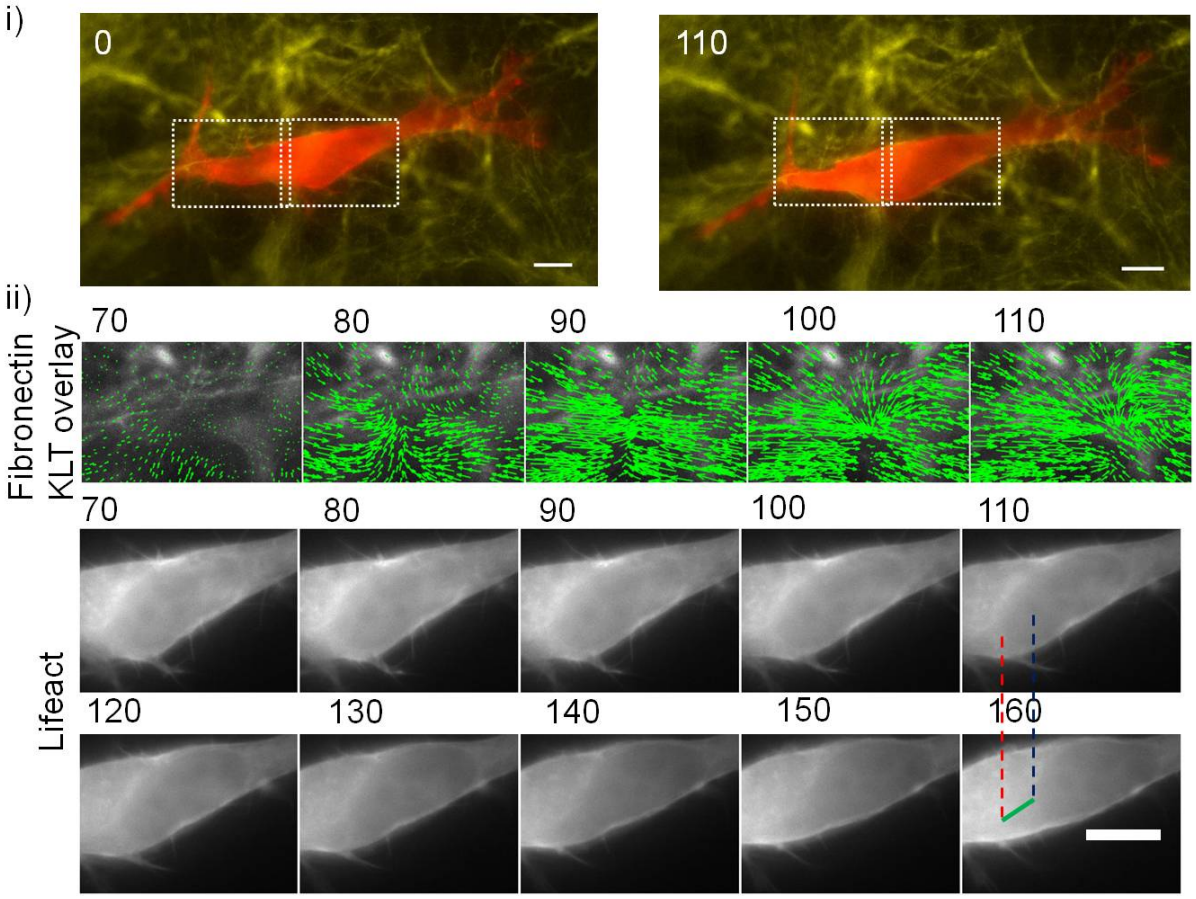

FIGURE 3.30: i) Cell expressing mCherry Lifeact at time point zero in red and FN in yellow, time in s. White boxes represent region of interest shown underneath. Scale bar 10 μm. ii) Image sequence of cell at onset of migration. Top shows FN and KLT overlay in green, bottom shows cell, nucleus position at 110 s (red dashed line) is compared with position at 160 s (blue dashed line). The path of the nucleus is highlighted in green. Scale bar 10 μm and time in sec.

To investigate the relation between speed oscillation period and persistent speed we plottet the persistent speeds in function of the oscillation period of the speed (Figure 3.29). The error of the track was estimated to be 1 pixel, which was multiplied by the acquisition frequency. The error of the period was evaluated via the acquisition frequency: half of the time between two frames is the limit of resolution for the autocorrelation function. The values of persistent speeds are higher for shorter periods and diminish before they increase again towards the end of the spectrum. A tendency of decreasing persistent speed for higher periods can be observed.
To have a clearer picture we binned the graph by calculating the means for 0-10 min, 11-15 min, 16-20 min and 21-35 min. The error in Figure 3.29 iii) is given by the Standard error of the mean. With this representation, the curve starts with a high value for small periods, then diminishes and rises again for the last value. It is not obvious why the persistent speed is going up for large periods. It cannot be ruled out that the higher values of period correspond to the first peak of the autocorrelation analysis. Sometimes a first peak does not appear in the curve or gets screened out or just disappears in noise. We hypothesize that this speed oscillation is triggered by the two contraction centers front back and their time shift. Adding up mean values of period and time shift we are in the same range as speed oscillations. This suggests that speed oscillations are a signature of cyclic application of force.

A recurring question in our work is which contraction is the most relevant one for cell migration: the one at the front or the one at the back? To answer this question, we compared the time when contraction happens to the moment of nucleus translocation (as a reference for cell translocation) or cell rear translocation. Four options are possible: (1) contraction occurs before, (2) at the same moment or (3) after cell translocation or (4) there is no correlation between both events. This accounts for front and back contractions. We first looked at a sequence of a cell at the onset of movement shown in Figure 3.30 i). The regions of interest are indicated with white dashed boxes. At time 80 s a contraction occurs at the back of the cell, green arrows converge to the center of the box (Figure 3.30 ii)). Contraction continues for the rest of the sequence. Nucleus translocation is only visible 40 s after onset of contraction. Between 110 s and 160 s a clear movement is observed (path highlighted in green). Contraction at the back and cell movement seem to be correlated. It is also helpful to generate a heatmap of cumulative mesh displacement (Figure 3.31), this allows to visualize preceding deformation of the mesh. The plot of the three cell references (rear, nucleus front and nucleus back) enables us to detect movement of

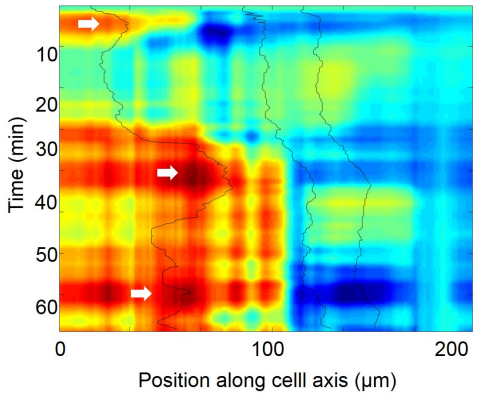

FIGURE 3.31: Heatmap of cumulative mesh displacement (red positive and blue negative displacement) with in black lines the position of cell rear, nucleus rear and nucleus front from left to right. White arrow indicates contraction in red and cell movement.

the cell relative to displacement of the mesh. In Figure 3.31 this cumulative displacement of mesh of the cell in Figure 3.30 is shown. The corresponding part of the contraction shown in Figure 3.30 is located at 5 min. The heatmap captures three forward movements of the cell. For every forward movement, a contraction is present at the back of the cell (contraction/movement indicated with white arrow) confirming the relationship between contraction at the back and cell translocation.

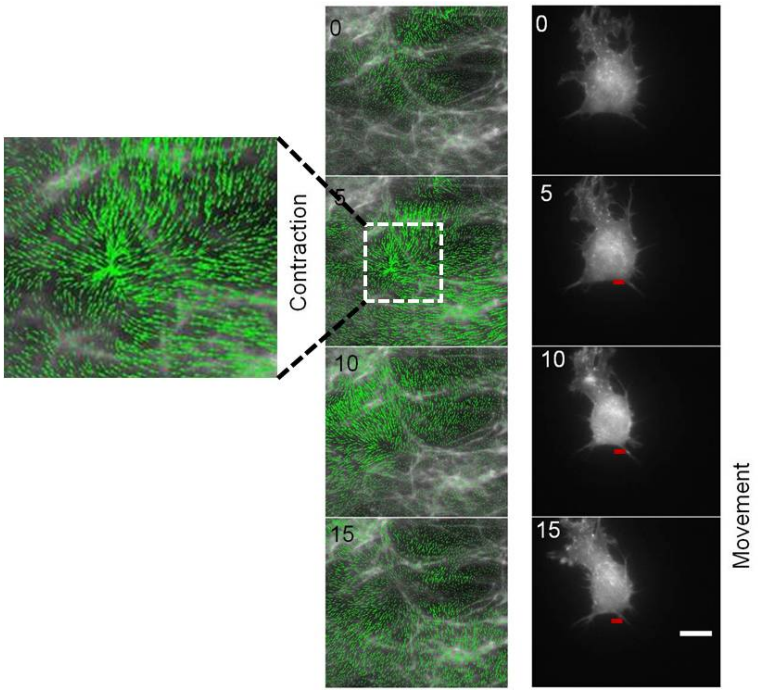

FIGURE 3.32: Overlay of FN and KLT analysis with green arrows. Cell expressing mCherry Lifeact. On the left the FN mesh and in green the arrows, the result of the KLT analysis. Inset shows contraction center and red bars highlight initial position of the cell. Scale bar 10 μm, time in min.

In Figure 3.32 a sequence of another cell is shown. Cell was imaged with an acquisition rate of 5 min. The period of contraction should be above this value as explained in the previous section. In the first column, the FN mesh with the overlay of the KLT is represented and in the second column, the cell expressing mCherry Lifeact. A cell translocation has taken place between 5 min and 15 min. Contraction is visible at 5 min preceding the cell movement. Both montages suggest that cell movement and back contractions are correlated. The later one seems to precede the nucleus displacement. To further disentangle what comes first, we performed a cross correlation analysis of the mesh displacement at back and front and the nucleus speed.

In Figure 3.33 the raw data for an example cell is shown. The position of the nucleus projected on the cell axis is changing along time as the cell migrates (Figure 3.33 i)). The mesh displacement along the cell axis is depicted in Figure 3.33 ii) and iii). The displacement at the back is more important at the end than at the beginning of the series (Figure 3.33 ii)). The cross correlation analysis reveals a peak at -5 min for the displacement at the back of the mesh and the speed of nucleus (Figure 3.33 iv) green curve). Another peak can be observed at 0 min for the displacement at the front of the mesh and the speed of nucleus (Figure 3.33 iv) red curve). We only consider the peak closest to zero and as previously discussed, within the value of the result of the autocorrelation

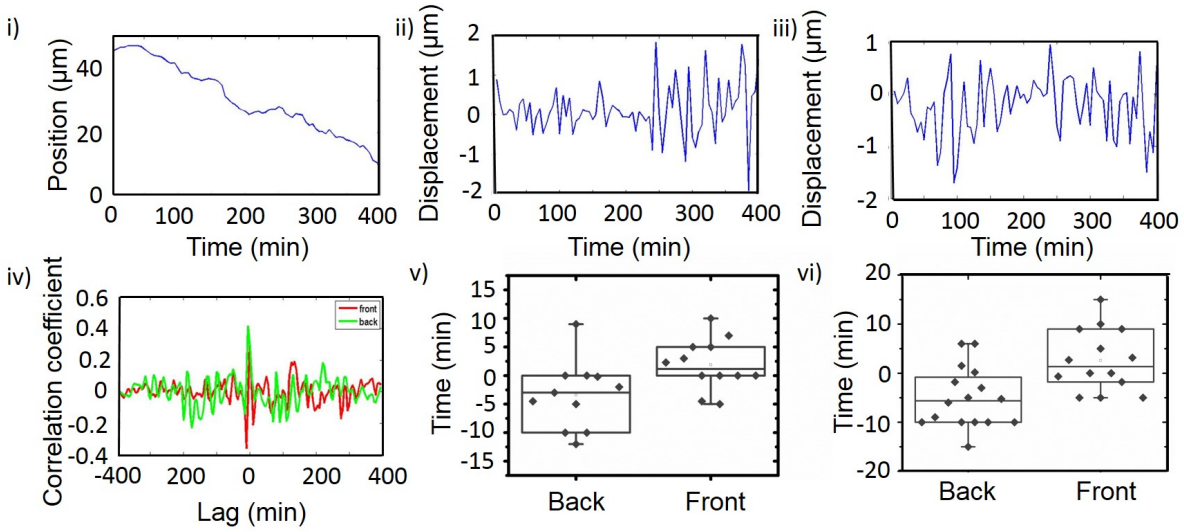

FIGURE 3.33: i) Position of nucleus rear projected on cell axis. ii) Displacement of mesh at back of cell averaged over a certain area(2 μm). iii) Displacement of mesh at front of cell averaged over a certain area (2 μm). iv) Cross correlation of displacement at back and speed of nucleus in green and cross correlation of displacement at front and speed of nucleus in red. v) Distribution of peaks extracted from cross correlation of mesh displacement and nucleus back displacement for back -3.4 ± 1.8 min and front 1.9 ± 1.3 min (n= 11, N> 3) and vi) cross correlation of mesh displacement and rear of cell displacement back -5.1 ± 1.5 min and front 2.6 ± 1.7 min (n= 14 N> 3).

of the mesh displacement. So for this specific cell, the contraction at the rear of the cell precedes the nucleus displacement whereas the relaxation at the front of the cell occurs simultaneously to nucleus displacement. The distribution for the lag time between mesh and nucleus displacement at the back reveals a mean value of -3.4 ± 1.8 min (error from SE of mean) and for the front 1.9 ± 1.3 min (error from SE of mean). The same calculation was performed for the mesh displacement and the rear of the cell with the distribution shown in Figure 3.33 iv). For the back a mean value of -5.1 ± 1.5 min and for the front 2.6 ± 1.7 min were found. The distribution of the mesh displacement and rear movement exhibited a wider spread than the previous distribution. Considering that cells with acquisition frequencies from 0.2 1/min to 6 1/min have been included the maximal error due to sampling is 2.5 min.

In conclusion, we showed that cells perform contraction-relaxation cycles at front and back of the cell while migrating in 3D CDM. These contraction-relaxation cycles have defined periods and experience a phase shift between front and back. Finally, we found out that the contraction at the back of the cell precedes its translocation thus suggesting that it is responsible for cell movement.

3.4 Identification of key molecular actors

Once the contraction was identified and characterized, we investigated what cellular entity generates these contractions. Since myosin, actin and microtubules are the cytoskeletal components which are dynamic and able to generate a force and/or motion of cells [19] we focused on those three.
Hélène Delanoë-Ayari performed the differential force calculation for drug application and Jordi Comelles wrote the code to extract and plot trajectories.

3.4.1 Molecular actors

The first step was to identify the molecular or supramolecular structure, that we might challenge later on. Cells in 3D have focal adhesions (Figure 3.34 i)), some sparse stress fibers (Figure 3.34 ii)), a prominent acto-myosin cortex (Figure 3.34 ii)), and in some cases an actin gel around the nucleus (Figure 3.34 iii)). To visualize focal adhesions we transiently transfected cells to express RFP zyxin. The focal adhesions are mainly located at the tip of the protrusion or at the sides of the cell (Figure 3.34 i)). As the displacement of the mesh corresponds to a puller and not to a pusher, we assume that the focal adhesions we see are actually adhered to the mesh.
In general we see few stress fibers in cells: two to three stress fibers located at the top

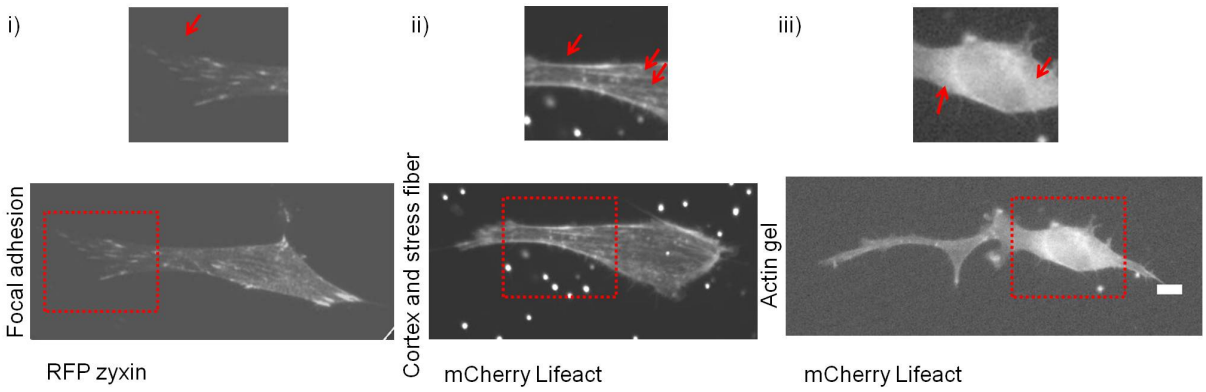

FIGURE 3.34: i) Cell in CDM expressing RFP zyxin. Focal contacts visible in protrusion at back and on side of cell. ii) Cell expressing mCherry Lifeact. Cortex and stress fibers visible and iii) actin gel around nucleus. Scale bar 10 μm.

and at the bottom of the nucleus in cells in 3D CDM. They are spanning from the back of the cell to the protrusion. In non-polarized cells, they span from the center to the protrusions. As there is no spread lamellipodia structure, no arches are visible in our cells. Stress fibers are visible for actin, myosin and even for zyxin, as it can also localize there [227].

The cortex is present in all cells as a thin layer underneath the cell membrane. It is visible when imaging actin and/or myosin. In some cases, some inhomogeneity in signal in the cortex can be detected. However, image acquisition is not sufficiently resolved to view a more detailed distribution of cortical actin or myosin.

In some cells, an actin gel is present around the nucleus. This gel seems to be patchy with foci and small fibers. The signal continues to the margin of the cell suggesting that it could be connected to cortex. Actin gel might be able to push, as for example for *Listeria*, which propels itself via actin polymerization at the back [57]. The force applied by such a gel has been measured by means of bead and micro-needle manipulation [228]. In vitro reconstituted gel experiments have shown that for a given actin concentration, a minimum of myosin II and cross-linkers are necessary for the gel to contract [229]. Focal adhesions are mainly connecting the cell with its surrounding [122]. Cortex, stress fibers and actin gels are good candidates to apply forces and deform the FN mesh. What is the contribution of each structure to the different steps of the movement needs to be elucidated. We first test the different molecular building blocks of the structures.

3.4.2 The Rho pathway

As formerly introduced (see Introduction Figure 1.11) the Rho pathway is the main responsible for cell contractility, whereas Rac and Cdc42 control lamellipodia and filopodia as a first approximation [230].

ROCK, that is downstream of Rho, acts on myosin activity by phosphorylating the

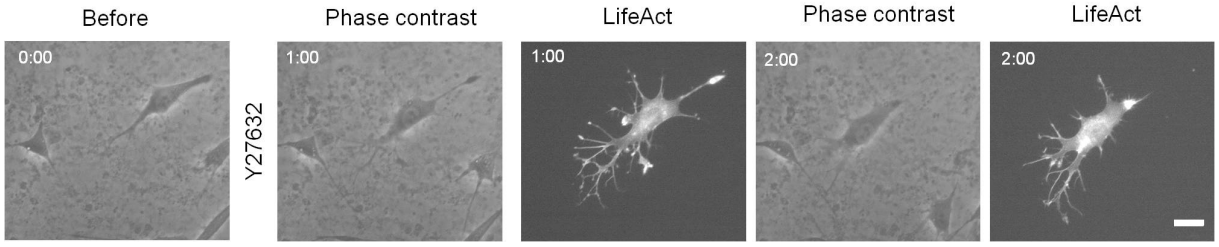

FIGURE 3.35: Phase contrast image of cell in CDM before application of drug. Cell after addition of Y27632 10 μM. Thin protrusions appear on the cell body. Time in h:mm. Scale bar 25 μm

myosin light chain and inhibiting the myosin light chain phosphatase. To inhibit ROCK actively, we used Y27632 [231] at a concentration of 10 μM [5]. The effect of the drug could be seen in the morphology of the cells. The number of protrusions increased, and they became thinner and more branched as shown in Figure 3.35. Cells are still capable of migrating, as it can be seen by the plot of trajectories and measurement of persistent speed (Figure 3.36).

Trajectories were similar to control trajectories in length and distribution. Persistent speed is of 0.47 ± 0.02 μm/min, which nearly corresponds to persistent speed in control. However, the deformation of the mesh was changed, it decreased upon addition of drug. This could be confirmed with the analysis of displacement as the differential force was lowered by $44\% \pm 10\%$ (Figure 3.36). The differential force describes the force between consecutive deformations. It is different from the total force. Since the differential force is normalized, the control is plotted to guide the eyes and to put the decrease of differential force in context. Although trajectories and persistent speed are similar to the control, ROCK inhibition has a clear effect by changing cell morphology and decreasing the relative

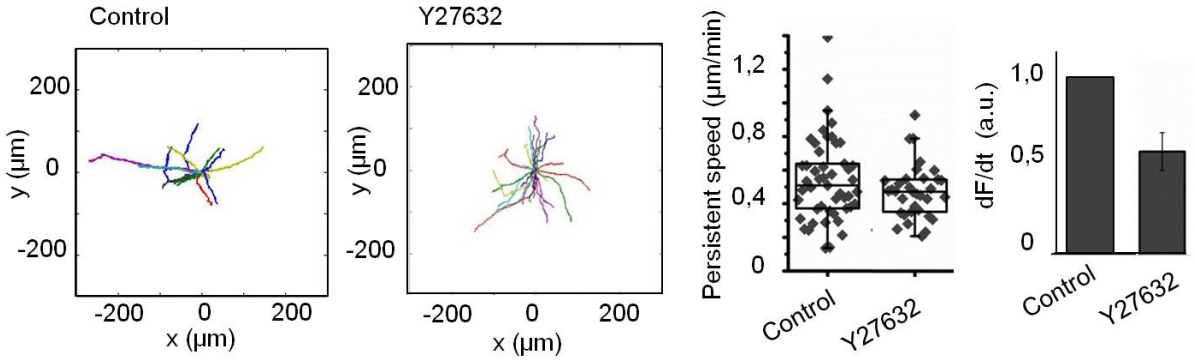

FIGURE 3.36: Trajectories of control cells and cells in presence of 10 μM Y27632 of 5h duration. The length and distribution of trajectories corresponds to control trajectories. Distribution of persistent speed of control and in presence of the drug. Mean value for control is 0.54 ± 0.04 μm/min and of drug 0.47 ± 0.02 μm/min. Differential force normalized by initial deformation before addition of drug. Under inhibition of ROCK differential force drops by $44\% \pm 10\%$. n=34, N=3.

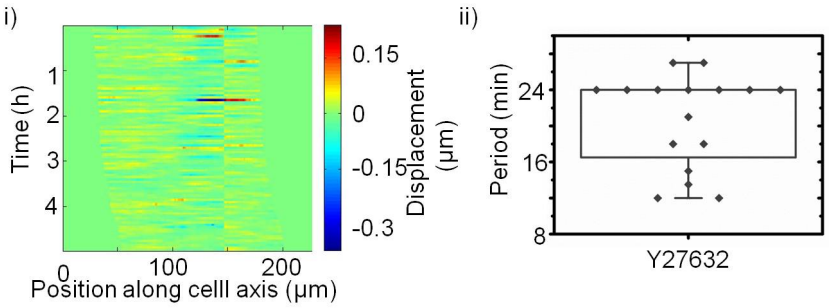

FIGURE 3.37: i) Heatmap of mesh displacement. Rows are centered at back of nucleus. Cell is migrating to to the left. Signs of displacement are inverted at the back of the nucleus. Red indicates contraction and blue relaxation. Time between rows 3 min. ii) Distribution of extracted speed periods by autocorrelation analysis. Mean value is 20.7 ± 1.3 min. N=3 n=16.

force applied while migrating.
Finally, we characterized the contraction-relaxation cycles by analyzing single cells of the experiments. We were able to extract the fluorescent FN signal for KLT analysis. Contraction-relaxation cycles could be detected for ROCK inhibition (Figure 3.37 i)). Pinching points could not be detected as deformation was too low to have converging arrows. Since we had a small number of cells with reliable contraction-relaxation cycles we were not able to extract a characteristic period front and back for this case. As for control cells, tracking revealed denser point regions and points further apart (pulsatile behaviour). Therefore, we performed autocorrelation analysis of speed of the nucleus as shown in Figure 3.37 ii). Mean period of speed variation is 20.7 ± 1.3 min, which is higher than control but not significantly. Therefore, contraction-relaxation cycles are still present when inhibiting ROCK.

3.4.3 Inhibition of myosin and increase of myosin activity

As myosin is a molecular motor able to exert forces on actin filaments, we decided to probe the role of myosin activity in generation of contraction-relaxation cycles. To modify myosin activity different drugs were used: Blebbistatin, inhibiting myosin [232], ML-7 a myosin light chain kinase inhibitor [233] and Calyculin A, permanently phosphorylating the myosin light chain [234].
As described in Materials and Methods, a control experiment was performed to ensure that cells are motile before addition of the drug. Since blebbistatin becomes toxic under exposure of blue light [235], the FN mesh was not acquired (as the YFP is been excited at 514 nm). For displacement studies for calculation of the relative force, the phase contrast image was used and displacement normalized by control part of the experiment before addition of drug.
Blebbistatin was used in a concentration of 25 μM [5]. Adding blebbistatin to the CDM

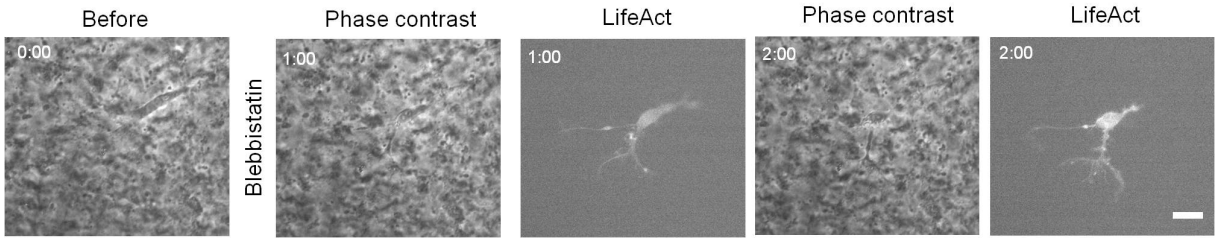

FIGURE 3.38: Phase contrast image of cell in CDM before application of drug. Cell after addition of blebbistatin 25 μM. Cell body condenses to nucleus and thin protrusions appear. Time in h:mm. Scale bar 25 μm

had an immediate effect on the cell, and relaxation of the mesh could be observed. In presence of the drug, deformation of the mesh was nearly zero. Moreover, cells had a peculiar phenotype. The cell body condensed to the nucleus and the cell had thin-branched protrusions as shown in Figure 3.38 and Movie 13. However, cells were still able to migrate. For cells transiently transfected with mCherry-Lifeact actin was accumulating at the back of the cell. Comparing the persistent speed of myosin inhibited cells with control cells it can be seen that it is divided by two: 0.28 ± 0.02 μm/min compared to 0.54 ± 0.04 μm/min (Figure 3.39). Comparing trajectories also reveals that cells in presence of blebbistatin have shorter trajectories than control cells. Additionally, the deformation of the CDM when myosin is inhibited reveals a much lower differential force: it is decreasing by $83\% \pm 5\%$ (Figure 3.39), and the main contribution to the mesh deformation comes from relaxation upon addition of drug. Therefore, under myosin inhibition the deformation by cells is minimal and complicated to detect. No contraction-relaxation has been observed.

ML-7 is acting upstream on myosin by inhibiting the myosin light chain kinase. It was used in a concentration of 10 μM [10]. Relaxation could be observed upon addition of the drug. In this experimental configuration, cells tended to have a more compacted morphology and not as many protrusions at the front as control cells (Figure 3.40). Cells performed more backward movements when migrating. Trajectories are slightly shorter than control case and mean persistent speed is 0.43 ± 0.03 μm/min. This is lower than control persistent speed. The differential force is dropping to $19\% \pm 1\%$ (Figure 3.41) of

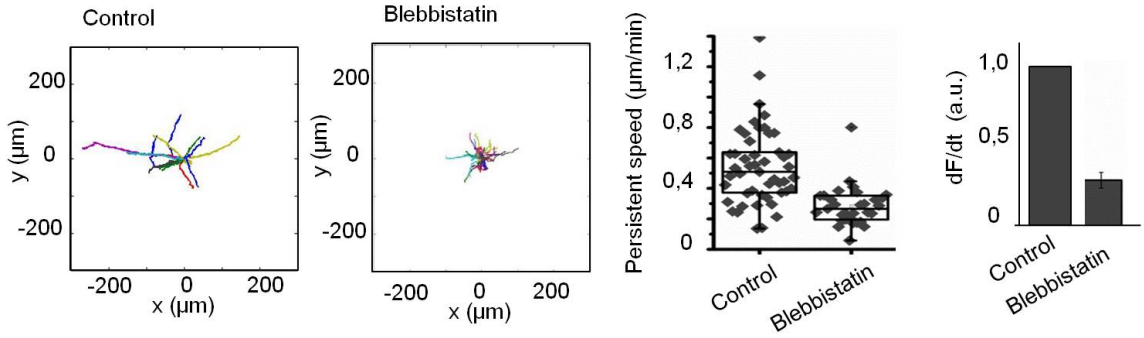

FIGURE 3.39: Trajectories of control cells and cells in presence of 25 μM blebbistatin of 5h duration. In the latter case, trajectories are shorter. Distribution of persistent speed of control and in presence of drug. Mean value for control is 0.54 ± 0.04 μm/min and of drug 0.28 ± 0.02 μm/min. Differential force normalized by initial deformation before addition of drug. Under myosin inhibition, differential force drops to $27\% \pm 5\%$. n=31, N=3.

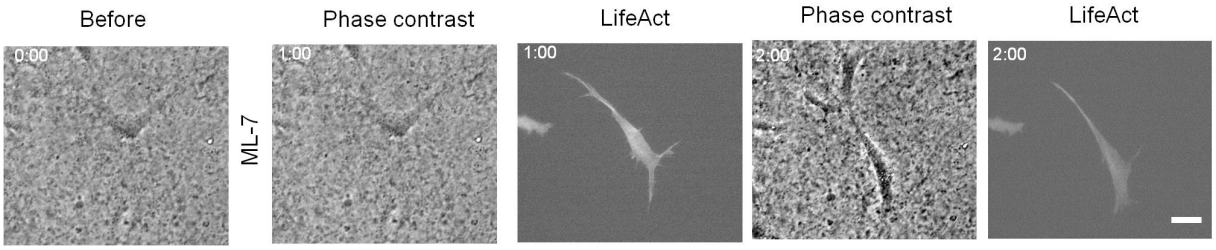

FIGURE 3.40: Phase contrast image of cell in CDM before application of drug. Cell after addition of ML-7 10 μM. Cell body becomes more compact. Time in h:mm. Scale bar 25 μm

the initial amount. We observe a variation in speed for ML-7 treated cells. Thus when inhibiting the MLCK period is increased to 24 ± 3 min compared to control. Since we assume that speed variation is a signature of contraction-relaxation cycles, we deduce that they still take place.
In both cases, when inhibiting myosin directly or the light chain kinase differential force is dropping dramatically down to 10-20 %. Inhibition of myosin with blebbistatin strongly affects cell migration. Inhibition of the MLCK kinase with ML-7 has a less pronounced effect but is still decreasing motility, speed is lower and trajectories shorter. No cycles have been detected for myosin inhibition upon blebbistatin. What happens on the contrary when myosin activity is enhanced?

To address this question, we applied Calyculin A, that phosphorylates the myosin light chain to cells in CDM [234]. We tested two different concentrations: 1nM and 10nM. The effect upon addition of 1nM Calyculin A took some time to be visible compared to the higher concentration, but eventually relaxation of the mesh occurred. Moreover, cells could not sustain connections to the CDM anymore (Figure 3.42). Then, they rounded up and started blebbing. Finally, after some time part of cell got extruded from the CDM. Similar results were obtained for high concentration (10nM), but in this case the effect

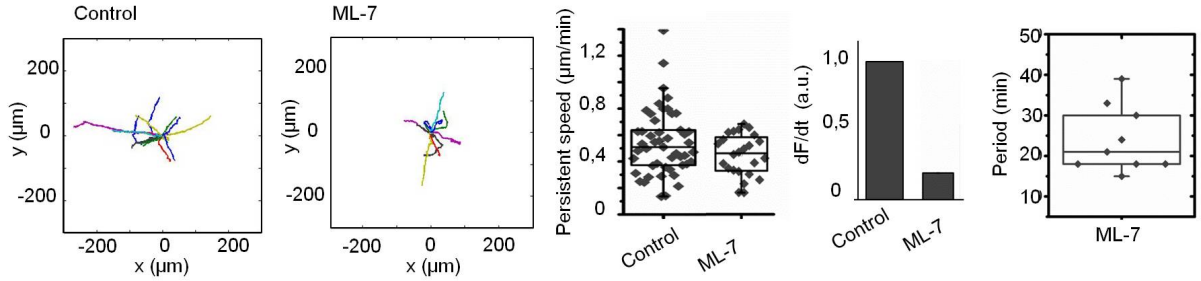

FIGURE 3.41: Trajectories of control cells and cells in presence of 10 μM ML-7 of 5h duration. In the latter case trajectories are slightly shorter. Distribution of persistent speed of control and in the presence of the drug. Mean value for control is 0.54 ± 0.04 μm/min and of drug 0.43 ± 0.03 μm/min. Differential force normalized by initial deformation before addition of drug. Under inhibition of myosin light chain kinase differential force drops to $19\% \pm 1\%$. n=24, N=3. Distribution of periods of speed variation 24 ± 3 min (N=3, n=9).

was instantaneous. The mesh relaxed and cells started to bleb. On a longer term, after 1-2 h cells extrude from CDM. For both concentrations cells did not migrate. Strikingly, an increase of the actin signal in the cortex upon rounding up of the cell could be seen. To diminish the effect of the drug and to allow the cells to reestablish migration, drug was washed out as reported in [188]. So we incubated cells in CDM with 1 nM Calyculin A leading to the same results. Upon washout deformation of the mesh was partially restored, but it did not reach control. Moreover, cells were not able to reconnect to the surrounding and did not grow protrusions. They jiggled while blebbing but did not migrate. No information about trajectories or persistent speed could be extracted from this experiment. Cyclic application of deformation was not observed.

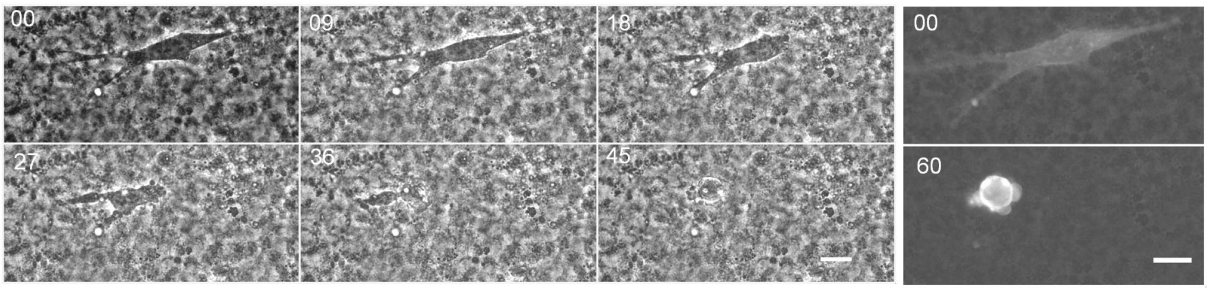

FIGURE 3.42: Image sequence of cell inside CDM with 1 nM Calyculin A added at time point 0. Cell detaches at rear and contracts before front also releases adhesion and contracts. At the end cell is round and blebbing. mCherry Lifeact signal of the cell at time 0 and after 1 h incubation, blebs are observed. Signal increases in the cortex. Time in min and scale bar 20 μm.

In conclusion, myosin seems to be necessary for effective migration, fine tuning of activity and contraction-relaxation cycles but not required for motion itself.

3.4.4 Inhibition of actin polymerization and actin related proteins

As actin is a building block of the cytoskeleton and a lot of structures related to migration include actin dynamics, altering its availability, structure and dynamics is expected to greatly affect cell migration. We used different drugs for this purpose: Latrunculin A, which is sequestering monomeric actin and thus leading to actin depolymerization [236], C8, a synthetic polyamine promoting lamellipodia growth [10] and CK666 an inhibitor of Arp2/3 [237].

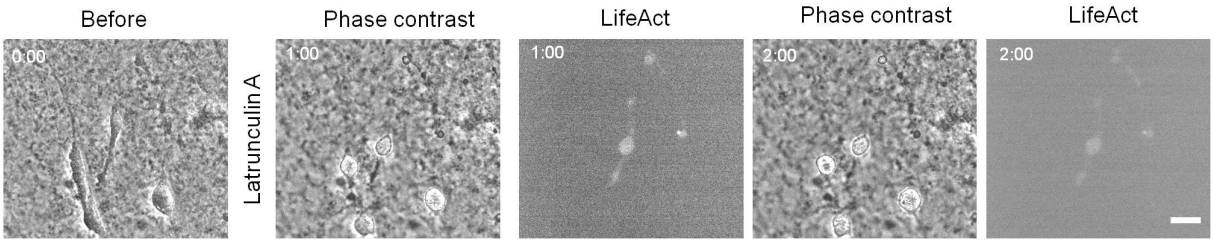

FIGURE 3.43: Phase contrast image of cell in CDM before application of drug. Cell after addition of Latrunculin A 1 μM. Cells round up and keep 2-3 protrusions reaching in the CDM. No displacement of the cell is visible. Time in h:mm. Scale bar 25 μm.

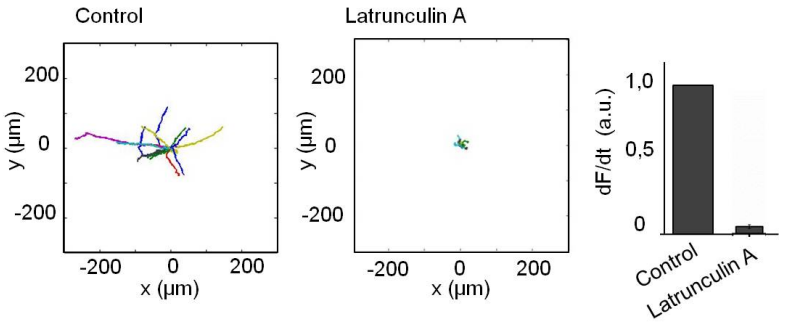

FIGURE 3.44: Trajectories of control cells and cells in the presence of 1 μM Latruncunlin A of 5h duration. Cells are not motile thus not migrating. Differential force drops to $4 \pm 1\,\%$. n=19, N=3.

Latrunculin A was used at 1 μM concentration [238]. The effect of the drug was visible instantaneously. The cells rounded up and had only some protrusions left (see Figure 3.43). Simultaneously, the mesh relaxed. No motion was observed in presence of the drug. Therefore, only the relaxation upon addition of the drug contributes to the trajectories in the plot (Figure 3.44). The differential force drops to 4 ± 1 % and no deformation of the mesh could be observed in the presence of the drug (see Figure 3.43 and Movie 14). The 4 ± 1 % differential force may originate in the initial relaxation when the drug is added. As no deformation can be detected we excluded the presence of contraction-relaxation cycles when actin is depolymerized. Depolymerizing actin seems to be a radical option for stalling cell migration in 3D. Somehow it was expected, since actin is the building block of cortex, lamellipodia, filopodia and stress fibers, thus the structure allowing cells

to apply a force. We further used C8 to probe actin behaviour in 3D CDM.
C8 is a synthetic polyamine that promotes lamellipodia growth [10]. It acts as an actin

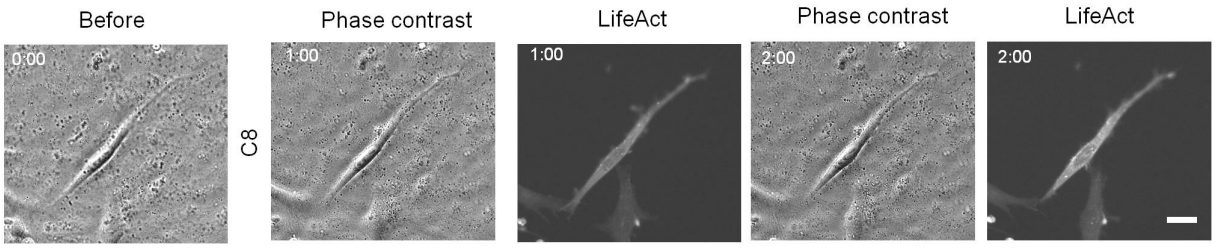

FIGURE 3.45: Phase contrast image of cell in CDM before application of drug. Cell after addition of C8 100 μM. Time in h:mm. Scale bar 25 μm.

nucleator thus it is expected to change actin dynamics. We wondered how this could affect migration behaviour. C8 was added in a concentration of 100 μM [10] to the cells in CDM. Morphology of the cells did not change significantly (Figure 3.45). Although protrusion activity was slightly higher in the presence of the drug, no big lamellipodia as reported for cells on 2D flat surfaces could be observed [10]. Cells were motile and migrated, but after addition of drug some cells did not maintain their polarity, depolarized and eventually repolarized to migrate in the opposite direction. Trajectories corresponding to 5 h of migration were plotted (Figure 3.46). In comparison to control case, the trajectories were shorter. Also persistent speed was lower at 0.39 ± 0.06 μm/min (Figure 3.46). Migration was altered compared to control case. The oscillation in speed is still observed with a higher period of 27 ± 3 min compared to control cases (Figure 3.46). Contraction-relaxation cycles are also visible in the displacement of FN mesh upon application of drug.

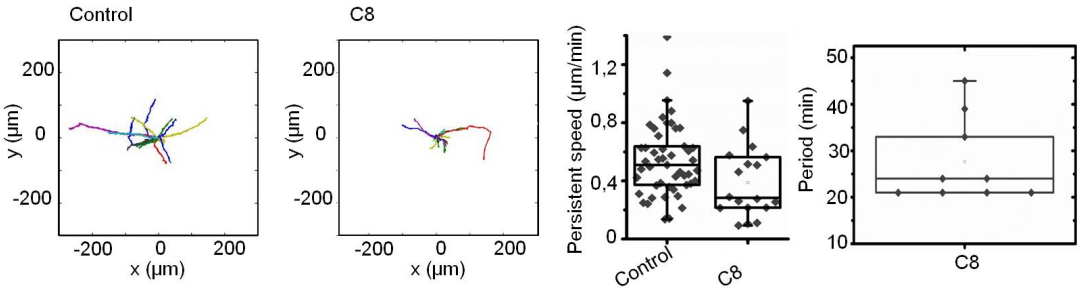

FIGURE 3.46: Trajectories of control cells and cells in presence of 100 μM C8 of 5h duration. In the latter case trajectories are shorter. Distribution of persistent speed of control and in presence of drug. Mean value for control is 0.54 ± 0.04 μm/min and of drug 0.39 ± 0.06 μm/min. n=18, N=2. Distribution of periods of speed variation 27 ± 3 min (N=2, n=9).

Another player in actin networks is the Arp2/3 complex. It is an actin nucleator and allows actin network to form branches [56]. As cells in CDM do not typically have lamellipodia it is interesting to know if other actin gel structures such as the cortex or the actin gel around the nucleus that might require Arp2/3 are affected by its inhibition and if we can observe a change in cell migration. In Figure 3.47 the morphology of a cell in

the presence of 50 μM CK666 [179], an Arp2/3 inhibitor [237] is shown. There is no clear morphology change visible. Cortex and actin gel are still visible in the cell, also cells continue migrating in CDM. However, migration is affected as shown in figure 3.48. The trajectories are shorter than control and persistent speed has a mean value of 0.40 ± 0.03 μm/min which is lower than the control. Cyclic behaviour in speed is also observed, but with a higher period of 27 ± 4 min. We assume contraction-relaxation cycles to still be present upon addition of drug. As Arp2/3 is not the only nucleator in the cell, it is not surprising that migration is not stalled.

Depolymerizing the actin cytoskeleton with Latrunculin A had a severe effect on cell

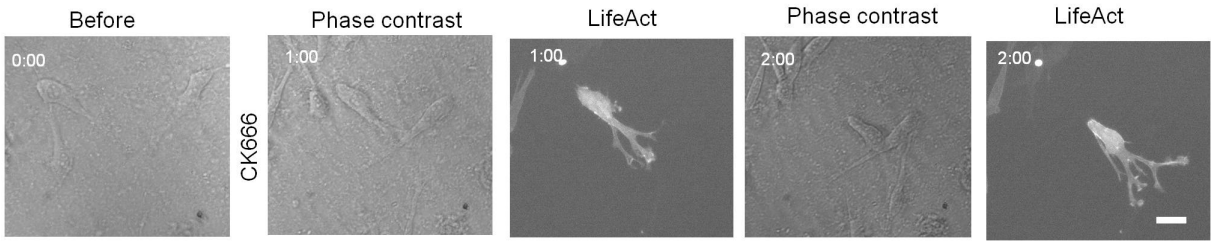

FIGURE 3.47: Image sequence of cell inside CDM with 50 μM CK666 added at time point 0. No morphology change is visible in the cells. Time in h:mm and scale bar 25 μm.

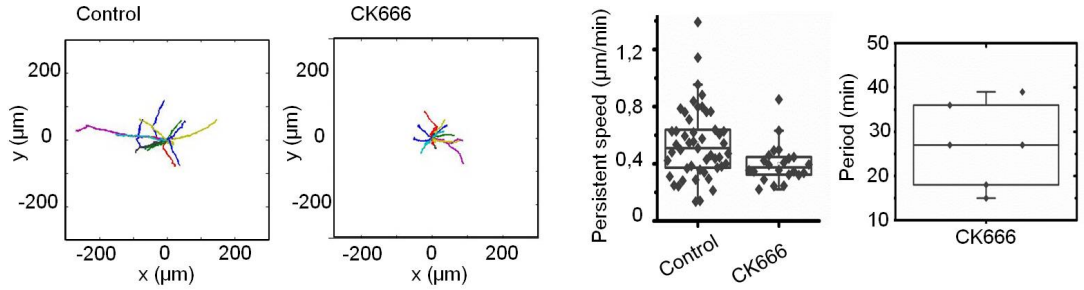

FIGURE 3.48: Trajectories of control and Arp2/3 inhibited cells of 5h duration. In presence of 50 μM CK666 trajectories are shorter. Distribution of persistent speed, mean value 0.40 ± 0.03 μm/min. N=3 n=22. Distribution of periods of speed variation 27 ± 4 min (N=3, n=9).

migration which was completely stalled. Also interfering with actin dynamics by adding C8 altered cell migration characteristics of cells. Removing nucleators of actin also shifts the dynamics. As a consequence of inhibiting actin nucleator, persistent speed and overall migration diminished. The period of speed oscillation increases. This shows that the integrity of actin cytoskeleton is required for migration in 3D CDM. It also suggests that modifying actin dynamics will have an impact on migration characteristics and contraction-relaxation cycles.

3.4.5 Depolymerization of microtubules

Having probed different components of the actin cytoskeleton and of the active gel, we probed the other dynamic cytoskeletal component in order to investigate if microtubules

have a contribution to the contraction-relaxation cycles. Therefore, we used Nocodazole at 10 μM [155] [6]. This drug provokes the depolymerization of microtubules.

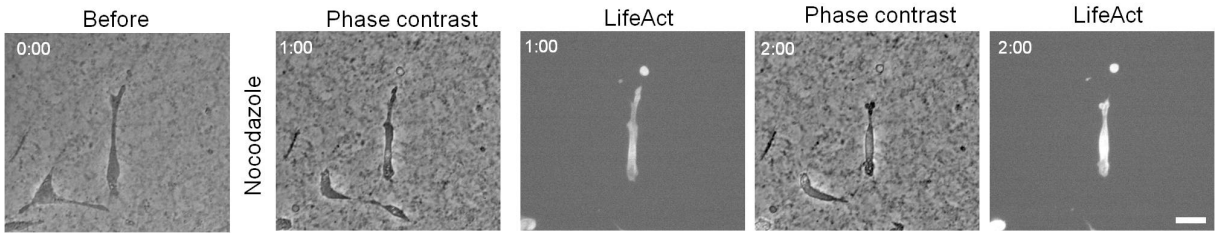

FIGURE 3.49: Phase contrast image of cell in CDM before application of drug. Cell after addition of Nocodazole 10 μM. Cells condense and have alternating protrusion at "front" or "back". Time in h:mm. Scale bar 25μm.

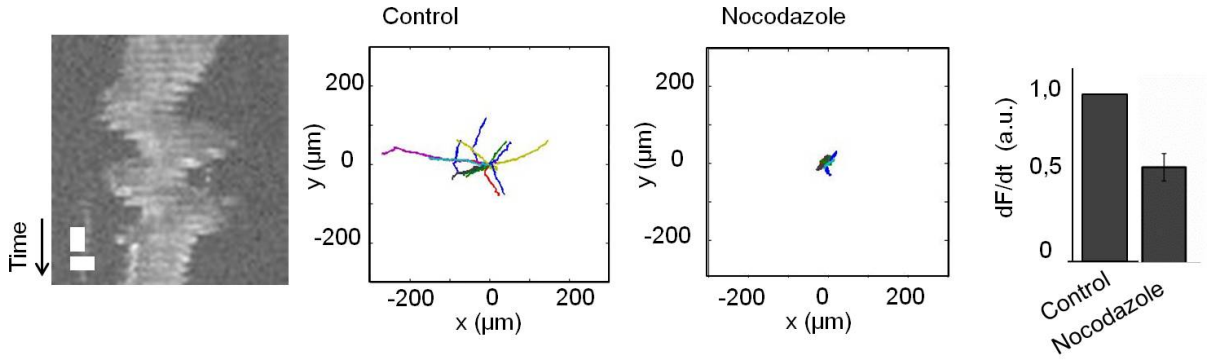

FIGURE 3.50: Kymograph of a transiently transfected cell expressing mCherry Lifeact. Time bar 20 min and scale bar 10 μm. Trajectories of control cells and cells in presence of 10 μM Nocodazole of 5h duration. Solely movement around a center can be observed after addition of drug. Differential force is normalized by initial deformation before addition of drug. When depolymerizing microtubules differential force drops to $54\% \pm 7\%$. N=3 n=26.

The effect of the drug could be directly seen on the morphology of the cells. They became more condensed or compact as shown in Figure 3.49 with protrusions at alternating sides of the cells. Some of the cells were motile: they oscillated around a center position moving back and forth in the CDM. This can be seen in the trajectory plot but also in the kymograph in Figure 3.50. The kymograph was built from the actin signal (mCherry LifeAct) along cell axis. Persistent migration itself did not take place and therefore there was no persistent speed to extract from this experimental condition. Differential force is dropping to $54\% \pm 7\%$.

This cyclic behaviour was striking (see Movie 15). It seemed to correspond to the contraction-relaxation cycles in control case. It reminds of cell oscillation in suspension [239]. First we aimed to analyze the frequency or period of these oscillations. Therefore, either kymographs were generated, the position identified and the period calculated or peaks and minima in the position of the nucleus along time were identified. To have

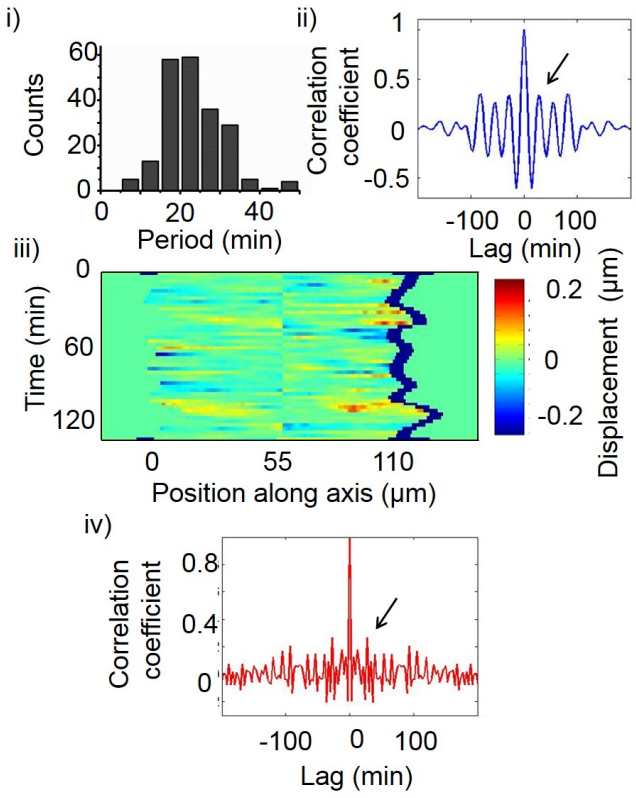

FIGURE 3.51: i) Distribution of periods for oscillations in presence of 10 μM Nocodazole. Peaks in trajectory were determined with origin peak finder or manually with kymographs. Mean value is 22.1 ± 1.0 min. ii) Correlation coefficient of autocorrelation analysis of cell speed. Peak is situated at 27 ± 1.5 min (arrow). iii) Heatmap of deformation. Rows are centered at nucleus back and sign at the back of the nucleus is inverted. Blue represents a relaxation and red a contraction. Oscillations of the nucleus are visible at the border of the heatmap. Alternating blue and red rows indicate that contraction-relaxation cycles occur. iv) Autocorrelation analysis of the mesh displacement at one side of the cell. A peak emerges at 24 ± 1.5 min (arrow).

the cleanest signal, the cell axis was arranged parallel to the x axis. The distribution of the obtained period is shown in Figure 3.51 i). We have a mean value of 22.1 ± 1.0 min. This is the period at which cells have done one cycle of oscillation. Then, we wanted to know if we could also detect the variation in speed as for control and ROCK inhibition case. So we performed an autocorrelation analysis of the speed for one example cell. The result is also depicted in Figure 3.51 ii). The autocorrelation exhibits a peak at 27 min.

In the following we addressed the question if cells without microtubules are still performing contraction-relaxation cycles. Therefore, we checked the movement of the single cells of our experiments and performed KLT analysis. We subtracted the cell from the phase contrast image to exclude contribution of cell movement to the results of mesh displacement. Meaning that only transiently transfected cells could be used for this analysis. Two cells have been obtained for this experimental configuration. In Figure 3.51 iii) the deformation heatmap for one cell is depicted. As before the rows of the heatmap are centered at the back of the nucleus and the sign of deformation at the "back" of the nucleus is inverted. One can see that blue and red rows are alternating. Meaning that also in the absence of microtubules contraction-relaxation cycles persist. The oscillation of the position can be seen at the border of the right row, they have an undulated shape. Pinching points could not be detected in the overlay of KLT and phase contrast movie due to the diminishing amplitude of deformation. Moreover, autocorrelation can be performed on the displacement of the mesh. This allows us to extract a characteristic period for the contractions. In Figure 3.51 iv) a spectrum of the correlation coefficient is depicted. A peak can be identified at 24 min. Independently of the applied method used for extracting the period, it seems that periods are larger in presence of Nocodazole compared to control.
To summarize, contraction-relaxation cycles persist without microtubules. Together with the results described above, it strongly suggests that this phenomenon is acto-myosin driven. The result also suggests that microtubules are necessary in 3D migration to maintain polarity.

3.4.6 What we can learn from spontaneously forming cytoplasts

When cells migrate in CDM they send protrusions in various directions. Sometimes it can be observed that such a protrusion detaches from the cell body: for example when protrusion and cell travel nearly parallel to each other and the connecting part forms a closed angle, or when a trailing edge does not detach and a rupture occurs. These parts of the cell are named cytoplasts and lack nucleus. Even though, they are able to travel considerable distances. Moreover, a striking observation has been made: the cytoplasts oscillate in the CDM. These cytoplasts perform a forward-backward movement in the CDM, similar to cells with depolymerized microtubules with Nocodazole.
In Figure 3.52 i) the movement of a cytoplast is depicted. First it moves to the left, stops for approximately 10 min, and then continues to the left before returning to the right. It reaches an extreme point before turning again to the left. The "front" of the cytoplast seems to have a protrusion whereas the "back" is round. At the end the cytoplast stops, blebs and dies. Not all cytoplasts oscillate in the same manner or for the same amount of

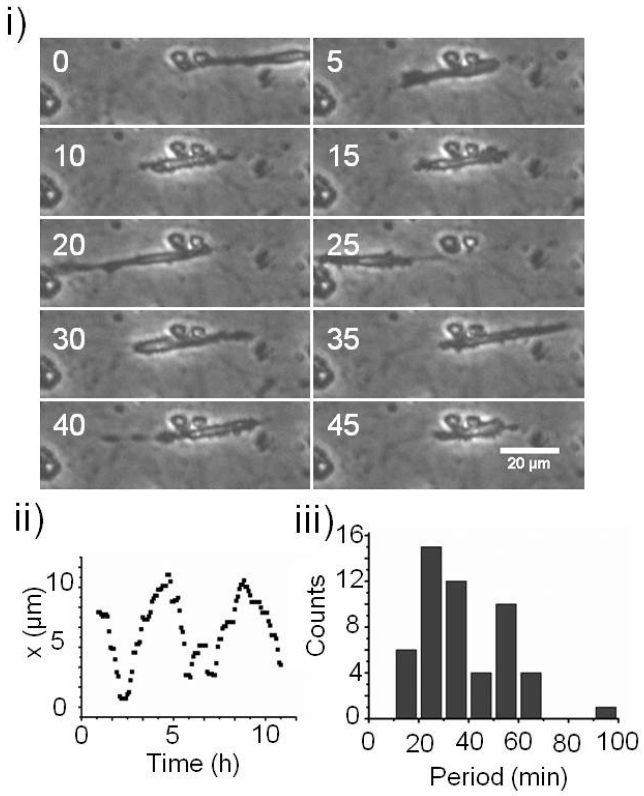

FIGURE 3.52: i) Phase contrast image of a cytoplast moving back and forth in CDM. Scale bar 20 μm and time in min. ii) Plot of trajectory of a cytoplast (Cell axis aligned with x-axis). Cycles are visible. iii) Distribution of periods. Mean value at 36.0 ± 2.4 min. n=52 N>3.

cycles. Sometimes only one cycle is accomplished. This different behaviour might depend on the size of the cytoplast, which is variable. In Figure 3.52 ii) a trajectory of a cytoplast is plotted. The x-axis has been aligned with the cytoplast axis. Peaks and minima in the curve show the turning point of the cytoplast. A forward-backward movement is clearly visible: the cytoplast performs cycles of motion. On the bottom right of the Figure (panel iii)) the distribution of periods for the cycles is represented. The peak or minimum positions were identified and the period was calculated. The mean value of the period is 36.0 ± 2.4 min. This is considerably higher than for cells, both in control or in drug experiments presented in the previous section. This observation demonstrates that nucleus is not required for a cell to perform oscillations in the CDM. It also suggests that the oscillations may be based on an intrinsic characteristic of acto-myosin system as reported for cell fragments in suspension [96].

To sum up how challenging acto-myosin cytoskeleton affects cell motility and cyclic behaviour of cells, we analyze persistent speed in function of speed oscillation period. This is plotted in Figure 3.53 i) together with data of control shown in Figure 3.29 ii). The higher periods in presence of acto-myosin drugs correspond to a lower persistent speed. The curve follows an exponential decay. Data from Nocodazole is not included, since no persistent speed can be obtained. This confirms that higher speed oscillations are correlated with a faster migration and that acting on acto-myosin dynamics affects the motility of cells and the dynamics of contraction-relaxation cycles. Further parameters are currently being analyzed and correlated to cell migration.

In Figure 3.53 ii) a flowchart describes how acting on cytoskeleton and its dynamics alters cell migration and contraction-relaxation cycles. When the cytoskeleton is affected, no migration or even no motility is observed. This is the case when applying Nocodazole or Latrunculin A to cells in CDM. It corresponds to the first arrow to the right in the flowchart. The next question is if myosin is functional. If not (blebbistatin) no contraction-relaxation cycles are observed (second right arrow). Finally acting on the acto-myosin dynamics by adding ML-7, C8 and CK666 is altering the dynamics of oscillatory behaviour to higher periods and lower motility of the cells.

Globally, we can say that myosin is required for the force application and for an effective

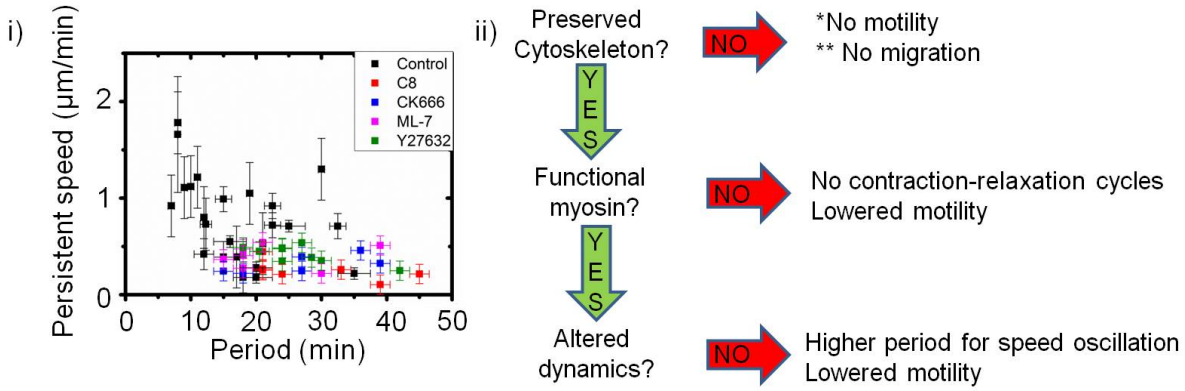

FIGURE 3.53: i) Plot of persistent speed oscillation period obtained by autocorrelation analysis of control (n=25) and in presence of 10 μM Y27632 (n=9), 10 μM ML-7 (n=7), C8 100 μM (n=7) and CK666 50 μM (n=6). Persistent speed in dependence of oscillation period. Error for the oscillation period was evaluated as half of time between two acquisitions. For the tracking, an error of one pixel was estimated and multiplied by acquisition frequency to obtain a speed. A tendency of decreasing persistent speed for higher periods is shown. ii) Flowchart showing the requirements for migration in 3D CDM and the impact of probing the cytoskeleton with different drugs on speed oscillations.

migration and contraction-relaxation cycles. Actin is required as the basic entity of the cytoskeleton where myosin acts. Altering its dynamics also leads to decreased migration. Microtubules and nucleus are needed for migration but not for oscillations, making the contraction-relaxation cycles an acto-myosin based phenomenon.

3.5 Cyclic behaviour of cells in CDM is not triggered by the chemical environment

So far, we have been observing acto-myosin based contraction-relaxation cycles in 3D CDM cell migration. Since the CDM is produced by cells, there is no way to control what proteins are being deposited. So, a kind of protein soup is left in the CDM after lysis of producer cells. This means that even if it is not likely, we cannot rule out if the phenomenon we observe is triggered by chemical components of the CDM. Therefore, we decided to probe another fully controllable setup to exclude that the chemical environment is triggering the oscillatory behaviour. Part of experiments have been performed by Basile Jacquel (Master student in the lab). The experiment on GFP BANF-1 3T3 fibroblast was conducted in collaboration with Anastasja Grabarz from Evi Soutoglou lab (IGBMC).

3.5.1 The microchannel setup

Microchannels as their name states are channels of micrometer scale produced by microfabrication. A device with cell sized channels can be produced, as described in the Material and Methods part with photolithography, PDMS replica molding and bonding of the structure to a glass CS. Cells are introduced through holes which are punched in a reservoir before bonding. We let them adhere and enter the channels.
Microchannels with a straight design were preferred over channels with turns to avoid directional cues in the device (Figure 3.54). In order to be in a confining configuration such as in CDMs, channel width was varied between 2 μm and 20 μm (in 2 μm steps), in order to be able to compare a wide range of channel width with CDM. Each device is limited to one channel width. Channels are made of PDMS and the bottom is a glass CS. The Young's Modulus of PDMS for a 1:10 crosslinker: pre-polymer ratio [240] and of glass [241] is in the MPa range. This is much higher than the Young's Modulus of the CDM of 50 Pa. Cells are not able to deform these materials. Channel height was chosen to be 5 μm. They were not incubated with any ECM protein. Whatever is present

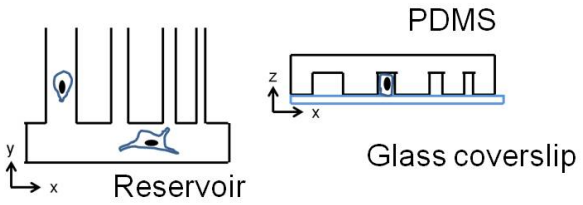

FIGURE 3.54: Schematic top and side view of microchannel design. Channel width is vayied from 2 μm to 20 μm and channel height is 5 μm. Cells are deposited in reservoir and are free to migrate. Side view shows a confined cell in a microchannel feeling four walls.

in the microchannel comes from deposition of serum of medium in which cells are suspended. Neither a chemotactic gradient was applied to guide cell migration. Entry of cells in microchannel and migration relies on stochastic process. Cells seem to enter in wider channels more easily than in narrower ones. The amount of cells entering 2 μm wide channels is less than the amount entering 10 μm wide channels. Cells in 20 μm wide channel can be flown inside the channel when deposited solely by the pressure of

the syringe or by carefully shaking the device in one direction. It has been observed that cells dividing in the chamber parallel to channels were more likely to enter the channel eventually due to a preset polarity after division. Once inside the channels cells exhibit different morphologies depending on the different channel widths.

3.5.2 Cells in microchannels

In wider channels, cells have a more 2D like morphology with a lamellipodia at the cell front and a trailing edge at the back of the cell. For this channel width the cell is qualitatively spending more time migrating at the border of one channel (close to the channel wall) than in the center of the channel. For 10 μm wide channels cells start being in contact with both walls of the channel simultaneously. The different morphologies are depicted in Figure 3.55.

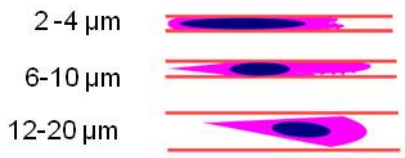

FIGURE 3.55: Schematic of cell morphology in 2 μm, 4 μm, 6-10 μm and 12-20 μm channels. In 2 μm and 4 μm channels cell have a round edge, in 6-10 μm channels cells have a round or a trailing edge and in 12-20 μm channels they have a trailing edge and a more 2D like morphology.

For channels widths ranging from 6 μm to 10 μm cells are either exhibiting a round or a trailing edge. For lower channel width only round edges are observed. We hypothesize that this might be linked to confinement and cell contractility. It has been shown that contractility of cells increases with higher confinement [242]. This might explain the round edge observed in cells inside channels with small width.
The deformation of the nucleus while entering microchannels has also been observed (Figure 3.56 i)). Deformation occurs while entering or escaping the channel and it is reminiscent to the squeezing phenomenon observed in CDM except that only half of the process is taken into account. In collaboration with Evi Sotouglou team (IGBMC) we started to investigate this deformation with NIH3T3 BANF-1 GFP expressing cells. BANF-1 is a protein of the nucleus potentially sensitive to nucleus deformation. Once inside the channels, it accumulates at the poles of the nucleus where curvature is highest as shown in Figure 3.56 ii). Confinement of cells increases with smaller channel width. This can also be seen in the nucleus elongation. We fitted the outline of the nucleus by ellipse fitting and extracted the long and short axis. The coefficient $\frac{long}{short}$ axis indicates the elongation of the nucleus. In Figure 3.56 iii) cells in 2 μm and 20 μm wide channels are depicted and their nucleus outlined. At the bottom the axis ratio and the area of the nucleus are plotted against the channel width. Whereas the area does not change dramatically, the nucleus ratio increases after 10 μm towards smaller channel width to reach an aspect ratio of 9 for 2 μm channels. From 10-20 μm channels the ratio is stable around 1.5. Nucleus deformation increases when decreasing channel width.
Nucleus width in CDM ranges from 4 μm in deformed to 14 μm in natural state, therefore channels of this size would be taken into account to compare CDM and microchannel

migration.
Before comparing both setups, we wanted to assess if cytoskeletal structure remains the same for the two configurations. In the CDM we had focal adhesions, cortex, some sparse stress fibers and in some cells gel around the nucleus. For focal adhesions we used RFP zyxin transfected cells and let them migrate in channels. Focal adhesions are present on the apical and basal side of the cell and on channel lateral walls. Some focal adhesions are stable and others are traveling with the cell (Figure 3.56 v)). Stress fibers were also visible in cells, depending on channel width one or two stress fibers run on top and underneath the nucleus and terminate in the protrusion. Focal adhesions and stress fibers ends colocalize. A signal in the cortex has also been detected, especially at the back of round cells the signal is evident. The main difference in structure between channels and CDM might be in the protrusion as focal adhesions are only present on the basal side and not in the tip of the protrusion like in the CDM. The overall cytoskeletal structures are similar in confining microchannels and 3D CDMs.

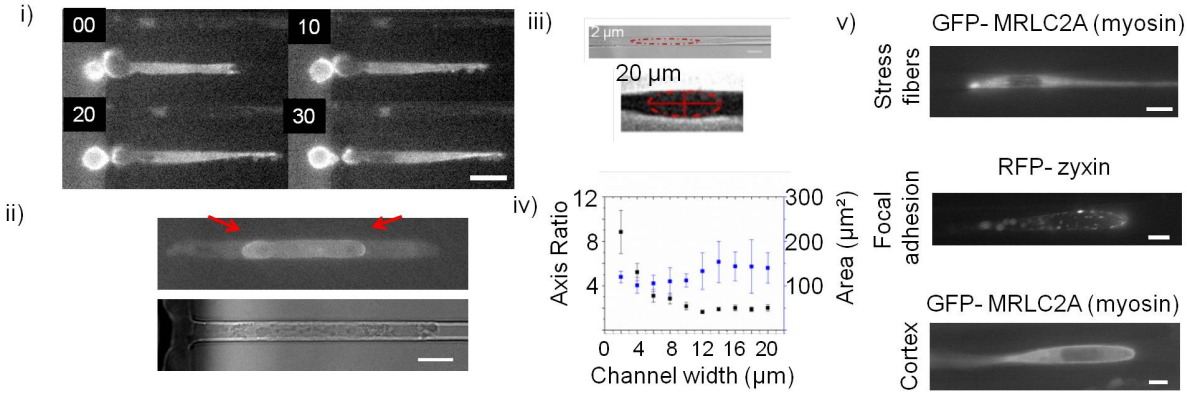

FIGURE 3.56: i) Entry of a cell in 2 μm channel upon deforming nucleus (RFP zyxin expressing cell). Scale bar 10 μm, time in min. ii) GFP BANF-1 expressing NIH3T3 fibroblasts in 4 μm channel. Protein accumulates at the poles of the deformed nucleus. Scale bar 10 μm. iii) Nucleus outlined in 2 and 20 μm channel. Scale bar 10 μm. Nucleus is ellipse fitted and long and short axis extracted. Nucleus axis ratio is calculated as long/short axis. iv) Plot of axis ratio and nucleus area in function of channel width. From 2-10 μm axis ratio increases. It is stable from 10-20 μm around a value of 1.5. v) Cells expressing GFP NMHC or RFP zyxin. Stress fibers, focal adhesions and cortex are visible. Scale bar 10 μm.

3.5.3 Migration behaviour in channels

We first scanned migration behaviour extracting persistent speed, time and length for each channel width. This is represented in Figure 3.57. Persistent length, time and speed are changing for different channel width. Persistent length is increasing towards 10 μm channel where it has its maximum before decreasing again. Persistent speed shows a similar behaviour as persistent length. It increases towards 10 μm width before it decreases between 12 μm and 20 μm. Persistent time is highest for 2 μm channels, and then

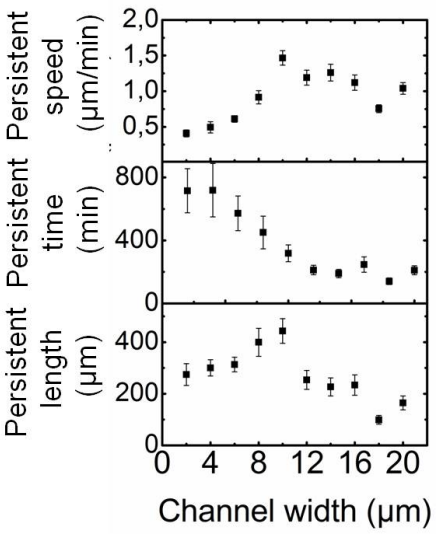

FIGURE 3.57: Persistent speed, length and time plotted against channel width. Persistent speed increases towards 10 μm channel before it decreases again. Persistent length has a similar behaviour as it increases to 10 μm where the maximum is and decreases again. Persistent time continuously decreases. For each channel width n>18 and N>3

it decreases continuously for the other channel widths. It is striking that for persistent length and speed, a maximum is found at 10 μm width. This is the value where cells start touching both lateral channel walls.
Except for 2 μm and 4 μm wide channels, persistent speed is much higher in microchannels than in 3D CDM or on flat surfaces (reference David Caballero unpublished data). Persistent length and times are also higher in channels compared to CDM. We hypothesize that the continuous confined environment has less directional cues and thus cells are more persistent.
In terms of morphology, confinement, persistent speed values and cell size, channel widths of 4-10 μm are more similar to 3D CDM migration. A general impression of cell migration can be derived when observing cells migrating in microchannels with a higher magnification objective. Cells do not seem to migrate continuously. Their movement seems to be abrupt and pulsatile (see Movie 16). This reminded us of the speed variation seen in CDM. In Figure 3.58 this migratory behaviour is depicted. Nucleus back position for several time points is marked with a white dashed line. Cell is moving forward, stopping or moving backward and moving forward again. No continuous sliding movement is observed.
This is also visible in the plot of the x position of the back of the nucleus versus time. Points of backward or stopping movement are highlighted with red arrows. We guessed that we would also have a cyclic behaviour of the speed of the nucleus. To test this hypothesis, we plotted the speed versus time and identified manually the speed peaks and calculated the period. To lower noise and make peaks more visible, speed was averaged over 2,3 and 4 time points. If the averaged and the non-averaged data were coinciding in a peak, the peak was extracted. With this method, we obtained an averaged speed oscillation with a mean period of 24.1 ± 1.4 min.
We are not able to extract a deformation pattern for cells migrating in microchannels because walls are too stiff to be deformed by cells. Thus migratory behaviour in terms of cycles in cell speed seems similar to what can be observed in 3D CDM. As we did not pretreat channels in any manner we are able to exclude chemical cues coming from cells

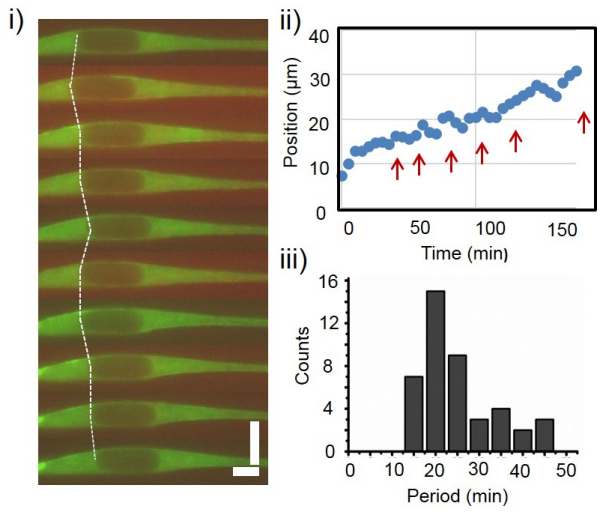

FIGURE 3.58: i) Image sequence of a GFP-NMHC, RFP zyxin expressing cell migrating in a 6 μm channel. Scale bar 10 μm and time 5 min. Back of nucleus connected between frames with white dashed line to highlight forward backward movement during migration process. ii) Position along channel of nucleus back along time of cell on the left. Forward backward cycles are pointed out with red arrows. iii) Distribution of periods for forward backward movement. Mean value is 24.1 ± 1.4 min. n=45 N>3.

producing the CDM to be responsible for contraction-relaxation cycles in 3D CDM. We further conclude that these cycles are tightly linked to confinement.

3.6 Induced contractions lead to cell movement

The next step to understand better contraction-relaxation cycles was to challenge the cell mechanically, and to see how contraction-relaxation cycles might change. Microsurgery is commonly used to locally induce a cut or rupture in cells or tissue. It has been widely used in the field of embryology for *C. elegans* [243], *Zebrafish* [244] or *Xenopus* [243]. Stephan Grill lab showed that laser ablation in frog oocytes induced a relaxation of the oocyte followed by a contraction. Contraction was attributed to acto-myosin flow [93]. This method has also been used to test stress fibers in cells on 2D [76]. The response of the object to the cut is related to its tension.
We decided to use this method to induce contractions, which we compare to control case and also to test the contribution of different supramolecular structures such as actin gel or acto-myosin cortex to contraction-relaxation cycles.

3.6.1 Mechanical probing of cells

First, laser ablation was tested on cells spread on 2D surfaces. Optimal ablation parameters need to be determined to limit the damage caused to the cells during the ablation process. Different cellular structures such as the lamellipodium, the lamella or stress fibers were tested. In Figure 3.59 the ablation of a stress fiber in a cell on a surface is shown. The ablation point extends up to 5s after ablation. Nucleus moves away from cut and the cell experiments a global relaxation. The lamellipodium at the left starts to retract. Interestingly the nucleus is more visible after the ablation. In conclusion, laser cutting can be used to probe cellular structures.
We transposed the cutting to 3D CDM with adjusted parameters. The difficulty of the

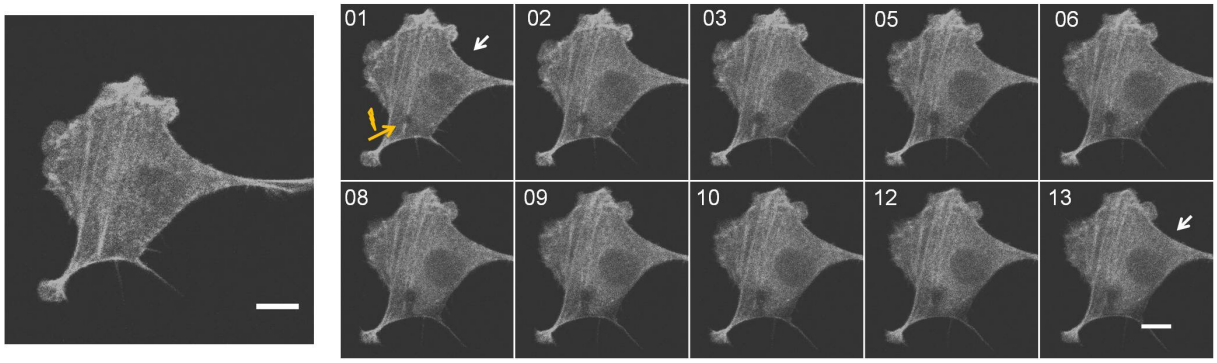

FIGURE 3.59: Laser ablation of stress fiber of a mCherry Lifeact expressing NIH3T3 fibroblast. Point of ablation indicated with yellow arrow. Hole becomes larger between 0 and 5 s. White arrows highlights the curvature at the top part of the cell. Curvature diminishes indicating a relaxation. Scale bar 10 μm, time in sec.

experiment arises from the fact that determining the cutting plane is not always straightforward. Moreover, a slight excess in ablation power and/or time can induce cell death, that can be easily identified as they loose their fluorescence and decompose with large blebs.

Ablating cells in 3D provokes a 4-steps response in the cell. First, we could observe (1) a relaxation of the cell, followed by (2) the appearance of an actin rim around the nucleus. Afterwards, (3) an accumulation of actin around the point of ablation could be seen because actin signal increases. And finally, (4) a contraction occurs. All these effects depend on the size, position and targeted structure of the ablation spot. Cut size might vary minimally from one cut to the other. Below we will describe each event separately.

In Figure 3.60 the cell is embedded in the CDM. Laser ablation is performed top left of the nucleus. The cortex was targeted. After cutting, a relaxation can be observed: the two parts adjacent to the cut move away from each other. This event is followed by the formation of an actin rim around the nucleus, which is transient and disappears again. During the presence of the rim the nucleus is more visible also in bright field. An actin rim around the nucleus is normally viewed as a death signal [245], however our cells survive and the rim disappears. Then actin intensity increases at the former ablation spot and contraction occurs. In this example, we targeted the cortex. What happens if we ablate a stress fiber or the actin gel that can be observed around the nucleus? In Figure 3.61 the ablation of a stress fiber is depicted. After cutting, relaxation can be observed and the remaining parts of the fiber move in opposite directions. In this case, no actin accumulation appears at the ablated spot. The cell retracts. The laser cut might ultimately lead to a cytoplast and the cell gets torn apart. Although in this example, a non-polarized cell has been ablated. Ablation of stress fibers in polarized cells follows the same path. Relaxation after ablation and movement away from the cut are observed. No further subsequent contraction has been detected.

As mentioned before, in some cells we observed an actin gel behind the nucleus. This can also be ablated (Figure 3.62). When we target this actin gel at the back of the nucleus we observe an increase of the actin signal at 9 s indicated with white arrow. Cell shape fluctuates and a small contraction might occur. Thus it is very small, except for some

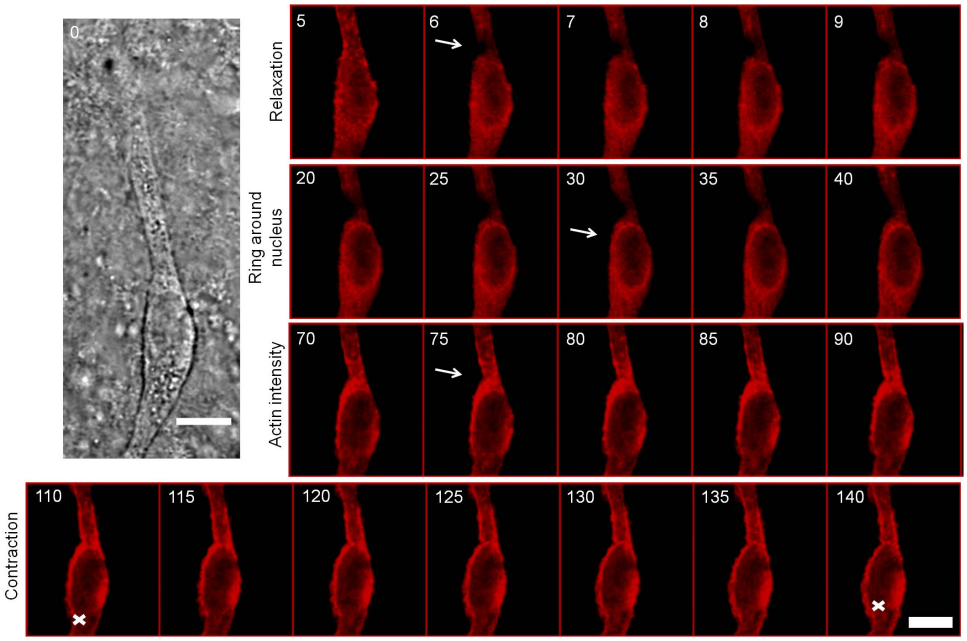

FIGURE 3.60: Bright field image of cell ablated in the following. Ablation at top left of nucleus (mCherry Lifeact expressing cell). Relaxation of the cell occurs. Ablation point grows larger. Increase of actin signal around nucleus. It forms a transient rim. Actin intensity increases at the former ablation spot. Contraction occurs, nucleus is moving upwards (initial and final position highlighted by white cross. Scale bar 10 μm, time in sec.

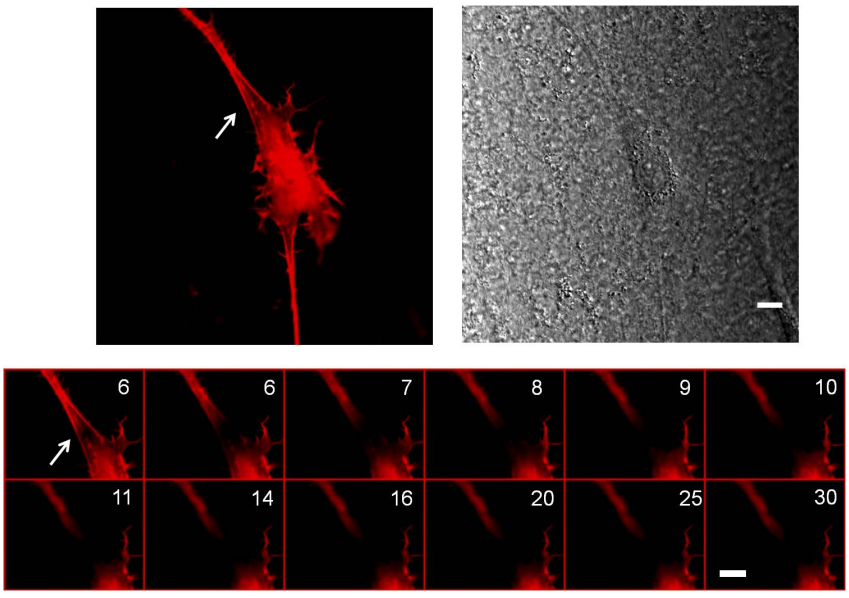

FIGURE 3.61: Laser ablation in a mCherry Lifeact expressing cell. After the cut remaining parts of the stress fibers move in opposite direction. Overall the cell relaxes. No further contractions or increase of actin signal at the ablation spot are observed. Scale bar 10 μm and time in sec.

special cases, we will treat further in this chapter. The nucleus is not changing position; the increase of actin at the back visible at 16 s does not lead to a forward movement of the nucleus. It does not have an effect on the cell. Still actin signal is prominent at the

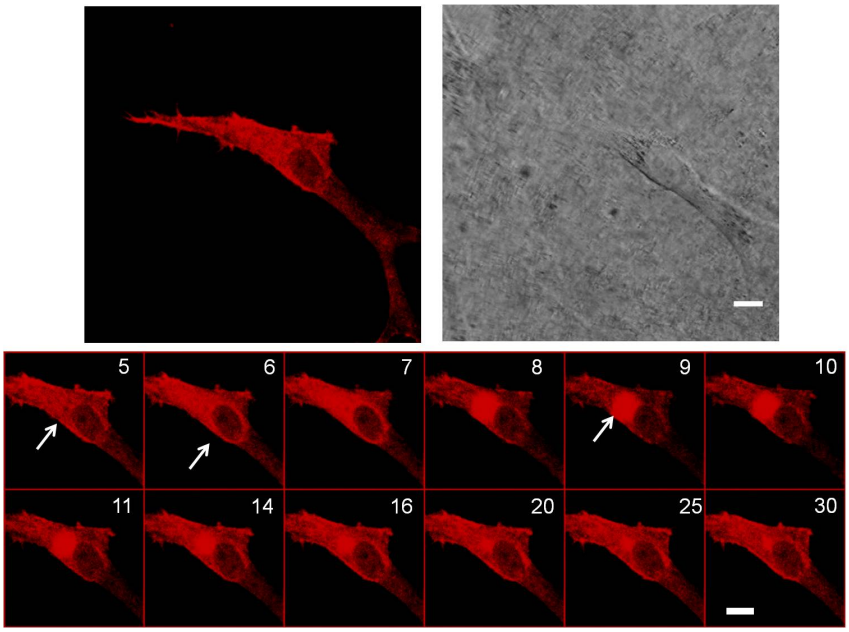

FIGURE 3.62: Ablation of the gel at the back of the nucleus in a mCherry Lifeact expressing cell. Ablation spot is highlighted with white arrow, actin rim appears around nucleus (arrow) and actin signal increases locally at former ablation spot (arrow). Minimal relaxation contraction can be detected. Scale bar 10 μm time in sec.

back of the cell. The beginning of the cortex and the end of the gel do not show a clear delimitation. Hence, gel and cortex might be connected to some extent.
From these experiments, we see that tension inside different cytoskeletal structures all based on actin, can have a wide range of behaviour upon tension release. As contraction-relaxation could only be induced upon cutting the cortex, it suggests that it is probably the structure responsible for contraction-relaxation cycles.

3.6.2 Induced contractions

In the following we probed different ablation spots in the cortex of the cell and compared their contraction patterns. Therefore, we subtract the fluorescent cell from the brightfield image and perform KLT analysis. We make a difference between polarized and non-polarized cells. Polarized cell means it has a front with a protruding side and a back with trailing or round edge. These cells have a broken symmetry. Non-polarized cells have no predetermined front or back, mostly they have more than two protrusions anchored at different sides of the cell. This is schematically shown in Figure 3.63. The polarized cell (Figure 3.63 top) has two protrusions on one side (one longer than the other) and a trailing edge on the other side. The non-polarized cell has two similar protrusions on opposite sides of the cell. Possible ablation spots are depicted with purple crosses. We expect different ablation spots to lead to differing results.

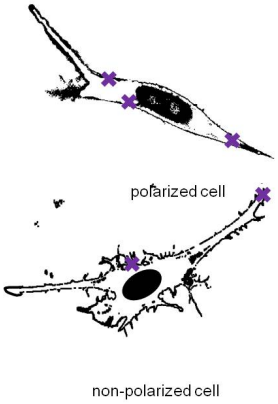

FIGURE 3.63: Schematics of a polarized and non-polarized cell. Ablation points are marked with purple crosses.

In Figure 3.64 a cell with three main protrusions (non-polarized) is shown. The ablation point is set between the two protrusions forming a 180° angle. The ablation occurs as described before: (1) relaxation, (2) actin rim, (3) actin signal increase and (4) contraction. The white lines in the cell plot limit the integrated area of deformation along the long axis of the cell (Figure 3.64 i)). Ablation occurs at 5 s. Blue rows indicate how

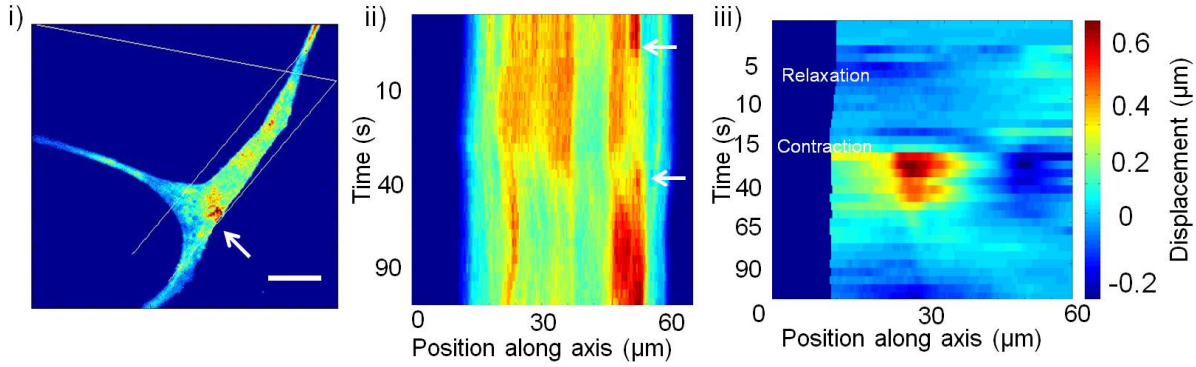

FIGURE 3.64: i) Ablation of non-polarized mCherry Lifeact expressing cell. Ablation spot is marked with arrow. ii) Actin intensity along cell axis is depicted. The signal at the ablation spot disappears upon cutting and reappears at 30s. iii) Heatmap of ablation. Cutting occurs after 6 s and is followed by a relaxation and a contraction starting at 25 s. The mesh displacement is radial towards the ablation spot. Scale bar 20 μm, time in sec.

the mesh moves away from ablation point as shown in Figure 3.64 iii). Approximately

30 s after ablation contraction occurs, mesh displacement towards the ablation spot in red and blue. After 90 s the mesh relaxes again. The actin intensity at the ablated spot vanishes as cutting occurs at 5 s as shown in the intensity plot in Figure 3.64 ii), then intensity increases again indicated with white arrow at 35 s (Movie 17 and Movie 18).

Ablation in polarized cells has various probing options: front or back of the cell at

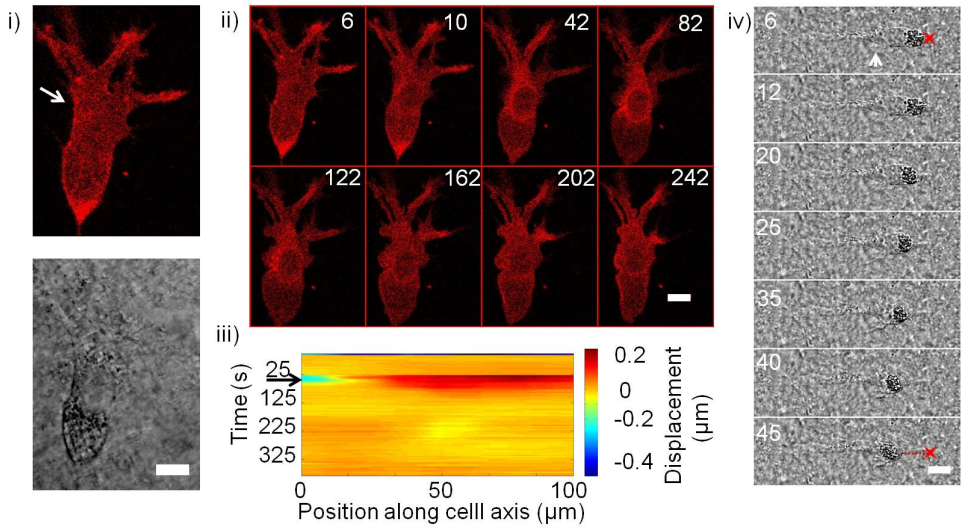

FIGURE 3.65: i) Laser ablation of a polarized mCherry Lifeact expressing cell. Ablation spot was set at front left of nucleus (white arrow). ii) Time-lapse of the ablation: Cell relaxes, big blebs are forming, actin rim forms around nucleus and cell recovers initial shape. Also protrusion retract. Whole cell seems to contract. Scale bar 20 μm. iii) Heatmap of mesh deformation, relaxation visible (black arrow). iv) Time-lapse of laser ablation at front of nucleus (white arrow), contraction at back follows and cell moves forward. Initial position highlighted with red star, final path with dotted line. Scale bar 10 μm, time in sec.

different distances from the nucleus and at the tip of the protrusion. In Figure 3.65 i) we aimed at the cortex frontal to the nucleus on the left side (indicated with an arrow). After cutting cell relaxes as depicted in the heatmap of displacement in Figure 3.65 iii). Starting from 25 s blue and red indicate the movement in opposite directions away from the laser cut. The cell also shows large blebs, which are best visible at 122 s (Figure 3.65 ii)). The actin rim around the nucleus appears at 42 s (Figure 3.65 ii). Then cell recovers initial shape at 242 s. During the ablation, the nucleus has performed a backward and forward movement. The protrusion at the front of the cell retracts giving the impression that after ablation the cell is overall contracting. At 242 s they are less extended than at 6s (Figure 3.65) A second cell is presented in Figure 3.65 iv). The cutting spot is set at the front of the nucleus (white arrow at 6 s). Interestingly for this cell no relaxation can be detected. The ablation spot increases in intensity (not shown) and the back of the cell contracts as can be seen by comparing initial position highlighted at 6 s and 45 s with a red cross. It seems that the nucleus gets pushed strongly by the back of the cell and engages in squeezing. Surprisingly this ablation at the front of the cell nearer to the nucleus is able to induce a contraction and motility. We are not able to say where exactly

the highest displacement, thus the contraction takes place and by which mechanism the phenomenon is transmitted.

The next probed spot in the cell is set in the cortex at the back of the cell (Figure 3.66).

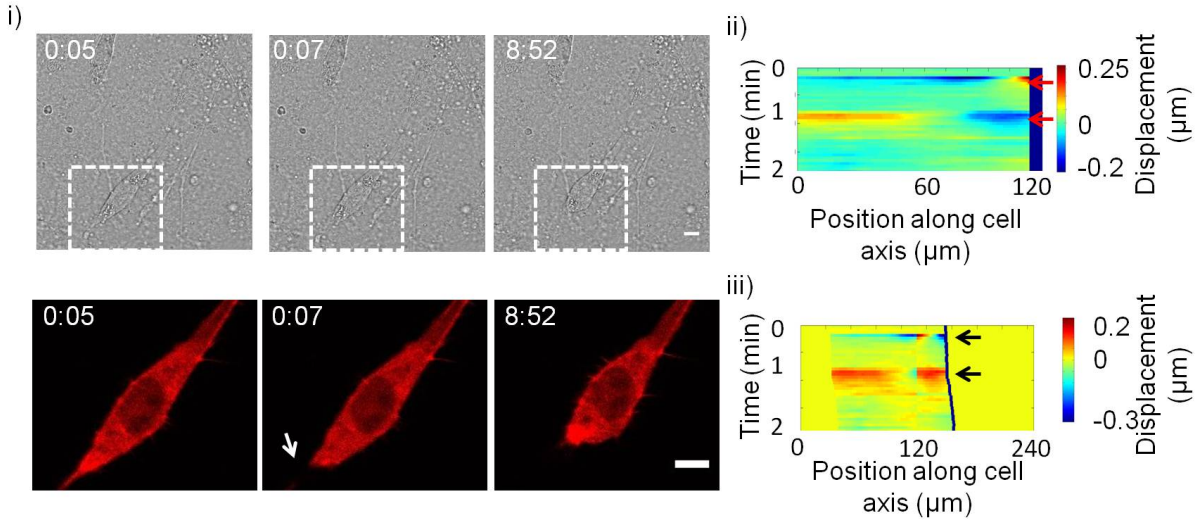

FIGURE 3.66: i) Laser ablation of mCherry Lifeact expressing cell at the rear. Time-lapse of ablation: After ablation rear detaches and back of cell contracts. Actin intensity at rear increases. After contraction (arrow) cell motility is observed (arrow). Scale bar 20 μm, time in m:ss. ii) Heatmap of mesh displacement in external framework. Colour code describes movement in x direction in red and -x direction in blue. iii) Heatmap of mesh displacement in cell framework. Colour code describes contraction in red and relaxation in blue. Onset of movement after contraction triggered by ablation (arrow).

The ablation spot was set near the rear, as indicated in Figure 3.65 i) with a white arrow. After cutting a relaxation can be observed, step (1) of the ablation process (Figure 3.65 ii) at 7 s) followed by a rounding up of the cell rear. Actin signal is also increasing at the ablated spot, step (3) of ablation process . And finally the contraction occurred, visible in the heatmap of mesh in Figure 3.66 ii) at 40 s (step (4). First, the mesh is moving away from the ablated spot. Afterwards, it moves back. Following interpretation of contraction or relaxation depends on position of cell. At the bottom in Figure 3.65 iii), the cell has been tracked and the rows of heatmap centered at the back of the nucleus and also the sign at the rear has been inverted. Interestingly, the cell moves forward after contraction at the back (like in migration associated to contraction-relaxation cycles), as it can be seen in the heatmap (3.66 (iii) timepoint 50 s, movement of cell indicated with arrow). Here again we are able to induce motility by choosing the proper ablation spot in the cell.

As previously described, cutting the actin gel at the back of the nucleus did not lead to contraction, although actin signal was still increasing. Intriguingly, this was not the case for two particular cells. As shown in Figure 3.67, the gel at the back of the nucleus was cut. The usual actin rim formed around nucleus visible at 56 s, and actin intensity increased at the ablation spot at 106 s. What followed was an increase of actin intensity at the rear of the cell visible at 256 s, contraction and cell movement. The actin intensity plot along cell axis reflects this behaviour 3.67 ii). The ablation is visible at 6 s, the actin

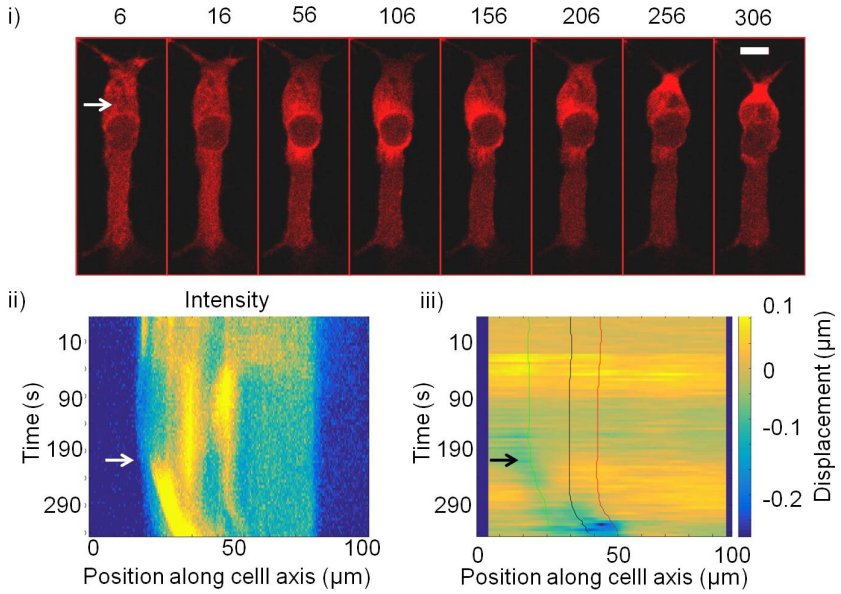

FIGURE 3.67: i) Ablation of gel at back of nucleus of mCherry Lifeact expressing cell. Cutting is followed by actin rim formation around nucleus and actin signal increase in ablation spot. Cell contracts at the back and starts migration. ii) Heatmap of actin signal: cut at 6s, increase of actin signal at 40 μm and 50 μm along cell axis corresponds to actin rim formation. Increase of signal at back of cell in rear (arrow). iii) Heatmap of mesh displacement and position of front, back of nucleus and rear of cell. contraction at 240-340s. Beginning of motion is indicated with arrow. Scale bar 20 μm, time in sec.

signal diminishes, and then two bright lines form at 40 μm and 50 μm along the cell axis, corresponding to the rim around the nucleus. This is followed by an increase of signal at the back of the cell after 200 s. No actin movement towards the back can be detected. Heatmap of displacement in Figure 3.67 iii) shows position of nucleus front and back and cell rear. A small contraction occurs at the back at 60-80 s. This behaviour was observed for two cells out of ten, both had an already polarized shape. The interesting feature is that the contraction does not seem to take place at the ablation spot. It seems to generate at the back of the cell. We hypothesize that gel and cortex are connected and that this somehow triggers the contraction at the back.
We wanted to further characterize the contractions and therefore extracted the time between ablation and onset of contraction and duration of contraction. In average contraction takes place 39 ± 18 s after ablation for 42 ± 13 s Figure (3.29). The time between ablation and contraction might indicate how long the cytoskeleton needs to reorganize. The duration is shorter than what we obtain for control case in Figure 3.29. The contraction induced by laser ablation seems to be faster than control case. Contractions produced by ablation have different temporal characteristics than natural occurring contractions.

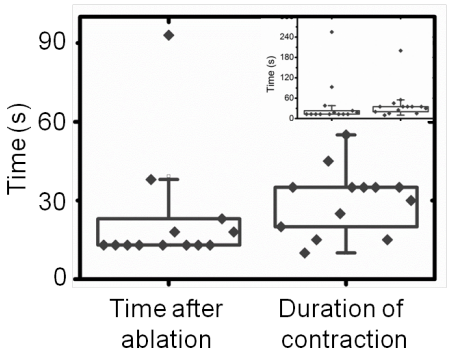

FIGURE 3.68: Plot of the time between ablation and onset of contraction (mean of 39 ± 18 s) and duration of contraction (mean of 42 ± 13 s). Inset shows one outlier. n=14 N>3 .

Overall the ablation experiments describe how the tension or focal adhesion strength within the cell are different. In a non-polarized cell ablation leads to a relaxation and contraction which seems to be symmetric. The ablation at the front of a polarized cell leads to relaxation and contraction. The ablation at the back of a polarized cell leads to a contraction that probably disrupts adhesion at the back of the cell and allows it to move forward, the symmetry of the cell is broken. These three cuts show that the outcome of the ablation depends on the location of the ablation spot. We suspect a different structure front and back of nucleus in polarized cells leading to different reactions when cut. The tension at the front triggers a nearly symmetric reaction whereas cutting at the back leads to an asymmetric reaction, a contraction and detachment of rear.

3.6.3 Mechanical probing under myosin inhibition

As we could not observe contraction-relaxation cycles when inhibiting myosin, we decided to probe if we could induce contractions in presence of the drug.
The experiments were conducted with 25 μM blebbistatin. Cell shape changed as in

previous experiments. So we assumed the drug was working. Ablating with inhibited myosin is more challenging than in control case. A cut that in control case results in the formation of a bleb that is easily recovered by the cell, could lead to cell death when myosin is inhibited. As myosin is not functional the cortex does not seem to be able to take back the bleb. As a result cells completely decompose. Therefore, ablation parameters have been tuned to cut only minimal holes. As we only want to see contraction we did not target polarized or non-polarized cells specifically, both were taken.

In Figure 3.69 i) an ablation time-lapse is described. The cutting spot is located at

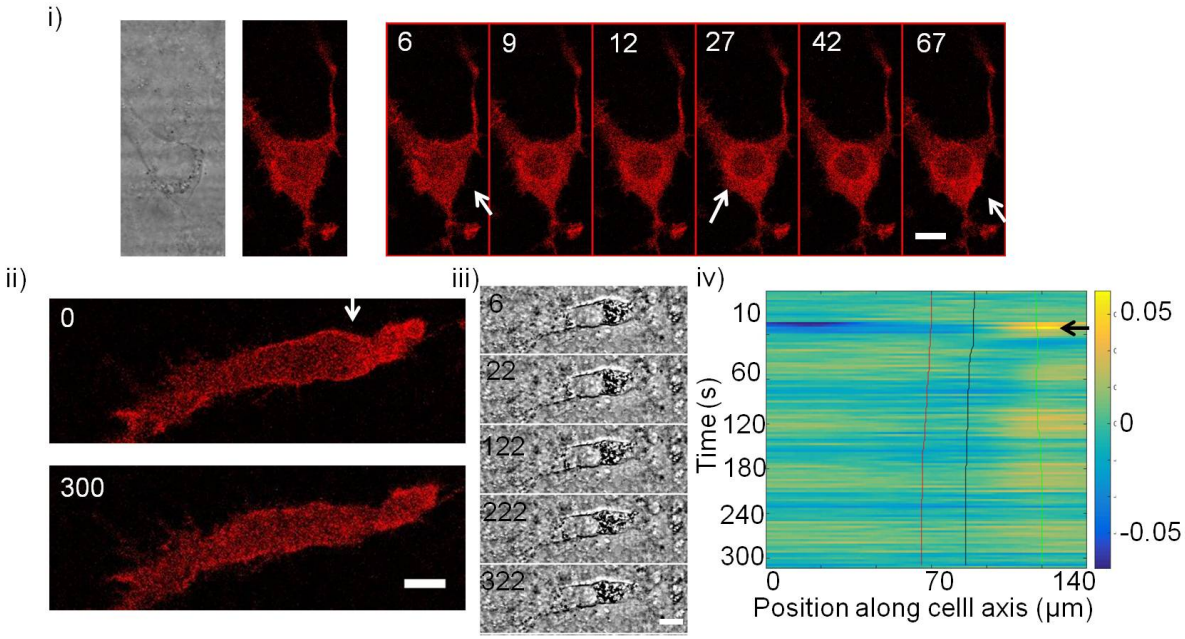

FIGURE 3.69: i) Ablation of myosin inhibited mCherry Lifeact expressing cells (25 μM blebbistatin). Time sequence of ablation. After cutting, actin rim appears around nucleus and actin signal increases in ablation spot. ii) First and last frame of ablated cell. iii) Timelapse of ablation. After cutting cell relaxes followed by nucleus movement forward. iv) Heatmap of mesh displacement (of iii)) shows relaxation (arrow). Scale bar 20 μm, time in sec.

the back of the cell indicated at 6 s. After ablation the actin rim around the nucleus still appears at 27 s. But neither major relaxation nor a contraction can be detected, although actin signal increases at the former ablation point, visible at time point 67 s. The membrane moves slightly backward after ablation. This movement is not deforming the mesh in a detectable manner. Eight out of ten cells (two biological repeats) showed this behaviour upon ablation. A second cell is shown in Figure 3.69 ii). The cut is set at the back of the nucleus. After ablation, an actin rim is observed around the nucleus. Surprisingly in this case the nucleus moves forward (Figure 3.69 iii)). The heatmap of mesh displacement (Figure 3.69 iv)) shows that only a relaxation takes place. The plot of nucleus front, back and cell rear position (red, blue and green lines respectively) indicate the movement of the nucleus. For this cell, a relaxation at the back of the cell leads to nucleus movement. Solely the nucleus is moving cell rear does not move forward even

rather backward. If a relaxation can occur it also means that tension has been built up before in the cell. It suggests that tension built up is possible also without myosin, but the timescale, potentially relying on actin and actin crosslinkers, might be different from the timescale of contraction mediated by myosin. Therefore, we are not able to induce a contraction by laser ablation when inhibiting myosin.

Overall when myosin is inhibited contractions or net movement cannot be triggered. This suggests that myosin is required for contraction and moreover for contraction-relaxation cycles. Motility when myosin is inhibited, may only rely on actin activity.

3.6.4 Induced motion

Having elucidated the importance of myosin in contractions, we wondered if we could reproduce not only one contraction but even two or three by laser ablation. Would we be able to control cell movement? As we identified two centers of contraction in migrating cells with a phase shift, we tried to reproduce cell motility by ablating front and back of cells in a sequential manner with a certain time shift.
We first tried to polarize non-polarized cells. Cortex next to anchoring points was targeted. In non-polarized cells, it is difficult to detach the protrusion by this method. Even various cuts could not detach the protrusion. On cells where this could be reached, the second ablation led to an overall cell contraction. Cells were rounding up and retrieving all protrusions. This was observed for various cells (five cells).

It was not possible to polarize cells with this method. The attachment of cells was hard to overcome and also cells had the tendency to completely contract. This means that contraction alone cannot generate polarity. As we could only trigger contraction and not relaxation we left the non-polarized cells and switched to already polarized cells.

This is shown in Figure 3.70, an already polarized cell is first ablated at the back, triggering a contraction of the rear then at the front of the nucleus, triggering a second contraction, and finally at the rear again, triggering a third contraction. The first ablation leads to release of the rear and a generation of a round edge. This results in a forward movement of the cell. Before the second ablation occurs, the nucleus starts to move slightly backward. This indicates that 10 min between ablation is too long for a net movement. The next ablation is set on the front of the nucleus. Relaxation can be observed after ablation, before contraction and onset of movement. In this case too, the nucleus starts moving backward again before the third ablation. The third ablation is set at the back of the cell. Thus cell continues moving. The contraction, the nucleus and cell movement are depicted in the heatmap of mesh displacement in Figure 3.70 ii). After every ablation movement can be observed (highlighted with arrows). Preceding the movement a small contraction is visible for the first two ablations. Cell moves to the right. The ablation and following motion can be visualized in Movie 19. At the first cut at 5s relaxation is visible. The double or triple ablation triggering motion could be performed on three different cells.
Here, the two or three ablations should mimic what happens in control case. Cells might have migrated in the predicted direction at some point, but we triggerd this motion. The

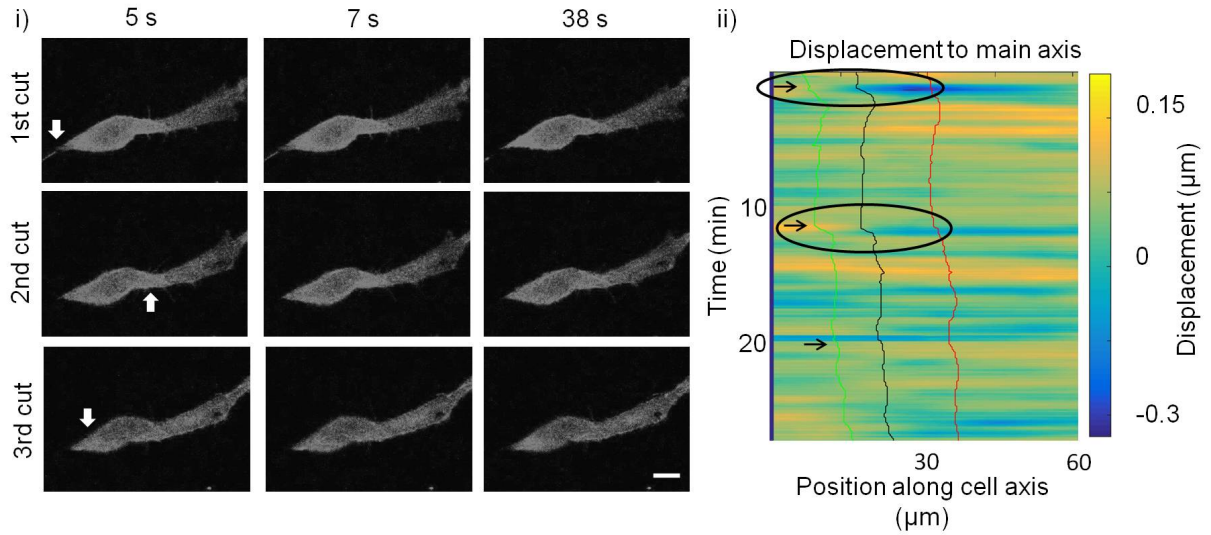

FIGURE 3.70: i) Triple laser ablation of a polarized mCherry Lifeact expressing cell. Ablation spots are indicated with white arrows. The first is located at the back of the cell next to the rear, then in front of the nucleus and the third again at the back of the nucleus. Time between ablations was 10 min. Scale bar 20 μm, time in sec. ii) Heatmap of deformation, red line indicates front black line back of nucleus and green line back of cell. Deformation calculated for time intervall of 30 s. Motion occurs after ablation. Movement after ablation is indicated with arrow and contraction highlighted with circle.

alternating contractions front and back of the cell seem to actually allow cell motion. This would confirm our hypothesis that cyclic front back contractions permit cells to migrate through a dense entangled network.

4 Discussion

The aim of this thesis was to study cell migration in a more physiological context, to ultimately understand the mechanism leading to cell motility in a 3D environment. To address this question, we developed fluorescently labeled CDMs that allowed us to monitor the forces exerted by cells while migrating by looking at displacement of FN matrix. Therefore, linking the force pattern to motility and cellular read-outs. These deformations showed intriguing spatio-temporal dynamics.

We first characterized the mechanical properties of the matrix by optical tweezers measurement. Interestingly, the CDM matrix is elastic (elastic modulus of 50 Pa), which means that we have access to calculation of the applied forces. It also means that no dissipation in plastic deformation occurs.

Different cell types were tested in terms of survival and migration behavior. All cell types used entered the CDM, instead of remaining on top of the matrix. Upon observation of cell migration, it was clear that cells indeed deform the matrix.

Such 3D deformation was different compared to deformation patterns associated to 2D cell migration. They were dynamic and cyclic. We identified two centers of contraction: one at the front and one at the back of the cell, contracting and relaxing in a defined time period of 13-14 min. These front and back contraction-relaxations had a time shift of 4 min. Motion was related to the back contraction and the front relaxation. This pulsatile behaviour seems to be related to cell confinement, since cell migration in microchannels with similar dimensions to CDM pore size led to contraction-relaxation cycles. Therefore, it is unlikely that chemical components trigger this cyclic process.

Acto-myosin was identified to drive contraction-relaxation cycles. Probing of different actors of the cytoskeleton showed that acto-myosin was necessary for contraction-relaxation cycles. Neither microtubules were needed, nor the nucleus, as cytoplasts persisted in oscillatory behaviour. Nevertheless microtubules are involved in maintaining polarity thus a persistent migration.
Different supramolecular structures such as stress fibers, gel and cortex were probed mechanically by laser ablation to access their role in cell migration in 3D CDM. Results suggest that cortex might generate contraction-relaxation cycles. We recapitulated cell motility by inducing local contractions. A migration could be achieved by sequentially ablating front and back.

In the following I will resume and discuss different aspects of the results such as CDM characteristics, cell migration in CDM, and the spatio-temporal deformation dynamics of the matrix. I will discuss how molecular actors cooperate to generate contraction-relaxation cycles. I will also suggest future lines of investigation and experiments.

4.1 Comparison of CDM with other extracellular scaffolds

We produced fluorescent CDMs adapting an established protocol [11] by adding fluorescently labeled fibronectin or having cell produce and secrete fluorescent fibronectin into the matrix. In the following we compare our CDM with other matrices (collagen [246], PEG hydrogels [247] and CDMs [217] [5] [221]) and analyze how the characteristics of our network might influence cell migration.

Dimensions of CDM. Pore size has been reported to be crucial for cell migration and survival [7] [191]. Synthetic extracellular scaffold pore size can be tuned by changing parameters of synthesis. Previous cell migration studies performed in collagen scaffolds reported x-z pore cross sections ranging from 5 μm^2 to 30 μm^2 [7]. Synthetic PEG hydrogel scaffolds can be produced with pore diameter of 0.025 μm [247]. We evaluated the dimension of pores by different methods. We obtained a range of pore areas from 100 nm^2 to 100 μm^2 with a clear majority of small pores. For CDM derived from lung fibroblasts a mean matrix fiber spacing of 2 μm has been reported [217]. We observed that the top layer of the CDM is denser than the space inside CDM (small pore sizes). The limit of pore size inside CDM is given by cell size as they secrete the proteins forming the CDM. The space occupied by cells remains fiber free upon removal of cells. This corresponds to the range of pore areas reported in the literature [217].

The CDM is a soft elastic matrix. As we established, cells systematically enter the CDM, therefore we used optical tweezers measurements to obtain elastic modulus inside the matrix. Beads were embedded inside the CDM to measure bulk properties. We obtained a Young's modulus of 50 Pa, that represents a soft material for a cell. Tissue elasticity spans from 100 Pa for brain tissue to 100 kPa for cartilage [248]. Results obtained by Tello *et al* for various CDMs measured by AFM yielded values in the kPa range [221]. Petrie *et al* [5] report values of 500 Pa measured by AFM, which is 10 times higher than what we obtained. Lung fibroblast derived matrices revealed values of around 100 Pa [217], also using AFM measurements. These results are systematically higher than the ones that we obtained. This could be due to the fact that AFM measures the top layer of CDM in the z direction, whereas optical tweezers explore the bulk properties in the x-y plane which corresponds to what cells see inside the CDM. Moreover, the discrepancy of Young's modulus found in literature can emerge from using different cell types [221] secreting different amount of proteins, or having different pore size.
We ruled out strain-stiffening behaviour of the matrix by using the laser at different power leading to a different spring constant of the trap. Neither strain stiffening nor dependence of the z position within the CDM was detected for elastic modulus. Meaning that our CDM was linear elastic within the explored range. Similar mechanical behavior of the CDM was reported by Soucy *et al* [217] and Petrie *et al* [5]. Soucy *et al* [217] compared the state of their CDM before and after cell passage and Petrie *et al* [5] established that their matrix is linear elastic by calculating the quotient of E_{mean} and E_{med} to be one. This means that they did not observe strain-stiffening in their matrices.

Synthetic extracellular matrices such as collagen matrices might not show the same elasticity [246] as CDMs. Cells have the possibility to form tracks in these matrices [249]

also related to metallo-proteinase activity, thus cleaving the matrix. We do not observe tracks or disappearance of mesh. The state of the CDM was compared before and after cell migration, as well as the path of the bead in the optical tweezers measurements. Therefore, the elasticity of our meshwork would allow us to derive the force from the deformation of the substrate, as the energy is not dissipated in plastic deformation.

Cellular deformation is required for cells evolving in CDM. Cells do not spread on the surface of the CDM. They systematically migrate inside (see Figure 3.16). Such behavior is intriguing, since they could, in principle, spread and migrate on top of the CDM. We hypothesize that focal adhesion distribution of cells inside the CDM is favorable compared to focal adhesion distribution of cells on top of the CDM, like a tension homeostasis [250]. The CDM as stated above is a soft material and cells spread to less extend on soft compared to rigid surfaces [251]. We hypothesize that then the balance of stable focal adhesions drives the cell to enter the CDM. For the other side of elasticity range, in cases where cells can (accidentally) sense and have access to the glass surface they spread on it (Figure 3.16 iv)). This behaviour can be explained by the fact that glass is more rigid than CDM, therefore cells can sustain stronger focal adhesions and perform durotaxis [29].
To enter and subsequently to migrate in the CDM cells need to deform, it is mostly visible when nucleus is deformed during the process. In this deformation, the morphology of an hourglass shape as described in [7] is observed. The degree of deformation might depend on the mesh size encountered by cells; even reaching a prolapsed shape, where a small portion of the nucleus engages in the pore when cells are blocked. Such deformation process is known as squeezing [7]. Its dynamics is quite interesting, with a speed peak during unsqueezing. This speed behaviour associated to nucleus deformation is similar to the one shown for cells migrating between microfabricated pillars [252] with a limit "pore" size of 2 μm. It also suggests that nucleus is being pushed by back of the cell as in [253]. Since the nucleus is blocked contractility increases at the back, therefore pushing the nucleus. Also, a significant increase of the blebbing activity at the back of the cell while squeezing indicates local high pressure [254], which might be due to a higher contractility. The global blebbing observed in blocked cells also points to an increase in contractility. We hypothesize that cells encountered a pore that is too small to pass through, therefore squeezing might be considered as the limit of cell migration in CDM. Above this limit the cell is stuck and no migration takes place. Overall, the CDM is a complex system with various geometrical cues. This might explain the lower persistence length and speed in CDM compared to the ones observed in 2D- or channel migration. Fiber entanglement as a depolarizing cue could limit persistent migration.

4.2 Deformation is applied in a specific pattern

We observed contraction-relaxation cycles for cells migrating in 3D CDM. These cycles showed centers at front and back of cells. This pattern is distinct from 2D cell migration and has to our knowledge not been reported so far. In the following we compare our

observed phenomenon to other oscillatory behaviour reported for cells. We also discuss the role of cyclic deformation for cell motility and the role of confinement.

Deformation is applied in a specific pattern. For a 2D surface, traction force microscopy has revealed, that cells deform the substrate in centripetal way pulling at the front with high deformation observed in the lamellipodia area and the back [163]. This allows to model the cell and its elastic interaction as a force dipole [175]. Active mechanosensing can be modeled as anisotropic force contraction dipole [176]. Our experiments of cells migrating in CDMs show that mesh displacement occurs in cycles, at the front and at the back of the cell. These displacements converge to one point at the front and one point at the back of the cell. Therefore, two centers of contraction can be identified, although it can be sometimes challenging. Recently multipole analysis of traction stress applied by *Dictyostelium* on 2D deformable substrate described cells with dipole and quadrupole moments thus reflecting front rear and rotational asymmetries [16]. Moreover, it allows to correlate traction stress and directionality of migration. A force modulation of the pole force has as well been reported for *Dictyostelium* [255]. Another study of migrating neurons on 2D gel showed that three contraction centers could be identified [178]. The description of cells with various contraction centers relates to our centers of contraction. In our case two contraction centers have been identified. However, the cyclic behavior was not explicitly studied in these cases. We extracted periods for front and back contraction to be 14 min and 13 min respectively by autocorrelation analysis, and the relation of contraction-relaxations by cross-correlation analysis revealed a phase shift of 4 min. Leoni *et al* [256] proposed to model a cell with two dipoles contracting in cycles with a phase shift. Their study reported speed fluctuations and propose the adaptation of oscillation to mechanical properties of the environment. The readout of this theoretical description of a migrating cell matches what we observe in our experiments. Such multipole analysis should allow us to derive a physical description for these contraction centers and is included in future plans.

Oscillatory behaviour of cells. Other oscillatory phenomenons have been reported for cells in different configurations. Non-adhering fibroblasts have been reported to oscillate in shape with a frequency of 37 s [238]. The oscillations depend on myosin activity and extracellular calcium concentration [238], which were proposed to work in cooperative manner. Contraction on one side of the cortex leads to a Ca^{2+} influx on the opposite side followed by a contraction. In another study L929 cells in suspension showed an oscillatory constricting ring leading to shape oscillation [96]. It oscillated from on side of the cell to the other with a semi-period of 4.7 min [96]. Although this timescale is closer to our range of periods of contraction the cell environment of our system, the CDM, and a cell in suspension might not be analogous and no information about forces is available. We could argue that apical basal polarity that cells have on 2D surfaces, could be abolished in 3D [4] like in suspension [96]. But it is not clear though if the observed phenomena are enabled by the suppression of this forced polarity. However, the actor of both might still be the same: the cortex.
In 3D environment, oscillations have been observed for zyxin depleted tumor cells in collagen matrix. In contrast to 2D, these oscillations only take place in 1D and 3D. Cells

migrated forward and backward with an amplitude of 150 μm and with a period of approximate 160 min. This is an oscillation phenomenon linked to 3D environment and influencing cell migration. Nevertheless the time period is much higher than what we observe and also the amplitude of displacement of cells is larger than what we measured for 3T3 NIH in CDMs. Another oscillatory behavior has been reported on a simplified 3D to 1D system: cells migrating along a FN coated suspended fiber [195]. On this configuration, cyclic fin-like protrusive waves extending lateral to the cell body have been observed. The protrusion originates at the cell body and travels as a wave to the front. The authors suggest that this oscillatory protrusions are a mechanism to extend the leading edge [195]. This fin-like structure might emerge at the pulling side of the cell, thus be linked to force application. A cyclic force might be associated to cyclic protrusions. This might then be another cyclic phenomenon related to cell migration and force generation in a simplified 3D (1D) environment.
At a smaller length scale, force oscillation applied by focal adhesions of cells platted on pillars has been observed by Galbraith *et al* [164]. Pillars have been reported to bend in an oscillatory manner. Moreover, force fluctuation within focal contacts have been reported [156]. Focal contacts apply either a stable or a fluctuating force. This force is closely linked to stiffness sensing and guiding of cell migration. Also at the focal adhesion scale, local contractions on PDMS pillars have been observed [257]. Another study reports cyclic behavior in podosomes [258], an acto-myosin-based structure in dendritic cells. These oscillations are related to actin network integrity and myosin mediated contractility. Such subcellular oscillations might lead to a larger scale cyclic behaviour when integrated over the whole cell. Various oscillatory phenomena have been reported for cells. A common actor might be acto-myosin cytoskeleton.

Movement connected to contraction pattern: comparing 3D migration modes. Neurons moving in two dimensions translocate the soma by applying up to three contractions with different centers. The direction is set by the higher strain energy in pulling direction [178]. In this case, the movement is the result of a pulling, not pushing, force. Multipole analysis performed on *Dictyostelium* migration in 2D shows that dipole axis sets the axis of migration and quadrupoles the direction along this axis. The movement of the cell correlates with the disappearance of force spots at the back of the cell, probably related to unbinding and retraction of the rear [16]. In 2D, back contractility pushes the cell, but it is also responsible to detach focal adhesions [23]. After identification of the contraction-relaxation cycles we related them to the movement of the cell. A contraction at the back (1) precedes the movement of the cell (2) (that we track by using the back of the nucleus as reference). Following the movement of cell, a relaxation can be observed at the front of the cell (3). This 3-step process is accompanied by a variation in cell speed. Suggesting that the cell rear pushes the nucleus forward. This is in agreement with leukocytes moving in 3D collagen matrices, they were reported to migrate by an integrin-independent manner by flowing and squeezing. In this case, it is the rear that pushes the nucleus through small pores via myosin II contractility [185]. Nevertheless, we do observe focal adhesions in our CDMs. A study of 3D migration in collagen gels [184]

reported that phases of cell elongation, migration and persistence were correlated. Fast moving passages were seen in combination with elongated cells and high forces [184]. For *Dictyostelium* cell length varies in a periodical manner while migrating. The shorter the period the higher the observed speed [255]. We obtained a similar dependency for plotting persistent speed in function of the period of speed oscillation. Higher periods yielded faster cells.
However, the mechanism proposed for lobopodia-based migration in CDM is pressure driven: a high pressure region at the front of the nucleus and a low pressure region at the back. Thus, the nucleus is compartmentalizing the cell; it acts as a piston. This pressure driven mechanism relies on myosin II activity on one hand, and the nesprin anchorage to the front of the cell on the other hand. Cell movement is achieved by a pulling mechanism through vimentin-nesprin connection to the nucleus. In this case, the nucleus movement is de-correlated from cell back movement [6]. We do not observe this behavior in our cells. Such discrepancy could come from the fact that we do not have a "typical" lobopodia morphology either: blebbing is observed sporadically, but not locally at the front of the cell which would indicate a higher pressure at the front of the nucleus. As a consequence we are not likely to have the same piston driven migration mechanism. Moreover, we are observing effects on migration when depolymerizing microtubules which is not the case for Petrie *et al* [6]. Differences can be a consequence of the stiffness or the relation of pore to cell size in our CDM, which might be different from the one used in [5]. However, we do not exclude local pressure difference front back in our cells, or contractility gradients in cell cortex as suggested in [239] and [259].

The role of confinement. We hypothesized that pulsatile behavior in CDM is not linked to chemical composition of CDM but due to 3D confining environment. Therefore, we used microchannels to confine cells and studied their migration. We observed further pulsatile behavior for migration in microchannels. The importance and effect of confinement has been already described in various work. How motility would emerge in such scenario has been answered for dendritic cells in microchannels. Hawkins *et al* [190] proposed a model, where no specific adhesion sites are necessary. Unspecific friction is sufficient for a polymerizing cytoskeletal gel to induce motion in microchannels. Liu *et al* [188] established that high confinement and low adhesion triggered fast amoeboid migration. In their case, cells were put in between plates and compressed. Some cells showed a very peculiar morphology with a trailing uropod. The switch to this migration mode required a higher contractility and was connected to acto-myosin flow in the cortex. In Bergert *et al* [179] adhesion-free migration in channels was as well observed with acto-myosin retrograde flow. In this case the force distribution was computed and revealed an extensile force for adhesion-free migration under confinement. As we have migration in presence of focal adhesion in CDMs, we are not in adhesion free mode and we do not inhibit focal adhesion nor adhesion (by covering channel walls with chemical repellents, for example). Even more, our deformation patterns are contractile and not extensile, thus also pointing to an adhesion based migration. We do not observe typical retrograde acto-myosin flow reported for adhesion-free high contractility migration [179] [179] [202]. We deduce that our migration mode is distinct.

Contractility still plays a role for adhesion dependent migration in microchannels. Hung *et al* [199] showed that migration speed depends on channel width and confinement. Migration was strongly affected upon myosin inhibition. In another study conducted by Lautscham *et al* [242] the combination of adhesiveness, nuclear volume, contractility and cell stiffness has been tested for migration in straight channels with segments of different widths. The movement in this channels might be generated by ratchetaxis [31] [8]. It resulted that overcoming steric hindrance results as a combination of these previously named parameters, with cell migration impeded when adhesion is low. Interestingly the overcoming of narrower parts results in a velocity oscillation similar to the one that we observe in CDMs. This might be due to a squeezing phenomenon. It might also enhance the pulsatile behaviour we observe in our channels.

4.3 Molecular and supramolecular basis of contraction-relaxation cycle: acto-myosin based process

We report a link between acto-myosin activity and contraction-relaxation cycles. Disrupting actin cytoskeleton led to impeded motion and force decrease, whereas acting on actin nucleators only reduced migration with lower persistent speed and shorter trajectories and increased the period of speed oscillations. We showed that myosin is required for contraction-relaxation cycles; otherwise motility is lowered represented by a lower persistent speed and shorter trajectories. In cases where speed oscillation was still occurring, a higher period in combination with a lower persistent speed could be observed. And microtubules are key actors for maintaining polarity, thus enabling persistent migration. Probing the mechanical integrity of the cell revealed that cortex is more likely generating contraction-relaxation cycles than actin gel. In the following we will discuss the implication of molecular and supramolecular entities in the cyclic behavior.

Lowering contractility via the Rho pathway. The effect of inhibiting Rho by Y27632 was minimal. It had no effects on migration capacities of cells. This result is in agreement with previous results by Petrie *et al* in terms of speed [5]. This might be explained by a sufficient contractility recovery of the cells due to confinement and therefore cell migration is not affected. When Rho is inhibited, contraction-relaxation cycles are still observed. Regarding the decrease in stress fibers contractility, which is mainly controlled by Rho [260], we observed no effect for cells in CDM (few stress fibers are present even when Rho is active). Motility was not affected by the drug, suggesting that migration in 3D CDM might not require stress fiber traction. We observed a significant decrease of the force relative to the control case (around 40%); however, this loss of relative force did not disturb motility. Similar results have been reported for 2D traction microscopy [261].

Microtubules are necessary for persistent migration but do not generate contraction-relaxation cycles. Microtubules have a dynamic behavior: they can grow and shrink [19] and as a result also apply forces [262]. We disrupted microtubules by treatment with

Nocodazole. Upon depolymerization, we still observed cell motion and cyclic deformation of the meshwork. However, cells did not migrate, no net displacement could be detected. Their motion turned around the center of mass of the cells. This behaviour of cells treated with Nocodazole has been reported for cells spreading on 2D surfaces [263]. Oscillations were observed mainly in the cell body, not in flat peripheral parts. It could be linked to increased acto-myosin contractility. Actually, microtubules can influence specific sites of cortex and their stability be can be influenced by cortex [264]. These experiments suggest that contraction-relaxation cycles are not based on microtubule dynamics. Moreover, it points to cortex contractility as a key actor for generating contraction-relaxation cycles. We report a decrease in relative force. However, an increase in absolute force has been reported for NIH fibroblasts in [265]. Nocodazole treatment might affect cells in the same way as Calyculin A, increasing contractility. This increase in contractility might prevent formation of anchoring points necessary for migration. Microtubules seem to be involved in tail retraction in 2D, in this case depolarization leads to gluing the cell to the surface [266] [267]. This was not our case, as cells were able to oscillate thus detach from the matrix showing that respective rear was not anchored to CDM at that moment. The absence of migration when disrupting microtubules might not have the same mechanism in 2D and 3D. Oscillations might be an intrinsic phenomenon to the cell, as it was still observed in cell fragments able to move on the spot, performing a forward-backward movement. Thus, the nucleus does not seem to be required. This has also been reported for cell fragments in suspension [96]. Cytoplasts serve as a simplified system for studying migration or related events such as cell polarization [268]. The presence of contraction-relaxation cycles without microtubule cytoskeleton or even without nucleus allows us to propose that these elements are not required for the cycles, and points to an acto-myosin driven mechanism.

Functional cytoskeleton is necessary for generation of cyclic behaviour. Actin cytoskeleton was disrupted by latrunculin A. The effect was immediate: motility came to an arrest, cells rounded up and had thin protrusions. It is not surprising that dismantling the inner cell scaffold stalls migration. Myosin does not have the actin filaments as binding partner anymore, and can not perform power stroke, so no pulling can occur. This shows that the actin cytoskeleton is needed for migration in general.

Cortex is able to generate contraction after ablation. Laser ablation allows us to probe cell tension and structure, and to investigate further contraction-relaxation cycles. This method of mechanical probing has been used in various organisms such as *C. elegans* [269], *Xenopus* [243] or *Zebrafish* [244]. Contraction can be induced upon laser ablation of cell structures as shown in [93]. Ablation yielded to various results depending on (i) the polarization state of ablated cell, (ii) the cellular structures ablated, and (iii) the location of the ablated structure within the cell (front-back, for example). We assume that relaxation indicates that the cellular structure is under tension; and that the stronger the relaxation, the higher the initial tension (assuming a constant cutting point). Surprisingly, besides initial relaxation, we could measure a subsequent contraction at the ablated spot for some subcellular structures. We tested the response of stress fibers to ablation. As reported for 2D soft substrates [76], cell relaxes and stress fibers move apart.

This indicates that fibers are under tension at the cutting location. Mechanical probing of stress fibers does not generate further contraction, neither locally nor of the whole cell. As we cut the whole stress fiber, partial cutting might yield different results. However, no contraction has been reported neither for this configuration in 2D experiments [76]. Moreover, ablation of actomyosin cable in *Drosophila* showed relaxation of cortex but no subsequent contraction [270].
Cutting in cortex of cells resulted in an initial relaxation, followed by an actin flow and finally a contraction. Such an effect of ablation was dependent on position of the cut and on the polarization state of the cell. In polarized cells, cutting in the cortex at the front resulted in a symmetric contraction, whereas cutting at the back led to the detachment of the back of the cell and a contraction. This suggests that tension may not be evenly distributed in the cortex. A contraction at the front may not provoke a net displacement if focal adhesions are not remodeled. Focal adhesions at the back of the cell might have a weaker connection to CDM [27], thus a contraction could easily detach them and a net movement be observed. On the contrary, ablation in non-polarized cells led to a symmetric contraction independently to the position of the cut. This could be explained by a symmetric tension in non-polarized cell. Moreover, since it is anchored at both sides with its protrusions and the cell does not move, tension between these two points should be constant. Cell contours can be described by circular arcs and line tension be extracted [166].
Acto-myosin flow has been reported after ablation for *C. elegans* zygote after cut of 6 μm line [93]. Acto-myosin from the cytoplasm and ring closure has been observed for this organism. For *Xenopus* oocytes an acto-myosin ring formation has been observed for wound closure [243]. The ring closure includes cortical flow recruiting F-actin to wound and also *de novo* actin polymerization. As we perform point ablation our cut is much smaller than 20μm in diameter, the closing is *de facto* instantly so that we exclude *de novo* synthesis. Otherwise the actin signal is similar to the one reported in [243]. In our case actin flow seems not limited to cortex but also occurs in the cytosol.
We observe an actin rim forming around nucleus when ablating, classically this is a sign of cell death [245], we rather take it as a sign of mechanical probing of the cell. Actin rim formation around nucleus has been reported for MCF7 adenocarcinoma cells upon exposure to taxol [271] pointing to an association of microtubule and actin cytoskeleton. We hypothesize that it is linked to mechanotransduction to the nucleus [272]. This has been reported for mechanical probing of cell periphery with beads. A nuclear actin rim depending on formind-dependent actin assembly could be observed after mechanical stimulation [273]. The nucleus rounding up can be interpreted both ways. Either it is constricted due to the actin rim or what we observe is a release of tension. It might also be the case that actin contributes to recover initial morphology after a tension release. This has been observed in 2D cytosol ablation where nucleus was rounding up after ablation. The nucleus was assumed to have a prestress in this configuration which was then released [274].
Interestingly, cells do not react in the same manner to cutting on stiff and soft substrates [76], on an oocyte with a shell such as *C. elegans* [93] and in our 3D elastic environment. Therefore, besides the dependency on the size and position of the cut, mechanical properties of the environment might also play a role in the response of the cell.

For instance ablating whole cells in cell monolayers lead to the formation of a constricting ring and wound closure can be observed [275]. However, no contractile forces similar to what is observed in ablating cortex, was reported in this case. Also the timescale is different for ring closure [275]. To our knowledge, an ablation followed by a contraction has only been observed for single cells embedded in an elastic environment such as oocytes in an eggshell [243]. Although laser ablation of cortex was used to generate blebbing for cells on 2D, no associated contraction was reported [86]. It might be possible that the elastic environment could help the cell generate the contraction after cutting, as it provides it with a scaffold.

Gel is not able to generate a contraction after ablation. Ablation in actin gel did not provoke the same reaction as cutting in cortex. Although it led to an increase of actin intensity, and the formation of an actin rim around nucleus could be observed as well; no further response was seen. Since myosin could not be observed in this gel, the absence of reaction could be explained in terms of its composition: in absence of myosin, it would not be contractile, it could be pushing but it would not induce contraction. Still, there seems to be a connection between cortex and gel as ablation in gel can be followed by contraction in cortex in already polarized cells. Such connections have been shown in [276].

Myosin generates contraction-relaxation cycles. Myosin is the molecular motor providing contractility for various cytoskeletal structures such as stress fiber or cortex [19] and it is the main force generator [261]. Surprisingly, cells are still able to migrate under myosin inhibitory conditions. Several studies have shown that actin can exert pushing forces, such as beads displacement [228]. Moreover, we have seen growth of focal contacts in the absence of myosin. This might explain the observed movement in terms of an actin pushing force. Indeed, cells show higher actin intensity at the back when migrating in presence of blebbistatin. Intriguingly nucleus deformation still occurs. This could be explained by the link of contractility state of cells and nucleus deformability [277]. The nucleus might be softer in presence of blebbistatin, as lamin A levels connected to nucleus stiffness might be decreased [278] [279].
No contraction-relaxation cycles could be detected in the presence of the drug, which does not exclude that they cannot be externally triggered. Therefore, we laser ablated the cortex in the presence of blebbistatin. The ablation was not followed by a contraction. Blebs were appearing but the cell could not shrink them back, contrary to functional myosin [100]. We state that myosin is necessary for contraction and by this also necessary for contraction-relaxation cycles.

Cycles depend on acto-myosin dynamics. Acto-myosin structures were further probed by acting on Arp2/3, introducing a synthetic polyamine C8, inhibiting the MLCK with ML-7 and increasing contractility via Calyculin A. The motility, the appearance of contraction-relaxation cycles and the period of speed oscillation were investigated.
We probed Arp2/3 complex which was lowering motility of cells. In 2D Arp2/3 is required for lamellipodia extension and thus directional migration [280]. There is some data suggesting that Arp2/3 is linked to cortical actin structures via cortactin [281]. It has also

been reported to be one of the main actin nucleators together with mDia1 in cortex [282]. We also expected it would localize in the actin gel visible around the nucleus. There is some evidence that actin gel around nucleus leads to oscillation of the nucleus during migration of progenitor cells nuclei during interkinetic nuclear migration (IKNM) [283]. As we do not observe typical lamellipodia growth Arp2/3 inhibition should not affect the cell as much as in 2D [248, 284]. Eventually changing actin dynamics in the cortex or the gel leads to a diminished cell motility as reported for HL60 neutrophil-like cells in microchannels [285]. *In vitro* studies have shown that lowering actin nucleation rate yielded to networks with larger mesh sizes and thicker bundles [286]. This might also play a role when inhibiting Arp2/3 and decrease cell motility.
C8 is a synthetic polyamine and promotes lamellipodia growth [10]. It also promotes bundling of actin. Persistent speed is lower and trajectories are shorter thus migration is lowered in presence of this drug. This might be explained by lamellipoda growth itself. As suggested in [287] the cell might not have enough space to grow a flat sheet, and it might even slow it down as it might increase friction to the environment. It can also be explained by lower treadmilling induced by the drug [10]. Perturbing actin dynamics led to diminished motility and longer periods of speed cycles.
Myosin was also challenged by inhibiting the myosin light chain kinase (MLCK) with ML-7. The differential force was dropping similar to blebbistatin case, but the phenotype was less severe and motion less affected. Cycles in speed could still be observed. MLCK might mainly act in the periphery of the cell [260], which could explain the lower effect observed in this experimental configuration compared to blebbistatin. MLCK might rather control peripheral stress fiber system, which might not be fully developed in our 3D CDM [288].
As contractility has been reported to be crucial in 3D confined space, we tried to increase contractility using calyculin A treatment. We expected periods to decrease for higher contractility. The effect was immediate: the disruption of anchoring points could be observed and the following contraction on this side of the cell until the cell was round and started blebbing. It has been reported that cells treated with calyculin A had lower adhesion strength (on 2D surfaces) [289]. To our surprise, no motility could be observed. At least for 3D CDM, the relation of low adhesion and high contractility as suggested in [198] does not lead to cell migration. It also confirms that being inside the CDM requires anchorage, as cells are slipping out of the CDM for long incubation times of the drug. No blebbing mode as suggested in [239] could be observed. It might also be the case that a higher contractility leads to a stiffer cell [290] thus less deformable, and that this might play a role in impeding the motion [291]. It has been reported for *Dictyostelium* that silencing myosin II light or heavy chain affected length oscillation of the cell. The period of oscillation was increased and speed was lower [255]. Changing dynamics or functionality of acto-myosin shifted cyclic behaviour of speed cycles (see Figure 3.53 i)). Cells in presence of drug had a higher period of speed oscillation corresponding to a lower persistent speed. Therefore, motion is lowered in presence of the drugs. The result suggests that lower period lead to a higher persistent speed thus a more efficient migration. Acto-myosin can form various supramolecular structures, which could account for contraction-relaxation cycles.

4.4 Reproduce motility by induction of contraction-relaxation

As a main result, we detected contraction-relaxation cycles in cells migrating in CDM. Moreover, we observed that contractions at specific spots could be induced by laser-ablating the cell cortex. Therefore, we wondered if we could reproduce migration by correctly choosing the ablation spot and the time between ablation points.
We tried first with non-polarized cells. As the generated contraction was not sufficient to detach protrusions, we deduced that focal adhesion in these protrusions are stronger; or the tension symmetric, so that no net movement could be observed. In cases were detachment was obtained, cell movement was induced at first. However, the second ablation led to a complete contraction of the cell body, leaving a condensed roundish cell and no further net movement was obtained. It seems that tension distribution in non-polarized cells is different than in already polarized cells. Probably, to polarize cells by laser ablation, something more than inducing contraction might be required. As we cannot trigger protrusion growth by ablation, we reach the limit of this method for non-polarized cells.
In already polarized cells, we obtained motility when ablating at the back of the cell. The challenge was to induce a second ablation able to trigger a second contraction. Ablating just at the front of the nucleus also triggers forward movement, so this is where the second ablation spot is chosen. It is possible to generate migration by reproducing contractions at different spots of the cell. One might argue that the definition of front or back is arbitrary and that the second cut is not close enough to the front of the cell. To tackle this issue, we assume that the nucleus is the bulkiest organelle of the cell [292] and thus we consider it a good reference to make the difference between front and back of the cell. It has also been reported to compartmentalize the cell [6]. Moreover, the position of the nucleus in a migrating cell is systematically biased towards the back. The experiments where squeezing is observed and where squeezing is induced via ablation and contraction at the back highlight this relation of decoupling of front and back. We do not know how force generation and protrusions generation are linked, therefore we cannot account that contractions are sufficient to sustain long-term motion. No protrusion activity enhancing or *de novo* formation has been observed upon ablation. Therefore, the limit of inducing motion might be obtained when the front protrusion has been reached. The multiple ablation mimicking natural contraction-relaxation cycles is able to recover cell migration, thus two contraction centers allow the cell to migrate in 3D CDM.

4.5 Physiological relevance of the oscillatory phenomenon- is it an advantage to oscillate?

Oscillatory patterns have been observed during development. For example during dorsal closure in *Drosphila* embryos, pulsed forces drive directed tissue movement [293]. Also in *Drosophila* during gastrulation apical constriction occurs in a pulsed manner allowing the formation of ventral furrow [294]. Oscillations are reminiscent of contraction-relaxation

cycles based on spontaneous acto-myosin activity such as in sarcomeres [295]. We wondered if cyclic contractions are an intrinsic property of the acto-myosin cytoskeleton and if additionally there was a physiologic relevance for migrating in this manner. Is it necessary to apply cycles of contraction and is there an advantage in applying cyclic deformations to the surrounding?
We propose that applying deformation in cycles allows the cell to migrate more efficiently in confined space. As stopping the cycles by inhibiting myosin or shifting cycles by perturbing acto-myosin dynamics yielded lower cell motility. We followed this reasoning and propose that cycles of contraction allow cells to enlarge pores in the CDM. It also guarantees them that pore stay open during passage of the cell. One contraction would account for pore opening and the second one for pushing the cell body though. This would also mean that cell with only one contracting center would not be able to pass. It might be the case that relaxation is needed to pass through the pore as blocked cells only showed contraction. We speculate that pore opening and passage cannot occur at the same time. Probably, subsequent displacement of mesh is energetically more beneficial for the cell compared to maintaining tension. Applying cycles might also be an effect of the elasticity of the CDM. The FN is moving back when force disappears, not as in collagen matrices where cells are able to form tracks [246]. Eventually, a constant dynamic deformation of the mesh is required to create new adequate pores for passing through holes once the previous one has been overcome. Another possibility might be that the elastic modulus of the CDM and the cytoskeleton are coupled. The possibility of exciting cytoskeleton-membrane waves has been investigated in the past [296].

4.6 Conclusion and Outlook

We identified key factors for analyzing deformation applied by cells such as the binding location fibronectin (i), the binding partner the focal adhesion (ii), the elasticity of the mesh (iii) and acto-myosin (iv) as a force generating actor. We succeeded to visualize all these components connected to our study and extracted deformation patterns. We present that cells apply contraction-relaxation cycles with contraction centers front and back of the cell in 3D elastic CDMs. Cycles of contraction have a period for the front of 14 min and a period for the back contraction center of 13 min. A phase shift between contraction-relaxations of 4 min is revealed, presumably allowing the cell to move forward. Contraction-relaxation has been related to cell motility and we suggest that nucleus is being pushed by contraction at the back. Acto-myosin has been identified as the driving component for these cycles and microtubules as necessary for maintaining polarity. Via laser ablation we could determine that the cortex is the main candidate rather than the actin gel, to be the supramolecular structure generating these contractions. For future experiments different lines can be considered, including (i) analyzing deeper the molecular origin of contraction-relaxation cycles, (ii) confirm that other cell types apply the same dynamics or (iii) rendering the setup more physiologic to include cell interactions in the observations. In the future, correlation between contraction centers and acto-myosin accumulation should be addressed to understand the molecular process more in detail and to find the origin of these hypothetical accumulations. We propose to use super-

resolution microscopy for this purpose. For testing various cell lines we think of using epithelial cells, which are not supposed to be motile and to see if they show the same contraction-relaxation cycles. A possible influence of the cell size on the cycles might be understood. The same accounts for cancer cells. It would be interesting to know if they show the same deformation pattern as common cells or if one could identify them already by their deformation pattern. The setup could mimic *in vivo* to a larger extend by including epithelial cells when observing single cell migration as tissues and extracellular matrix are coexisting in organisms.

Bibliography

[1] BÉNAZÉRAF, B. et al., Nature **466** (2010) 248.

[2] ROW, R. H. et al., Developmental Biology **354** (2011) 102.

[3] FRIEDL, P. et al., Nature Cell Biology **14** (2012) 777.

[4] BAKER, B. M. et al., Journal of Cell Science **125** (2012) 3015.

[5] PETRIE, R. J. et al., The Journal of Cell Biology **197** (2012) 439.

[6] PETRIE, R. J. et al., Science **345** (2014) 1062.

[7] WOLF, K. et al., The Journal of Cell Biology **201** (2013) 1069.

[8] COMELLES, J. et al., Biophysical Journal **107** (2014) 1513.

[9] MARBACH, S. et al., European Physical Journal E **38** (2015) 1.

[10] NEDEVA, I. et al., Nature Communications **4** (2013) 2165.

[11] CASTELLÓ-CROS, R. et al., Methods in Molecular Biology (Clifton, N.J.) **522** (2009) 275.

[12] MÜLLER, A. et al., Nature **410** (2001) 50.

[13] KRAWCZYK, W. S., The Journal of Cell Biology **49** (1971) 247.

[14] FRIEDL, P. et al., Nature Immunology **9** (2008) 960.

[15] WEBER, M. et al., Science **339** (2013) 328.

[16] TANIMOTO, H. et al., Biophysical Journal **106** (2014) 16.

[17] RIDLEY, A. J. et al., Science **302** (2003) 1704.

[18] DICKINSON, R. B. et al., J. Math. Biol. **31** (1993) 563.

[19] ALBERTS, B. et al., *Molecular Biology of the Cell*, Garland, 4th edition, 2002.

[20] BINAMÉ, F. et al., Molecular BioSystems **6** (2010) 648.

[21] ANANTHAKRISHNAN, R. et al., International Journal of Biological Sciences **3** (2007) 303.

[22] ETIENNE-MANNEVILLE, S. et al., Nature **420** (2002) 629.

[23] LAUFFENBURGER, D. A. et al., Cell **84** (1996) 359.

[24] De Rooij, J. et al., Journal of Cell Biology **171** (2005) 153.

[25] PALECEK, S. P. S. et al., Nature **388** (1997) 537.

[26] FRANCO, S. J. et al., Journal of Cell Science **118** (2005) 3829.

[27] WEBB, D. J. et al., Nature Cell Biology **4** (2002) E97.

[28] ZIGMOND, S. H. et al., The Journal of Experimental Medicine **137** (1973) 387.

[29] LO, C. M. et al., Biophysical Journal **79** (2000) 144.

[30] AZNAVOORIAN, S. et al., Journal of Cell Biology **110** (1990) 1427.

[31] CABALLERO, D. et al., Biophysical Journal **107** (2014) 34.

[32] KRUSE, K. et al., *Spontaneous Mechanical Oscillations. Implications for Developing Organisms*, volume 95, Elsevier Inc., 1 edition, 2011.

[33] WHANGBO, J. et al., Molecular Cell **4** (1999) 851.

[34] REICHMAN-FRIED, M. et al., Genes and Development **8** (1994) 428.

[35] FAURE-ANDRE, G. et al., Science **322** (2008) 1705.

[36] SNAPPER, S. B. et al., Journal of Leukocyte Biology **77** (2005) 993.

[37] ENTERLINE, H. T. et al., Cancer **3** (1950) 1033.

[38] TESTER, A. M. et al., Clinical and Experimental Metastasis **18** (2000) 553.

[39] STERNLICHT, M. D. et al., Cell **98** (1999) 137.

[40] ALLARD, W. J. et al., Clinical Cancer Research **10** (2005) 6897.

[41] CONDEELIS, J. et al., Nature Reviews. Cancer **3** (2003) 921.

[42] YAMAGUCHI, H. et al., Current Opinion in Cell Biology **17** (2005) 559.

[43] HOWARD, J., *Mechanics of Motor Proteins and the Cytoskeleton*, Sinauer Associates, Inc., 1st edition, 2001.

[44] BARTOLINI, F. et al., Journal of Cell Biology **181** (2008) 523.

[45] ZIGMOND, S. H. et al., Current Biology **13** (2003) 1820.

[46] HIGASHIDA, C. et al., Nature Cell Biology **15** (2013) 395.

[47] ROHATGI, R. et al., Cell **97** (1999) 221.

[48] WACHSSTOCK, D. H. et al., Biophysical Journal **65** (1993) 205.

[49] SPUDICH, J. A., Nature Medicine **18** (2012) 1478.

[50] MURPHY, C. T. et al., Nature Cell Biology **3** (2001) 311.

[51] ABERCROMBIE, M. et al., Experimental cell research **60** (1970) 437.

[52] ABERCROMBIE, M. et al., Experimental cell research **62** (1970) 389.

[53] ABERCROMBIE, M., Proceedings of the Royal Society of London. Series B, Biological Sciences **207** (1980) 129.

[54] VERKHOVSKY, A. B. et al., Current Biology **9** (1999) 11.

[55] SVITKINA, T. M. et al., Journal of Cell Biology **145** (1999) 1009.

[56] AMANN, K. J. et al., Proceedings of the National Academy of Sciences of the United States of America **98** (2001) 15009.

[57] MOGILNER, A. et al., Biophysical Journal **71** (1996) 3030.

[58] WATANABE, N. et al., Science **295** (2002) 1083.

[59] LIN, C. H. et al., Neuron **16** (1996) 769.

[60] KRUSE, K. et al., Physical Biology **3** (2006) 130.

[61] KRESS, H. et al., Proceedings of the National Academy of Sciences of the United States of America **104** (2007) 11633.

[62] CHAN, C. E. et al., Science **322** (2008) 1687.

[63] MALLAVARAPU, A. et al., Journal of Cell Biology **146** (1999) 1097.

[64] YANG, C. et al., PLoS Biology **5** (2007) 2624.

[65] MEDALIA, O. et al., Current Biology **17** (2007) 79.

[66] LI, T. et al., Journal of Applied Physics **114** (2013) 214701.

[67] FIÉVET, B. et al., Biochimica et Biophysica Acta - Molecular Cell Research **1773** (2007) 653.

[68] DENT, E. W. et al., Nature Cell Biology **9** (2007) 1347.

[69] NIEDERGANG, F. et al., Current Opinion in Cell Biology **16** (2004) 422.

[70] MILLARD, T. H. et al., Development (Cambridge, England) **135** (2008) 621.

[71] SVITKINA, T. M. et al., Journal of Cell Biology **160** (2003) 409.

[72] STEFFEN, A. et al., Genetics **125** (2006) 351.

[73] NAUMANEN, P. et al., Journal of Microscopy **231** (2008) 446.

[74] SMALL, J. V. et al., Biochimica et Biophysica Acta - Molecular Cell Research **1404** (1998) 271.

[75] KOONCE, M. P. et al., Experimental Cell Research **141** (1982) 375.

[76] KUMAR, S. et al., Biophysical Journal **90** (2006) 3762.

[77] CHARRAS, G. T. et al., Journal of Cell Biology **175** (2006) 477.

[78] TOOLEY, A. J. et al., Nature Cell Biology **11** (2009) 17.

[79] KUNDA, P. et al., Trends in Cell Biology **19** (2009) 174.

[80] ESTECHA, A. et al., Journal of Cell Science **122** (2009) 3492.

[81] EISENMANN, K. M. et al., Current Biology **17** (2007) 579.

[82] FEHON, R. G. et al., Nature Reviews. Molecular Cell Biology **11** (2010) 276.

[83] SALBREUX, G. et al., Trends in Cell Biology **22** (2012) 536.

[84] BRAY, D. et al., Science **239** (1988) 883.

[85] STEWART, M. P. et al., Nature **469** (2011) 226.

[86] TINEVEZ, J.-Y. et al., Proceedings of the National Academy of Sciences of the United States of America **106** (2009) 18581.

[87] ANANTHAKRISHNAN, R. et al., Journal of Theoretical Biology **242** (2006) 502.

[88] MATZKE, R. et al., Nature Cell Biology **3** (2001) 607.

[89] FERNÁNDEZ, P. et al., Biophysical Journal **90** (2006) 3796.

[90] THOUMINE, O. et al., Journal of Cell Science **110** (1997) 2109.

[91] BROEDERSZ, C. P. et al., Physical Review Letters **105** (2010) 238101.

[92] BAUSCH, A. R. et al., Biophysical Journal **75** (1998) 2038.

[93] MAYER, M. et al., Nature **467** (2010) 617.

[94] HORWITZ, A. R., Nature Reviews Molecular Cell Biology **10** (2009) 778.

[95] EVANS, E. et al., Biophysical Journal **56** (1989) 151.

[96] PALUCH, E. et al., Biophysical Journal **89** (2005) 724.

[97] TOKUMITSU, T. et al., The Journal of Cell Biology (1967) 677.

[98] ROBERTSON, A. M. G. et al., The Journal of Pathology **126** (1978) 181.

[99] CUNNINGHAM, C. C., Journal of Cell Biology **129(6)** (1995) 1589.

[100] CHARRAS, G. et al., Nature reviews. Molecular Cell Biology **9** (2008) 730.

[101] KELLER, H. et al., Experimental Cell Research **277** (2002) 161.

[102] JÜLICHER, F. et al., Physics Reports **449** (2007) 3.

[103] De Gennes, P.-G., *Scaling concepts in polymer physics*, Cornell university press, 1979.

[104] MARTIN, P. C. et al., Physical Review A **6** (1972) 2401.

[105] KRUSE, K. et al., European Physical Journal E **16** (2005) 5.

[106] JOANNY, J.-F. et al., HFSP Journal **3** (2009) 94.

[107] LIVERPOOL, T. B. et al., Europhysics Letters (EPL) **69** (2004) 846.

[108] KRUSE, K. et al., Physical Review Letters **85** (2000) 1778.

[109] KRUSE, K. et al., Physical Review. E, Statistical, nonlinear, and soft matter physics **67** (2003) 051913.

[110] SURREY, T. et al., Science **292** (2001) 1167.

[111] HALL, A. et al., Science **279** (1998) 509.

[112] MACHACEK, M. et al., Nature **461** (2009) 99.

[113] SIT, S.-T. et al., Journal of Cell Science **124** (2011) 679.

[114] MATSUMURA, F., Trends in Cell Biology **15** (2005) 371.

[115] SMALL, J. V. et al., Trends in Cell Biology **12** (2002) 112.

[116] KRAYNOV, V. S. et al., Science **290** (2000) 333.

[117] SCHLESSINGER, K. et al., Journal of Cell Biology **178** (2007) 355.

[118] SIEGRIST, S. E. et al., Genes & Development **21** (2007) 483.

[119] RIDLEY, A. J., Journal of Cell Science **114** (2001) 2713.

[120] HUMPHREY, J. D. et al., Nature Reviews Molecular Cell Biology **15** (2014) 802.

[121] MOUW, J. K. et al., Nature Reviews. Molecular Cell Biology **15** (2014) 771.

[122] GEIGER, B. et al., Nature Reviews. Molecular Cell Biology **2** (2001) 793.

[123] ARRIBAS, S. M. et al., Pharmacology and Therapeutics **111** (2006) 771.

[124] KIELTY, C. M., Expert Reviews in Molecular Medicine **8** (2006) 1.

[125] ZHONG, C. et al., Journal of Cell Biology **141** (1998) 539.

[126] SCHWARZBAUER, J. E. et al., Current Opinion in Cell Biology **11** (1999) 622.

[127] ERICKSON, H. P., Proceedings of the National Academy of Sciences of the United States of America **91** (1994) 10114.

[128] HOCKING, D. C. et al., Journal of Cell Biology **133** (1996) 431.

[129] OHASHI, T. et al., Proceedings of the National Academy of Sciences of the United States of America **96** (1999) 2153.

[130] BANEYX, G. et al., Proceedings of the National Academy of Sciences of the United States of America **99** (2002) 5139.

[131] KUBOW, K. E. et al., Nature Communications **6** (2015) 8026.

[132] NAGASE, H. et al., Cardiovascular Research **69** (2006) 562.

[133] LEUNG, D. Y. M. et al., Science **191** (1976) 475.

[134] RUBERTI, J. W. et al., Biochemical and Biophysical Research Communications **336** (2005) 483.

[135] LAMBERT, C. A. et al., Matrix Biology **20** (2001) 397.

[136] VALENTÍN, A. et al., Phil. Trans. R. Soc. A **367** (2009) 3585.

[137] SADA, M. et al., Cancer letters **372** (2016) 210.

[138] LEE, H. O. et al., BMC Cancer **11** (2011) 245.

[139] GOETZ, J. G. et al., Cell **146** (2011) 148.

[140] BUACHE, E. et al., Cancer medicine **3** (2014) 1197.

[141] MALIK, R. et al., Trends in Biotechnology **33** (2015) 230.

[142] CHARRAS, G. et al., Nature Reviews Molecular Cell Biology **15** (2014) 813.

[143] ZAIDEL-BAR, R. et al., Journal of Cell Science **123** (2010) 1385.

[144] BALABAN, N. Q. et al., Nature Cell Biology **3** (2001) 466.

[145] RIVELINE, D. et al., The Journal of Cell Biology **153** (2001) 1175.

[146] TAN, J. L. et al., Proceedings of the National Academy of Sciences of the United States of America **100** (2003) 1484.

[147] BENINGO, K. A. et al., Journal of Cell Biology **153** (2001) 881.

[148] GALBRAITH, C. G. et al., Journal of Cell Biology **159** (2002) 695.

[149] NOBES, C. D. et al., Cell **81** (1995) 53.

[150] BALABAN, N. Q. et al., Nature Cell Biology **3** (2001) 466.

[151] ZAMIR, E. et al., Journal of Cell Science **112 (pt11)** (1999) 1655.

[152] PANKOV, R. et al., Journal of Cell Biology **148** (2000) 1075.

[153] CUKIERMAN, E. et al., Science **294** (2001) 1708.

[154] BREVIER, J. et al., Physical Review Letters **98** (2007) 98.

[155] BREVIER, J. et al., Physical Biology **5** (2008) 016005.

[156] PLOTNIKOV, S. V. et al., Cell **151** (2012) 1513.

[157] MITROSSILIS, D. et al., Proceedings of the National Academy of Sciences of the United States of America **107** (2010) 16518.

[158] MITROSSILIS, D. et al., Proceedings of the National Academy of Sciences of the United States of America **106** (2009) 18243.

[159] TRICHET, L. et al., Proceedings of the National Academy of Sciences of the United States of America **109** (2012) 6933.

[160] THOMPSON, D. W., *On Growth and Form*, Cambridge University Press, 1917.

[161] SANFORD, K. K. et al., Journal of the National Cancer Institute **15** (1954).

[162] HARRIS, A. K. et al., Science **208** (1980) 177.

[163] DEMBO, M. et al., Biophysical Journal **76** (1999) 2307.

[164] GALBRAITH, C. G. et al., Proceedings of the National Academy of Sciences of the United States of America **94** (1997) 9114.

[165] ZIMMERMANN, J. et al., Proceedings of the National Academy of Sciences of the United States of America **113** (2016) 2660.

[166] SCHWARZ, U. S. et al., Reviews of Modern Physics **85** (2013) 1327.

[167] WANG, J. H. C. et al., Biomechanics and Modeling in Mechanobiology **6** (2007) 361.

[168] SABASS, B. et al., Biophysical Journal **94** (2008) 207.

[169] SINHA, S. et al., EDGE, Workshop on Edge **012** (2006) 1.

[170] SCHWARZ, U. S. et al., Biophysical Journal **83** (2002) 1380.

[171] HALL, M. S. et al., Experimental Cell Research **319** (2013) 2396.

[172] LANDAU, L. D. et al., Theory of Elasticity: Vol. 7 of Course of Theoretical Physics, 1960.

[173] LANDAU, L. D. et al., *Elasticity Theory*, Pergamon Press, Oxford, 1975.

[174] FRANCK, C. et al., Experimental Mechanics **47** (2007) 427.

[175] SCHWARZ, U. S. et al., Physical Review Letters **88** (2002) 048102.

[176] BISCHOFS, I. B. et al., Physical Review E - Statistical, Nonlinear, and Soft Matter Physics **69** (2004) 021911.

[177] HATWALNE, Y. et al., Physical Review Letters **92** (2004) 118101.

[178] JIANG, J. et al., The Journal of Cell Biology **209** (2015) 759.

[179] BERGERT, M. et al., Nature Cell Biology **17** (2015) 524.

[180] DELANOË-AYARI, H. et al., Cell Motility and the Cytoskeleton **65** (2008) 314.

[181] DELANOË-AYARI, H. et al., Physical Review Letters **105** (2010) 248103.

[182] JANNAT, R. A. et al., Biophysical Journal **101** (2011) 575.

[183] MOORE, S. W. et al., Developmental Neurobiology **71** (2011) 1090.

[184] STEINWACHS, J. et al., Nature Methods **13** (2015) 171.

[185] LÄMMERMANN, T. et al., Nature **453** (2008) 51.

[186] LAUTENSCHLAGER, F. et al., Proceedings of the National Academy of Sciences of the United States of America **106** (2009) 15696.

[187] PRENTICE-MOTT, H. V. et al., Proceedings of the National Academy of Sciences of the United States of America **110** (2013) 21006.

[188] LIU, Y.-J. et al., Cell **160** (2015) 659.

[189] LÄMMERMANN, T. et al., Current Opinion in Cell Biology **21** (2009) 636.

[190] HAWKINS, R. et al., Physical Review Letters **102** (2009) 058103.

[191] HARADA, T. et al., Journal of Cell Biology **204** (2014) 669.

[192] MAK, M. et al., Lab Chip **13** (2012) 340.

[193] DOYLE, A. D. et al., The Journal of Cell Biology **184** (2009) 481.

[194] FRALEY, S. I. et al., Nature Communications **3** (2012) 719.

[195] GUETTA-TERRIER, C. et al., The Journal of Cell Biology **211** (2015) 683.

[196] MEEHAN, S. et al., Biophysical Journal **107** (2015) 2604.

[197] WASNIK, V. et al., Physical Review E - Statistical, Nonlinear, and Soft Matter Physics **90** (2014) 1.

[198] TOZLUOGLU, M. et al., Nature Cell Biology **15** (2013) 751.

[199] HUNG, W. C. et al., Journal of Cell Biology **202** (2013) 807.

[200] KERAMATI, M. R. et al., Physical Review E - Statistical, Nonlinear, and Soft Matter Physics **91** (2015) 1012705.

[201] STROKA, K. M. et al., Cell **157** (2014) 611.

[202] RUPRECHT, V. et al., Cell **160** (2015) 673.

[203] HAWKINS, R. J. et al., Biophysical Journal **101** (2011) 1041.

[204] ELLIOTT, H. et al., Nature Cell Biology **17** (2015) 137.

[205] WU, P.-H. et al., Proceedings of the National Academy of Sciences of the United States of America **111** (2014) 3949.

[206] METZNER, C. et al., Nature Communications **6** (2015) 7516.

[207] FRANSILLA, S., *Introduction To Microfabrication*, Wiley, 2004.

[208] QIN, D. et al., Nature Protocols **5** (2010) 491.

[209] BINNIG, G. et al., Physical Review Letters **56** (1986) 930.

[210] DROBCZYNSKI, S. et al., Optical Engineering **48** (2009) 113601.

[211] BERG-SÖRENSEN, K. et al., Review of Scientific Instruments **75** (2004) 594.

[212] BAUSCH, A. R. et al., Biophysical Journal **76** (1999) 573.

[213] TOMASI, C., Detection and Tracking of Point Features Technical Report CMU-CS-91-132, in *Image Rochester NY*, volume 91, pages 1–22, 1991.

[214] LUCAS, B. D. et al., An Iterative Image Registration Technique with an Application to Stereo Vision, in *7th international Joint Conference on Artificial Intelligence*, volume 2, pages 121–130, 1981.

[215] BRADSKI, G. et al., *Learning OpenCV: Computer vision with the OpenCV library*, " O'Reilly Media, Inc.", 2008.

[216] PETIT, L. et al., Langmuir **25** (2009) 12048.

[217] SOUCY, P. A. et al., Acta Biomaterialia **7** (2011) 96.

[218] STOITZNER, P. et al., Journal of Investigative Dermatology **118** (2002) 117.

[219] AMATANGELO, M. D. et al., The American Journal of Pathology **167** (2005) 475.

[220] RAMBERG, W. et al., National Advisory Committee For Aeronautics (1943) Technical Note No. 902.

[221] TELLO, M. et al., Methods **94** (2015) 85.

[222] AHLFORS, J. E. W. et al., Biomaterials **28** (2007) 2183.

[223] LAURENT, V. M. et al., Journal of Biomechanical Engineering **124** (2002) 408.

[224] DIEZ-SALES, O. et al., Journal of Applied Polymer Science **21** (2006) 2122.

[225] HAKKINEN, K. M. et al., Tissue Engineering. Part A **17** (2011) 713.

[226] MAZUMDER, A. et al., Biophysical journal **95** (2008) 3028.

[227] YOSHIGI, M. et al., Journal of Cell Biology **171** (2005) 209.

[228] MARCY, Y. et al., Proceedings of the National Academy of Sciences of the United States of America **101** (2004) 5992.

[229] BENDIX, P. M. et al., Biophysical Journal **94** (2008) 3126.

[230] HEASMAN, S. J. et al., Nature Reviews Molecular Cell Biology **9** (2008) 690.

[231] ISHIZAKI, T. et al., Molecular Pharmacology **57** (2000) 976.

[232] STRAIGHT, A. F. et al., Science **299** (2003) 1743.

[233] SAITOH, M. et al., The Journal of Biological Chemistry **262** (1987) 7796.

[234] ISHIHARA, H. et al., Biochemical and Biophysical Research Communications **159** (1989) 871.

[235] KOLEGA, J., Biochemical and Biophysical Research Communications **320** (2004) 1020.

[236] SPECTOR, I. et al., U.S. Bur. Mines. Invest. **5932** (1983) 1.

[237] NOLEN, B. J. et al., Nature **460** (2009) 1031.

[238] SALBREUX, G. et al., Physical Biology **4** (2007) 268.

[239] PALUCH, E. et al., Trends in Cell Biology **16** (2006) 5.

[240] FUARD, D. et al., Microelectronic Engineering **85** (2008) 1289.

[241] SCHROERS, J. et al., Physical Review Letters **93** (2004) 20.

[242] LAUTSCHAM, L. A. et al., Biophysical Journal **109** (2015) 900.

[243] MANDATO, C. A. et al., Journal of Cell Biology **154** (2001) 785.

[244] ESSNER, J. J. et al., Development (Cambridge, England) **132** (2005) 1247.

[245] PITZER, F. et al., FEBS Letters **394** (1996) 47.

[246] VADER, D. et al., PLoS ONE **4** (2009) e5902.

[247] RAEBER, G. et al., Biophysical Journal **89** (2005) 1374.

[248] SWIFT, J. et al., Science **341** (2013) 1240104.

[249] SIEMINSKI, A. L. et al., Proceedings of the National Academy of Sciences of the United States of America **103** (2006) 15.

[250] WENG, S. et al., Nature Materials (2016) 1.

[251] SOLON, J. et al., Biophysical Journal **93** (2007) 4453.

[252] DAVIDSON, P. M. et al., Integrative Biology : quantitative biosciences from nano to macro **7** (2015) 1534.

[253] THOMAS, D. G. et al., The Journal of Cell Biology **210** (2015) 583.

[254] CHARRAS, G. T. et al., Nature **435** (2005) 365.

[255] MEILI, R. et al., Molecular Biology of the Cell **21** (2010) 405.

[256] LEONI, M. et al., Physical Review E - Statistical, Nonlinear, and Soft Matter Physics **91** (2015) 022720.

[257] GHASSEMI, S. et al., Proceedings of the National Academy of Sciences of the United States of America **109** (2012) 5328.

[258] VAN DEN DRIES, K. et al., Nature Communications **4** (2013) 1412.

[259] DEBIASIO, R. L. et al., Molecular Biology of the Cell **7** (1996) 1259.

[260] TOTSUKAWA, G. et al., Journal of Cell Biology **150** (2000) 797.

[261] BENINGO, K. A. et al., Archives of Biochemistry and Biophysics **456** (2006) 224.

[262] HOWARD, J., Physical Biology **3** (2006) 54.

[263] PLETJUSHKINA, O. J. et al., Cell Motility and the Cytoskeleton **48** (2001) 235.

[264] AKHSHI, T. K. et al., Cytoskeleton **71** (2014) 1.

[265] RAPE, A. et al., Journal of Cell Science **124** (2011) 4233.

[266] BALLESTREM, C. et al., Molecular biology of the cell **11** (2000) 2999.

[267] LIAO, G. et al., Journal of Cell Science **108** (1995) 3473.

[268] KOZLOV, M. M. et al., Biophysical Journal **93** (2007) 3811.

[269] SAHA, A. et al., Biophysical Journal **110** (2016) 1421.

[270] FERNANDEZ-GONZALEZ, R. et al., Developmental Cell **17** (2009) 736.

[271] ROSENBLUM, M. D. et al., Comparative Biochemistry and Physiology - C Pharmacology Toxicology and Endocrinology **125** (2000) 121.

[272] MANIOTIS, A. J. et al., Proceedings of the National Academy of Sciences of the United States of America **94** (1997) 849.

[273] SHAO, X. et al., Proceedings of the National Academy of Sciences of the United States of America **112** (2015) E2595.

[274] MAZUMDER, A. et al., Journal of the Royal Society, Interface / the Royal Society **7 Suppl 3** (2010) S321.

[275] TAMADA, M. et al., Journal of Cell Biology **176** (2007) 27.

[276] MORI, M. et al., Current Biology **21** (2011) 606.

[277] MAKHIJA, E. et al., Proceedings of the National Academy of Sciences of the United States of America **113** (2015) E32.

[278] LEE, J. S. H. et al., Biophysical Journal **93** (2007) 2542.

[279] BUXBOIM, A. et al., Current Biology **24** (2014) 1909.

[280] SURANENI, P. et al., Journal of Cell Biology **197** (2012) 239.

[281] WEED, S. A. et al., Journal of Cell Biology **151** (2000) 29.

[282] BOVELLAN, M. et al., Current Biology **24** (2014) 1628.

[283] NORDEN, C. et al., Cell **138** (2009) 1195.

[284] KOESTLER, S. A. et al., Molecular Biology of the Cell **24** (2013) 2861.

[285] WILSON, K. et al., Nature Communications **4** (2013) 1.

[286] FALZONE, T. T. et al., Biophysical Journal **104** (2013) 1709.

[287] STARKE, J. et al., Biochemical Society transactions **42** (2014) 1356.

[288] KATOH, K. et al., American Journal of Physiology. Cell Physiology (2011) 1669.

[289] LIEBER, A. D. et al., Current Biology **23** (2013) 1409.

[290] WANG, N. et al., American Journal of Physiology. Cell Physiology **282** (2002) C606.

[291] ARTHUR, W. T. et al., Current Biology **10** (2000) 719.

[292] MCGREGOR, A. L. et al., Current Opinion in Cell Biology **40** (2016) 32.

[293] SOLON, J. et al., Cell **137** (2009) 1331.

[294] MARTIN, A. C. et al., Nature **457** (2009) 495.

[295] OKAMURA, N. et al., Journal of Muscle Research and Cell Motility **9** (1988) 111.

[296] SHLOMOVITZ, R. et al., Physical Review E - Statistical, Nonlinear, and Soft Matter Physics **78** (2008) 041911.

[297] PURCELL, E., American Journal of Physics **45** (1977) 3.

[298] PROST, J. et al., Nature Physics **11** (2015) 131.

[299] CODLING, E. A. et al., Journal of the Royal Society Interface **5** (2008) 813.

[300] KEMMER, N., *Vector Analysis*, Cambridge University Press, 1977.

[301] IGARASHI, H. et al., NeuroReport **24** (2013) 209.

A Appendix

A.1 Abbreviation

Table A.1: Table of Abbreviations

Abbrivation	Full name
BSA	Bovine serum albumin
$CaCl_2$	Calciumchloride
CCD	Charge-coupled device
CDM	Cell Derived Matrix
DAPI	4',6-Diamidino-2-phenylindole
DIC	Differential interference contrast
DMEM	Dulbecco's modified eagle's medium
DMSO	Dimethyl sulfoxide
DNA	Deoxyribonucleic acid
DPBS	Dulbecco's phosphate-buffered saline
EM	Electron microscopy
ECM	Extracellular matrix
EDTA	Ethylenediamine tetraacetic acid
EM	Electron microscopy
FA	Focal adhesion
FN	Fibronectin
GAP	GTPase activating protein
GEF	Guanine nucleotide exchange effectors
GFP	Green fluorescent protein
HyD	Hybrid detectors
KLT	Kanadé- Lucas-Tomasi
IL4	Interleukin-4
L-15	Leibovitz-15
LB medium	Lysogeny broth medium
LPS	Lipopolysaccharide
MLCK	Myosin light chain kinase
PBS	Phosphate buffered saline
PDMS	Polydimethylsiloxane
PFA	Paraformaldehyde
PMT	Photomultiplier tube

Continued on next page

Table A.1 – continued from previous page

Abbrivation	Full name
PRW	Persistent random walk
PS	Polystyrene
RBC	Red blood cell
RNA	Ribonucleic acid
ROCK	Rho kinase
RT	Room temperature
RPMI medium	Roswell Park Memorial institute medium
StDev	Standard deviation
UV	Ultraviolet

A.2 Term definitions

Reynolds number: The ratio of viscous force to the inertial force $Re = \frac{\rho v a}{\eta}$ with ρ density, v speed of the fluid, a dimension of the object and η viscosity. At low Reynolds number inertia does not play a role [297].

***Active gel* theory**: Theoretical description of a energy consuming crosslinked network for example for acto-myosin formed supramolecular structures. A more physical definition: "We define active gels as soft materials in which detailed balance is broken locally [298]".

Persistent random walk: A random walk describes successive random steps (any direction is equiprobable). The persistent random walk is a random walk with an introduced bias [299].

Dyadic product The dyadic product is the product of the multiplication of two vectors. It is a squared matrix representing a tensor [300].

A.3 Supplementary information concerning products

A.3.1 Microfabrication

In the following tables the products and devices used for microfabrication are listed.

Table A.2: Products for microfabrication

Product	Brand (Supplier)	Reference	Comment
Silicon wafer	Si-Mat		3", P/Boron, <100>
SU-8 photoresist	MicroChem		
Developer SU-8	Chimie Tech Services	DevSU8/4	
PDMS, Sylgard 184	Dow Corning (Neyco, Ellsworth)	DC184-1.1 , 0002-01-000032	
Polystyrene, film	Good Fellow	ST311025	25 µm

Table A.3: Equipment for microfabrication

Product	Company	Reference	Comment
Mask aligner	SUSS MicroTec	MJB3	
Oxygen plasma cleaner	Diener Electronic	Zepto B	Usual settings: 30 s, O_2, flow 5,5, power 2,5
Photolithography mask, chromium	Selba		
Photolithography mask, acetate	Selba		50800 dpi
Spin coater	Laurell Technologies corporation	WS-400B-6NPP/Lite	

A.3.2 Cell culture

Table A.4: Products for CDM

Product	Brand (Supplier)	Reference
DPBS (Dulbecco's Phosphate-Buffered Saline)	Invitrogen Gibco (Thermo Fisher Scientific)	11530486
gelatin	Sigma Aldrich	
glutaraldehyde 50%	Sigma Aldrich	G7651
glycine	Sigma Aldrich	410225
L-Ascorbic Acid	Sigma Aldrich	A5960
TRITC fibronectin	Cytoskeleton Inc	FNR01
Triton	Sigma Aldrich	93443
NH_4OH	Sigma Aldrich	318612
Dynabeads Myo carboxylic acid 1 μm	Invitrogen (Thermo Fisher Scientific)	65011
Latex beads carboxylate-modified polystyrene 2 μm, fluorescent yellow-green	Sigma Aldrich	L4530
Latex beads 2 μm, amino modified polystyrene	Sigma Aldrich	L0780
Fluo Spehres Carboxylate-modified microspheres 0.1 μm red fluorescent	BioSpehres (Thermo fisher Scientific)	F8801

A.3.2.1 Stable cell lines

Table A.5: Products and references used for culturing mammalian cells

Product	Brand (Supplier)	Reference	Comment
BCS (Bovine Calf Serum)	Sigma Aldrich	C8056	
DMEM (Dulbecco's Modified Eagle Medium)	Invitrogen Gibco (Thermo Fisher Scientific)	12007559	high glucose
Geneticin	Invitrogen (Thermo Fisher Scientific)	11548616	Added after replating 75-150 μg/ml concentration (Ypet NIH3T3)
Puromycin	Invitrogen Gibco (Thermo Fisher Scientific)	12122530	Added for cell sorting
Penicillin streptomycin	Invitrogen Gibco (Thermo Fisher Scientific)	11548876	Dilution in culture medium 1 %
Trypsin-EDTA	Invitrogen Gibco (Thermo Fisher Scientific)	11570626	
Leibovitz L-15 medium	Invitrogen Gibco (Thermo Fisher Scientific)	11540556	
DMSO (Dimethyl sulfoxide)	Sigma Aldrich	D8418	

Table A.6: Cytoskeleton drugs

Product	Brand (Supplier)	Reference	Comment
(–) Blebbistatin	Sigma Aldrich	B0560	stored at -20°C, light sensitive
Y27632	Sigma Aldrich	Y0503	stored at -20°C
Calyculin A	Sigma Aldrich	C5552	stored at -20°C
C8	Jean-Marie Lehn laboratory (ISIS)		stored at 4°C
CK666	Sigma Aldrich	SML0006	stored at 4°C
Latrunculin A	Sigma Aldrich	L5163	stored at –20°C
ML-7	Sigma Aldrich	I2764	stored at –20°C
Nocodazole	Sigma Aldrich	M1404	stored at 4°C
TGN-020	Sigma Aldrich	SML0136	stored at 4°C
$GdCl_3$	Sigma Aldrich	439770	stored at RT
EDTA	Sigma Aldrich	E6758	stored at RT

Table A.7: Products used for DNA amplification and transfection

Product	Brand (Supplier)	Reference
Competent bacteria (One Shot TOP10)	Invitrogen Gibco (Thermo Fisher Scientific)	1066-6493
LB medium and agar plates	IGBMC media facility	
EndoFree® Plasmid Maxi Kit	Qiagen	12362
Plasmid *Plus* MaxiKit(25)	Qiagen	12963
Lipofectamine 2000®	Invitrogen Gibco (Thermo Fisher Scientific)	11668
Opti-MEM®	Invitrogen Gibco	11058-021

Table A.8: Product information for fixation and immunostaining protocols

Product	Brand (Supplier)	Reference	Comment
PFA (Paraformaldehyde)	Sigma Aldrich	P6148	PFA solution is prepared in a 3 % dilution in PBS
DPBS (Dulbecco's Phosphate-Buffered Saline)	Invitrogen Gibco (Thermo Fisher Scientific)	11530486	
Triton	Sigma Aldrich	93443	
Glycerol	Sigma Aldrich	G2025	
BSA (Bovine Serum Albumin)	Sigma Aldrich	A2153	
TBS (Tris Buffered Saline)	Sigma Aldrich	94158	

Table A.9: List of antibodies and dyes for staining

Antibody	Brand/Source	Reference
Anti- Fibronectin (H-300)	Santa Cruz Technology	sc-9068
Phalloidin AlexaFluro 488	Invitrogen (Thermo Fisher Scientific)	A12379
Phalloidin AlexaFluro 546	Invitrogen (Thermo Fisher Scientific)	A22283
AlexaFluro 488 (anti-rabbit)	Molecular Probes (Thermo Fisher Scientific)	A-11034
AlexaFluro 647 (anti-rabbit)	Molecular Probes (Thermo Fisher Scientific)	A-21245
Cy3 (anti-rabbit)	Jackson ImmunoResearch	111-166-047
Cy3 (anti-mouse)	Jackson ImmunoResearch	115-165-146
DAPI (4',6-Diamidino-2-phenylindole dihydrochloride)	Sigma Aldrich	32670
Hoechst 33342	Thermo Fisher Scientific	10150888

Table A.10: Plasmids used for transfection

Plasmid	Resistance	Source and Reference
FN-Ypet	Kanamycin/Geneticin	Harold P. Erickson
mCherry Lifeact	Kanamycin/Geneticin	Ewa Paluch
RFP zyxin	Kanamycin/no secondary resistance	Anna Huttenlocher
mCherry MRLC2	Kanamycin/Geneticin	Addgene
GFP NMHC2A	Kanamycin/Geneticin	Ewa Paluch

A.3.2.2 Primary cells

Lymphocytes ACK : For 1l of H_2O: 8.29g NH_4Cl (0.15 M), 1g $KHCO_3$ (1mM), 37.2 mg Na_2EDTA (0.1mM). Add 800ml of H_2O and adjust the pH to 7.2-7.4 with 1N HCl (sterilize by filtering through a 0.2 μm filter).

LPS : Lipopolysaccharide from Sigma (L-2630, From E. coli serotype 0111:B4). 25 mg/ml stock in incomplete RPMI kept in small aliquots at -20°C or -80°C for long term storage.

IL-4 : Interleukin-4(IL-4) Mouse, Recombinant from Sigma (I 1020). 1000 X Stock at 5 μg/ml in PBS 0.1% FCS kept in small aliquots at -20°C or -80°C for long term storage.

Table A.11: Product information for complete RPMI

Product	Volume
RPMI-1640	500 ml
50% cels heat inactivated (1hs)	FCS 10% (50 ml)
Penicillin-Streptomicin	1X (5.5 ml)
Glutamine	1% (5.5 ml)
Sodium Pyruvate	1% (5.5 ml)
4μl 2-B-mercapto ethanol	1.8μl of 14.2M (53μM final)
HEPES 1M	10mM (5.5 ml)

Mouse embryonic fibroblasts Medium: DMEM (4,5 g/L glc) w/GLUTAMAX-I +10% FCS ES tested+gentamycine

A.4 Supplementary information concerning protocols

A.4.1 Microfabrication

Table A.12: Overview parameters for photolithography

Photoresist	Desired thickness [μm]	Spincoating speed [rpm]	prebake 65°C/95°C time [min]	exposure time [sec]	postbake 65°C/95°C time [min]
2005	5	2000	1/2	17	1/2
2007	5	3000	1/2	17	1/2
2025	50	1500	3/9	60	2/7
2050	50	3000	3/9	60	2/7

A.4.2 Molecular biology

A.4.2.1 DNA amplification in bacteria

- Depending on the storage form of the DNA it has to be extracted from paper. Therefore the paper containing DNA is cut into small pieces, put in an Eppendorf tube and rinsed with endotoxin free (TE) buffer. After the centrifugation, the DNA is in the buffer.
- Competent bacteria are put on ice for 10 min.
- 50 μl of competent bacteria are mixed with 1 μg of DNA and kept on ice for 30 min.
- The mixture is put on 42°C for exactly 90 s and then back on ice.
- 500 μl of LB medium is dropped to the bacteria DNA mixture and shaken for 30 min at 250 rpm and 37°C.
- 250 μl of the bacteria are poured on an agar plate of required resistance an homogeneously distributed with home made glass rake (a bent glass pipette). The rest of the bacteria is kept in the fridge.
- The agar plate is put overnight upside down at 37°C.
- A colony is picked with a toothpick and dropped in a tube with LB medium and antibiotics.
- The tube is shaken at 250 rpm and 37°C for around 8 h. 0.7 ml bacteria solution and 0.3 ml glycerol are mixed and frozen at -80°C. Those bacteria can be used for future amplification.

- 1 ml of bacteria solution is diluted in 4 ml LB medium with antibiotics and shaken at 37°C and 250 rpm for about 8h. In this step also 1 μl of the frozen bacteria can be used.

- 2 ml of bacteria culture is added to 100 ml LB medium with antibiotics and shaken at 37°C and 250 rpm overnight.

A.4.2.2 DNA purification

The following steps are described in detail in the Qiagen Endofree Plasmid Purification Handbook or the Qiagen Plasmid Plus MaxiKit Handbook corresponding to the two used kits.

(a) Bacteria are harvested by centrifugation and lysed

(b) Lysate is cleared by filtering from proteins and genomic DNA.

(c) Quiagen Anion-Exchange Resin is used to bind the plasmids. Low-molecular weight impurities, dyes, proteins and RNA are removed by rinsing with medium-salt buffer.

(d) High-salt buffer is used to elute plasmids

(e) They are washed and concentrated by isopropanol precipitation.

(f) Plasmids are washed with ethanol 70 % and and re-dissolved in endo-toxin free buffer.

(g) Purity and concentration of DNA are measured with a absorption spectrometer (Nanodrop)

A.4.2.3 Immunostaining

Table A.13: Primary and secondary antibodies used for immunostaining

Antibody	Mono- or polycolonal	Concentration	Stock solution concentration
Anti-Fibronectin	Polyclonal	1:50	200μg/ml
Phalloidin 647	-	1:200	6,6μM
Phalloidin 488	-	1:200	6,6μM
DAPI	-	1 μg μl	1 mg/μl
Alexa Fluor 647	Polyclonal	1:1000	2mg/ml
Cy3 Anti-mouse	Monoclonal	1:1000	1,3 mg/ml

A.5 Results - Supplementary information

In the following section, I will describe results we obtained for characterization of CDM and while trying to challenge different entities of the cell. We analyzed the effect of different drugs on cell blockage in the CDM. The aim was to identify if inhibition of periodic deformation of the mesh could abolish cell migration.

A.5.1 CDM characterization

To probe whether the CDM has an intrinsic tension, we thought of performing laser ablation on the network. Cutting a fiber might lead to a recoil of the fiber where the recoil speed would give access to the material tension. In Figure A.1 the network before and after cut is depicted. No recoil could be detected the cut size is not increasing after cutting. It might be the case that the time between cut and image acquisition is too long,

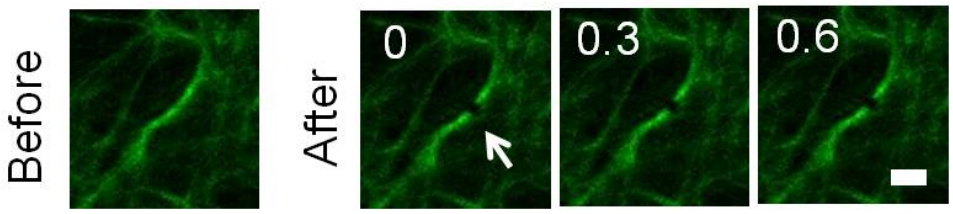

FIGURE A.1: CDM before and after cut of a fibronectin fiber. Cut highlighted with white arrow. Scale bar 10 μm and time in sec.

thus the time resolution too low to detect the movement of the fiber. A hint towards this direction is that the cut is larger than what it should be considering that point ablation is performed and the size is determined by the pinhole. Another option is that there is no intrinsic tension in the CDM. It can be extracted from the pictures that fibers are not floating after cutting thus mesh seems to have stable connections. This might also be the reason why no relaxation of the mesh could be observed upon cutting. The mesh is highly reticulated and the cut fiber might still be retained by other fibers of the mesh, preventing a relaxation. Hence, another method needs to be considered to access matrix tension.

A.5.2 Deformation of nucleus

We tested molecular structure of the cytoskeleton and more precisely lowered the contractility of cells via the Rho pathway. ROCK was inhibited by Y27632, myosin by blebbistatin and MLCK by ML-7 as presented in the Results. We report that cells are still able to deform their nucleus in this experimental configuration as shown in Figure A.2. Cells in presence of drugs and squeezed nucleus are depicted. As for control case the deformation factor has been calculated and the normalized instantaneous speed centered at the largest deformation (lowest deformation factor). One can see that speed increases for the unsqueezing process as in control cases. In terms of absolute value persistent speed of cells treated with Y27632 corresponds to control. For cells treated with blebbistatin

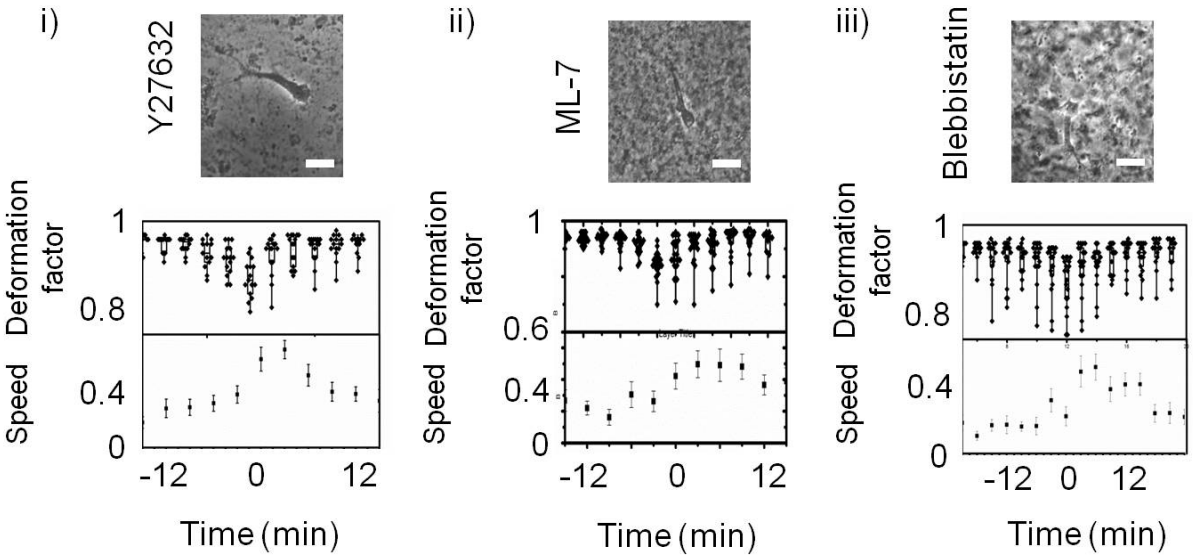

FIGURE A.2: i) Deformation coefficient and instantaneous speed after addition of 10 μM Y27632 (N=3, n=16). ii) Deformation coefficient and instantaneous speed after addition of 10 μM ML-7 (N=3, n=14) iii) Deformation coefficient and instantaneous speed after addition 25 μM blebbistatin (N=3, n=19). Scale bar 10 μm.

or ML-7 persistent speed is decreased as reported in Results. The highest speed is obtained right after the highest deformation for Y27632 and blebbistatin case. For ML-7 the highest speed is obtained after unsqueezing. Globally, the squeezing process is conserved in presence of the drugs. The squeezing time is consistent with duration of control. Altogether, drug treatment with Y27632, blebbistatin and ML-7 and following decrease of differential force did not impede nucleus squeezing and cell passage. The dynamics of squeezing also seem preserved.

A.5.3 The role of aquaporin channels in contraction relaxation cycles

Aquaporin channels are located in the cell membrane and permeable for water. As volume of the cell does not seem conserved, we hypothesized that cell migration and squeezing was related to water transport through the membrane. To test this, we inhibited aquaporin-4 channel by TGN-020 [301]. A control sequence was acquired before addition of drug to check on the motility of the cell. In Figure A.3 one can see that the cell still migrates and

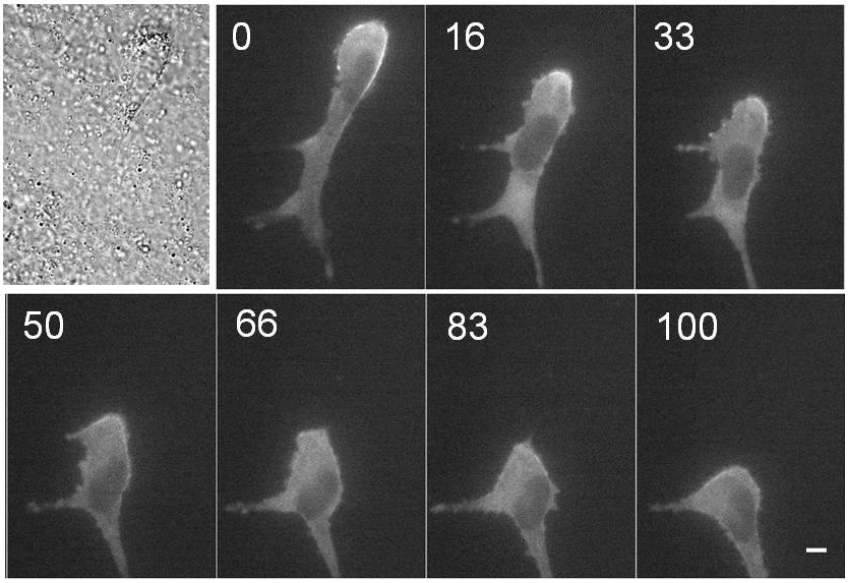

FIGURE A.3: Image sequence of a cell expressing GFP-NMHC2A migrating in CDM in presence of TGN-020 100 μM an aquaporin-4 inhibitor. Time in min and scale bar 10 μm.

still squeezes in presence of the inhibitor. Overall, cell behaviour corresponds to control case. The family of aquaporin channels is broad and inhibitors are selective for specific channels of the aquaporin families. There is no guarantee that with our inhibitor all channels are blocked. Further experiments with various inhibitors are needed to conclude for the role of aquaporines for cell motility in 3D CDM.

A.5.4 The role of calcium for contraction relaxation cycles

As reported in Salbreux *et al* [238] cells in suspension oscillate with a frequency of 37 s. The mechanism is Ca^{2+} dependent and oscillation stops when depleting Ca^{2+} with EDTA (> 4 mM) or blocking mechanically activated calcium channels by gadolinium ions. To probe whether we could stop contraction relaxation cycles and block migration by this means, we performed similar experiments.

A.5.4.1 Depletion of calcium from medium

Calcium was depleted by EDTA from the medium and calcium concentration restored by calciumchloride ($CaCl_2$). PH of EDTA was adapted prior to experiment to physiological pH. To check the effect of EDTA and $CaCl_2$, we first performed the experiment on cells migrating on 2D surfaces and added 4 mM of EDTA. The cells rounded up in 10 min and blebbed heavily (see Figure A.4). Upon addition of $CaCl_2$ (same concentration as for EDTA) cells adhered again on the substrate. A ramp of addition of EDTA (1,2 and

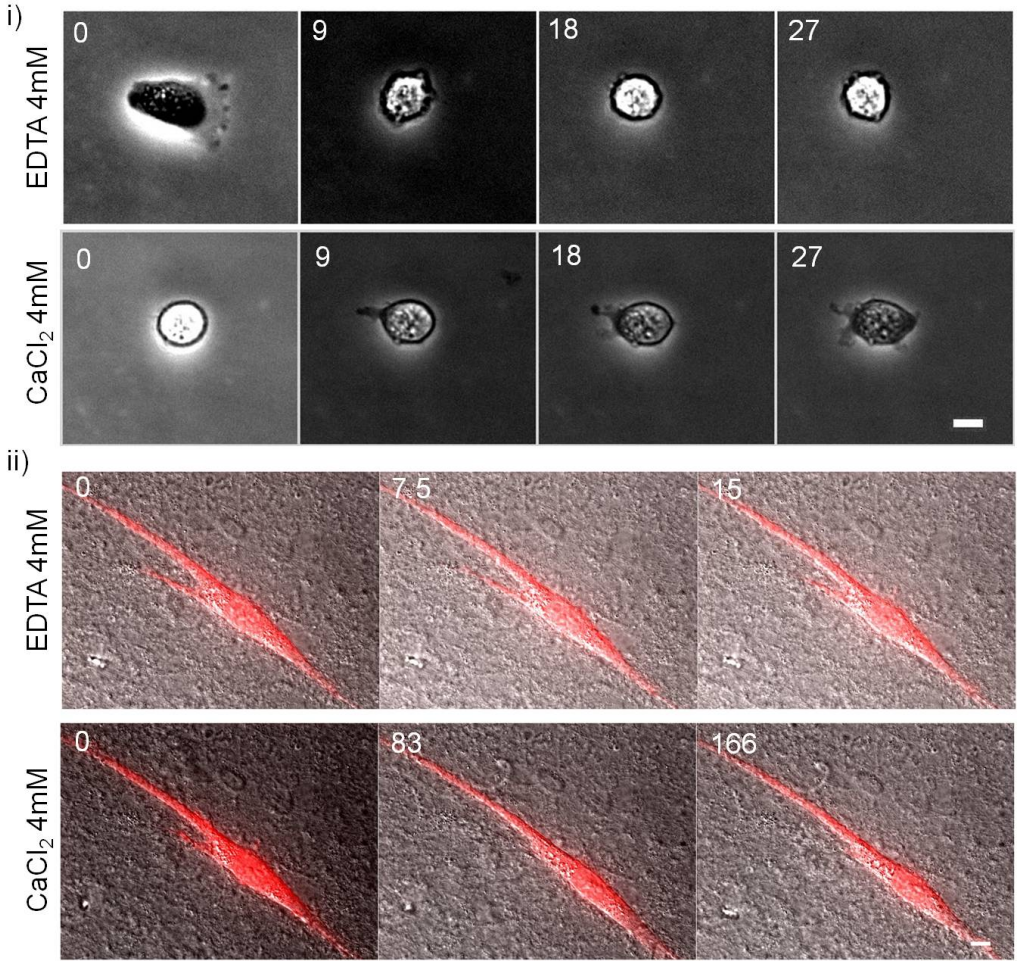

FIGURE A.4: i) Cells round up and bleb upon addition of EDTA 4mM. When adding $CaCl_2$ cells adhered again on the CS. Time in min and scale bar 10 μm. ii) Cells in CDM exposed to 4 mM EDTA and subsequently $CaCl_2$. Time in min and scale bar 10 μm.

4 mM, only 4 mM shown) was conducted for cells in 3D CDM. The cell in CDM did not round up during incubation. Addition of $CaCl_2$ did not change behaviour of the cell neither.
The experiment yielded different results for cells on 2D surface and cell in 3D CDM. EDTA in 3D did not show the expected result, cells did not seem affected by the calcium change. Further experiments are needed to evaluate if a change in contraction-relaxation cycles is occurring.

A.5.4.2 Inhibition of calcium channels

Gadolinium (Gd^{3+}) has been used in the past to block mechanically activated calcium channels. We used the same concentration as in [238]. A control was performed to make sure that cells behave normally and are motile. Cells continued migrating in presence

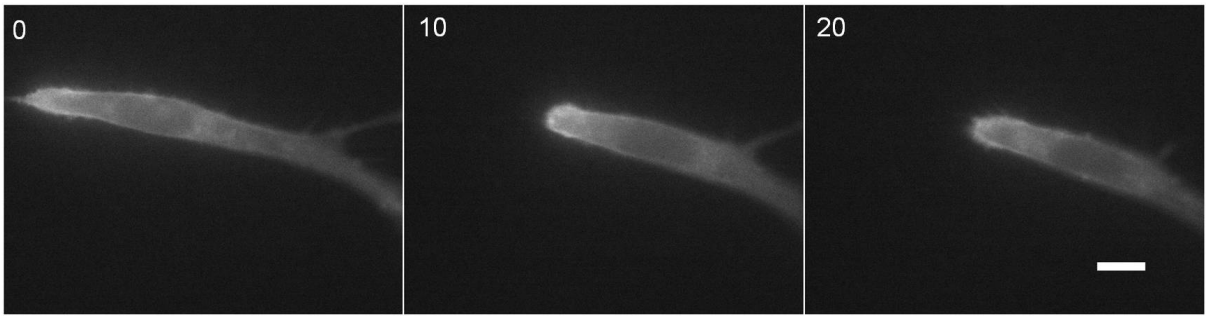

FIGURE A.5: Time series of cell expressing mCherry Lifeact evolving in CDM in presence of Gd^{3+} 100 μM. Time in min and scale bar 10 μm.

of the drug. Deformation of the CDM is still observed. For analysis of contraction-relaxation cycles further experiments need to be performed. We deduce that we do not have the same mechanism as described in [238], still we do not exclude a role for calcium in contraction-relaxation cycles.

A.5.5 Error calculation

In this section I will describe, how we evaluated the limitations of the extraction of peaks from autocorrelation and cross correlation analysis. This allows us to define a range of error for our calculations.

A.5.5.1 KLT

The average error in the KLT[1] program for pyramid level 1 and 3 as a function of the added Poisson noise are shown in Figure A.6. The images (100x100 pixels) are made by generating 1000 random points in the center area of 50x50 pixels. A Gaussian distribution with a σ of 2 pixels at the position of all random points is used to calculate the intensities of every pixel; a sum of the contributions from all the particles. In (a) subsequently the points are moved vertically according to a sine function with amplitude of 5 pixels and a

[1]Error estimation done by Hélène Delanoë-Ayari.

wavelength of 10 pixels and the moved image is generated. In (b) noise is added to all the pixels according to a Poisson distribution (b, c, d). In the main graph the average error of the KLT program is given as a function of the signal to noise ratio S/N for pyramid levels 1 and 3 and window size 6.

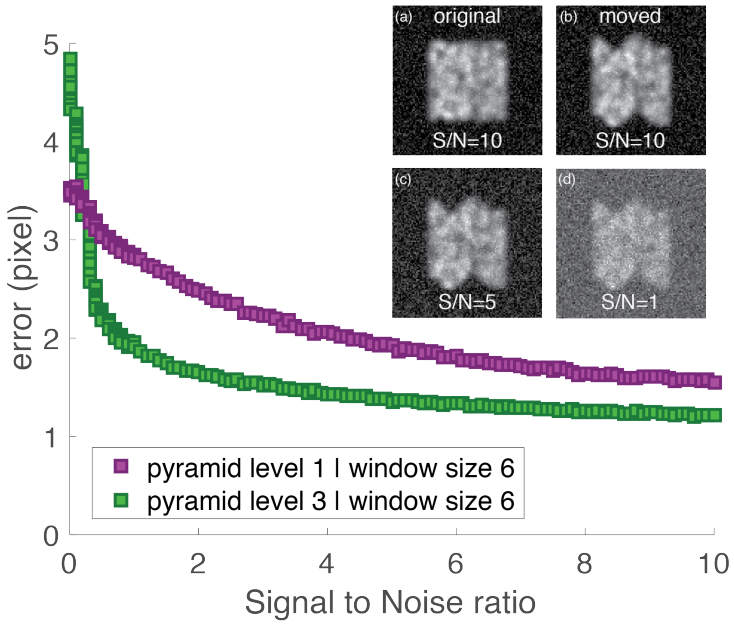

FIGURE A.6: Error plotted against signal to noise ratio for pyramid level 1 (purple) and pyramid level 3 (green) for window size 6. (a) original picture with S/N 10 and (b) the picture after displacement. (c) original picture with S/N 5 and (d) moved picture with S/N 1.

A.5.5.2 Autocorrelation

The challenge in the identification of peak in the autocorrelation analysis is to differentiate the signal from the noise. Therefore, we evaluated which height and which periodicity a peak extracted from the autocorrelation of white noise might have. In Figure A.7 i) white noise of 10 dB is depicted. We first performed an autocorrelation analysis on this signal. The calculated white noise is represented in Figure A.7 ii). A peak might be detected at 5 min with a value of correlation coefficient of 0.2. As a consequence, we discarded all peaks below this value as we would not be able to differentiate them from noise.
Moreover we calculated a cross correlation of two different white noise signals. As can be seen correlation coefficient values can reach values of 0.3. This means that when a peak of a signal reaches this value it can not be differentiated from noise. Therefore, this represents the limit of peak identification for cross correlation.
In Figure A.7 iv) we overlaid our initial signal of mesh displacement with 10 % white noise. Then, we performed autocorrelation analysis on the initial signal and the signal with artificially added noise (Figure A.7 v)). The peak height is decreased when noise is added, but peak position is not affected. This means that for noisy data, low peak heights can be expected.

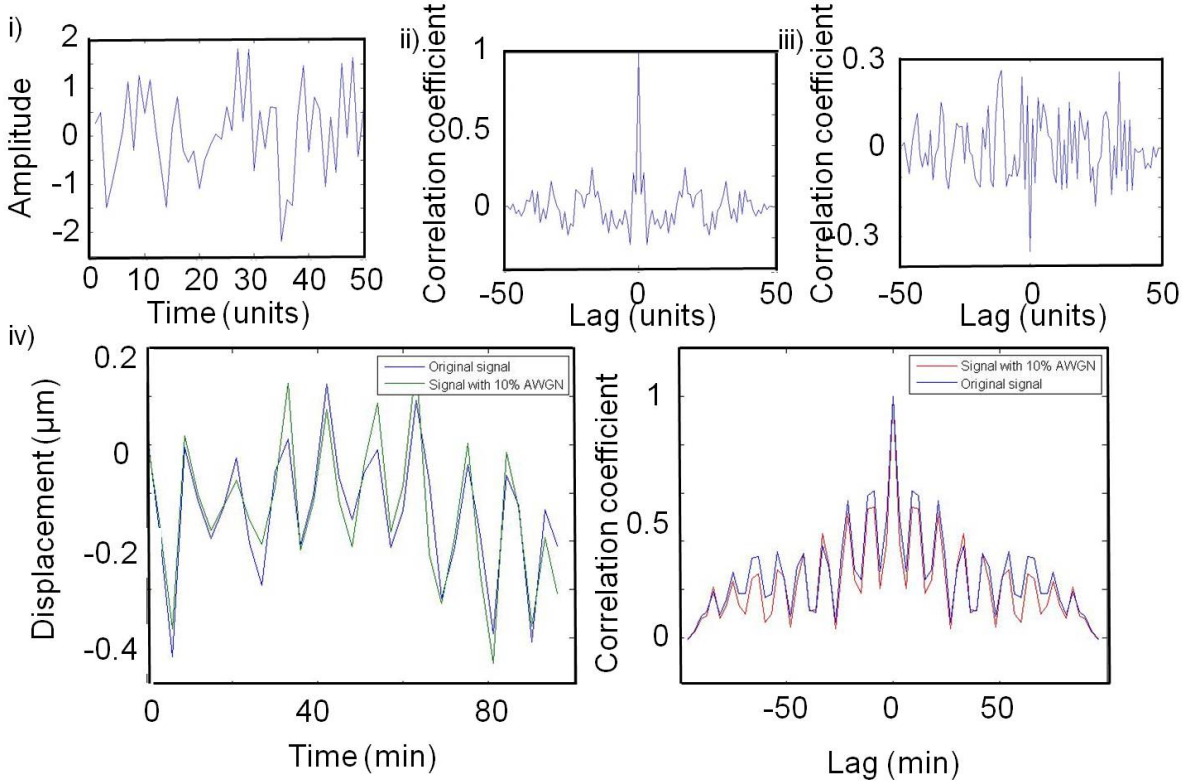

FIGURE A.7: i) Signal of 10% white noise. ii) Autocorrelation of i), peaks reach values of 0.2. iii) Cross correlation of white noise. iv) Calculation of displacement and calculation of displacement with 10% white noise. Result of autocorrelation. Peak height decreases, position stays unchanged.

A.5.5.3 Cross correlation peak finding

To evaluate how reliable we can identify a peak in the cross correlation analysis and how much the tracking of the nucleus plays a role, one cell has been tracked various times and the cross correlation calculated. In Figure A.8 the graphs are plotted. One can see that the value of the peak varies thus position of the peak which indicates the lag stays unchanged. Also the signal away from the central peak varies. As only the peak next

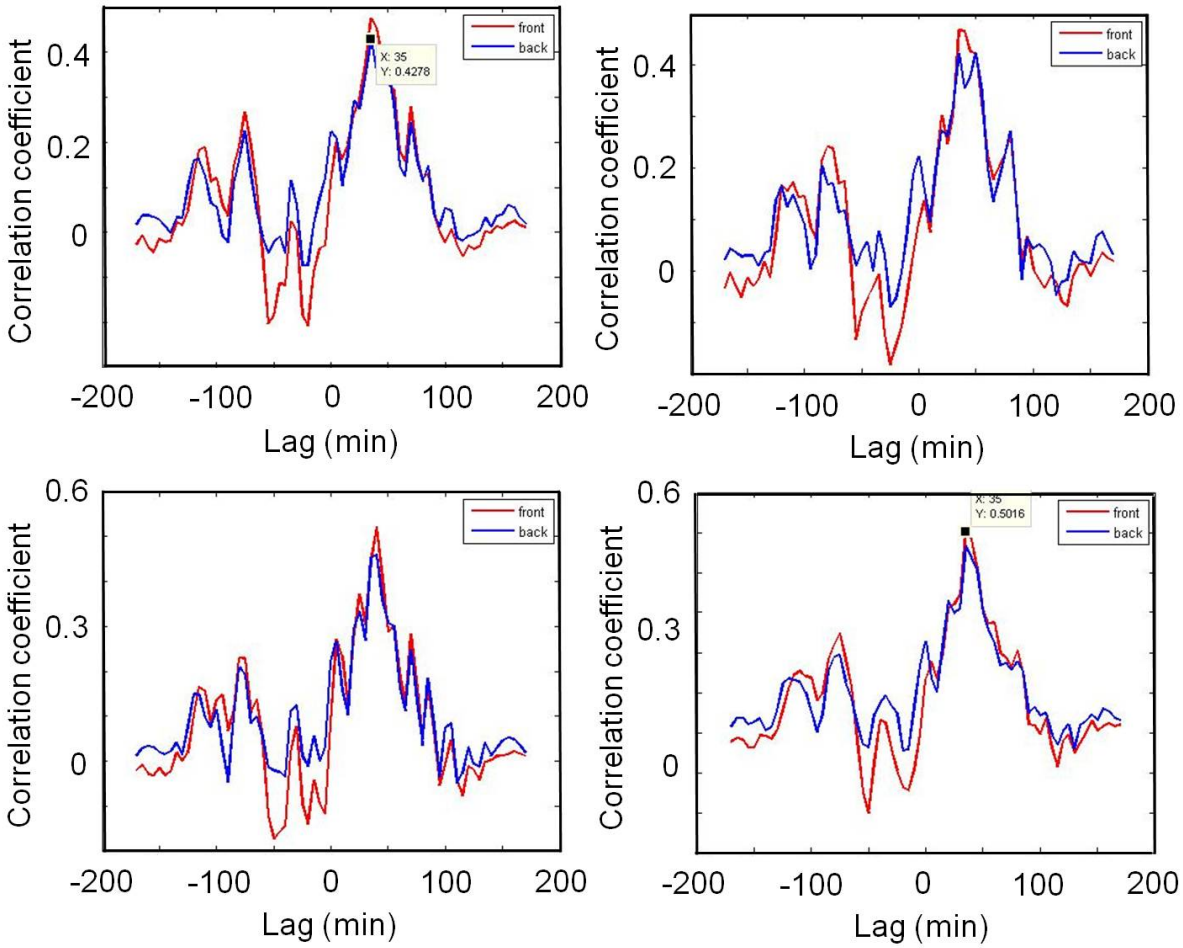

FIGURE A.8: Correlation coefficient of cross correlation analysis between displacement of mesh back (blue), front (red) and nucleus displacement. Tracking of nucleus back has been performed 4 times. Correlation coefficient value varies, peak position stays the same.

to zero is taken into account, we extract the same peak for each correlation analysis and thus obtain the same result for various trackings. We deduce that peak identification is reproducible.

A.6 Publications

Comelles, J., Caballero, D., Voituriez, R., Hortigüela, V., Wollrab, V., Godeau, A. L., Samitier, J., Martinez, E.,and Riveline, D. (2014). **Cells as active particles in asymmetric potentials: Motility under external gradients.** Biophysical Journal, 107(7), 1513-1522.

Contribution: I contributed to the experiments namely the zyxin-myosin transfections and provided a movie of cell migration on 2D imaging focal adhesions and stress fibers.

Marbach, S., Godeau, A. L., Riveline, D., Joanny, J. F., and Prost, J. (2015). **Theoretical study of actin layers attachment and separation.** European Physical Journal E, 38(11), 1-14. http://doi.org/10.1140/epje/i2015-15122-4

Contribution: I performed the experiments of this work and discussed results.

Article

Cells as Active Particles in Asymmetric Potentials: Motility under External Gradients

Jordi Comelles,[1,2,3] David Caballero,[1,2] Raphaël Voituriez,[7,8] Verónica Hortigüela,[4,5] Viktoria Wollrab,[1,2] Amélie Luise Godeau,[1,2] Josep Samitier,[3,5,6] Elena Martínez,[4,5,6] and Daniel Riveline[1,2,*]

[1]Laboratory of Cell Physics ISIS/IGBMC, CNRS UMR 7006 and University of Strasbourg, Strasbourg, France; [2]Development and Stem Cells Program, IGBMC, CNRS UMR 7104, INSERM (U964) and University of Strasbourg, Illkirch, France; [3]Nanobioengineering Group, Institute for Bioengineering of Catalonia (IBEC), Barcelona, Spain; [4]Biomimetic Systems for Cell Engineering, Institute for Bioengineering of Catalonia (IBEC), Barcelona, Spain; [5]Centro de Investigación Biomédica en Red en Bioingeniería, Biomateriales y Nanomedicina, Zaragoza, Spain; [6]Department of Electronics, University of Barcelona, Barcelona, Spain; [7]Laboratoire de Physique Théorique de la Matière Condensée, CNRS UMR 7600, Université Pierre et Marie Curie, Paris, France; and [8]Laboratoire Jean Perrin, CNRS FRE 3231, Université Pierre et Marie Curie, Paris, France

ABSTRACT Cell migration is a crucial event during development and in disease. Mechanical constraints and chemical gradients can contribute to the establishment of cell direction, but their respective roles remain poorly understood. Using a microfabricated topographical ratchet, we show that the nucleus dictates the direction of cell movement through mechanical guidance by its environment. We demonstrate that this direction can be tuned by combining the topographical ratchet with a biochemical gradient of fibronectin adhesion. We report competition and cooperation between the two external cues. We also quantitatively compare the measurements associated with the trajectory of a model that treats cells as fluctuating particles trapped in a periodic asymmetric potential. We show that the cell nucleus contributes to the strength of the trap, whereas cell protrusions guided by the adhesive gradients add a constant tunable bias to the direction of cell motion.

INTRODUCTION

Cell migration plays key roles in a variety of physiological processes, ranging from development (1) to pathological processes, such as cancer (2). Cells can migrate directionally, following a persistent trajectory along the same direction of an axis (3). Such cell behavior drives the tissue rearrangements that shape organs in embryos (4). Directed cell movement is also associated with cancer metastasis (5). In adults, dendritic cells migrate directionally from the interstitial space into the lymphatic vessels, thereby participating to the onset of the immune response (6). Altogether directional motility is a generic feature of living cells.

Mechanisms behind cell migration have been studied in several in vitro assays. Topographical features in the shape of grooves have been shown to guide nondirectional cell migration along the main axis of grooves in both directions, in a mechanism known as contact guidance (7–11). In these situations, cells align according to features much smaller than the size of the cell itself by attaching mainly to the top of the topographical structures (7,10,11). Furthermore, several studies report directional cell motion in vitro by imposing asymmetric cues to the cells. In addition to asymmetric one-dimensional paths, both chemical (12–15) and topographical (16–18), adhesive (19) and stiffness gradients (20) also direct cell migration. On these substrates, cell motion is often understood to be directional—with a persistent trajectory along the same direction of an axis— because the cell symmetry is broken by the external cues. For example, it was shown that there is greater activity of cell protrusions at the front of the cell than at its tail (21). However, when directional cell motion is achieved in these experiments, the cellular organelle setting directions is often not known. In addition, the prediction of cell direction as a function of the cues and geometries imposed is not straightforward. Finally, the quantitative comparison of cell motion with a model is often lacking. In light of these observations, new approaches that link the biology of the cell to the physics of living matter are required.

Here, we report a new, to our knowledge, assay in which we tested the effects of external cues on single fibroblast cell directed motion. The cellular mechanisms at play were identified and motions were quantified and compared with a model. Specifically, using substrates with ratchet-shaped topographical patterns, we show that the nucleus dictates the directions of cell movement through mechanical guidance. A ratchet stands as a paradigm for studying symmetry breaking (22–24). Directionality can be tuned when topography is combined with a superimposed fibronectin adhesion gradient. We observed competition and cooperation between the effects of the two external cues depending on their relative orientations. We adapt a theory of fluctuating particles trapped in a periodic asymmetric potential, introduced by Prost et al. (23,24), to model cell behavior.

Submitted December 16, 2013, and accepted for publication August 1, 2014.

*Correspondence: riveline@unistra.fr

Editor: Ewa Paluch.

0006-3495/14/10/1513/10 $2.00

http://dx.doi.org/10.1016/j.bpj.2014.08.001

We found that the nucleus contributes to the strength of the topographical trap, whereas cell protrusions guided by the adhesive gradients add a constant tunable bias to the motion.

MATERIALS AND METHODS

Substrate fabrication

The ratchet-shaped topographical pattern was made on Poly(methyl methacrylate) (PMMA) substrates. Topographical motifs were produced by standard photolithography and nanoimprint lithography (25,26). Briefly, first a SU-8-2015 (MicroChem Corp, Newton MA) positive master with microstructures was obtained by standard photolithography, the resulting mold was replicated on a poly(ethylene naphthalate) (Goodfellow, Huntingdon,UK) sheet (125 μm thick) by nanoembosing to obtain a negative replica. This secondary mold was then used to transfer the structures to the PMMA surface. The design of the structures is an array of triangles of 100 μm in length, 22 μm in width, and 1 μm in height, forming a ratchet-like topographic pattern (see Fig. S1, *b* and *c* in the Supporting Material) over a total area 25 mm in length and 1 mm in width. The dimensions of the triangles were chosen on the basis of the mean size of a NIH 3T3 cell (see Fig. S2). The triangle area (1100 μm^2) corresponds to the mean half-area of a NIH 3T3 fibroblast spread on a homogeneous fibronectin layer (100 ng.cm^{-2}).

The imprinted structures were characterized by means of scanning electron microscopy (Strata DB235, FEI, The Netherlands) and white light interferometry (Wyko NT110, Veeco Metrology, USA).

Gradient formation

The procedure used for gradient formation is described elsewhere (26). Briefly, a fibronectin gradient was generated on a previously hydrolyzed PMMA surface (either flat or structured) by means of a polydimethylsiloxane Y-shaped microfluidic channel (Sylgard 184 Silicon Elastomer, Dow Corning, Wiesbaden, Germany), which allowed the control of protein concentration across the channel. The flow rates and exposure times were set to obtain a linear protein gradient (26). A 1:39 mixture of fluorescently labeled and unlabeled fibronectin was used (20 μg ml^{-1} solution of fibronectin in phosphate buffered saline, rhodamine fibronectin from bovine plasma (Cytoskeleton, Denver, CO) and fibronectin from bovine plasma (Sigma-Aldrich, Saint-Quentin Fallavier, France). After gradient formation, the PMMA substrate was detached from the microfluidic channel. The remaining regions on the surface were saturated with a poly(L-lysine)-graft-poly(ethylene glycol) co-polymer (PLL-g-PEG) molecule (PLL (20)-g [3.5]-PEG (2), Susos, Dübendorf, Switzerland) to prevent adsorption of molecules from the cell culture medium and to reduce nonspecific cell adhesion. The shape of the fibronectin gradient was checked before each experiment by fluorescence microscopy (Fig. S1, *d* and *f*), with a CKX41 microscope (Olympus) using the Wasabi acquisition system (Hamamatsu) and a cooled couple-charge device camera (Hamamatsu). Homogenous fibronectin surfaces (either flat or structured) were achieved using the same microfluidic system. For this purpose, only the fibronectin solution was flowed through the channel and with the conditions used for high-density fibronectin regions of the gradient (100 ng.cm^{-2}) (26).

Cell migration experiments

The NIH 3T3 mouse embryonic fibroblast cell line (ATCC) was grown for 3 days at 37°C in Dulbecco's modified Eagle medium (D-MEM) (Invitrogen, Cergy Pontoise, France) supplemented with 10% bovine calf serum (BCS) (Invitrogen, Cergy Pontoise, France). Before the experiments, cells were trypsinized and replated on the PMMA surface in D-MEM with 10% BCS. After 20 min, unattached cells were removed by washing with fresh medium. Finally, for time-lapse experiments the medium was replaced by L-15 (Leibovitz's L-15 medium, Invitrogen, Cergy Pontoise, France) with 1% BCS serum.

Cells were observed under a CKX41 Olympus microscope using a 4× phase-contrast objective for around 48 h at 37°C. Images were acquired every 5 min. A 20× phase-contrast objective was used for high-magnification observations.

Cell migration experiments-side view

NIH 3T3 fibroblasts were plated on a glass coverslip and incubated for 1 h in the incubator. The coverslip was held by two binder clips. Clips allowed to place the coverslip vertically oriented under the microscope. Cells were visualized on the side in L-15 medium with 10% BCS.

Transfections and staining

NIH 3T3 fibroblasts were transfected with zyxin-red fluorescent protein (RFP) and nonmuscle myosin heavy chain II - Green Fluorescent Protein (called here myosin-GFP). Transient transfection was performed 1 day before experiment using Lipofectamine 2000 (Life Technologies), according to the manufacturer's instructions. Cells were fixed using 3% PFA (Sigma-Aldrich), and nuclei were stained with DAPI.

Cell trajectory evaluation

The centroid trajectories of cells were tracked using the manual tracking plug-in in ImageJ (http://rsb.info.nih.gov/ij, NIH). Data analysis was performed using a custom-made code in MATLAB (The MathWorks, Natick, MAA). Cell positions were characterized by a vector $\mathbf{r}(t)$, with t denoting time and $\mathbf{r}$ position in space (bold letter refers to a vector). Every recorded cell position during the time-lapse experiment was defined as $\mathbf{r}_i = \mathbf{r}(t_i)$, where $t_i = i\Delta t$ are the times of recording and Δt denotes the duration of time-lapses. The vector difference between two positions is then defined as $\Delta\mathbf{r}_{ij} = \mathbf{r}_i$-$\mathbf{r}_j$ and its length $||r_i||$ and angle with the x axis of the frame of reference of the laboratory $\cos(\theta_{ij}) = \Delta\mathbf{r}_{ij}\cdot\mathbf{i} / ||\Delta\mathbf{r}_{ij}||$, can be computed. To describe cell trajectories, a displacement vector ($\boldsymbol{\delta}$) and an angular distribution $\{\theta_{ij}\}$ were used. The displacement vector is calculated as the vector difference between the initial ($t = t_0$) and final point ($t = t_f$), $\boldsymbol{\delta} = \mathbf{r}(t = t_f) - \mathbf{r}(t = t_0)$. And the angular distribution was obtained from $\cos(\theta_{ij})$, being $i\Delta t$ - $j\Delta t = 60$ min (see Fig. S3). This duration was longer than the 5 min time-lapse acquisition, but it captured displacements within the resolution of our experiment. >30 cells from at least 3 independent experiments were evaluated for each configuration.

When modeling cell trajectories, we focus our study on persistent movement (27), i.e., migrating without stopping. We define a cell pause when its centroid is still for 30 min within our spatial resolution; a new persistent trajectory then starts. Our measurement of steps in lattice units evaluates persistent trajectories and conditional probabilities with this rule.

RESULTS

Directing cell migration with a ratchet-like topography

We developed a topographical ratchet-like surface that was combined with a fibronectin coating of spatially controlled density (Fig. 1 and Fig. S1). We first tracked cells moving on a ratchet-like surface covered with a homogeneous layer of fibronectin (see Fig. 1 *c*, *left* and Movie S1). These trajectories were compared with those of cells moving on a flat surface covered with the same density of fibronectin

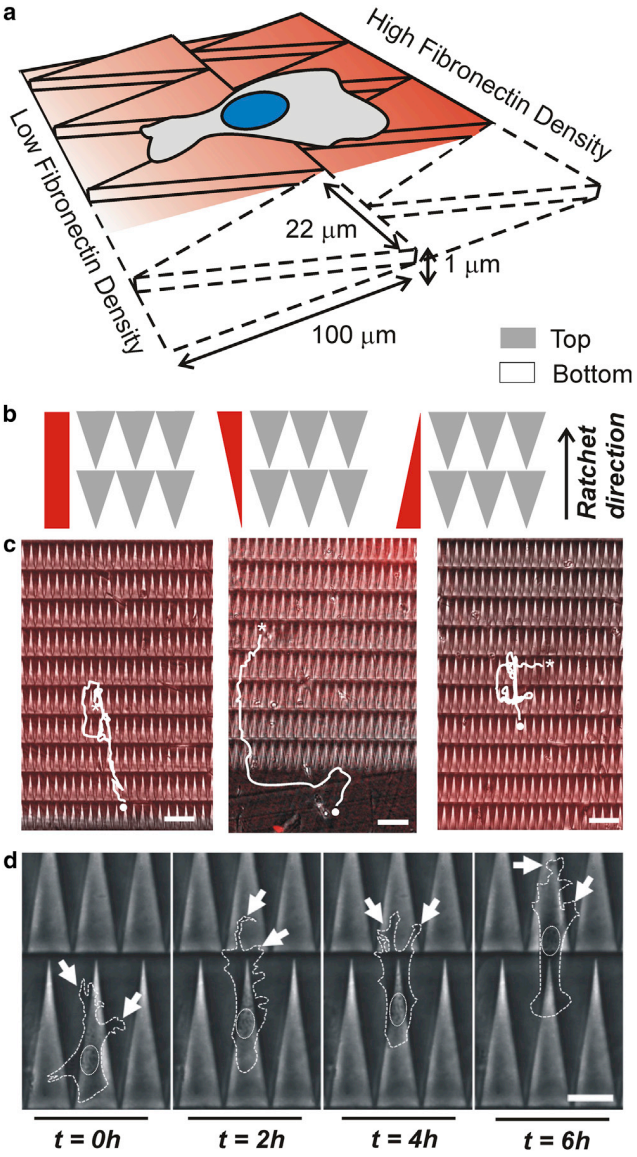

FIGURE 1 The motility assay. (*a*) Schematics of the experimental setup. Cells moved on topographical ratchets coated with fibronectin. The lattice unit of triangular shape measured 22 μm in width, 100 μm in length, and 1 μm in height. (*b*) Experimental conditions: topographical ratchet with homogeneous fibronectin coating; fibronectin gradient in the direction of the ratchet (indicated by an *arrow*); and fibronectin gradient against the direction of the ratchet. (*c*) Cells moving on topographical ratchets combined with homogeneous fibronectin coating, gradient up and gradient down, respectively. In white, cell trajectory, the red signal shows fibronectin, and • and * the start and end of the trajectories, respectively. Scale bar 100 μm. (*d*) Specific time sequence of a cell moving over topographical motifs. In this case, the cell migrates directionally along the bottom triangles. White arrows highlight cell protrusions. Scale bar 20 μm. To see this figure in color, go online.

(Fig. 2 *b*, configuration (i) and (ii)). Cells moved freely on the flat surface, leading to isotropically distributed tracks (Fig. 2 *b* configuration (i)). In contrast, ratchet-like patterns oriented the direction of cell migration along the *y* axis (Fig. 2 *b* configuration (ii)). We confirmed the isotropic behavior of cells on flat surfaces in the angular distribution plot of cell directions every 60 min (see Fig. 2 *c* configuration (i) *red curve*), where no peak was observed (see Fig. S4 *a*). Similarly, we observed an angular distribution asymmetry for cells moving on the topographical pattern (see Fig. 2 *c* configuration (ii)) with a primary peak ($\theta_1 = 86 \pm 20$ (°)) and a secondary peak ($\theta_2 = 264 \pm 29$ (°)), along the ratchet directions (Fig. S4 *b*). We next plotted the mean displacement vector, i.e., the averaged sum of vectors between the start and end points of each trajectory (see Fig. 2 *c* configuration (i) and (ii) *green arrow* and Fig. S5). The vectors indicated that net motion was isotropic and random on flat surfaces, whereas it was rectified toward the positive *y* axis on the ratchet pattern. Previous gradient-free strategies relied on cell confinement, either chemical (12–15) or physical (16–18). However, here we show that cells on an asymmetric topographical pattern, with no restriction in adhesiveness or physical confinement, moved in the direction imposed by the features of the ratchet itself.

Cell nucleus sets the direction

To further explore this symmetry breaking in cell migration, we analyzed cell behavior at a higher magnification (Movie S2 and Movie S3). When the cell nucleus interacted with the side walls of the triangular structures, the nucleus trajectory was rectified, which led to a change in the whole cell trajectory. A typical example is shown in Fig. 3 *a*: when the cell was moving from a top triangle (*dark*) to a bottom triangle (*bright*), the nucleus experienced two rectifications of trajectory (Fig. 3 *a*, *left* and Movie S2). On the other hand, a cell first performing a lateral movement was then directed toward the vertex of the triangle (Fig. 3 *a*, *right* and Movie S3). The correlation of the nucleus trajectory and the topography walls points to the occurrence of a contact interaction, which would explain the asymmetry observed in cell migration. This evidence is supported by inhomogeneity of the density and shape of nuclei outlines in Fig. 3 *a*. This finding indicates a mechanical interaction between the topographical walls and the cell nucleus.

We next obtained quantitative insight into this nucleus—wall mechanical interaction. We measured the fraction of time that the nucleus of migrating cells spent at the top and bottom of the structures, as well as the percentage of nuclei placed at the top and bottom of the motifs on fixed samples. In the former case, the nucleus was located $63 \pm 7\%$ of the time on the bottom triangles (Fig. 3 *b*). This tendency was maintained in fixed samples ($69 \pm 3\%$) (Fig. 3 *c*). Moreover, a noneven distribution of cell nucleus position was observed in the ratchet framework. We superimposed the nucleus position of >400 cells on a single ratchet unit and generated the corresponding color map (Fig. 3 *d*). Most of the nuclei were distributed in the widest region of a bottom triangle. This finding suggests

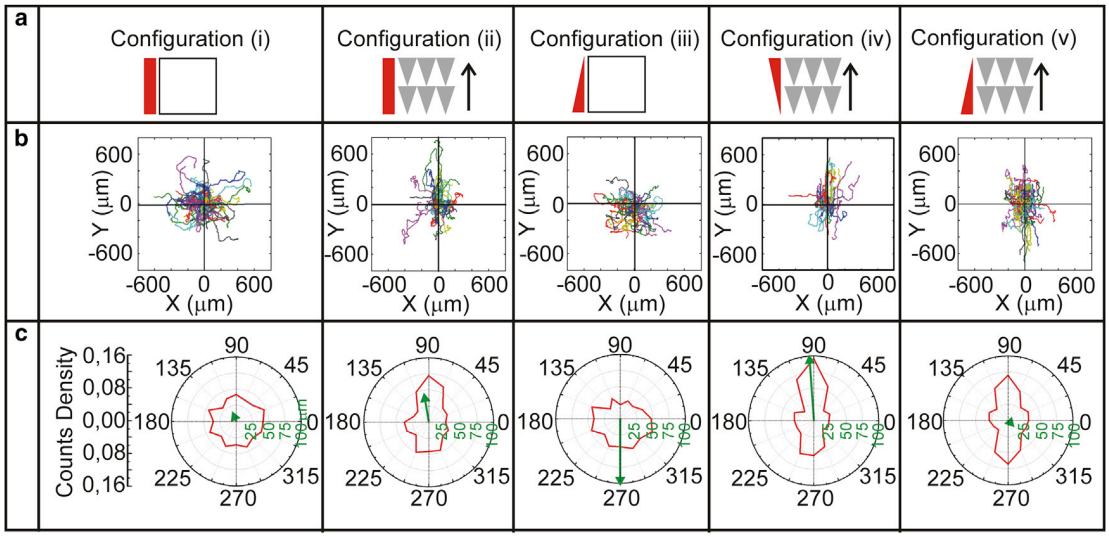

FIGURE 2 The cell trajectories. (*a*) Experimental configurations: (i) flat surface coated with a homogeneous layer of fibronectin, (ii) topographical ratchet coated with a homogenous layer of fibronectin, (iii) flat surface coated with a fibronectin gradient, (iv) topographical ratchet coated with a fibronectin gradient up, and (v) with a fibronectin gradient down. (*b*) Merge of cell trajectories for each configuration during the same total duration (48 h). All tracks start at the origin of the graph. $N_i = 6$, $n_i = 70$, $N_{ii} = 4$, $n_{ii} = 30$, $N_{iii} = 3$, $n_{iii} = 40$, $N_{iv} = 3$, $n_{iv} = 33$, $N_v = 3$, $n_v = 62$ (N number of biological repeats and n number of cells analyzed). (*c*) Angular distribution and displacement vectors. Red curve represents the histogram of the migration angle (every 60 min, $n_i = 2253$ steps, $n_{ii} = 953$ steps, $n_{iii} = 1275$ steps, $n_{iv} = 990$ steps, $n_v = 2060$ steps) and the green vector the mean displacement vector (the sum of the vectors between the start and end points of each cell, averaged by the number of cells $N_i = 6$, $n_i = 70$, $N_{ii} = 4$, $n_{ii} = 30$, $N_{iii} = 3$, $n_{iii} = 40$, $N_{iv} = 3$, $n_{iv} = 33$, $N_v = 3$, $n_v = 62$). The green scale corresponds to the length of the vector in μm. To see this figure in color, go online.

that the topographical ratchet pattern traps the nucleus in an analogous manner as an energy potential well would trap a particle.

To further study the nature of this interaction, we analyzed whether the nucleus shape and orientation were altered by the topographical patterns (see Fig. S6 and Fig. S7). For this purpose, we fit the nucleus edge to an ellipse and measured the major axis a, the minor axis b, and the angle $\boldsymbol{\alpha}$ between the ellipse and the laboratory framework axis (Fig. 3 *e*). On fixed samples, cell nuclei located at the top of the triangles were more elongated than those at the bottom (Fig. S6 *e* and Fig. S6 *f*). Moreover, nuclei showed a random angular distribution on the top triangles (Fig. 3 *f*). In contrast, a peak distributed around 90° appeared when nuclei were at the bottom. To obtain further insight into the dynamical interaction between the nucleus and the topographical landscape, change in nucleus orientation was studied in time-lapse experiments. The following results show that the nucleus is interacting with the topographical ratchet: i), as it can be seen in the examples shown in Fig. S7, *a* and *b*, nucleus orientation changed when moving from top to bottom; ii), nucleus tended to realign parallel to the direction set by the topographical walls; iii), nuclei were randomly oriented when moving on top of triangles, and they oriented around 90° when moving in bottom triangles (Fig. S7 *c*), as observed in fixed samples (Fig. 3 *f*); iv), whenever nuclei interacted with the topographical walls, they reoriented accordingly to the directions set by the walls (Fig. S7 *d*). These observations suggest that the orientation and the mechanical deformation of the nucleus depend on its interaction and its position on the ratchet framework (see also (28) for a related discussion based on a different setup). This feature is essential in the model proposed below.

To analyze the role of the cytoskeleton in cell behavior on topographical ratchets, we transfected 3T3 fibroblasts with myosin-GFP and zyxin-RFP (see Movie S4). No striking correlation was observed between protrusions and the topographical pattern. Cells spread on both top and bottom triangles, and there was no preferential orientation observed in cell shape (see Fig. S8 *a*). Moreover, peripheral focal contacts could be observed on top triangles, bottom triangles and, eventually at the topographical walls (Fig. S8 *b*). In contrast, we observed the appearance of focal contacts correlating with the topographical walls close to the nucleus (see Movie S5 and Fig. S8 *c*). When the nucleus contacted a wall, focal contacts nucleated at the location of the neighboring wall. These focal contacts then elongated and the nucleus passed over the structure. When the nucleus had passed the structure, the zyxin signal decreased and eventually disappeared. These observations support the idea of a mechanical interaction between the topographical pattern and the nucleus.

Tuning ratchet efficiency by using adhesive gradients

We addressed whether, in addition to the role of the nucleus setting cell direction based on the ratchet topography, we

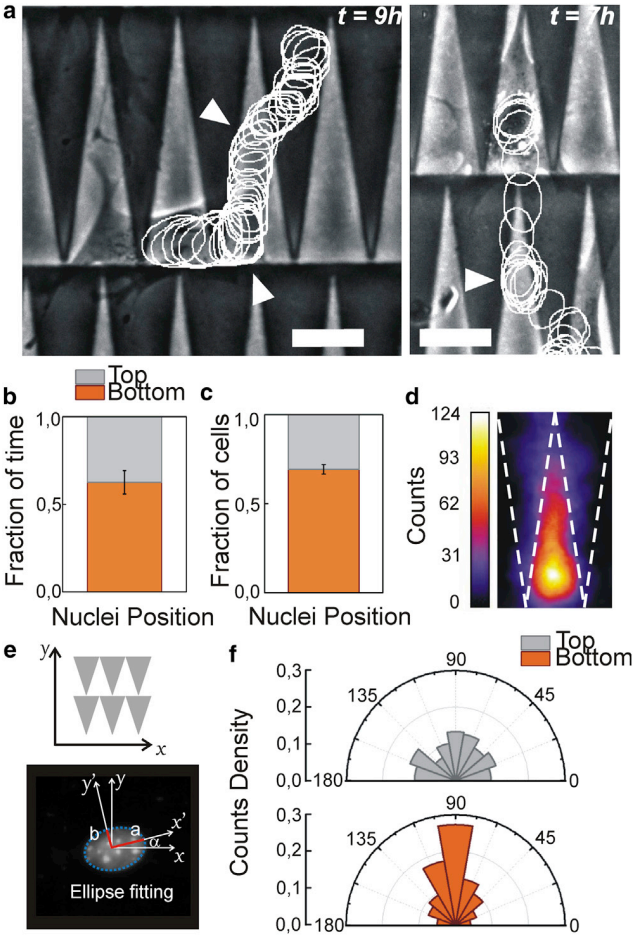

FIGURE 3 The role of the nucleus. (*a*) Image of a cell migrating in topographical ratchets coated with a homogenous layer of fibronectin. White circles outline the positions of the nuclei at various time points (every 15 min). White arrows show changes in directions after nucleus-wall contacts. Scale bar 20 μm, *t*: time spent to perform this particular movement. (*b*) Fraction of time that nuclei spent on top triangles and on bottom triangles during the motion. (total time $>$ 8 h, $N = 4$ experiments, $n = 11$ cells, mean values $\pm$ standard errors). (*c*) Fraction of cells in which the nucleus was positioned on top triangles and on bottom triangles on fixed samples ($N = 3$ experiments, $n = 654$ cells, mean values $\pm$ standard errors). (*d*) Color map of the mean nucleus position on a lattice unit. Bottom triangles pointing up and top triangles pointing down ($N = 3$ experiments, $n > 400$ cells). (*e*) Scheme for the ellipse fit of nuclei. Major (*a*) and minor (*b*) axes of the ellipse were obtained using ImageJ, and the relative angle between the ellipse and the ratchet framework was measured. (*f*) Plot of the nuclei orientation, histogram of the angles α for nuclei at the top (*gray*) and at the bottom (*orange*) of the structures ($N = 3$ experiments, $n = 654$ cells). To see this figure in color, go online.

could externally induce cell polarization and asymmetry in lamellipodia activity, thus tuning ratchet efficiency. Fig. 2 *b* configuration (iii) shows the cell trajectories moving on a fibronectin gradient on a flat surface (gradient slope 0,1 $(\text{ng}\cdot\text{cm}^{-2})\cdot\mu\text{m}^{-1}$). Compared to configuration (i), cell trajectories were not restricted to the *x* or *y* axis, but were biased toward regions of high fibronectin density. The gradient directed cell motion from weakly adhering regions to strongly adhering ones (19,29). This result was further confirmed by both the angular distribution and the mean displacement vector (Fig. 2 *c*, configuration (iii) and Fig. S4 *c* and Fig. S5).

We next combined the fibronectin gradient with the topographical ratchet (change of fibronectin density within 1 triangle is 10 $\text{ng}\cdot\text{cm}^{-2}$). We first tested the situation where the gradient and the ratchet rectified cell motion to the same direction (Fig. 1 *c*, *middle* and Movie S6). Similar to the ratchet case, cell trajectories were distributed along the *y* axis and biased toward positive *y* values (Fig. 2 *b* configuration (iv)). However, compared to the ratchet alone, the angular distribution in this configuration was more biased to the 90° direction (primary peak $\theta_1 = 92 \pm 18$ (°) and secondary peak $\theta_2 = 262 \pm 22$ (°)) (see Fig. 2 *c* configuration (iv) and Fig. S4 *d* and Fig. S5), suggesting an increase in the rectification efficiency. This result was further confirmed by the mean displacement vector (Fig. 2 *c* configuration (iv)).

We finally set the gradient and the ratchet in opposite directions (Fig. 1 *c*, *right* and Movie S7). In this case, the tracks were again aligned with the *y* axis. The angular distribution showed two main directions with similar probability: primary peak $\theta_1 = 92 \pm 18$ (°) and secondary peak $\theta_2 = 269 \pm 19$ (°) (Fig. 2 *c* configuration (v) and Fig. S4 *e* and Fig. S5). This finding indicates that there was still a preferential cell movement along the *y* axis, but there was no net bias in cell motion rectification. Configuration (v) showed a mean displacement vector similar to that of (i) (Fig. 2 *c*). The ratchet efficiency was reduced and cell motion was no longer rectified. Thus, the ratchet and gradient competed.

Modeling cell trajectories

To analyze the degree of bias efficiency, we discretized cell motion in lattice units (l.u.) (1 triangle = 1 l.u.). We then quantified the number of steps that cells took in each direction and classified them into three types: 1), positive (+), when a cell moved from one row of triangles to the next in the ratchet direction; 2), minus (−), when the motion was in the opposite direction; and 3), lateral (0), when cells persistently moved laterally within one row of triangles, either right or left by symmetry (Fig. 4 *a*). We then obtained the probability of each type of step (Π_+, Π_-, Π_0), which allowed comparison between configurations (Fig. 4 *a* – *solid arrows* – and *b*). The bias (Fig. 4 *c*) associated with the ratchet (configuration (ii)) was $\Pi_+/\Pi_- = 1.42 \pm 0.07$. Bias increased to 1.64 ± 0.15 when the ratchet and the gradient were cooperating (configuration (iv)). Finally, the competition (configuration (v)) between the ratchet and the gradient led to a bias of $\Pi_+/\Pi_- = 1.04 \pm 0.26$, in agreement with the tendency observed for the displacement vectors. Therefore our results show that the bias in cell migration produced by the ratchet could be increased/decreased by superimposing an adhesive gradient in the same or opposite directions.

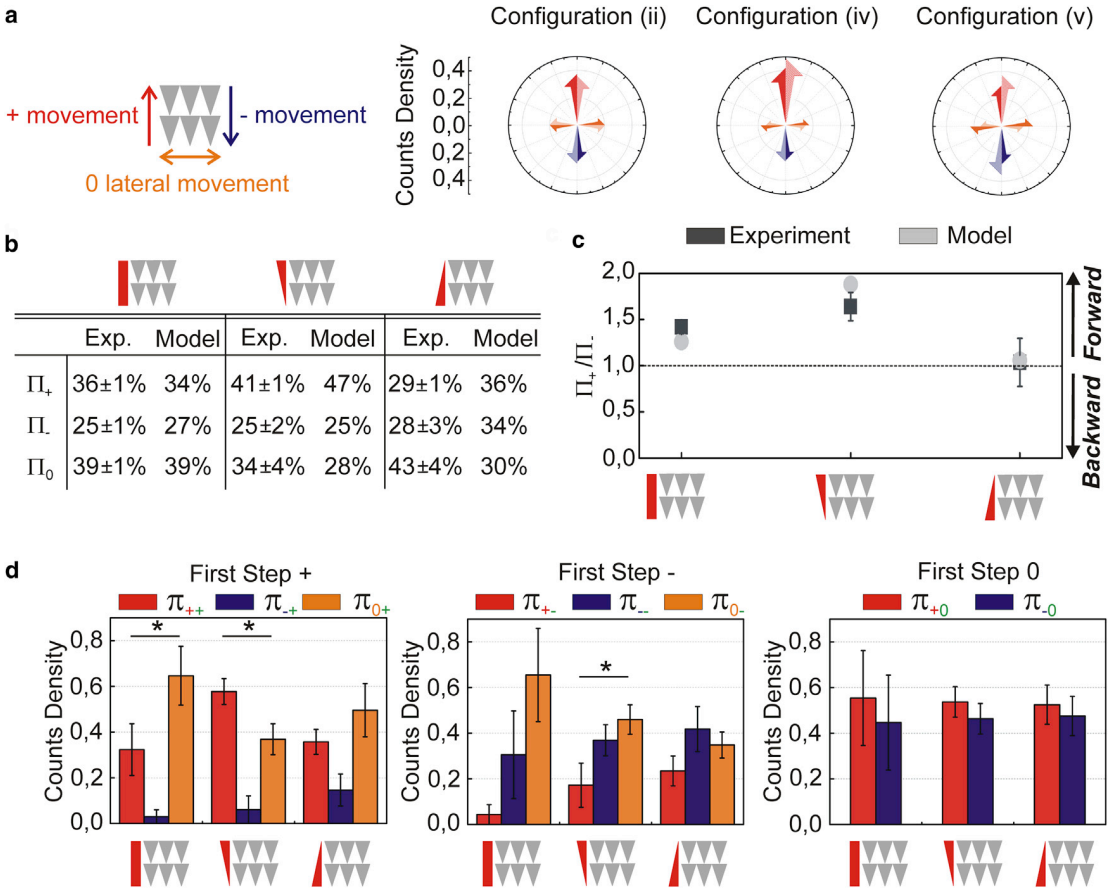

FIGURE 4 Comparisons between the experiments and the model. (*a*) Classification of the cell movements used to quantify the ratchet bias. Mean probabilities to move toward a given direction in configurations (ii), (iv), and (v) respectively. (*Solid half arrows* and percentages correspond to experimental values, *patterned half arrows* correspond to the values predicted by the model). (*b*) Comparison of the experimental and theoretical values of the moving probabilities (Π_i) for each configuration (Mean values ± standards error, $N_{ii} = 4$ experiments, $n_{ii} = 214$ movements, $N_{iv} = 3$ experiments, $n_{iv} = 147$ movements, $N_v = 3$ experiments, $n_v = 367$ movements). (*c*) Comparison of the experimental and theoretical biases Π_+/Π_- for the configurations (ii), (iv), and (v). (*d*) Probabilities of the eight possible transitions in each of the three experimental configurations (mean values ± standards error, First step + $N_{ii} = 4$ experiments, $n_{ii} = 59$ transitions, $N_{iv} = 3$ experiments, $n_{iv} = 37$ transitions, $N_v = 3$ experiments, $n_v = 63$ transitions, First step 0 $N_{ii} = 4$ experiments, $n_{ii} = 38$ transitions, $N_{iv} = 3$ experiments, $n_{iv} = 23$ transitions, $N_v = 3$ experiments, $n_v = 66$ transitions, First step - $N_{ii} = 4$ experiments, $n_{ii} = 39$ transitions, $N_{iv} = 3$ experiments, $n_{iv} = 29$ transitions, $N_v = 3$ experiments, $n_v = 66$ transitions). (*) statistically significant differences $p < 0.05$. To see this figure in color, go online.

To further analyze cell trajectories and assess the importance of potential memory effects, we experimentally measured the conditional probability of performing a +, −, or 0 step, which depends on the previous move performed in the absence of pauses, i.e., during a persistent trajectory (Fig. 4 *d* and Fig. S9; see Methods). More precisely, these transition probabilities π_{ji}, where $i,j = +, -, 0$, are defined as the probability that a cell performs a step in the direction j, knowing that the previous step was performed in direction i. Normalization then imposes $\pi_{+i} + \pi_{-i} + \pi_{0i} = 1$. The π_{ji} encodes two effects responsible for the direction of migration: the local asymmetry of both the topographic landscape and adhesion profile, and the direction of the previous move, which here encodes the polarization state of the cell. We have $\pi_{++} \neq \pi_{+-}$ (see Fig. 4 *d*): this clearly shows that the memory of the previous move influences the direction of the next one. This first move is likely to polarize cells (Fig. 1 *d*) and to affect the internal organization of organelles. We hereafter assume that the dependence on the previous only (1 step memory) is sufficient to describe cell trajectories, and that the dependence on earlier moves can be neglected. The direct analysis of such longer range memory would require longer persistent trajectories with no pauses and is not statistically significant with our data sets (4 ± 1 steps per persistent movement—including 0 steps—on average). Under this minimal hypothesis, cell motion can be modeled as a persistent random walk, an approach that has proved useful in the context of cell trajectory analysis (30,31).

This model allowed us to relate the observed large-scale properties in the trajectories to elementary transition probabilities π_{ji} introduced previously. We derive in the

Supporting Material the expressions of the main characteristics of the trajectories as a function of π_{ji} only: the stationary probabilities Π_+, Π_-, Π_0, which provide the probabilities that a step is performed in direction $+$, $-$, 0 in a steady state, regardless of the nature of the previous step; and the persistence lengths, which give the mean number of consecutive steps performed in a given direction. With the experimentally measured values of π_{ji}, we computed the theoretical values of Π_+, Π_-, Π_0, and the persistence lengths. As seen in Fig. 4 *a* (*patterned arrows*) and Fig. 4 b, the predicted values of Π_+, Π_-, Π_0, and the biases (Fig. 4 *c*) are in good agreement with the experimental observations, as well as persistence lengths (see Fig. S10). The observed discrepancy in configuration (v) results from steps 0 where cells can be in any polarity state or even unpolarized, which is not taken into account explicitly in the model; this is especially relevant in this configuration where two external cues are competing. This finding indicates that cell trajectories are well described by persistent random walks, which constitute a minimal model that takes into account both the cell polarization state (through the memory of the previous step) and external cues that can bias the motion.

Finally, we aimed to link the π_{ji} to the properties of the local environment of the cell, i.e., both topography and adhesion properties. We followed the picture of a particle in a tilted washboard potential, as introduced in Constantini et al. (32). Therefore, the central hypothesis was, as suggested previously, that cell movement is impaired mainly by the nucleus, which must mechanically deform to pass the successive obstacles formed by the topographic landscape (28), as observed in Fig. 3. Here, we assume that the nucleus is confined to the substrate by a normal force (for example the vertical component of the pulling force mediated by stress fibers (33)) (see Fig. 5 *a*). Actually, by imaging cell migration on the side on flat surfaces, we could observe that i), nucleus was occupying a large fraction of cell volume; ii), its height was varying with time and was correlated to the cell spreading; and iii), the nucleus was very close to the surface, suggesting a potential sensitivity to any change in surface profile (see Fig. S6 *a* and Movie S8). Moreover, when observing NIH 3T3 fibroblast transfected with myosin-GFP on flat surfaces, it can be seen that the appearance of prominent stress fibers correlate with an increase of nucleus projected area, suggesting that it is indeed flattening (see Fig. S6 *b*). These observations point to the presence of a normal force confining the nucleus to the surface related to stress fibers, which eventually correlate with the walls of the topographical pattern (Movie S5 and Fig. S8 *c*).

This implies that the cell nucleus effectively moves in an energetic potential $U_E(x,y)$ (Fig. 5 *b*), corresponding to the stored mechanical energy, which we propose is of elastic origin in a first approximation (34). Following the previous observation that the nucleus deformation depends on the

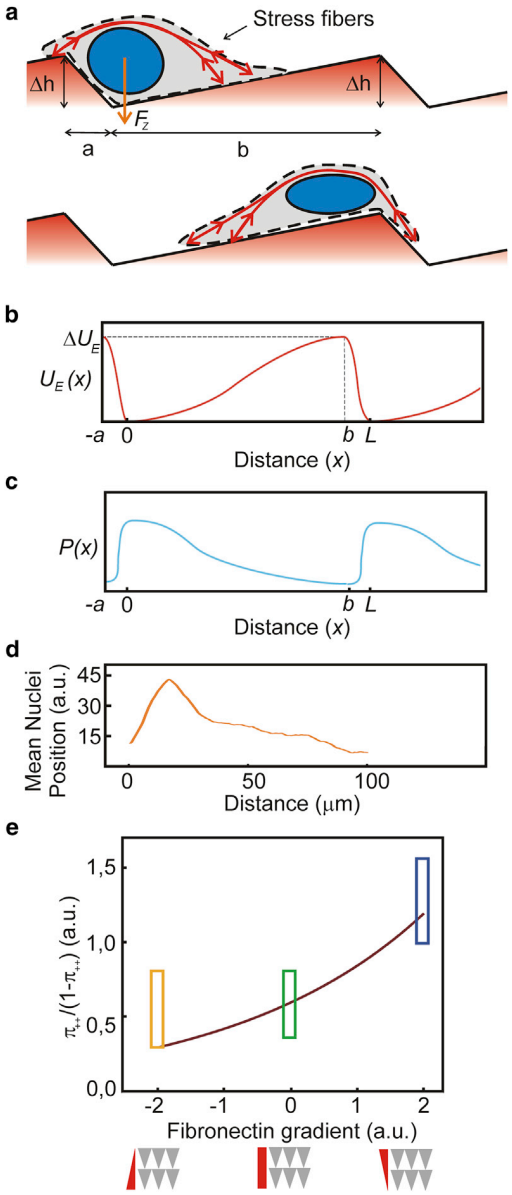

FIGURE 5 Cells as active particles in asymmetric potentials. (*a*) Schematics of a cell in an asymmetric topographical landscape. Cell nucleus experiences a normal compressive force F_z, imposing a mechanical deformation to pass the successive obstacles. (*b*) Energetic potential $U_E(x,y)$. (*c*) Probability distribution $P_n(x)$ of the nucleus position at steady state. (*d*) Mean nuclei position, obtained experimentally from Fig. 3 *d*. (*e*) Dependence of π_{ij} on the fibronectin gradient. The brown curve represents the evolution of the ratio $\pi_{++}/(1-\pi_{++})$ for different fibronectin gradient slopes. The yellow, green, and blue boxes are the measured values for this ratio in the three experimental configurations (v, ii, and iv), respectively. To see this figure in color, go online.

position in the ratchet, we assume that the energetic potential $U_E(x,y)$, which we do not aim to determine explicitly here, is directly correlated to the height profile $h(x,y)$ of the landscape (see Fig. S1). The resulting probability distribution $P_n(x)$ of the nucleus position in a steady state can readily be deduced and peaks at the minima of h (see

Fig. 5 *c*). This description is supported by the experimental observation that the stationary distribution of nuclei positions peaked at the location of local minima of $h(x,y)$ (Fig. 3 *d* and Fig. 5 *d*). The period of the ratchet in the y direction is denoted by $L = a + b$. The profile $U_E(x,y)$ is assumed to successively decrease with a slope $\Delta U/a = F_-$ over a distance a, and then increase with slope $\Delta U/b = F_+$ over a distance b, with $(a < b)$ (see Fig. 5 *c*). This shows that at least a force F_+ (*resp.* F_-) must be exerted along the $+y$ (*resp.* $-y$) direction to induce a step in the $+y$ (*resp.* $-y$) direction; the condition $F_+ < F_-$ then clearly indicates that the direction $+$ is favored.

To estimate the propulsion force experienced by a cell, we consider a minimal model of cell locomotion and assume that the cell propulsion force is mediated by individual protrusions. Following ideas developed in (27), we introduce the mean number (per unit time) of protrusions stabilized in direction i, z_{ij}, where $i = +,-$. Following the finding that the direction of motion depends on the direction of the previous move, z_{ij} depend on the direction of the previous move. Note that here we focus on the ratchet direction $+/-$, but similar definitions would hold for the direction 0. We define the probability $p(n_+)$ that n_+ protrusions are stabilized in the $+$ direction (and similarly in the $-$ direction). We assume that it follows a Poisson distribution of mean $z_+ \tau_0$, where τ_0 is the mean duration time of an elementary step and the dependence on the previous move is omitted for clarity. We then introduce the asymmetry of stabilized protrusions $\Delta = n_+ - n_-$. This quantity is shown in the Supporting Material to be distributed according to

$$P(\Delta) = e^{-(z_+ + z_-)\tau_0} \left(\frac{z_+}{z_-}\right)^{\Delta/2} I_\Delta(2\tau_0\sqrt{z_+ z_-}), \qquad (1)$$

where $I_\Delta(x)$ is the first kind, to our knowledge, of modified Bessel function of Δ-th rank. Assuming that each efficient protrusion transmits a unit force (in the properly normalized unit of force), Eq. 1 gives the probability that a total force Δ is transmitted by protrusions.

Finally, the condition $\Delta \geq F_+$ that motion occurs in the $+$ direction enables an explicit calculation of π_{+i} that reads:

$$\pi_{+i} = e^{-(z_{+i} + z_{-i})\tau_0} \sum_{\Delta \geq F_+} \left(\frac{z_{+i}}{z_{-i}}\right)^{\Delta/2} I_\Delta(2\tau_0\sqrt{z_{+i} z_{-i}}). \qquad (2)$$

A similar expression holds for π_{-i}.

These expressions combine in a simple form the effects of the topographic ratchet (through the dependence on F_+), adhesion properties (encoded in z_{ji}), and the polarization state of the cell (encoded in the dependence on the previous move) on cell motion. They allow a semiquantitative discussion of the experiments in configurations (ii), (iv), and (v). In particular, the bias can be quantified here by the ratio π_{+i}/π_{-i}, and was found, as expected, to increase with the ratchet asymmetry b/a and the efficiency of protrusion activity z_{ji}. Assuming that the mean number of effective protrusions is proportional to the local concentration of fibronectin, one can write $z_{+i} = z_{-i} + \alpha\nabla c$. The dependence of π_{ij} on the fibronectin gradient can then be calculated. Fig. 5 *e* shows that this dependence is well captured by the model, which in particular can account for both competition and cooperation effects.

DISCUSSION

We have proven that cell motion can be directed by a topographical asymmetric pattern with no previous confinement of cell movement, either physical or biochemical. We identified the mechanical interaction between the cell nucleus and the topographical walls as a possible mechanism to explain the rectification of cell movement. By combining the topographic ratchet with an adhesive gradient, we tuned its rectification efficiency, thereby suggesting that asymmetries in cell polarization increase or decrease the efficiency of the ratchet depending on their relative orientations.

Previous studies achieved biased cell motion by asymmetric patterns, either chemical (12–15) or physical (13,16–18), that induced cell polarization by means of confining cells and restricting their motion to one-dimensional. Geometrical asymmetries in the pattern design amplified natural differences in lamellipodia activity at the front and the rear of a polarized cell, leading to directed motion (12–15,17,18). Because we used homogeneous fibronectin coatings and topographical patterns smaller than the cell size and of a moderate height (35), we did not restrict cell migration in any direction. Thus, the bias that we observed stems from a different origin.

Recent studies have shown that nucleus trapping caused by spatial constraints of the three-dimensional (3D) environment is a limiting factor for cell migration (36), as cell movement is arrested when the nucleus cannot overcome physical barriers imposed by a 3D collagen network. Similar behavior has been observed for cells migrating in channels (37). Our results are in agreement with this phenomenon, confirming that physical interaction between the nucleus and the environment architecture is a determinant factor in cell migration, even in nonconfined cells. Moreover, we report a role for cell nucleus in setting directionality, where mechanical interaction between the nucleus and the physical constraints is a subtle interplay between nucleus elasticity, topographical landscape, and protrusion activity (36). Furthermore, we noticed the appearance of focal contacts colocalizing with the topographical walls when nucleus contacted the walls of the topographical pattern. This observation could be related to a noneven distribution of forces on the nucleus, thus leading to the nucleus reorientation.

Moreover, we show that the bias in cell migration induced by the nucleus-topography interaction can be tuned by adding an external adhesive gradient. This finding suggests that

both nucleus impairment and traction force, i.e., the adhesion to the fibronectin layer, cooperate or compete in setting cell migration. In other words, we show that when the traction force is in the opposite direction of the topographical ratchet, cells more easily overcome the topographical walls. Similarly, 3D cell migration experiments revealed that integrin-mediated traction force is required to propel the nucleus forward when its movement is impaired by physical constraints (36).

Finally, we successfully captured the essential features of the system by modeling cells as particles in asymmetric potentials. This theoretical model was based on two main experimental observations: i), cell motion within the ratchet depends on the direction of the previous movement, which is a minimal way to encode polarization; and ii), the motion is restricted by the mechanical interaction between the nucleus and the topographical landscape. Interestingly, this analysis, based on a microscopic modeling of motion at the cell scale, showed that long-term cell trajectories are robustly described as simple persistent random walks, in agreement with earlier results (38). This observation contrasts with findings at smaller scales where Lévy walk features have been reported (39). This new approach to cell motility with disentangled contributions is proposed as a generic framework for understanding cell motion in vitro and in vivo.

SUPPORTING MATERIAL

Ten figures, eight movies, and supporting data are available at http://www.biophysj.org/biophysj/supplemental/S0006-3495(14)00805-4.

We thank the members of Riveline's lab for critical discussions. We thank E. Fuchs (Rockefeller University) for the zyxin-RFP construct and E. Paluch (UCL) for the nonmuscle myosin heavy chain II-GFP construct. We acknowledge the Nanotechnology Platform of the IBEC and D. Izquierdo for technical support.

This work was supported by funds from the CNRS (D.R.), the University of Strasbourg (D.R.), the ci-FRC of Strasbourg (D.R.), Fondation Simone et Cino del Duca (J.C., D.R.), the CIBER-BBN initiative (V.H., E.M., J.S.), the "Generalitat de Catalunya" (2009 SGR 505 J.S. and BE fellowship to J.C.), and the "Fundación Botín" (E.M., J.S.). The authors declare no competing financial interests.

SUPPORTING CITATIONS

Reference (40) appears in the Supporting Material.

REFERENCES

1. Bénazéraf, B., P. Francois, …, O. Pourquié. 2010. A random cell motility gradient downstream of FGF controls elongation of an amniote embryo. *Nature.* 466:248–252.
2. Giampieri, S., C. Manning, …, E. Sahai. 2009. Localized and reversible TGFbeta signalling switches breast cancer cells from cohesive to single cell motility. *Nat. Cell Biol.* 11:1287–1296.
3. Petrie, R. J., A. D. Doyle, and K. M. Yamada. 2009. Random versus directionally persistent cell migration. *Nat. Rev. Mol. Cell Biol.* 10:538–549.
4. Lecaudey, V., G. Cakan-Akdogan, …, D. Gilmour. 2008. Dynamic FGF signaling couples morphogenesis and migration in the zebrafish lateral line primordium. *Development.* 135:2695–2705.
5. Calvo, F., N. Ege, …, E. Sahai. 2013. Mechanotransduction and YAP-dependent matrix remodelling is required for the generation and maintenance of cancer-associated fibroblasts. *Nat. Cell Biol.* 15:637–646.
6. Weber, M., R. Hauschild, …, M. Sixt. 2013. Interstitial dendritic cell guidance by haptotactic chemokine gradients. *Science.* 339: 328–332.
7. Teixeira, A. I., G. A. Abrams, …, P. F. Nealey. 2003. Epithelial contact guidance on well-defined micro- and nanostructured substrates. *J. Cell Sci.* 116:1881–1892.
8. Kim, D.-H., C.-H. Seo, …, K.-Y. Suh. 2009. Guided cell migration on microtextured substrates with variable local density and anisotropy. *Adv. Funct. Mater.* 19:1579–1586.
9. Kim, D.-H., K. Han, …, A. Levchenko. 2009. Mechanosensitivity of fibroblast cell shape and movement to anisotropic substratum topography gradients. *Biomaterials.* 30:5433–5444.
10. Kim, H. N., Y. Hong, …, K.-Y. Suh. 2012. Effect of orientation and density of nanotopography in dermal wound healing. *Biomaterials.* 33:8782–8792.
11. Kwon, K. W., H. Park, …, J. Doh. 2012. Nanotopography-guided migration of T cells. *J. Immunol.* 189:2266–2273.
12. Kumar, G., C.-C. Ho, and C. C. Co. 2007. Guiding cell migration using one-way micropattern arrays. *Adv. Mater.* 19:1084–1090.
13. Mahmud, G., C. J. Campbell, …, B. A. Grzybowski. 2009. Directing cell motions on micropatterned ratchets. *Nat. Phys.* 5:606–612.
14. Kushiro, K., S. Chang, and A. R. Asthagiri. 2010. Reprogramming directional cell motility by tuning micropattern features and cellular signals. *Adv. Mater.* 22:4516–4519.
15. Kumar, G., C. C. Co, and C.-C. Ho. 2011. Steering cell migration using microarray amplification of natural directional persistence. *Langmuir.* 27:3803–3807.
16. Yoon, S.-H., Y. K. Kim, …, M. R. Mofrad. 2012. Passive control of cell locomotion using micropatterns: the effect of micropattern geometry on the migratory behavior of adherent cells. *Lab Chip.* 12:2391–2402.
17. Ko, Y.-G., C. C. Co, and C.-C. Ho. 2013. Directing cell migration in continuous microchannels by topographical amplification of natural directional persistence. *Biomaterials.* 34:353–360.
18. Ko, Y.-G., C. C. Co, and C.-C. Ho. 2013. Gradient-free directional cell migration in continuous microchannels. *Soft Matter.* 9:2467–2474.
19. Smith, J. T., J. K. Tomfohr, …, W. M. Reichert. 2004. Measurement of cell migration on surface-bound fibronectin gradients. *Langmuir.* 20:8279–8286.
20. Lo, C. M., H. B. Wang, …, Y. L. Wang. 2000. Cell movement is guided by the rigidity of the substrate. *Biophys. J.* 79:144–152.
21. Ananthakrishnan, R., and A. Ehrlicher. 2007. The forces behind cell movement. *Int. J. Biol. Sci.* 3:303–317.
22. Feynman, R., R. Leighton, and M. Sands. 1963. The Feynman Lectures on Physics. *In* The Feynman Lectures on Physics Addison-Wesley, Reading, MA, 41–I.
23. Prost, J., J.-F. Chauwin, …, A. Ajdari. 1994. Asymmetric pumping of particles. *Phys. Rev. Lett.* 72:2652–2655.
24. Jülicher, F., A. Ajdari, and J. Prost. 1997. Modeling molecular motors. *Rev. Mod. Phys.* 69:1269–1281.
25. Mills, C. A., J. G. Fernandez, …, J. Samitier. 2008. The use of high glass temperature polymers in the production of transparent, structured surfaces using nanoimprint lithography. *Microelectron. Eng.* 85:1897–1901.
26. Comelles, J., V. Hortigüela, …, E. Martínez. 2012. Versatile gradients of covalently bound proteins on microstructured substrates. *Langmuir.* 28:13688–13697.
27. Caballero, D., R. Voituriez, and D. Riveline. 2014. Protrusion fluctuations direct cell motion. *Biophys. J.* 107:34–42.

28. Le Berre, M., Y.-J. Liu, …, M. Piel. 2013. Geometric friction directs cell migration. *Phys. Rev. Lett.* 111:198101–198106.

29. Smith, J. T., J. T. Elkin, and W. M. Reichert. 2006. Directed cell migration on fibronectin gradients: effect of gradient slope. *Exp. Cell Res.* 312:2424–2432.

30. Selmeczi, D., S. Mosler, …, H. Flyvbjerg. 2005. Cell motility as persistent random motion: theories from experiments. *Biophys. J.* 89:912–931.

31. Selmeczi, D., L. Li, …, H. Flyvberg. 2008. Cell motility as random motion: A review. *Eur. Phys. J. Spec. Top.* 157:1–15.

32. Constantini, G., and F. Marchesoni. 1999. Threshold diffusion in a tilted washboard potential. *Europhys. Lett.* 48:491–497.

33. Khatau, S. B., C. M. Hale, …, D. Wirtz. 2009. A perinuclear actin cap regulates nuclear shape. *Proc. Natl. Acad. Sci. USA.* 106:19017–19022.

34. Pajerowski, J. D., K. N. Dahl, …, D. E. Discher. 2007. Physical plasticity of the nucleus in stem cell differentiation. *Proc. Natl. Acad. Sci. USA.* 104:15619–15624.

35. Ghibaudo, M., L. Trichet, …, B. Ladoux. 2009. Substrate topography induces a crossover from 2D to 3D behavior in fibroblast migration. *Biophys. J.* 97:357–368.

36. Wolf, K., M. Te Lindert, …, P. Friedl. 2013. Physical limits of cell migration: control by ECM space and nuclear deformation and tuning by proteolysis and traction force. *J. Cell Biol.* 201:1069–1084.

37. Mak, M., C. A. Reinhart-King, and D. Erickson. 2013. Elucidating mechanical transition effects of invading cancer cells with a subnucleus-scaled microfluidic serial dimensional modulation device. *Lab Chip.* 13:340–348.

38. Tranquillo, R. T., D. A. Lauffenburger, and S. H. Zigmond. 1988. A stochastic model for leukocyte random motility and chemotaxis based on receptor binding fluctuations. *J. Cell Biol.* 106:303–309.

39. Harris, T. H., E. J. Banigan, …, C. A. Hunter. 2012. Generalized Lévy walks and the role of chemokines in migration of effector CD8+ T cells. *Nature.* 486:545–548.

40. Hughes, B. D. 1995. Random Walks and Random Environments: Random Walks. Oxford University Press.

Eur. Phys. J. E (2015) **38**: 122
DOI 10.1140/epje/i2015-15122-4

THE EUROPEAN PHYSICAL JOURNAL E

Regular Article

Theoretical study of actin layers attachment and separation

Sophie Marbach[1,2,a], Amélie Luise Godeau[4,5], Daniel Riveline[4,5], Jean-François Joanny[1,3,b], and Jacques Prost[1]

[1] Physico-Chimie Curie (Institut Curie, Cnrs UMR 168, UPMC), Institut Curie Centre de Recherche, 26, rue de l'Ulm, 75005, Paris, France
[2] ICFP, Physics Department, Ecole Normale Supérieure de Paris, 24 rue Lhomond, 75005, Paris, France
[3] ESPCI, 10 rue Vauquelin, 75005, Paris, France
[4] Laboratory of Cell Physics, Institut de Science et d'Ingénierie Supramoléculaires, Institut de Génétique et de Biologie Moléculaire et Cellulaire, Université de Strasbourg and Centre National de la Recherche Scientifique UMR 7006, Strasbourg, France
[5] Development and Stem Cells Program, Institut de Génétique et de Biologie Moléculaire et Cellulaire, Centre National de la Recherche Scientifique UMR 7104, Institut National de la Santé et de la Recherche Médicale (U964), Université de Strasbourg, Illkirch, France

Received 23 February 2015 and Received in final form 18 June 2015
Published online: 25 November 2015 –

Abstract. We use the theory of active gels to study theoretically the merging and separation of two actin dense layers akin to cortical layers of animal cells. The layers bind at a distance equal to twice the thickness of a free layer, thus forming a single dense layer, similar in this sense to a *lamellipodium*. When that unique layer is stretched apart, it is resilient to break apart up to a critical length larger than twice the thickness of a free layer. We show that this behavior can result from the high contractile properties of the actomyosin gel due to the activity of myosin molecular motors. Furthermore, we establish that the stability of the stretched single layer is highly dependent on the properties of the gel. Indeed, the nematic order of the actin filaments along the polymerizing membranes is a destabilizing factor.

1 Introduction

Fundamental biological processes such as adhesion, migration, and division of living animal cells strongly depend on the mechanics and the activity of their cytoskeleton. The cytoskeleton has a complex structure made of several components. It is generally accepted that the mechanical properties of animal cells essentially depend on the actomyosin component of the cytoskeleton, which is responsible for stress generation, and controls the response of cells to external mechanical perturbations [1, 2]. The actomyosin cytoskeleton has received much experimental [3, 4] and theoretical attention [5, 6]. It is composed of a dense meshwork of semi-flexible actin filaments interacting with myosin motor mini-filaments and actin-associated proteins. It is located in many cells in the vicinity of the cell membrane [7] where it forms the so-called cortical layer [8, 9]. Myosin motors hydrolyze adenosine triphosphate (ATP) molecules and can produce work. They crosslink actin filaments and create active contractile stresses in the actomyosin gel [10].

A hydrodynamic description that captures the behavior of active gels on large length and time scales was established to describe in particular the dynamics of the actomyosin gel [11–13]. It has been successfully applied to various situations: the discovery of spontaneous flows [14,15], spontaneous waves [16] and more recently to the closure of the contractile ring during cytokinesis [6,17]. The interaction of two layers of actomyosin gel has to our knowledge never been theoretically investigated. It is however of critical interest as a first step to understand the formation of a *lamellipodium* during cell motility. The *lamellipodium* is a dense layer of actin protruding from the main cytoskeletal structure of the cell body. Although actin flow inside the *lamellipodium* has been studied [18], the understanding of the precise shape of the protrusion linked to its structure remains to be explored.

In this work we are interested in the effect of the active contraction of actin gels on the interaction between two actin cortical layers. A recent theoretical work [5] has shown that the key element for the formation of a condensed actin layer in a stationary state at the membrane surface is the contractility of the actomyosin gel induced by the myosin molecular motors. In the cortical layer, in a simplified description, actin is treadmilling: it polymerizes at the cell membrane and depolymerizes in the bulk of the layer. Within the theory of active gels, the layer thickness is determined by the ratio between the polymerization velocity and the depolymerization rate of actin [5]. It is clear

[a] e-mail: sophie@marbach.fr
[b] e-mail: jean-francois.joanny@curie.fr

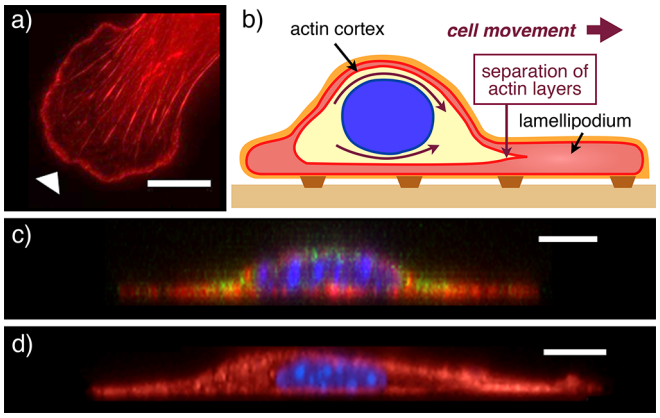

Fig. 1. a) *Lamellipodium* (at the arrowhead) promoted with incubation with 100 μM C8-BPA for 10 min (scale bar: 5 μm). b) Schematic of the cell contour. The cell moves in the direction of the *lamellipodium*. At the inner edge, the dense actin bundle is separated into two layers to form the actin cortex. c) Symmetric cell along the z-axis. C8-BPA was added 80 min after cell resuspension using trypsin treatment (scale bar: 5 μm). d) Non-symmetric cell along the z-axis. C8-BPA was added 10 min on spread cells (scale bar: 10 μm). F-actin is labeled in red in a), c), d), myosin in green in c), the nucleus in blue in c), d). See appendix A for details.

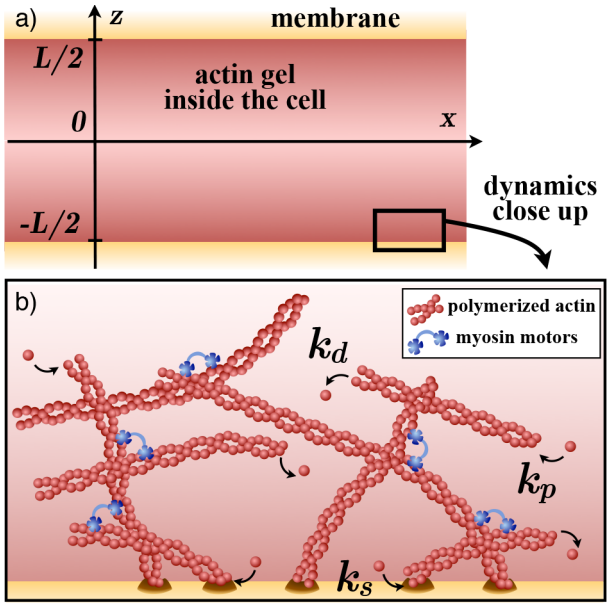

Fig. 2. a) Illustration of two interacting layers. The schematic shows two infinite planar membranes located at a distance L. The actin gel is distributed in between. The dynamics of polymerization and interaction close to the membrane are illustrated in b): Actin polymers are nucleated from the membrane surface at rate k_s. Polymerization and depolymerization of the polymers happen in the bulk at rate k_p and k_d, respectively. Myosin motors (blue stars) act as active cross-linkers between actin polymers, giving strong contractile properties to the gel.

that the interplay between contractility and average depolymerization impacts the interaction between two close layers.

Experimentally, dense actin can be observed in the *lamellipodium*. The lamellipodial protrusion is mainly generated by continuous growth of actin filaments from the leading edge [19] (see figs. 1(a) and (b)). Synthetic polyamines C8-BPA were recently shown to promote the growth of *lamellipodia* within minutes [20] (see fig. 1(a)). We used them and visualized the cell cortex along the z-axis on single spread cells with different experiments, as presented in figs. 1(c) and (d). These acquisitions demonstrate that the actomyosin cortex is spanning the cell contour and that there are multiple locations where the cytoplasm between layers presents a dense actin content. An important goal is therefore to understand how one single dense layer of actin (as in the *lamellipodium* at the cell front) can separate into two layers of actin cortex (see fig. 1(b)) and vice versa. To study the merging and separation of actin cortical layers we generalize here the hydrodynamic description of active gels to the case of two infinite planar membranes facing each other. We restrict the study to flat membrane surfaces. In the following we show that in the case of highly contractile actomyosin gels, with a high myosin activity and relatively low depolymerization rate, the merging and separation process is hysteretic. Contractility is the driving force, either maintaining separated layers firmly condensed near the membranes, or preventing a stretched single layer, similar to the *lamellipodium*, from breaking apart.

This paper is organized as follows. In sect. 2 we present the hydrodynamic equations for an actin gel between two infinite planar membranes, in a two-dimensional geometry. We then solve these equations in sect. 3 in the one-dimensional steady state. We study precisely the actin density between the layers as a function of the distance between the membranes, upon a change in the gel contractility. Finally we discuss in sect. 4 the stability of a single "stretched" layer in the presence of both isotropic and anisotropic contractility.

2 Hydrodynamic description

We present here the hydrodynamic equations governing the temporal and spatial dynamics of an assembling active actin gel. The gel and the solvent are localized between two planar membranes located at $z = -L/2$ and $z = L/2$, as shown in fig. 2(a). We assume locally planar membranes because the typical thickness of the actin gel in a cell (200–500 nm) is very small compared to the cell curvature radius (1 μm or more), except at the *lamellipodium* outer front. We restrict ourselves to a symmetric case, where the properties of the actin cortex are the same near each membrane. As suggested by the experiments, we assume furthermore that the gel is assembled by actin polymerization at the membrane surface at a rate k_s (see fig. 2(b), in the main body [21] and also in the *lamellipodium* [22]). The polymerization at the membrane is promoted by nucleating proteins [7]. Away from the surface, the actin gel assembles by elongation of existing filaments or by nucleation of new filaments and disassembles

because of monomer removal at the filament minus-ends or by filament severing. In our coarse-grained approximation, we model elongation and nucleation by a single effective polymerization rate k_p, which takes into account the bulk nucleating proteins, and disassembly by a single depolymerization rate k_d.

The whole system lies in the cytoplasm which acts as a reservoir containing, among other molecules, myosin free motors and actin monomers. Myosin molecular motors assemble as minifilaments and act as cross-links between actin filaments, thus generating mechanical stress in the filamentous network. Following the approach of [5] we limit ourselves to the case where the exchange of motors between the actin network and the solvent is so fast that we can assume chemical equilibrium. Motor diffusion is also assumed to be fast enough that the concentration of free motors in the solvent is constant. In a first approximation, the concentration of motors bound to actin is then proportional to the local density of actin monomers assembled into polymers.

The actin gel possesses a polarization field dependent on the local orientation of the filaments. The orientational order is in general nematic with the filaments oriented on average parallel to the surface but we consider also the isotropic case for the sake of generality.

We model the direction of each filament by a unit vector in Cartesian coordinates: $\boldsymbol{p}(x,y,z,t) = (\cos(\varphi)\sin(\theta)+\delta p_x)\boldsymbol{e_x}+(\sin(\varphi)\sin(\theta)+\delta p_y)\boldsymbol{e_y}+(\cos(\theta)+\delta p_z)\boldsymbol{e_z}$ with φ and θ the usual spherical coordinates and δp_x, δp_y and δp_z represent small fluctuations. φ is uniformly distributed (no preferred direction in the plane parallel to the membrane surface) in $[0, 2\pi]$, and θ may have a more complex distribution.

The nematic tensor is defined as $Q_{\alpha\beta} = \langle p_\alpha p_\beta - \frac{1}{3}p^2\delta_{\alpha\beta}\rangle$, where the average is a local average over the filament orientation. It reads at a $O(\delta p_{x,y,z})$:

$$Q = \begin{pmatrix} \frac{\langle\sin^2(\theta)\rangle}{2} - \frac{1}{3} & 0 & 0 \\ 0 & \frac{\langle\sin^2(\theta)\rangle}{2} - \frac{1}{3} & 0 \\ 0 & 0 & \langle\cos^2(\theta)\rangle - \frac{1}{3} \end{pmatrix}. \tag{1}$$

For further simplicity, we also consider that the gel is homogeneous in the y direction along the membrane, so that its properties only depend on the z and x coordinates.

2.1 Mass conservation

The density ρ of actin monomers assembled into polymers follows the conservation law:

$$\partial_t\rho + \partial_\alpha(\rho v_\alpha) = k_p - k_d\rho, \tag{2}$$

where $\boldsymbol{v}$ is the gel velocity field. We adopt Einstein's summation convention. The rates k_p and k_d can depend on the local actin density and on the local stresses in the gel. Such dependences were considered in the description of actin gels in [23, 24]. In our study, these dependences do not add physical content, and do not change the main results. The rates can also depend on the membrane considered, wether it is the free membrane or the one attached to the substrate, or wether it is the membrane in the main cell body or in the *lamellipodium*. Because we do not intend to describe the longitudinal profile of the *lamellipodium* in this paper, we restrict ourselves to the case where k_p and k_d are uniform constants in the following. We introduce in particular $\rho_\infty = k_p/k_d$, which measures the density ρ far from any boundaries and in a gel at steady state.

The fact that polymerization occurs also at the membrane surface with a surface rate k_s yields the boundary condition $\rho v_z|_{z=-L/2} = -\rho v_z|_{z=L/2} = v_p\rho_0$, where ρ_0 is the density of the actin gel at the surface and $v_p = k_s\delta$ is the polymerization velocity, δ being the effective size of an actin monomer. The density ρ_0 and the polymerization velocity v_p depend, among other factors, on the density of nucleating sites at the membrane. We consider that the boundary conditions are invariant by translation along x, so that ρ_0 and v_p are constant.

2.2 Force balance

We need yet another equation to characterize the mechanical equilibrium and the molecular fluxes in the system. We combine here multiple approaches on the theory of active permeating gels [5, 11–13, 25] to derive equations that are relevant in our case. In the following, we give only the general methodology to derive the equations. In our system the thermodynamic fluxes involved are the stress tensor σ, the time derivative of the elastic strain tensor in the gel, the relative current between the actin gel and the solvent $\boldsymbol{j} = \rho(\boldsymbol{v} - \boldsymbol{v_s})$, and the rate r of ATP consumption. The conjugated forces are the gradient of the relative chemical potential $\bar{\mu}$ between gel and solvent, the velocity gradient, the partial stress tensor of the gel and the activity of the system. Active processes in the system are essentially driven by the hydrolysis of ATP into adenosine diphosphate (ADP) and inorganic phosphate P_i, with chemical potentials μ_{ATP}, μ_{ADP} and μ_{P_i} respectively. We then measure the system's activity through $\Delta\mu = \mu_{\mathrm{ATP}} - \mu_{\mathrm{ADP}} - \mu_{P_i}$.

The general theory of active gels then uses the Onsager linear relation between fluxes and forces. Here, we give only the final equation for the relative current between actin gel and solvent for an apolar active gel

$$j_\alpha \equiv \rho(v_\alpha - v_{s,\alpha}) = -\gamma\partial_\alpha\overline{\mu} + \chi\partial_\beta\sigma_{\alpha\beta}, \tag{3}$$

with γ and χ two transport coefficients, and $\boldsymbol{v_s}$ the velocity field of the solvent.

In eq. (3), we consider that the Onsager coefficients are independent of the nematic order of the gel; the viscosity for instance is isotropic. The general theory includes other anisotropic terms that we ignore here. As the filaments can present anisotropic ordering, we must consider the

contribution of $Q_{\alpha\beta}$ to the stress tensor

$$2\eta v_{\alpha\beta} = \left(1 + \tau \frac{\mathrm{D}}{\mathrm{D}t}\right)\left(\sigma_{\alpha\beta} + \zeta' \Delta\mu Q_{\alpha\beta} + \zeta \Delta\mu \delta_{\alpha\beta}\right), \quad (4)$$

where $v_{\alpha\beta} = \frac{1}{2}(\partial_\alpha v_\beta + \partial_\beta v_\alpha)$, $\frac{\mathrm{D}}{\mathrm{D}t}$ is the convective time derivative, and τ is the viscoelastic relaxation time. The active coefficients ζ and ζ' denote the contributions of the active stress to the partial stress tensor. They are negative in the cell cortex because experimentally, activity leads to contractile stresses, and they depend on the gel density ρ. Equation (4) is a generalization of the Maxwell model for an active gel with nematic order. For the actin cortex, we consider that the experimental time scales are large compared to the viscoelastic relaxation time, so that we can neglect the convective time derivative.

We rewrite the term involving the relative chemical potential $\bar{\mu}$ in eq. (3), using the Gibbs-Duhem equation $\mathrm{d}\tilde{\Pi} = \rho \mathrm{d}\bar{\mu}$ that gives the evolution of the osmotic pressure $\tilde{\Pi}$ as a function of $\bar{\mu}$ in the case where the total volume of the system is constant (independent of composition, and incompressible). We then define an effective osmotic pressure, adding the active terms: $\Pi_{\alpha\beta} = \tilde{\Pi}\delta_{\alpha\beta} + \zeta \Delta\mu Q_{\alpha\beta} + \zeta \Delta\mu \delta_{\alpha\beta}$. With $\gamma = \chi\rho$, eq. (3) can be rewritten as

$$\frac{\rho}{\chi}(v_\alpha - v_{s,\alpha}) = 2\partial_\beta(\eta v_{\alpha\beta}) - \partial_\beta \Pi_{\alpha\beta}. \quad (5)$$

We proceed using the same approximation as in [5] to neglect the permeation current. The permeation constant ρ/χ can be estimated as η_s/ξ^2, where ξ is the gel mesh size and η_s the solvent viscosity. We then compare the two competing dissipative mechanisms, namely the gel viscosity and the permeation of the solvent through the actin gel. This comparison defines a permeation length $L_p = (\eta\chi\rho^{-1})^{1/2} = (\eta/\eta_s)^{1/2}\xi$. The experiments of [26] allow us to estimate $\eta_s \sim 10^3$ Pa s (effective viscosity measured for reference parameters of the actin gel). We take a solvent viscosity of 10^{-3} Pa s (close to water). With typical mesh sizes ξ of a few tens of nanometers, we obtain a permeation length of the order of tens of microns. This permeation length is sufficiently large compared to the thickness of the cortex. This argument allows us to neglect the left-hand side of eq. (5) compared to the viscous dissipation term if we consider the dynamics on length scales smaller than the permeation length scale.

From now on, we consider the gel density ρ and the gel velocity $\boldsymbol{v}$ as the only hydrodynamic variables. All quantities are considered to be invariant in the y direction, with no velocity along the y axis. Consequently, we write $\boldsymbol{v}$ as the vector $(u, 0, v)$. The projections of the constitutive eqs. (2) and (5) on the x and z axis read

$$\begin{cases} \partial_t \rho + \partial_z(\rho v) + \partial_x(\rho u) = -k_d(\rho - \rho_\infty), \\ \partial_z\left(\eta(\partial_x v + \partial_z u)\right) + 2\partial_x(\eta \partial_x u) - \partial_x \Pi_x = 0, \\ \partial_x\left(\eta(\partial_z u + \partial_x v)\right) + 2\,\partial_z(\eta \partial_z v) - \partial_z \Pi_z = 0, \end{cases} \quad (6)$$

with, using eq. (1)

$$\Pi_x = \tilde{\Pi} + \Delta\mu\zeta_x, \qquad \Pi_z = \tilde{\Pi} + \Delta\mu\zeta_z,$$
$$\zeta_x = \zeta + \zeta'\left(\frac{\langle \sin^2(\theta)\rangle}{2} - \frac{1}{3}\right),$$
$$\zeta_z = \zeta + \zeta'\left(\langle \cos^2(\theta)\rangle - \frac{1}{3}\right).$$

3 Interaction between two cortical actin layers

We now solve the equations in the one-dimensional case, considering that the problem is invariant in the x direction. We also look for stationary solutions. The equations governing the gel fluid flow and the gel density are then easily obtained from eqs. (6)

$$\begin{cases} \partial_z(\rho v) = -k_d(\rho - \rho_\infty), \\ 2\eta \partial_{zz} v - \partial_z \Pi(\rho) = 0, \end{cases} \quad (7)$$

where $\Pi(\rho)$ is considered in this section to be a function of ρ only. We do not consider here contributions to the effective pressure involving the derivative of ρ, or higher order derivatives. Such contributions could account for a surface tension between the layer and the solvent.

3.1 Analytic solution of the bilayer problem

We look for a solution on the half-domain $[-\frac{L}{2}, 0]$ and deduce the solution on the other half by symmetry. In this half-domain, the boundary conditions are

$$\rho\big|_{z=-L/2} = \rho_0, \qquad v\big|_{z=-L/2} = v_p, \qquad v\big|_{z=0} = 0.$$

The two first conditions are required by the polymerization at the membrane surface and the last one is required by symmetry. Symmetry could also impose, *a priori*, that $\frac{\mathrm{d}\rho}{\mathrm{d}z}|_{z=0} = 0$. In the following analytical derivation, we find solutions on the half-plane that verify $\frac{\mathrm{d}\rho}{\mathrm{d}z}|_{z=0^-} = -\infty$. These solutions are still symmetric, but the derivative of ρ is not well defined at $z = 0$. There is no mathematical contradiction, since eqs. (7) do not allow to conclude on the continuity of the derivative of ρ near points where the velocity field vanishes.

We integrate the second line of eqs. (7) with respect to z and evaluate the integration constant by using the boundary conditions in $z = 0$. This yields $2\eta\partial_z v = \Pi(\rho) - 2\eta k_d(1 - \frac{\rho_\infty}{\rho_c}) - \Pi(\rho_c)$, where $\rho_c = \rho(z = 0)$ is the density at the center of the domain to be determined. We then define $f(\rho, \rho_c) = g(\rho) - g(\rho_c)$ with $g(\rho) = -\Pi(\rho) + 2\eta k_d(\frac{\rho_\infty}{\rho})$, such that

$$2\eta v = \left(\frac{\mathrm{d}\rho}{\mathrm{d}z}\right)^{-1} \rho f(\rho, \rho_c). \quad (8)$$

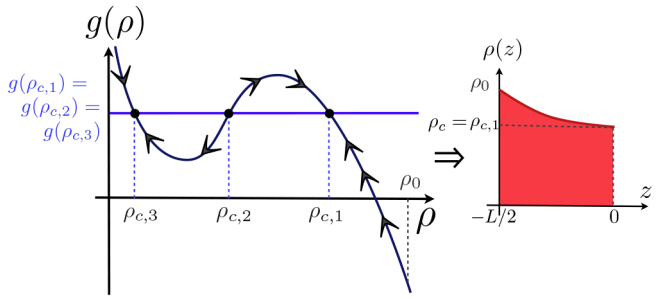

Fig. 3. Schematic of the graphical construction of a solution $\rho(z)$. On the left-hand side graph, the effective gel tension $g(\rho)$ is drawn. According to the position of the curve of $g(\rho)$ to the horizontal line, we deduce the sign of $f(\rho, \rho_{c,1}) = g(\rho) - g(\rho_{c,1\ldots3})$. This allows (eq. (9)) to draw arrows indicating the evolution of ρ as a function of z. If $\rho(z = -L/2) = \rho_0$, then $\rho(z)$ decreases until $\rho_{c,1}$ in $z = 0$, as reported on the right-hand side graph.

We call $g(\rho)$ the effective gel tension[1]. Finally, using eq. (8) and integrating the first line of eqs. (7) yields

$$\frac{\mathrm{d}\rho}{\mathrm{d}z} = \frac{\rho^2 f(\rho, \rho_c)}{2\rho_0 \eta v_p} \exp\left(\int_{\rho_0}^{\rho} \frac{2\eta k_d(\rho' - \rho_\infty)}{(\rho')^2 f(\rho', \rho_c)} \mathrm{d}\rho'\right). \quad (9)$$

The study of the zeros of $f(\rho, \rho_c)$ is essential to find the values of the density to which the profile converges at $z = 0$. Equation (9) indicates that ρ converges to the root of $f(\rho, \rho_c)$, with negative slope, closest to ρ_0. This is not straightforward, and to make the argument clearer, we detail briefly the construction of one solution, with the help of the schematic of fig. 3. We pick three values $\rho_{c,1}$, $\rho_{c,2}$ and $\rho_{c,3}$ that are such that $g(\rho_{c,1}) = g(\rho_{c,2}) = g(\rho_{c,3})$ and $\rho_{c,1\ldots3} \leq \rho_0$. We try to build up the profile $\rho(z)$ and in particular the value of $\rho(z = 0)$. We look first for the sign of $f(\rho, \rho_{c,1\ldots3}) = g(\rho) - g(\rho_{c,1\ldots3})$. If $g(\rho) \leq g(\rho_{c,1\ldots3})$ on an interval, then f is negative on that interval and from eq. (9), we deduce that $\rho(z)$ is a decreasing function of z, and vice versa. This means that the intersections between $g(\rho)$ and $g(\rho_{c,1\ldots3})$ with negative (respectively, positive) slopes give stable (respectively, unstable) fixed points of the density profile. Thus, if we start with $\rho(z = -L/2) = \rho_0$ as in fig. 3, $\rho(z)$ decreases until $\rho(z = 0) = \rho_{c,1}$, and cannot become smaller. To conclude the only possible value of ρ_c is the closest stable fixed point to ρ_0.

The boundary condition: $v|_{z=0} = 0$ must also be satisfied. Combining eqs. (8) and (9) in $z = 0$ yields the condition $\rho_c \geq \rho_\infty$. We consider the experimentally relevant case for which the polymerization in the vicinity of the surface is more efficient than in the bulk, and assume $\rho_0 \geq \rho_\infty$. Knowing from eq. (9) that ρ is a monotonous function of z, we deduce for all z, $\rho(z) \geq \rho_\infty$.

Finally, to compute the value of the density at the midplane ρ_c as a function of the thickness L, we integrate eq. (9) and use the fact that $\rho|_{z=-L/2} = \rho_0$ to obtain the implicit relation

$$\frac{L(\rho_c)k_d}{2v_p} = \int_{\rho_0}^{\rho_c} \frac{2\eta k_d \rho_0}{\rho^2 f(\rho, \rho_c)} \times \ldots \exp\left(-\int_{\rho_0}^{\rho} \frac{2\eta k_d(\rho' - \rho_\infty)}{(\rho')^2 f(\rho', \rho_c)} \mathrm{d}\rho'\right) \mathrm{d}\rho. \quad (10)$$

[1] Not to be confused with the stress in the system.

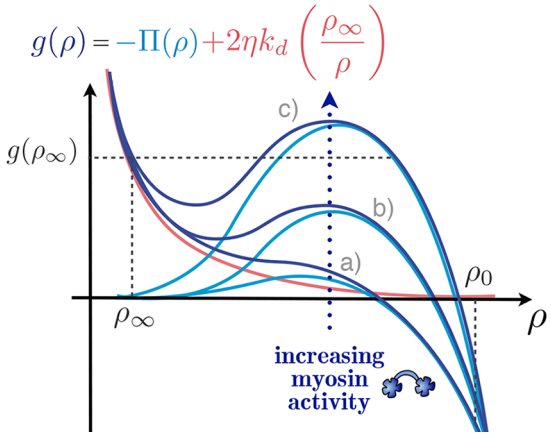

Fig. 4. Dark blue: schematic of the possible shapes of the effective gel tension g according to the contractile properties of the gel. Red: contribution to g associated with depolymerization. Light blue: contribution to g associated with pressure and activity. The cases elaborated in the paper are distinguished: a) *weakly contractile limit*, b) *intermediate contractile limit* and c) *strongly contractile limit*.

3.2 Dependence of the concentration profile on actomyosin contractility

We now emphasize the contributions of two very different terms in the effective gel tension. The contribution of polymerization ($+2\eta k_d \rho_\infty/\rho$) is well known: it is a decreasing function that can be more or less important according to the value of $k_p = k_d \rho_\infty$. The part associated with pressure and activity ($-\Pi(\rho)$) is increasing for small values of ρ (due to myosin activity that is responsible for gel contractility) and then decreasing for higher values of ρ. According to the ratio of $k_d \rho_\infty$ to contractility, g can only have two possible shapes. If the contractility is weak (or $k_d \rho_\infty$ is high), the resulting profile is a monotonous decreasing function (curve (a) of fig. 4). If the contractility is strong (or $k_d \rho_\infty$ is low), the resulting profile has one local minimum and one local maximum (curves (b) and (c) of fig. 4). This results in a strong difference in terms of possible actin density profiles for a given thickness L.

In each limit, two regimes of merging between the two cortical layers are possible. The regime where ρ_c is close to ρ_∞ corresponds to a situation where the layers are separated, and do not interact. We call this regime the *cortical regime*, because the layers are condensed near the surface as the actin cortex [5]. The regime where ρ_c is close to ρ_0 corresponds to a situation where the layers merge and strongly interact. We call this regime the *single*

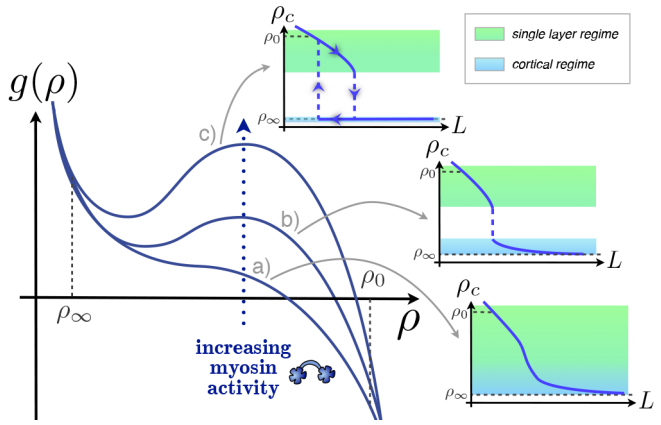

Fig. 5. Left: Schematic of the possible shapes of the effective gel tension g for increasing contractile properties, *e.g.* myosin activity. Right: Associated diagrams of ρ_c, density at the center of the layers, as a function of L, distance between the layers, in different limits: a) *weakly contractile limit*, b) *intermediate contractile limit* and c) *strongly contractile limit*.

layer regime. Because this solution is topologically similar to the actin density located in the *lamellipodium* where only a single dense actin layer may be observed, our study could be a starting point for the study of the transition of the acto-myosin gel from the cortex to the *lamellipodium*. In the subsequent subsection we show the following results:

- In the *weakly contractile limit* there is no clear distinction between the *cortical* and *single layer* regimes. As the layers are brought closer together, the density of actin increases continuously at the center (see inset (a) of fig. 5).
- In the *intermediate contractile limit* g presents a local maximum, which is not larger than $g(\rho_\infty)$ (curve (b) of fig. 4). In this limit, a range of values are not accessible for ρ_c. When the layers are brought closer together, the density at the center of the domain has a sudden jump at a distance L (see inset (b) of fig. 5). There is in this limit a clear distinction between the *cortical* and the *single layer* regimes.
- The *strongly contractile limit* corresponds to even higher contractility, where g presents a local maximum that exceeds the value of $g(\rho_\infty)$ (curve (c) of fig. 4). In this limit, there is hysteresis in the merging of the layers. At large distances, the layers are well separated in the sense that they have a finite thickness smaller than $L/2$. At a distance equal to twice the thickness of a free layer, the layers start interacting. When streched apart the layers do not split in two cortex-like layers until a membrane separation distance significantly larger than twice that of a free layer is reached (see inset (c) of fig. 5).

3.3 Graphical solution

The analytical form of L given by eq. (10) is not very convenient. Indeed, it does not allow to answer explicitly the question of finding the actin density profile (represented by ρ_c) for any value of the spacing between membranes L, since ρ_c is only implicitly expressed in eq. (10). In pratice we eventually fix ρ_c to find L and revert to the more natural relation of ρ_c as a function of L.

Equation (10) allows to derive a few useful results (see appendix B for the derivation):

- *L is a continuous function of ρ_c*. This does not mean however that when the distance between membranes varies, the corresponding evolution of the density profile of actin at the midplane ρ_c is smooth. For instance in the *intermediate* and *strongly* contractile limit, ρ_c is not a smooth function of L (see the insets of fig. 5).
- *L is a decreasing function of ρ_c*. Intuitively, a higher density of actin at the center is more easily achieved when the membranes are closer together.
- *As L goes to 0, ρ_c diverges to $+\infty$*. No limiting value for ρ_c is indeed expected, given that for small L, the total amount of actin filaments is finite, being permanently fed by the surfaces.
- *As L goes to $+\infty$, ρ_c converges to ρ_∞*. Indeed, when the membranes are far apart from each other, the layers interact less, and the density at the midplane approaches that of the free gel.
- *The distance between membranes L_0 to get a uniform density profile*, or $\rho_c = \rho_0$, verifies $\frac{L_0 k_d}{v_p} = \frac{2\rho_0}{\rho_0 - \rho_\infty}$. As a consequence of the second item, as soon as $L \geq L_0$, the density at the center is smaller than ρ_0. For $L \leq L_0$, the membranes are so close that $\rho_c \geq \rho_0$.

The first four results warrant the existence of at least one solution for any value of L.

Furthermore, we notice that eqs. (7) guarantee the continuity of v and ρv as functions of z. The continuity of $\rho(z)$ is not ensured however, in particular if v vanishes, which is the case at least at the midplane. In appendix C we show the following result concerning the condition for the existence of a discontinuity in the profile of $\rho(z)$:

- *The only possible discontinuity in the profile of $\rho(z)$ is between ρ_f and ρ_∞, where ρ_f is the solution to the problem*

$$\begin{cases} g(\rho_f) = g(\rho_\infty) \\ g'(\rho_f) \leq 0 \\ \rho_f \neq \rho_\infty \end{cases} \tag{11}$$

We plot for clarity the construction of this solution in fig. 6.

Such a solution is possible if the effective gel tension g has a local maximum higher than $g(\rho_\infty)$, *e.g.* in the strongly contractile limit. This particular solution corresponds to *free* layers, in the sense that each layer has a

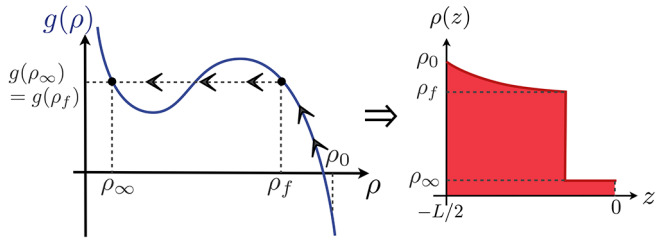

Fig. 6. Schematic of the graphical construction of the solution $\rho(z)$ with a discontinuity in ρ_f as defined by eq. (11). On the left-hand side graph, the effective gel tension $g(\rho)$ is drawn and a graphical construction similar to the one done in fig. 3 is performed. On the right-hand side, the profile $\rho(z)$ with a discontinuity from ρ_f to ρ_∞ is plotted.

finite width corresponding to the part of the density profile that goes from ρ_0 at the membrane to ρ_f. The region where $\rho(z) = \rho_\infty$ can have any width from zero to infinity, allowing to match any distance between membranes larger than $L(\rho_f)$.

These rules of evolution of L with ρ_c allow to build up a plot of L *versus* ρ_c. For a given value ρ_0, we simply look at the function $g(\rho)$. The density profile evolves from ρ_0 to all nearest possible stable fixed points (*e.g.* points where g has a negative slope), which define all values of ρ_c. The corresponding values of L are deduced from the rules.

For simplicity we take in the following a value of ρ_0 rather high, in the sense that it is higher than any relevant variation of the effective gel tension g. The results below can however be easily extended to smaller values of ρ_0.

We conclude now on the solutions of the bilayer problem for the different limits of contractility.

3.3.1 Weakly contractile limit

In the weakly contractile limit, the effective gel tension g is a monotonously decreasing function of ρ (see curve (a) of fig. 4). We start out with $L = L_0$ and thus $\rho_c = \rho_0$. All values of $\rho_c \leq \rho_0$ can be directly reached. ρ_c is thus a continuous decreasing function of L in this case (see fig. 7).

We check our results numerically by simulating a very slow variation of the distance between membranes. A sufficiently slow displacement allows to approach the steady state solutions of the problem. In the numerical solution, we must specify the functional $\Pi(\rho)$. We choose $\Pi(\rho) = a\rho^3 + b\rho^4$ as in [5], where $a < 0$ represents the contractility of the gel and $b > 0$ is a high density coefficient. The cubic power represents the contractile interaction of two actin filaments and one myosin motor (supposed to be present in the gel with a density proportional to that of the actin filaments). We give in appendix D further details on the numerical scheme. In fig. 7 we present both the analytic variation of ρ_c with L and the numerical values obtained at different times as we simulate the displacement of the membranes. The two curves are in perfect agreement. We also show three density profiles to illustrate the transition between the *single layer* (left-hand side) and *cortical regime* (right-hand side).

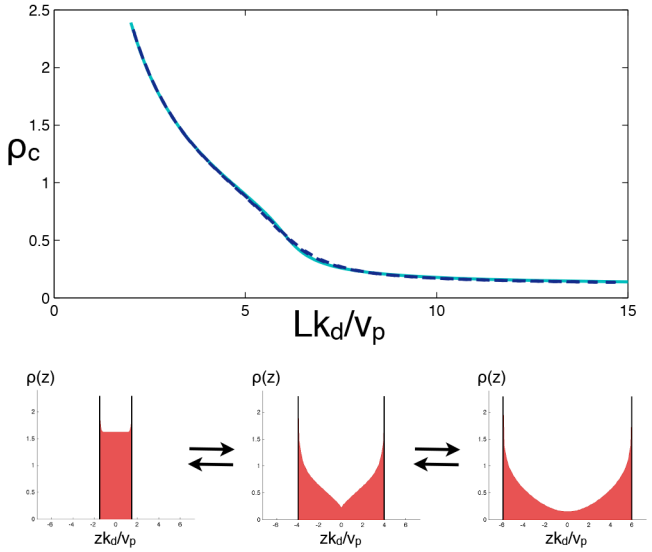

Fig. 7. Top: Evolution of ρ_c as a function of Lk_d/v_p in the weakly contractile limit. The solid light blue line is an analytic integration of L from eq. (10). The dashed dark blue line corresponds to the reported density at the midplane ρ_c during the numerical simulation where L is varied continuously. The parameters are $a = -1\eta k_d$, $b = 2\eta k_d$, $\rho_\infty = 0.1$, $\rho_0 = 2.3$. Bottom: Density profiles chosen from the numerical simulation, for $Lk_d/v_p = 3, 8, 12$ from left to right. The black vertical lines in each density profile represent the membranes.

3.3.2 Intermediate contractile limit

In the intermediate contractile limit, the effective gel tension g has one local minimum and one local maximum. We recall that $g(\rho_{\mathrm{loc\,max}}) \leq g(\rho_\infty)$, where $g(\rho_{\mathrm{loc\,max}})$ is the value of g at the local maximum.

We start out with $L = L_0$ and $\rho_c = \rho_0$ and construct solutions from ρ_0 to smaller and smaller values of ρ_c, and larger and larger values of L, until $\rho_{\mathrm{loc\,max}}$. At that point, $L = L_c^+$. If we want to go on decreasing ρ_c, the only solution is for ρ_c to jump to the other value ρ_{jump} that verifies $g(\rho_{\mathrm{jump}}) = g(\rho_{\mathrm{loc\,max}})$. At that other point, $L = L_c^-$. Afterwards, we may go on decreasing ρ_c until ρ_∞, with L increasing continuously.

This raises the question of the existence of a solution for any L, in other words whether $L_c^- = L_c^+$. We use the expression of $L(\rho_c)$ of eq. (10) and recall that $g(\rho_{\mathrm{loc\,max}}) = g(\rho_{\mathrm{jump}})$. Writing $L_c^- - L_c^+ = L(\rho_{\mathrm{jump}}) - L(\rho_{\mathrm{loc\,max}})$ yields the integral of a function that always vanishes, so that $L_c^- = L_c^+ = L_c$.

In summary, we have found, in the intermediate contractile limit, that the distinction between the *cortical* and the *single layer regime* is clearly characterized by a critical length between membranes L_c.

In the same way as for the weakly contractile limit, we check our results numerically by simulating a very slow displacement of the membranes. We take a larger value of a in absolute value than for the weakly contractile limit (the contractile properties are thus enhanced). In fig. 8 we present both the analytic variation of ρ_c with L and the

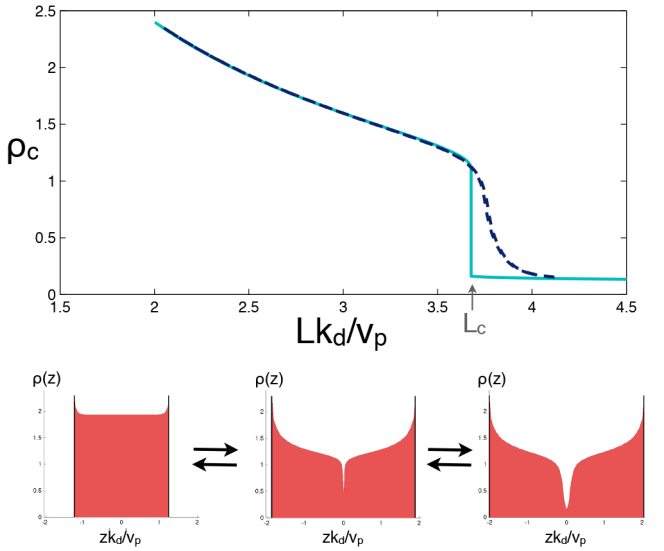

Fig. 8. Top: Evolution of ρ_c as a function of Lk_d/v_p in the intermediate contractile limit. The solid light blue line is an analytic integration of L from eq. (10). The dashed dark blue line corresponds to the reported density at the midplane ρ_c during the numerical simulation where L is varied continuously. The parameters used are $a = -3\eta k_d$, $b = 2\eta k_d$, $\rho_\infty = 0.1$, $\rho_0 = 2.3$. Bottom: Density profiles chosen from the numerical simulation, for $Lk_d/v_p = 2.5, 3.8, 4.1$ from left to right. The black vertical lines in each density profile represent the membranes.

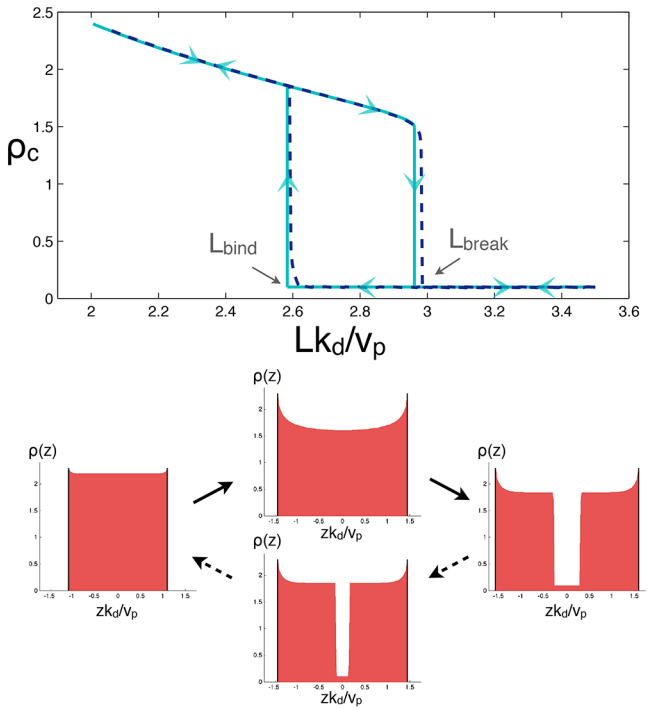

Fig. 9. Top: Evolution of ρ_c as a function of Lk_d/v_p in the strongly contractile limit. The solid light blue line is an analytic integration of L from eq. (10). The dashed dark blue line corresponds to the reported density at the midplane ρ_c during the numerical simulation where L is varied continuously. The parameters are $a = -4\eta k_d$, $b = 2\eta k_d$, $\rho_\infty = 0.1$, $\rho_0 = 2.3$. Bottom: Density profiles chosen from the numerical simulation, for $Lk_d/v_p = 2.2, 2.9, 3.2$ from left to right. The black vertical lines in each density profile represent the membranes. The profile for $Lk_d/v_p = 2.9$ is plotted in the case of layers being stretched apart (right solid arrows) and being pushed together (left dashed arrows).

numerical calculation *versus* time as we simulate the displacement of the membranes. Both variations are in close agreement. Near the critical length L_c, the numerical calculation (dashed line) demonstrates smoother variations than the analytical profile. This is due to the finite displacement speed of the membranes.

3.3.3 Strongly contractile limit

Single layer and cortical regimes

We now focus on the strongly contractile limit. The profile of the effective gel tension g has a local minimum and a local maximum as before, but the contractile pressure contribution to g is very important, *e.g.* $g(\rho_{\mathrm{loc\,max}}) \geq g(\rho_\infty)$. The construction of the variations of L as a function of ρ_c starts as above. As L increases, ρ_c gets closer to $\rho_{\mathrm{loc\,max}}$. At this particular point, we try to find some stable value of $\rho_c \leq \rho_{\mathrm{loc\,max}}$ and such that $g(\rho_c) \geq g(\rho_{\mathrm{loc\,max}})$. This leads to $\rho_c \leq \rho_\infty$ which we have demonstrated to be impossible (in that limit the velocity field at the center is infinite). We denote the distance at which the layers can no longer be merged $L_{\mathrm{break}} = L(\rho_{\mathrm{loc\,max}})$.

We call $L_{\mathrm{bind}} = L(\rho_f)$ the critical length for which the separated layers (solution with discontinuous density mentioned in eq. (11)) barely touch. L_{bind} corresponds to twice the width of the single free layer. From eq. (11) we have $\rho_f \geq \rho_{\mathrm{loc\,max}}$, and as $L(\rho_c)$ is a decreasing function of ρ_c we easily get $L_{\mathrm{bind}} \leq L_{\mathrm{break}}$.

This reasoning demonstrates the existence of two solutions for lengths L in the interval $[L_{\mathrm{bind}}, L_{\mathrm{break}}]$. One solution corresponds to the *cortical* regime with sharp delimited layers and $\rho_c = \rho_\infty$. The other solution corresponds to merged layers, with $\rho_c > \rho_\infty$. It is the *single layer* regime. For $L \leq L_{\mathrm{bind}}$ the layers are merged. For $L \geq L_{\mathrm{break}}$ the layers are clearly separated.

Hysteresis effects

In order to determine in which regime the layers are for a given L in the critical interval $[L_{\mathrm{bind}}, L_{\mathrm{break}}]$, one must rely on the history of the double layer.

We consider the thought experiment of two *cortical* layers well separated and far apart. Infinitesimally slowly, the membranes are moved closer to one another. If fluctuations are small, the layers stay separated until $L = L_{\mathrm{bind}}$. At this critical length, they merge, the density at the center jumps from ρ_∞ to ρ_f. The system is now a *single layer*. As the membranes are moved closer still, the density at the center increases continuously. Upon moving the membranes apart the density at the center continuously decreases. For $L = L_{\mathrm{bind}}$, the density at the center is ρ_f. Pulling the membranes further apart, the *single layer*

starts to stretch, and the density at the center continues to decrease. At some critical point, where $\rho_c = \rho_{\mathrm{loc\,max}}$, and $L = L_{\mathrm{break}}$ the layer breaks apart and forms two well separated layers again, relaxing in the *cortical* regime.

This is well reproduced numerically, as illustrated in fig. 9. The analytic integration of eq. (10) and the numerical simulation are in close agreement, and demonstrate the hysteresis phenomenon between L_{bind} and L_{break}. Near these critical lengths, the numerical curve (dashed line) shows again smoother variations than the analytic profile. This is again due to the finite displacement speed of the membranes. We also present in fig. 9 density profiles to illustrate the transition with hysteresis from *single layer* (on the left-hand side) to *cortical* regime (on the right-hand side).

4 Stability of a stretched single layer

The coexistence of two regimes in the strongly contractile limit leads to the question of their relative stability. In this section, we study the stability of the stretched *single layer*. The general methodology for the study of the stability of the solutions is a linear expansion for small perturbations. Here this expansion is difficult and cannot lead to a simple answer because the system reacts very differently to a small addition or removal of matter. Indeed, numerically, it is easy to observe that an addition of matter on a stretched *single layer* leaves it intact. On the contrary, a removal of matter may damage the merged configuration irreversibly and the system relaxes to two separate *cortical* layers.

That explains why we choose to study the stability of the stretched *single layer* solutions in the following way: we study numerically the impact of a small removal of matter at the center of the domain, which respects the symmetry of the steady state solution.

4.1 Qualitative discussion of stability

We perform the following "numerical experiment". The initial condition is a stretched *single layer* steady state profile, into which a "hole" is introduced by lowering locally the density at the midplane. The hole depth ε is varied (in units of concentration). The width of the hole is chosen so that the hole is not too thin, but never wider than the space between the layers of the separate regime at $L = L_{\mathrm{break}}$. The width of the hole is not varied, and we checked that it has little impact on the final result. We study the effect of the removal for various values of $L \in [L_{\mathrm{break}}, L_{\mathrm{bind}})$.

This allows to draw a stability diagram for the stretched layer in the plane L *versus* damage depth ε, as shown in fig. 10. As expected, the more stretched the *single layer*, the smaller the critical depth to break apart the layer. As the layer is stretched up to $L = L_{\mathrm{break}}$, almost any removal depth breaks the *single layer* into two separated layers.

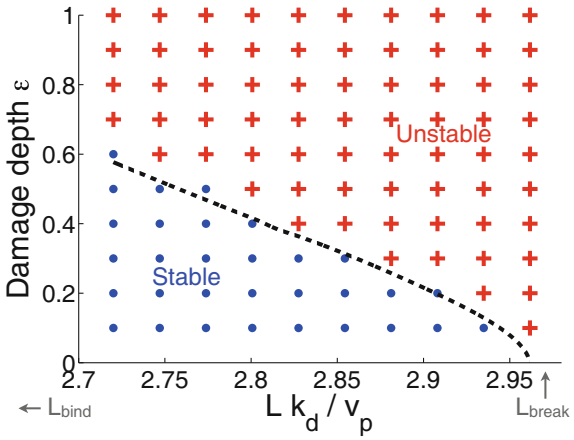

Fig. 10. Stability of the stretched layer as a function of the spacing between membranes (Lk_d/v_p) and the depth of the hole performed (ε). Each numerical experiment is represented by a data point. Red crosses represent coordinates that are unstable with respect to such a removal (*e.g.* the *single layer* breaks apart), blue spots represent coordinates that are stable. The dashed black line represents the analytical condition discussed in the text and corresponding to $\Pi(\rho_c(L) - \varepsilon) = \Pi(\rho_c(L))$. It ensures that all points below the line are stable. The numerical parameters used are the same as in fig. 9.

An interpretation of these results is based on the consideration of the initial velocity profile, just after the perturbation of the concentration profile. Let the velocity field be written as $v(z,t) = v_s(z) + w(z,t)$ where $v_s(z)$ is the steady state solution, and $w(z,t)$ the time-dependent correction to the steady state. In the same way we write $\rho(z,t) = \rho_s(z) + \delta\rho(z,t)$. With these notations the stress balance from eqs. (7) reads

$$2\eta\partial_{zz}w(z,t) = \partial_z\Pi(\rho_s(z) + \delta\rho(z,t)) - \partial_z\Pi(\rho_s(z)). \tag{12}$$

Equation (12) yields, at time $t = 0$, a good intuition of the initial velocity field induced by the perturbation.

We assume for simplicity that the hole in the concentration profile is performed roughly on a domain where $\rho_s(z) \simeq \rho_c$. On that interval $\delta\rho(z,0) = -\varepsilon$ with $\varepsilon > 0$. Away from the hole, $\delta\rho(z,0) = 0$. We remind also the boundary conditions on $w(z,0)$: $w(-L/2,0) = w(0,0) = w(L/2,0) = 0$.

Near the stability limit of the *single layer* ($\rho_{\mathrm{loc\,max}}$), the effective pressure as a function of ρ has a minimum. Therefore, $\Pi(\rho_c - \varepsilon)$ can either be greater or smaller than $\Pi(\rho_c)$. For instance, if ε is small and that we are far enough from $\rho_{\mathrm{loc\,max}}$, we have $\Pi(\rho_c - \varepsilon) \leq \Pi(\rho_c)$. Then, from eq. (12) the velocity field $w(z,0)$ is positive for $z < 0$ and negative for $z > 0$. This actin flow thus contributes to the healing of the layer, by filling up the initial hole. If, on the contrary, ε is large and that we are close to the concentration $\rho_{\mathrm{loc\,max}}$, *e.g.* close to the breaking point of the *single layer*, $\Pi(\rho_c - \varepsilon) > \Pi(\rho_c)$. Then, the resulting actin flow $w(z,0)$ from eq. (12) contributes to the breaking of the layer.

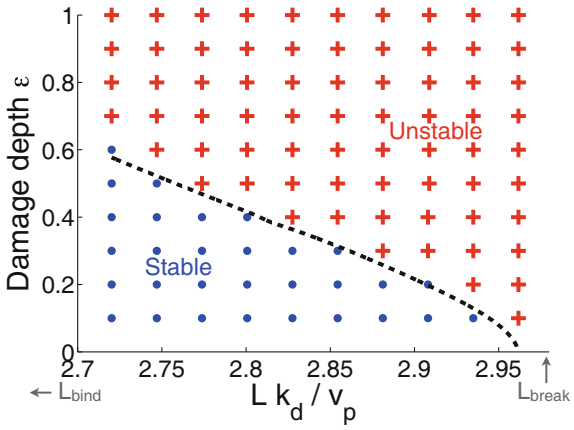

Fig. 11. Stability of the stretched layer as a function of the spacing between membranes (Lk_d/v_p) and the depth of the hole performed (ε) for a two-dimensional geometry with isotropic contractile properties. Each numerical experiment is represented by a data point. Red crosses represent coordinates that are unstable with respect to a removal of matter, blue spots represent coordinates that are stable. The dashed black line represents the analytical condition for stability in 1D discussed in the text. It is reported from fig. 10. The numerical parameters used are the same as for fig. 9 with specifically $a = a' = -4\eta k_d$.

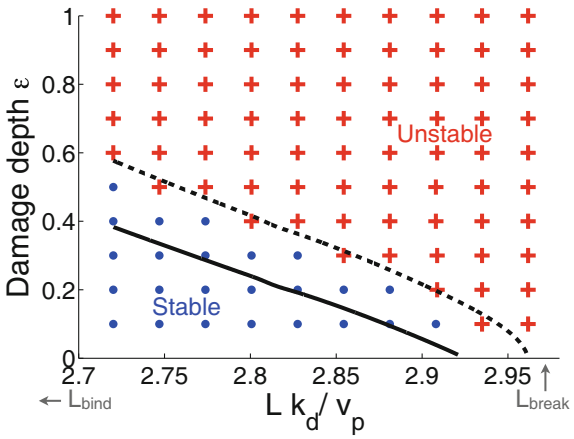

Fig. 12. Stability of the stretched layer as a function of the spacing between membranes (Lk_d/v_p) and the depth of the hole performed (ε) for a two-dimensional geometry with anisotropic contractile properties. Each numerical experiment is represented by a data point. Red crosses represent coordinates that are unstable with respect to a removal of matter, blue spots represent coordinates that are stable. The dashed black line represents the analytic condition for stability in 1D discussed in the text. The solid black line represents the 2D extension of this condition. It ensures that all points below the line are stable. The numerical parameters used are the same as for fig. 9 with specifically $a = -4\eta k_d$ and $a' = -4.2\eta k_d$.

One must however consider the total velocity field at the initial time $v(z,0) = v_s(z) + w(z,0)$ where the steady state flow $v_s(z)$ always contributes to the healing of the layer. The condition of monotonous increase of the pressure is therefore only a sufficient condition for the healing of the layer. The limit $\Pi(\rho_c - \varepsilon) = \Pi(\rho_c)$ is reported on fig. 10 as a dashed black line. On fig. 10 we verify that all points beneath the line are stable. All points above the line are not unstable: those closest to the line are still stable. Altogether this analytical condition yields an interesting intuition on the reasons for stability. The stability of the layer is closely related to the contractility of the gel.

4.2 Two-dimensional anisotropy

We recall from eqs. (6) that the actin layer in two dimensions has anisotropic contractile properties. Because contractility is essential in the study of stability, we study here the two-dimensional extension of the problem. Numerical solutions require the expressions for the functions $\Pi_x(\rho)$ and $\Pi_z(\rho)$. We write $\Pi_z(\rho) = a\rho^3 + b\rho^4$ as in the one-dimensional case, and choose $\Pi_x(\rho) = a'\rho^3 + b\rho^4$, where $a' < 0$ can be different from a and characterizes the contractile properties in the x direction.

For completeness we study first the case of isotropic contractility, *e.g.* $a = a'$ (this corresponds to an isotropic distribution of the orientation of filaments θ in eq. (1)). We perform the same "experiments" as in one dimension, studying the evolution of a rectangular shaped hole in the concentration profile at the center of the domain. Only the depth of the hole is varied, keeping the width constant as in the one-dimensional case, as well as the length in the x direction, parallel to the membranes. We also checked that this parameter has little influence on the results.

The results for isotropic contractility are summarized in fig. 11. As expected, the simulations prove to be fairly comparable to the one-dimensional case. On fig. 11, only one data point ($Lk_d/v_p = 2.77$ and a hole depth of 0.5) differs from the one-dimensional case, which is unstable whereas it is stable in one dimension. This difference has little relevance on the global aspect of the diagram. Moreover, the analytical condition for the one-dimensional case, reported on fig. 11, remains a good indicator for the stability of the stretched solutions.

We now perform the same "experiments" in the case of anisotropic contractility. Phenomenologically we expect contractility to be larger in the plane parallel to the main filament direction than in the direction perpendicular. In the *single layer*, where the membranes are closely facing each other, we expect the filaments to be mainly parallel to the plane of the membranes (x, y plane). In eq. (1), this can be coarsely modeled by setting $\theta \equiv \pi/2$. This yields $\zeta_x - \zeta_z = \zeta'/2 < 0$ in eqs. (6), and $a' < a$, that we expected.

We summarize the results in fig. 12. We observe that the increased contractility in the x direction results in the extension of the unstable domain. The former condition on Π obtained in the one-dimensional case, represented by the dashed black line on fig. 12, stipulating that all points below the line are stable, is no longer valid. This is because the condition only considers Π_z, and takes into account only the coefficient a, *e.g.* only the contractile

activity perpendicular to the membranes. Since $a' < a$, to write a valid analytical condition, we must now apply the same reasoning as in subsect. 4.1 for the velocity u in the x direction. We obtain that the stability of the layer is insured if $\Pi_x(\rho_c - \varepsilon) \leq \Pi_x(\rho_c)$ and $\Pi_z(\rho_c - \varepsilon) \leq \Pi_z(\rho_c)$. The combined conditions yield the new solid black line in fig. 12. This sufficient condition for stability is well verified: all points beneath the solid line are stable points.

We conclude that an excess contractility in the tangential direction destabilizes the stretched *single layer*.

On the other hand, if the filaments are mainly aligned with the direction z, perpendicular to the membranes, contractility is more important in that direction compared to the x, y directions. This writes $a < a'$. Lowered contractility in the tangential direction would then stabilize the stretched *single layer*.

5 Discussion

In this paper we have applied the theory of active gels to investigate the merging of two cortical actin layers into a single dense layer, similar in that way to the *lamellipodium*. We have shown that the activity of the actomyosin gel is essential for the understanding of the merging mechanism. Our main result is that a gel with strong contractility shows hysteresis in the merging of the two cortical layers. The transition from the single dense layer to two separate layers of actin cortex happens through a stretched configuration of the single layer. This stretched configuration has interesting stability properties, also monitored by contractility. As expected the more stretched the single layer, the less it is stable. In addition, an excess contractility in the tangential direction, due to alignment of the actin filaments along the membranes, is a source of instability of the stretched single layer.

In this study we did not consider the effect of actin density gradients in the effective pressure for simplicity. We do not expect that such terms play a major role in the physics we presented. It is easy to verify that the addition of a term proportional to $\nabla^2\rho$ in the effective pressure smoothens steep concentration profiles and suppresses the artificial jumps in concentration that we found here. It does not affect either the key role of contractility or the hysteresis phenomenon. On stretched one-dimensional solutions, it also has a stabilizing effect. This is interesting because it could balance the destabilizing effect of tangential contractility in two-dimensions. It is also of physical relevance because such a term could account for surface tension between the gel and the solvent.

Another limitation of our work is that we did not consider in details the orientation of the actin filaments. We have imposed that they are either parallel to the membrane with no preferred direction in the tangential plane, or isotropically distributed. A more complete theory will have to consider an orientation profile of the actin filaments that is coupled to the concentration and velocity profiles. For instance, in the study of the healing of a wounded stretched *single layer*, one should consider the variations of filament orientation around the wound. Neglecting such variations is only possible when the elastic modulus anisotropy is small. Here also, we do not expect any qualitative changes in the results.

The assumption of symmetric conditions of actin polymerization on each membrane can also be discussed. The cortex images of fig. 1(c) and (d) seem to indicate that the layer attached to the substrate and the layer attached to the "free" membrane have different thicknesses, although the precise trend is unclear. Asymmetric boundary conditions on the one-dimensional problem can be treated in a similar way as the symmetric boundary conditions. Because actin is polymerizing from each side, and because the velocity of the gel is a continuous function of z, the velocity has to vanish at a point z_0, which is no longer the middle of the actin slab. At this point however the density is still continuous, and we can redefine $\rho_c = \rho(z_0)$. The graphical construction can then be conducted on each side, in the same way as was done in sect. 3.3. For high actomyosin activities, the layers can bind at a distance equal to the sum of their respective free layer widths. When stretched again, they will separate at a larger distance. The hysteresis predicted for the symmetric case should also exist in the asymmetric one.

Several extensions of this work are possible. An important one would be to go beyond the steady state and consider the kinetics of formation of merging of two cortical layers. This requires the solution of the time-dependent equations for the cortical layers and is left for future work. Contractile waves are also often observed in cells [10] and it would be interesting to investigate their existence within the framework of our model.

Our predictions could be tested experimentally in different ways, not only to test the hysteretic behavior of the acto-myosin gel but also to confirm that the theory of active gels is able to describe in particular the acto-myosin gel. Pulling the upper membrane of a cell fragment with a well-defined surface and recording the force to pull and push it would allow a direct visualization of the hysteretic behavior of attachment of the actin layers. One could also confine cells between parallel plates monitoring carefully their separation and measuring the actin density profile as a function of thickness. It would also be of interest to track by fluorescence the actin distribution over time in moving cells, especially at the separation point. In any of these experiments, acto-myosin contractility could be increased or decreased using for instance myosin activators or inhibitors.

Other extensions of the theory could aim at a more realistic description of the *lamellipodium* in cells, in particular by investigating the height and shape of a cell from the near nucleus region to the edge of the *lamellipodium*. Apart from a possible three-dimensional extension of the theory, this would require writing explicitly force balance equations both perpendicular and parallel to the substrate. It would also require to investigate the longitudinal actin flux, and the variation in the polymerization conditions near the membranes.

Author contribution statement

Several people contributed to the work described in this paper. S.M., J.-F.J., and J.P. conceived the basic idea for this work. S.M. developed the theory and the simulations to identify the mechanisms of attachment of actin layers. A.L.G. and D.R. designed and performed the experiments to visualize *lamellipodia*. J.-F.J. and J.P. supervised the research and, with D.R., helped with the development of the paper.

The authors would like to thank Andrew Callan-Jones for discussions regarding [13]. They also would like to thank Pr. Karsten Kruse for enlightning meetings on the theory of active gels, and Pascal Kessler from IGBMC. They thank Matthieu Piel for useful discussions concerning experimental suggestions to check the predictions of the theory. Finally, they are indebted to Tatyana Svitkina and Günther Gerisch for helpful discussions on the acto-myosin cortex and the *lamellipodium*.

Appendix A. Cell culture and observations

Synthetic polyamines (C8-BPA) were recently shown to promote growth of *lamellipodia* within minutes [20]. In our context, we used them and visualized the cell cortex along the z-axis on single spread cells with different experiments (see fig. 1). Symmetric (fig. 1(c)) and non-symmetric (fig. 1(d)) cells were recorded depending on the experimental conditions. When C8-BPA is added on already spread cells, *lamellipodia* growth is promoted as well, but cortical layers stay non-symmetric around the nucleus.

Mouse NIH3T3 fibroblasts (ATCC, Manassas, VA) were grown in high glucose Dulbecco's Modified Eagle's Medium (Invitrogen, Reims, France) supplemented with 1% Pen Strep antibiotics (Invitrogen, Reims, France) and 10% bovine calf serum (BCS, Sigma-Aldrich, Lyon, France) at 37 °C and 5% CO_2. For symmetric cells, C8-PBA was added 1 hour and 20 min after cell resuspension using trypsin treatment. For non-symmetric cells, C8-BPA (100 μM) was incubated 80 min after seeding or on spread cells for 10 min before fixation with 3% paraformaldehyde (Sigma-Aldrich, France) at 37 °C for 17 min. Then, 0.5% Triton (Sigma-Aldrich, France) was added for 3 min to permeabilise cells, and samples were washed twice for 5 min with 1X PBS. For staining, we used fluorescent phalloidin (Molecular Probes) for F-actin, rabbit anti-myosin IIB (Sigma-Aldrich, France) for myosin with a fluorescent secondary antibody, and DAPI (4.6-diamidino-2-phenylidole, Sigma-Aldrich, France) for the nucleus. Cells were observed on a Leica SP5 inverted microscope with a 63× oil immersion objective (N.A. 1.4). Images were acquired with stacks of x-y planes spanning the cells width with z-step sizes of 0.25 μm. Planes along various directions were reconstructed with Imaris and Image J.

Appendix B. Tools for graphical resolution

In the following we work with adimensional variables such that eq. (10) reduces to

$$L(\rho_c) = 2\int_{\rho_0}^{\rho_c} \frac{\rho_0}{\rho^2(g(\rho)-g(\rho_c))} \times \ldots \exp\left(-\int_{\rho_0}^{\rho} \frac{(\rho'-\rho_\infty)}{(\rho')^2(g(\rho')-g(\rho_c))} d\rho'\right) \mathrm{d}\rho \qquad \text{(B.1)}$$

and show the results of subsect. 3.3.

L is a decreasing function of ρ_c

We calculate L in the vicinity of the midpoint $L(\rho_c(1+\varepsilon))$ and we assume that $\rho_c \geq \rho_0$, and $\varepsilon > 0$. This leads, at $o(\varepsilon)$, to

$$\begin{aligned}
&L(\rho_c(1+\varepsilon)) - L(\rho_c) = \\
&2\int_{\rho_0}^{\rho_c} \frac{\rho_0 \mathrm{d}\rho}{\rho^2(g(\rho)-g(\rho_c))} \exp\left(-\int_{\rho_0}^{\rho} \frac{\rho'-\rho_\infty}{(\rho')^2(g(\rho')-g(\rho_c))} d\rho'\right) \\
&\times \ldots \varepsilon\left[\frac{g'(\rho_c)}{(g(\rho)-g(\rho_c))} - g'(\rho_c)\left(\int_{\rho_0}^{\rho} \frac{\rho'-\rho_\infty}{(\rho')^2(g(\rho')-g(\rho_c))^2} d\rho'\right)\right] \\
&+\int_{\rho_c}^{\rho_c(1+\varepsilon)} \frac{\rho_0 \mathrm{d}\rho}{\rho^2(g(\rho)-g(\rho_c))} \exp\left(-\int_{\rho_0}^{\rho} \frac{\rho'-\rho_\infty}{(\rho')^2(g(\rho')-g(\rho_c))} \mathrm{d}\rho'\right) \\
&\times \ldots \left(1+\varepsilon\left[\frac{g'(\rho_c)}{(g(\rho)-g(\rho_c))} - g'(\rho_c)\left(\int_{\rho_0}^{\rho} \frac{\rho'-\rho_\infty}{(\rho')^2(g(\rho')-g(\rho_c))^2} d\rho'\right)\right]\right).
\end{aligned}$$

There are two integrals to study. We study the first integral and more particularly the function

$$F(\rho) = \frac{g'(\rho_c)}{(g(\rho)-g(\rho_c))} - g'(\rho_c)\left(\int_{\rho_0}^{\rho} \frac{\rho'-\rho_\infty}{(\rho')^2(g(\rho')-g(\rho_c))^2} d\rho'\right).$$

The derivative of this function is

$$F'(\rho) = \frac{(\rho-\rho_\infty)}{(g(\rho)-g(\rho_c))^2}\left[\frac{g'(\rho)(\rho-\rho_\infty)}{\rho^2} - 1\right].$$

In the domains of interest, $g'(\rho)$ is always negative and $\rho \geq \rho_\infty$ such that $F'(\rho) \leq 0$ and $F(\rho) \leq F(\rho_0) \leq 0$. This shows that the first integral can be rewritten as $-\alpha\varepsilon$ with α a positive constant.

We now consider the second integral and perform the change of variables $\rho = \rho_c(1+\epsilon)$. We get

$$\begin{aligned}
&\int_{\rho_c}^{\rho_c(1+\varepsilon)} \frac{\rho_0 \mathrm{d}\rho}{\rho^2(g(\rho)-g(\rho_c))} \exp\left(-\int_{\rho_0}^{\rho} \frac{(\rho'-\rho_\infty)d\rho'}{(\rho')^2(g(\rho')-g(\rho_c))}\right)(1+O(\varepsilon)) \\
&= \int_0^{\varepsilon} \frac{\rho_0 \mathrm{d}\epsilon}{\epsilon\rho_c^2 g'(\rho_c)} \exp\left(-\int_{\frac{\rho_0}{\rho_c}-1}^{\epsilon}\left(\frac{\rho_c-\rho_\infty}{(\rho_c)^2 g'(\rho_c)\epsilon'} + O(1)\right)\mathrm{d}\epsilon'\right)(1+O(\varepsilon)) \\
&= \int_0^{\varepsilon} \frac{\rho_0 \mathrm{d}\epsilon}{\epsilon\rho_c^2 g'(\rho_c)} \exp\left(\frac{-(\rho_c-\rho_\infty)}{(\rho_c)^2 g'(\rho_c)} \ln\left(\frac{\epsilon}{\frac{\rho_0}{\rho_c}-1}\right) + O(\epsilon)\right)(1+O(\varepsilon)) \\
&= \int_0^{\varepsilon} \frac{\rho_0 \mathrm{d}\epsilon}{\rho_c^2 g'(\rho_c)} \exp\left(\frac{\rho_c-\rho_\infty}{(\rho_c)^2 g'(\rho_c)} \ln\left(\frac{\rho_0}{\rho_c}-1\right)\right) \\
&\times \ldots \left(\epsilon^{-1-\frac{\rho_c-\rho_\infty}{(\rho_c)^2 g'(\rho_c)}} + O\left(\epsilon^{-\frac{\rho_c-\rho_\infty}{(\rho_c)^2 g'(\rho_c)}}\right)\right)(1+O(\varepsilon)) \\
&= -\frac{\rho_0}{\rho_c-\rho_\infty} \exp\left(+\left(\frac{\rho_c-\rho_\infty}{(\rho_c)^2 g'(\rho_c)} \ln\left(\frac{\rho_0}{\rho_c}-1\right)\right)\right)\left(\varepsilon^{-\frac{\rho_c-\rho_\infty}{(\rho_c)^2 g'(\rho_c)}}\right) \\
&+O\left(\varepsilon^{-\frac{\rho_c-\rho_\infty}{(\rho_c)^2 g'(\rho_c)}+1} + \varepsilon^2\right).
\end{aligned}$$

With these notations, one sees that the highest-order term in ε contributing to the full second integral of the expansion of $L(\rho_c(1+\varepsilon)) - L(\rho_c)$, is the term

$$-\frac{\rho_0}{\rho_c - \rho_\infty} \exp(\ldots)\varepsilon^{-\frac{\rho_c-\rho_\infty}{(\rho_c)^2 g'(\rho_c)}},$$

which is negative, and that all other terms are at least $O\left(\varepsilon^{-\frac{\rho_c-\rho_\infty}{(\rho_c)^2 g'(\rho_c)}+1} + \varepsilon^2\right)$ so in the end $o(\varepsilon)$.

Finally we get

$$L(\rho_c(1+\varepsilon)) - L(\rho_c) = -\alpha\varepsilon - \beta\varepsilon^{-\frac{\rho_c-\rho_\infty}{(\rho_c)^2 g'(\rho_c)}} + o(\varepsilon),$$

with α and β positive constants. This result imposes that $L(\rho_c(1+\varepsilon)) \leq L(\rho_c)$ and thus that L is a decreasing function of ρ_c.

We performed the above calculations assuming that $\rho_c \geq \rho_0$. However, the principle of the calculation does not change if we assume the reverse and the main result stays identical.

As L goes to $+\infty$, ρ_c converges to ρ_∞

We perform an expansion of L by writing $\rho_c \simeq \rho_\infty(1+\varepsilon)$ where $\varepsilon > 0$.

$$\begin{aligned}
&L(\rho_\infty(1+\varepsilon)) \\
&= \int_{\rho_0}^{\rho_\infty(1+\varepsilon)} \frac{\rho_0 \mathrm{d}\rho}{\rho^2(g(\rho)-g(\rho_\infty))} \exp\left(-\int_{\rho_0}^{\rho} \frac{\rho'-\rho_\infty}{(\rho')^2(g(\rho')-g(\rho_\infty))}\mathrm{d}\rho'\right) \\
&= \int_{\frac{\rho_0}{\rho_\infty}-1}^{\varepsilon} \frac{\rho_0 \mathrm{d}\epsilon}{\epsilon\rho_\infty^2 g'(\rho_\infty)} \exp\left(-\int_{\frac{\rho_0}{\rho_\infty}-1}^{\epsilon} \left(\frac{\rho_\infty \epsilon'}{(\rho_\infty)^2 g'(\rho_c)\epsilon'} + O(\epsilon')\right)\mathrm{d}\epsilon'\right) \\
&= \int_{\frac{\rho_0}{\rho_\infty}-1}^{\varepsilon} \frac{\rho_0 \mathrm{d}\epsilon}{\epsilon\rho_\infty^2 g'(\rho_\infty)} \exp\left(-\left(\frac{\rho_\infty}{(\rho_\infty)^2 g'(\rho_c)}\left(\frac{\rho_0}{\rho_\infty}-1\right)\right)\right)(1+O(\epsilon)) \\
&= \frac{\rho_0}{\rho_\infty^2 g'(\rho_\infty)} \exp\left(-\left(\frac{\rho_\infty(\rho_0-\rho_\infty)}{(\rho_\infty)^2 g'(\rho_c)\rho_\infty}\right)\right) \ln\left(\frac{\varepsilon}{\frac{\rho_0}{\rho_\infty}-1}\right) + O(\varepsilon).
\end{aligned}$$

Under this form we observe that

$$\lim_{\varepsilon\to 0} L(\rho_\infty(1+\varepsilon)) = +\infty.$$

As L goes to 0, ρ_c diverges to $+\infty$

This result has little physical meaning, since we are not much interested by situations corresponding to $\rho_c \geq \rho_0$, or $L \leq L_0$. However, it is of mathematical interest to verify that we can obtain solutions corresponding to all values of L. For that we integrate the first line of eqs. (7), which yields

$$\frac{2\rho_0 v_p}{L} + \rho_\infty k_d = k_d \frac{1}{L}\int_{-L/2}^{L/2} \rho(z)\mathrm{d}z,$$

such that if we define $\rho_m = \frac{1}{L}\int_{-L/2}^{L/2}\rho(z)\mathrm{d}z$ the average value of $\rho(z)$, ρ_m diverges as $L \to 0$.

Appendix C. Conditions for a discontinuity in the density profile

We first assume that there is at least one point of discontinuity in the density profile. Let z_0 be the closest point to the left-hand side membrane, where a discontinuity happens.

Integrating the first line of eqs. (7) with respect to z between $z_0-\epsilon$ and $z_0+\epsilon$, and taking the limit $\epsilon \to 0$ yields the continuity of flux

$$\rho(z_0)^+ v(z_0)^+ = \rho(z_0)^- v(z_0)^-.$$

Integrating the second line alike yields the continuity of stress

$$2\eta\partial_z v(z_0)^+ - \Pi(\rho(z_0))^+ = 2\eta\partial_z v(z_0)^- - \Pi(\rho(z_0))^-,$$

and integrating the second line twice yields the continuity of the velocity

$$v(z_0)^+ = v(z_0)^-.$$

This last equation, combined with the continuity of flux, tells us that a discontinuity in z_0 is possible if and only if the velocity vanishes in that point

$$v(z_0)^+ = v(z_0)^- = 0.$$

We now look for the density $\rho(z_0)^-$ on the left of the jump. On the interval $[-L/2, z_0)$ we can solve the equations analytically and obtain

$$v\big|_{z=z_0^-} = v_p \frac{\rho_0}{\rho(z_0)^-} \exp\left(-\int_{\rho_0}^{\rho(z_0)^-} \frac{2\eta k_d(\rho'-\rho_\infty)\mathrm{d}\rho'}{(\rho')^2(g(\rho')-g(\rho_c))}\right).$$

The only way to let $v|_{z=z_0-} = 0$ is that $g(\rho(z_0)^-) = g(\rho_c)$. This defines a unique $\rho(z_0)^-$, corresponding to the solution of $g(\rho(z_0)^-) = g(\rho_c)$, with $\rho(z_0)^- \geq \rho_{\mathrm{loc\,max}}$.

We need now find the value of $\rho(z_0)^+$. We use the conservation of the stress, that boils down to the conservation of g, namely $g(\rho(z_0)^-) = g(\rho(z_0)^+)$. This yields $\rho(z_0)^+ = \rho_c$ or $\rho(z_0)^+$ is the other root of $g(\rho(z_0)^+) = g(\rho_c)$ with $\rho_c < \rho(z_0)^+ < \rho_{\mathrm{loc\,max}}$.

Suppose $\rho(z_0)^+$ is such that $\rho_c < \rho(z_0)^+ < \rho_{\mathrm{loc\,max}}$.

Near $\rho(z_0)^+$, we have

$$\partial_z v\big|_{z=z_0,+} = -k_d\left(1-\rho_\infty/\rho(z_0)^+\right) < 0.$$

Hence v is negative near $\rho(z_0)^+$, for instance on the interval $(z_0, z_0+\delta z]$. We recall here a simple reformulation of eq. (8):

$$2\eta\frac{\mathrm{d}\rho}{\mathrm{d}z}v = \rho(g(\rho)-g(\rho_c)).$$

On the interval $(z_0, z_0+\delta z]$, v is negative. Suppose we have $\frac{\mathrm{d}\rho}{\mathrm{d}z} \geq 0$ on this interval. We thus get $g(\rho) < g(\rho_c)$, which implies necessarily, that $\rho \geq \rho(z_0)^+$ and is thus in contradiction with $\frac{\mathrm{d}\rho}{\mathrm{d}z} \geq 0$.

A similar contradiction can be found if we suppose that $\frac{\mathrm{d}\rho}{\mathrm{d}z}$ is negative on this small interval.

We are left with the other scenario: $\rho(z_0)^+ = \rho_c$.

In that case, we again have a strictly decreasing velocity, and again a contradiction except if $\rho_c = \rho_\infty$. In that specific case, a plateau density profile of any length is possible.

As a conclusion, if there is a jump in the density profile, it is possible only from the single density value $\rho(z_0)^-$ that verifies $g(\rho(z_0)^-) = g(\rho_\infty)$ and $\rho(z_0)^- > \rho_{\mathrm{loc\,max}}$. We denote by ρ_f this value of density. ρ_f verifies $g(\rho_\infty) = g(\rho_f)$ and $\rho_f > \rho_{\mathrm{loc\,max}}$. The f stands for *free* because this specific profile characterizes the *cortical* regime where the layers are distinctly separated from one another. In this regime, the density goes from ρ_0 at the membrane to ρ_f, and then jumps to ρ_∞ and stays at that value until the boundary of the other layer is reached (where the density jumps back to ρ_f and continuously rises to ρ_0, as plotted in fig. 6).

Appendix D. Numerical methods

The simulations were performed using a finite-volume method to capture the sharp variations in the density profile. The mesh is constituted in 1D of 100 boxes with different sizes adapted to capture the critical behaviors at the midplane. The mesh was similarly adapted in 2D for a 60 by 60 pavement of boxes. The initial condition on the density profile is then propagated iteratively thanks to the integrated version of eqs. (7).

The first step is to update the velocity profile via the equilibrium of constraints equation. The second step is to propagate the concentration profile in time via the conservation of mass equation. This is done using a standard upstream/downstream explicit propagation, with autoadaptive time step.

For the simulations of sect. 3, implying temporal change of the domain size (slow movement of the distance between membranes), we renormalized the set of eqs. (7) in space. This results in a new advection term in the mass conservation equation, implying the time derivative of the domain size. The relative speed of the membrane planes was diminished until finding a convincing approximation of the steady state profiles.

For the simulations of sect. 4, the characteristics of the hole were monitored over time, for a sufficient amount of time, but not until complete relaxation of the system, to determine the outcome of the simulation. For instance, if the hole filled up till 90% of its initial depth, we concluded that the outcome of the experiment was a healed *lamellipodium*.

References

1. V.C. Abraham, V. Krishnamurthi, D.L. Taylor, F. Lanni, Biophys. J. **77**, 1721 (1999).
2. T.D. Pollard, G.G. Borisy, Cell **112**, 453 (2003).
3. J. Wu, I.A. Kent, N. Shekhar, T.J. Chancellor, A. Mendonca, R.B. Dickinson, T.P. Lele, Biophys. J. **106**, 7 (2014).
4. V. Achard, J.-L. Martiel, A. Michelot, C. Guérin, A.-C. Reymann, L. Blanchoin, R. Boujemaa-Paterski, Curr. Biol. **20**, 423 (2010).
5. J.-F. Joanny, K. Kruse, J. Prost, S. Ramaswamy, Eur. Phys. J. E **36**, 52 (2013).
6. H. Turlier, B. Audoly, J. Prost, J.-F. Joanny, Biophys. J. **106**, 114 (2014).
7. T.D. Pollard, L. Blanchoin, R.D. Mullins, Annu. Rev. Biophys. Biomol. Struct. **29**, 545 (2000).
8. O. Medalia, I. Weber, A.S. Frangakis, D. Nicastro, G. Gerisch, W. Baumeister, Science **298**, 1209 (2002).
9. G. Salbreux, G. Charras, E. Paluch, Trends Cell Biol. **22**, 10 (2012).
10. P.M. Bendix, G.H. Koenderink, D. Cuvelier, Z. Dogic, B.N. Koeleman, W.M. Brieher, C.M. Field, L. Mahadevan, D.A. Weitz, Biophys. J. **94**, 3126 (2008).
11. K. Kruse, J.-F. Joanny, F. Jülicher, J. Prost, K. Sekimoto, Eur. Phys. J. E **16**, 5 (2005).
12. J.-F. Joanny, F. Jülicher, K. Kruse, J. Prost, New J. Phys. **9**, 422 (2007).
13. A.C. Callan-Jones, F. Jülicher, New J. Phys. **13**, 093027 (2011).
14. R. Voituriez, J.F. Joanny, J. Prost, Europhys. Lett. **70**, 404 (2005).
15. S. Fürthauer, M. Neef, S.W. Grill, K. Kruse, F. Jülicher, New J. Phys. **14**, 023001 (2012).
16. S. Günther, K. Kruse, New J. Phys. **9**, 417 (2007).
17. G. Salbreux, J. Prost, J.F. Joanny, Phys. Rev. Lett. **103**, 058102 (2009).
18. K. Kruse, J.-F. Joanny, F. Jülicher, J. Prost, Phys. Biol. **3**, 130 (2006).
19. D.A. Lauffenburger, A.F. Horwitz, Cell **84**, 359 (1996).
20. I. Nedeva, G. Koripelly, D. Caballero, L. Chièze, B. Guichard, B. Romain, E. Pencreach, J.-M. Lehn, M.-F. Carlier, D. Riveline, Nat. Commun. **4**, 2165 (2013).
21. S. Diez, G. Gerisch, K. Anderson, A. Müller-Taubenberger, T. Bretschneider, Proc. Natl. Acad. Sci. U.S.A. **102**, 7601 (2005).
22. N. Watanabe, T.J. Mitchison, Science **295**, 1083 (2002).
23. F. Gerbal, P. Chaikin, Y. Rabin, J. Prost, Biophys. J. **79**, 2259 (2000).
24. V. Noireaux, R.M. Golsteyn, E. Friederich, J. Prost, C. Antony, D. Louvard, C. Sykes, Biophys. J. **78**, 1643 (2000).
25. F. Jülicher, K. Kruse, J. Prost, J.-F. Joanny, Phys. Rep. **449**, 3 (2007).
26. T. Kim, M.L. Gardel, E. Munro, Biophys. J. **106**, 526 (2014).

Amélie GODEAU

Cyclic contractions contribute to 3D cell motility

Résumé

La motilité des cellules est un phénomène fondamental en biologie souvent étudié sur des surfaces planes, conditions peu physiologiques. Nous avons analysé la migration cellulaire dans une matrice cellulaire 3D contenant de la fibronectine fluorescente. Nous démontrons que les cellules y sont confinées, et déforment leur environnement de manière cyclique avec une période de ~14 min avec deux centres de contractions à l'avant et à l'arrière de la cellule qui contractent avec un déphasage de ~3.5 min. Une perturbation de ces cycles entraîne une réduction de la motilité. Par l'utilisation d'inhibiteurs spécifiques, nous avons identifié l'acto-myosine comme étant l'acteur principal de ce phénomène. En imposant des contractions-relaxations locales par ablations laser, nous avons déclenché la motilité cellulaire ce qui confirme notre hypothèse. L'ensemble de cette étude met en évidence un nouveau mécanisme fondamental de dynamique cellulaire impliqué dans le mouvement des cellules.

Mots-clés: migration cellulaire 3D, matrice extracellulaire, oscillations, cytosquelette, mécanique cellulaire.

Résumé en anglais

Cell motility is an important process in Biology. It is mainly studied on 2D planar surfaces, whereas cells experience a confining 3D environment *in vivo*. We prepared a 3D Cell Derived Matrix (CDM) labeled with fluorescently labeled fibronectin, and strikingly cells managed to deform the matrix with specific patterns : contractions occur cyclically with two contraction centers at the front and at the back of the cell, with a period of ~14 min and a phase shift of ~3.5 min. These cycles enable cells to optimally migrate through the CDM, as perturbation of cycles led to reduced motility. Acto-myosin was established to be the driving actor of these cycles, by using specific inhibitors. We were able to trigger cell motility externally with local laser ablations, which supports this framework of two alternating contractions involved in motion. Altogether, this study reveals a new mechanism of dynamic cellular behaviour linked to cell motility.

Keywords: 3D cell migration, cell derived matrix, oscillations, cytoskeleton, cell mechanics.